Probing the Epoch of Reionization using line-intensity mapping

PhD Thesis

by

Chandra Shekhar Murmu

Roll No. 1901121005

Under the supervision of

Dr. Suman Majumdar

&

Dr. Kanan Kumar Datta

Department of Astronomy, Astrophysics and Space Engineering
Indian Institue of Technology Indore

Probing the Epoch of Reionization using line-intensity mapping

A THESIS

Submitted in partial fulfillment of the

requirements for the award of the degree

of

DOCTOR OF PHILOSOPHY

by

Chandra Shekhar Murmu

Roll No. 1901121005

Under the supervision of

Dr. Suman Majumdar

&

Dr. Kanan Kumar Datta

Department of Astronomy, Astrophysics and Space Engineering
Indian Institute of Technology Indore

INDIAN INSTITUTE OF TECHNOLOGY INDORE

I hereby certify that the work which is being presented in the thesis entitled **Probing the Epoch of Reionization using line-intensity mapping** in the partial fulfillment of the requirements for the award of the degree of **DOCTOR OF PHILOSOPHY** and submitted in the **Department of Astronomy, Astrophysics and Space Engineering, Indian Institute of Technology Indore**, is an authentic record of my own work carried out during the time period from **July 2019** to **November 2024** under the supervision of **Dr. Suman Majumdar**, associate professor, Indian Institute of Technology Indore and **Dr. Kanan K. Datta**, assistant professor, Jadavpur University.

The matter presented in this thesis has not been submitted by me for the award of any other degree of this or any other institute.

Chandra Shekhar Murmu
27/03/2025

Signature of the student with date
Chandra Shekhar Murmu

This is to certify that the above statement made by the candidate is correct to the best of my/our knowledge.

Suman Majumdar 27/03/2025
Signature of Thesis Supervisor #1 with date
Dr. Suman Majumdar

Kanan Kumar Datta
27/03/2025
Signature of Thesis Supervisor #2 with date
Dr. Kanan K. Datta

Chandra Shekhar Murmu has successfully given his/her Ph.D. Oral Examination held on **27th March 2025**.

Suman Majumdar 27/03/2025
Signature of Thesis Supervisor #1 with date
Dr. Suman Majumdar

Kanan Kumar Datta
27/03/2025
Signature of Thesis Supervisor #2 with date
Dr. Kanan K. Datta

Acknowledgements

I am pleased to have the opportunity at the Indian Institute of Technology Indore (IIT Indore) and the financial support from the *Council of Scientific and Industrial Research* (CSIR) via a CSIR-JRF and CSIR-SRF fellowship, under the grant 09/1022(0080)/2019-EMR-I, which allowed me to conduct research during my PhD. I am thankful to my supervisors, Dr. Suman Majumdar (IIT Indore) and Dr. Kanan Kumar Datta (Jadavpur University), for the valuable guidance and feedback throughout my PhD journey and on the projects I have worked on. They have encouraged and motivated me to thoroughly explore the literature available on line-intensity mapping, which is the current focus of this thesis, and to develop working knowledge in this domain. From time to time, I have received support and feedback from them on formulating the projects, developing computational codes, and approaching and solving problems for the projects. I have also received helpful advice on preparing presentations and developing presentation skills for annual progress seminars at IIT Indore and for various conferences, which have helped me to disseminate my research results to the broader community in an effective manner. During the preparation of the manuscripts, I also received thorough feedback. Over time, I have learned much from them, which has helped polish my skills. One of the critical periods in my PhD was during the COVID-19 lockdown when I was away from Indore (where IIT Indore is located) to avoid the harsh conditions there. I spent almost a span of two years in my hometown to continue my work remotely. However, my online discussions with my supervisors weren't hampered much during this time, which led to the smooth continuation of the projects. I was fortunate that remote access to the computational resources of the Cosmology with Statistical Inference (CSI) research group at IIT Indore was arranged such that one didn't have to stay connected to the intranet of IIT Indore, which made it possible for me to run the computational jobs remotely during the COVID-19 lockdown, that was necessary to continue the projects while I was afar from Indore.

I mention here my collaborators, Prof. Thomas R. Greve, Dr. Karen P. Olsen, Bryan R. Scott, Dr. T. K. Daisy Leung, Prof. Romeel Davé, Dr. Gergö Popping, Raul O. Ochoa, Dr. David Vizgan, Dr. Desika Narayanan, Prof. Garrelt Mellema, Prof. Dr. L. V. E. Koopmans and Dr. Bharat K. Gehlot, who have significantly contributed to the projects and acknowledge their support, comments, and feedback. I thank Prof. Thomas R. Greve for sharing pre-simulated data which has been crucial for a collaborative project. I also acknowledge support from the *Scheme for Promotion of Academic and Research Collaboration* (SPARC, No. SPARC/2018-2019/P39/SL, Indian PI: Dr. Suman Majumdar, IIT Indore and Indian co-PI: Prof. Abhirup Datta, IIT Indore, International PI: Prof. Garrelt Mellema, Stockholm University, and International co-PI: Dr. Erik Zackrisson, Uppsala University), for a SPARC-approved project titled "Imaging the first billion years of the universe with next-generation telescopes" that sponsored an international academic visit for me and one of my colleagues, Anshuman Tripathi, to the Stockholm University and Uppsala University. This was also the first international visit in my life. I was able to explore a new academic environment and meet and engage with Prof. Garrelt

Mellema, Dr. Erik Zackrisson, and other people there. This was also when, for the first time, I was able to pay an academic visit to the Cosmic Dawn Center, DTU Space, Technical University of Denmark, to meet with Prof. Thomas R. Greve, who is one of the collaborators in the projects I worked on. He had generously sponsored the visit to Copenhagen for me and Anshuman, where Cosmic Dawn Center is located. I acknowledge Prof. Garrelt Mellema, for sharing pre-simulated data that has been significantly useful for my collaborative PhD project.

I am thankful to the journal referees for providing useful comments and feedback that have been significant in improving the work that I have done. I also would like to thank the members of my PG Student Progress Committee (PSPC), Prof. Abhirup Datta, Dr. Manoneeta Chakraborty, and Prof. Subhendu Rakshit for serving as committee members to evaluate my annual research progress and provide helpful comments and feedback on my PhD work. I acknowledge financial support from the organizers of the conference ”Cosmology in the Alps” held during March 2024 in Les Diablerets, Switzerland, for the conference costs and travel support from IIT Indore, which sponsored the international visit to Les Diablerets to participate in the conference event and allowed me to reach to a broader community to disseminate my research results. I also acknowledge Dr. Hamsa Padmanabhan, for generously sponsoring a short visit to the University of Geneva, during this time in Switzerland. Further, I also acknowledge accommodation support from the organizers of the conference program, ”Cosmic Dawn at High Latitudes”, held during June - July 2024, in NORDITA, Stockholm, and thank the international travel scheme from *Science and Engineering Research Board* (SERB) for approving travel support (No. ITS/2024/001803) for the international visit to Stockholm to attend this program and present my research to the broader community. This was the second time I visited Sweden during my PhD, and I was happy to visit Prof. Thomas Greve again at Cosmic Dawn Center, who generously sponsored the visit.

I want to mention and thank my colleagues, batchmates, and friends, Soumen Datta, Chandrani Chatterjee, Harsha Avinash Tanti, Anshuman Tripathi, Swarna Chatterjee, Sushmita Agarwal, Gourav Giri, Arghyadeep Paul, and Hemapriya R., for the occasional get-togethers and creating cheerful moments. I am also fortunate that my senior colleague, Dr. Mohd. Kamran had shared his apartment with me for almost a month and a half during his time at IIT Indore when I came back to Indore from my hometown after nearly two years and before I visited Sweden. I must also thank Soumen for proposing that I shift to his apartment after returning to Indore from my visit to Sweden, where I continued the rest of my PhD journey. I also thank my junior colleagues, Samit Pal and Leon Noble, for the valuable discussions relevant to my PhD work.

Dedicated to my family

List of publications

- **Murmu, C. S.**, Majumdar, S., & Datta, K. K. (2021). CII and HI 21-cm line intensity mapping from the EoR: impact of the light-cone effect on auto and cross-power spectra. *Monthly Notices of the Royal Astronomical Society*, 507(2), 2500–2509, DOI: 10.1093/mnras/stab2347, arXiv: 2107.09072

- **Murmu, C. S.**, Ghara, R., Majumdar, S., & Datta, K. K. (2022). Probing the epoch of reionization using synergies of line intensity mapping. *Journal of Astrophysics and Astronomy*, 43(2), DOI: 10.1007/s12036-022-09882-z, arXiv: 2210.09612 (**Review article**)

- **Murmu, C. S.**, Olsen, K. P., Greve, T. R., Majumdar, S., Datta, K. K., Scott, B. R., Leung, T. K. D., Davé, R., Popping, G., Ochoa, R. O., Vizgan, D., & Narayanan, D. (2022). Revisiting the [C II]158μm line-intensity mapping power spectrum from the EoR using non-uniform line-luminosity scatter. *Monthly Notices of the Royal Astronomical Society*, 518(2), 3074–3082, DOI: 10.1093/mnras/stac3304, arXiv: 2110.10687

- **Murmu, C. S.**, Datta, K. K., Majumdar, S., & Greve, T. R. (2024). Impact of astrophysical scatter on the epoch of reionization [H I] 21cm bispectrum. *Journal of Cosmology and Astroparticle Physics*, 2024(08), 032, DOI: 10.1088/1475-7516/2024/08/032, arXiv: 2311.17062

- **Murmu**+2024, Forecasting the CO$\times$[H I]$_{21\mathrm{cm}}$ cross-power spectrum from the EoR with line-intensity mapping surveys (**In prep.**)

- Noble, L., Kamran, M., Majumdar, S., **Murmu, C. S.**, Ghara, R., Mellema, G., Iliev, I. T., & Pritchard, J. R. (2024). Impact of the Epoch of Reionization sources on the 21-cm bispectrum. *Journal of Cosmology and Astroparticle Physics*, 2024(10), 003, DOI: 10.1088/1475-7516/2024/08/032, arXiv: 2406.03118

- Mishra, A., **Murmu, C. S.**, Datta, K. K., Choudhuri, S., Majumdar, S., Nasreen, I., Ali, S. S. (2024), Detecting ionized bubbles around luminous sources during the reionization era using HI 21cm signal. *Journal of Cosmology and Astroparticle Physics* 2025(02), 055, DOI: 10.1088/1475-7516/2025/02/055, arXiv: 2408.01681

- Dutta, S., **Murmu, C. S.**, Majumdar, S., & Tiwari, H. (2024), Interpreting C II line intensity mapping power spectrum via ANN assisted Bayesian Inference (**In prep.**)

Note: The top five in the above list are part of this thesis.

Abstract

The **epoch of reionization** (**EoR**) is the period in the evolutionary history of the Universe when the first luminous sources were formed and emitted Lyman continuum photons capable of ionizing the neutral hydrogen in the intergalactic medium (IGM). This epoch marked an important episode in the cosmic timeline and was also the last major phase transition in the Universe. The earliest probes of this epoch include the optical depth measurement of Thomson scattering of the cosmic microwave background (CMB) photons, which can constrain the mid-point of the cosmic reionization. On the other hand, observations of the quasar spectra from high redshifts suggest that reionization might have ended around a redshift of ~ 6. However, these limited observations do not give a comprehensive picture of the reionization era, such as the nature of the ionizing sources and how the reionization process progressed. The galaxy surveys with **ALMA** and **JWST** are probing this mysterious era by detecting a limited number of galaxy samples from the EoR and helping to uncover their nature. The key drawback of these instruments is that surveying large cosmological volumes is expensive and can only provide detections of early galaxies within a small field of view. Therefore, these surveys are not suitable for comprehending the EoR alone. One proposed way to complement the galaxy surveys is the **line-intensity mapping** (**LIM**) technique, which detects the integrated flux of the unresolved galaxies and the diffuse IGM. It can therefore probe much larger scales with comparatively less observational time than conventional galaxy surveys and is expected to probe the EoR. The bright spectral lines like the $[\text{C II}]_{158\mu\text{m}}$, CO, $[\text{O III}]_{88\mu\text{m}}$, Ly-$\alpha$, etc., originating from the galaxies, are typically targeted by LIM instruments to investigate the clustering of luminous sources. The $[\text{C II}]_{158\mu\text{m}}$ emission, being a reliable indicator of star formation activity, is a strong candidate for LIM to study early galaxies during the EoR. Experiments such as the **CONCERTO**, **TIME**, and **FYST**, are expected to map the fluctuations of the LIM signal of $[\text{C II}]_{158\mu\text{m}}$ emission from the EoR galaxies. Similarly, the CO line emission, a tracer of molecular gas and star formation in galaxies, is expected to be probed by the **COMAP** LIM experiment from the same epoch. On the other hand, radio interferometers such as **HERA**, **MWA**, and the upcoming **SKA** will detect the redshifted $[\text{H I}]_{21\text{cm}}$ signal originating from the diffuse IGM during the EoR, which will help us to understand the evolution of IGM from this epoch. These line emissions from the galaxies and the IGM are determined by various astrophysical phenomena. Consequently, the corresponding LIM signals will capture this information, and the observable summary statistics will be sensitive to the underlying astrophysics of these line emissions. Therefore, it is essential to build forward models of these summary statistics, which will be useful, to interpret the observations from the LIM experiments. In the fiducial models of galaxy line emissions, one assumes a one-to-one scaling relation between the host halo mass of the galaxy and the corresponding line luminosity of the galaxy, which is computationally cheap to implement. However, astrophysical conditions such as multi-phase state of the ISM in the galaxies will introduce a significant halo-mass dependent line luminosity scatter in the $[\text{C II}]_{158\mu\text{m}}$ line emission from these galaxies. This is usually not taken into

account in the models, and how this would affect summary statistics such as the power spectrum of the [C II]$_{158\mu\mathrm{m}}$ emission **is** not known. Similarly, in the fiducial models of reionization of the IGM, the variability of the star-formation rate (SFR) with respect to the host halo mass is neglected and a one-to-one scaling relation is assumed. This variation, or astrophysical scatter, can affect the ionizing luminosity of the galaxies, thereby changing the nature of ionization in the IGM, and can introduce a non-Gaussian component to the [H I]$_{21\mathrm{cm}}$signal that may not be fully represented in the power spectrum. Therefore, higher-order Fourier statistics like the bispectrum of the [H I]$_{21\mathrm{cm}}$ signal might capture the imprints of astrophysical scatter in the IGM, which had not been investigated previously. Also, within the galaxies, the correlation between far-infrared luminosity and CO line luminosity can act as a proxy for the relation between SFR and gas depletion. In the post-EoR regime, this has been characterized by galaxy surveys, but it is challenging to achieve during the EoR due to limited observations. It is expected that CO LIM observations of the EoR with **COMAP** can constrain this correlation, although instrumental noise will contaminate the signal and challenge its detection. It is expected that cross-correlation with a complementary signal, such as the [H I]$_{21\mathrm{cm}}$ emission from the IGM during the same epoch, might have better prospects of detection. However, this is not well investigated in the context of detecting the various far-infrared luminosity and CO line luminosity correlation models that can determine the CO emission from the galaxies and how these models can be contrasted in the EoR. In this thesis, these broad ranges of astrophysical phenomena are addressed. In addition, there will be a line-of-sight anisotropy (LoS) in the observed LIM signals, due to the finite time taken by radiation to reach the observer. The impact of this light-cone effect on the galaxy LIM auto and cross-power spectra has also not been well explored before which has been addressed in this thesis. In this study, it has been demonstrated that the light-cone anisotropy can alter the power spectrum of [C II]$_{158\mu\mathrm{m}}$LIM signal by a magnitude greater than 15 percent at $k \sim 0.1$ Mpc^{-1} for redshift 6.8. Furthermore, it has been observed that the light-cone effect on the power spectrum of [C II]$_{158\mu\mathrm{m}}$LIM signal diminishes with decreasing redshift within the examined redshift range ($6 \lesssim z \lesssim 7.2$). The light-cone effect also affects the cross-power spectrum of the [C II]$_{158\mu\mathrm{m}}$ and [H I]$_{21\mathrm{cm}}$ LIM signal, and the magnitude of the impact and the scale that is affected vary with reionization history. The maximum impact on the cross-power spectrum of [C II]$_{158\mu\mathrm{m}}$and [H I]$_{21\mathrm{cm}}$LIM signal can reach up to 20 percent, in the models of cosmic reionization investigated, where reionization ends before $z = 6$. Therefore, incorporating the light-cone effect in the forward models of auto and cross-power spectrum is essential for accurately modeling and constraining reionization history and the astrophysical parameters related to EoR. This study also considers line-luminosity scatter with halo-mass dependence in [C II]$_{158\mu\mathrm{m}}$ emission, derived from a simulation of galaxies at $z = 6$ with cosmological hydrodynamic and radiative transfer calculations. Consequently, it is found that the mean intensity of the LIM signal is not preserved when the scenario is interpreted with the mean luminosity-halo mass correlation fit; therefore, the clustering power spectrum is altered in this case. However, in this scenario, a robust interpretation of the impact of halo-mass dependent scatter on the power spectrum of [C II]$_{158\mu\mathrm{m}}$ LIM signal can be given using the most probable fit.

Similarly, using the bispectrum of the $[\text{H I}]_{21\text{cm}}$ signal from the EoR derived from semi-numerical simulations, it is found that the small ionized regions are dominantly affected by the scatter in the SFR, whereas it does not largely affect the larger ionized bubbles. At smaller scales ($k_1 \sim 2.55$ Mpc^{-1}), the scatter's impact is both large in magnitude with $0.2 \lesssim |\langle \Delta B \rangle / B_{\text{no-scatter}}| \lesssim 1$ and statistically significant with $|\langle \Delta B \rangle / \sigma_{\Delta B}| \gtrsim 5$, for redshift of 7.4, at a neutral fraction of $\langle x_{\text{HI}} \rangle \sim 0.8$. This impact is even more pronounced ($|\langle \Delta B \rangle / B_{\text{no-scatter}}| \gtrsim 10$) for redshift of 10, at smaller scales and at $\langle x_{\text{HI}} \rangle \sim 0.8$, although the statistical significance diminishes somewhat ($|\langle \Delta B \rangle / \sigma_{\Delta B}| \sim 3$) at the same neutral fraction, compared to redshift of 7.4. Optimistically, the **SKA1-Low** telescope might detect these imprints of astrophysical scatter with a detection significance of roughly 3σ and 5σ at a redshift of 7.4 for $\langle x_{\text{HI}} \rangle \sim 0.8$ and 0.9, respectively, using the equilateral $[\text{H I}]_{21\text{cm}}$ bispectrum. Finally, using radiative transfer output for the $[\text{H I}]_{21\text{cm}}$ signal and a semi-analytic approach for the CO signal at $z \sim 7.2$, it is found that the detection prospects for the weakest CO emission model improve significantly in cross-correlation, considering 1200 and 2400 hours of **AARTFAAC** observing time, surveying $[\text{H I}]_{21\text{cm}}$ signal from the EoR. The $\text{CO}(1-0)$ signal has better detection prospects in the **COMAP-EoR** campaign compared to the $\text{CO}(2-1)$ signal in the **COMAP-Pathfinder** campaign, with a detection significance of 2.5σ in cross-correlation for the weakest model at $k \sim 0.12$ Mpc^{-1}. Additionally, using the $\text{CO}(1-0) \times [\text{H I}]_{21\text{cm}}$ cross-power spectrum, a wide range of $L_{\text{FIR}} - L'_{\text{CO}}$ correlation models can be contrasted with $\gtrsim 3\sigma$ significance for 2400 hours of **AARTFAAC** observing time. Therefore, LIM can address a wide range of astrophysical phenomena from the EoR and help us comprehend this mysterious epoch. It is essential to develop accurate forward models of the LIM summary statistics that can interpret the ongoing/upcoming observations with LIM experiments probing the EoR.

Contents

List of Figures

List of Tables

Chapter 1

Introduction

In the 21st century, we have seen excellent progress in the field of cosmology with the advent of modern technologies. In the past few decades, cosmologists have conducted detailed investigations of the cosmic microwave background, which carries information about the very earliest stages of the evolution of the Universe that one can probe. Recent observational missions like the **Planck** (Planck Collaboration, Aghanim, Akrami, Arroja, et al. 2020) have made high-resolution maps of the fluctuations in the CMBR compared to its predecessor, **Wilkinson Microwave Anisotropy Probe** (**WMAP**, Bennett et al. 2013), and allow us to understand its small-scale features. Also, large-scale galaxy redshift surveys have made progress in unveiling the distribution of luminous matter in our local Universe. It has been pushed to the distant Universe as well with the detection of $\sim$ 50,000 Lyman-α emitters with the **Hobby Eberly Telescope Dark Energy Experiment (HETDEX)**, up to $z \lesssim 3.5$ (Mentuch Cooper et al. 2023). It will allow us to probe the accelerated expansion of the Universe and shed light on the nature of dark energy.

However, some limitations remain in extending large-scale galaxy surveys to the Epoch of Reionization (EoR), when the first luminous objects were formed in the Universe. The most abundant element in the Universe, hydrogen, which is ubiquitously present in the Universe, started to get ionized when galaxies began to form. The ultraviolet (UV) radiation from these sources drove the reionization process, and these galaxies are assumed to be the primary agents of reionization. Other sources, such as uniform ionizing backgrounds contributed by mini-QSOs, X-ray binaries, or AGNs McQuinn 2012; Mesinger, Andrea Ferrara, and Spiegel 2013; Majumdar, Jensen, et al. 2016, can also play a role in reionization. This period was the last major phase of the transition of the Universe (see figure 1.1).

Halos are located in over-dense regions and therefore the gas density within the halos is considerably higher than that of the IGM. The ionizing photons emitted in the galaxies must escape this high-density gas to ionize the IGM. The escape fraction of these ionizing photons is a significantly uncertain quantity as it can vary with redshift and galaxy mass. This can affect the overall radiation intensity to varying degrees. Also, simulations of cosmic reionization often model the sources of ionizing radiation and their surroundings as point sources because of poor resolution (refer e.g., Gnedin 2000).

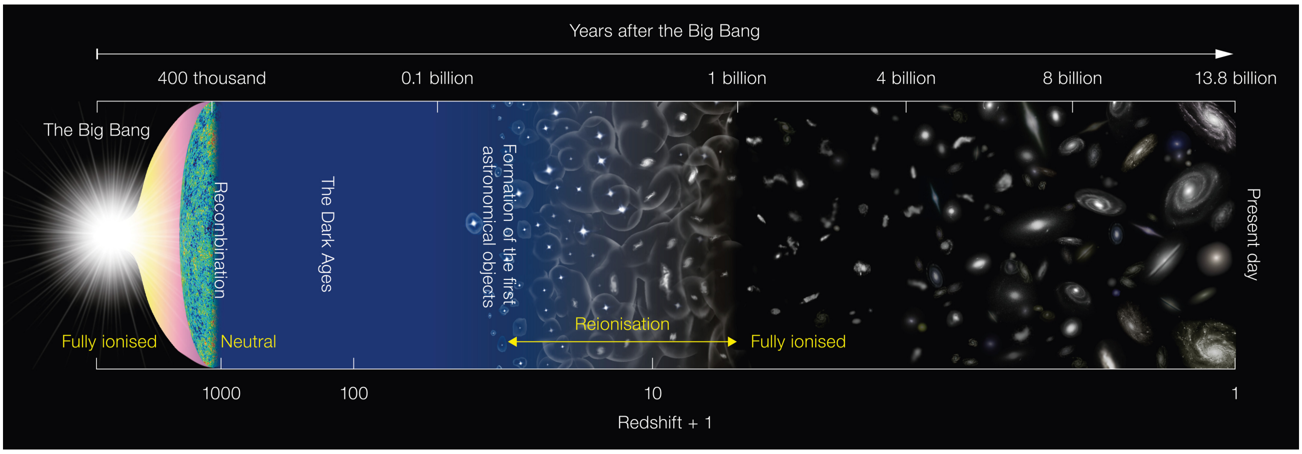

Figure 1.1: A cartoon diagram of the evolution of the Universe, along with the era of cosmic reionization is shown (Credit: NAOJ).

If high-redshift galaxies share similar escape fractions, it is possible that stars provided a significant portion of the reionizing background radiation (e.g., Madau and J. M. Shull 1996; Madau, Haardt, and Rees 1999). However, high-redshift galaxies formed in a denser Universe can have a different escape fraction from their low-redshift counterparts.

Each galaxy forms its own H II region due to the radiation generated by the stars inside the galaxies, that ionize hydrogen. These regions continue to grow, until they overlap with each other to merge and form a single H II bubble. Loeb and Barkana 2001 gave an account of the process of the reionization of hydrogen, which involves several distinct stages. The initial phase called the “pre-overlap” stage as per Gnedin 2000, involves ionization from individual sources. The earliest galaxies form within the most massive halos at high redshift, which are biased and tend to reside in the densest regions. Once these ionizing photons emitted from these high-density regions breakthrough, the ionization fronts can move more freely into low-density voids, leaving neutral, high-density gas pockets behind. Therefore, the IGM develops two distinct phases, with highly ionized regions separated by ionization fronts from neutral regions. The ionizing intensity within the ionized regions is non-uniform, determined by the proximity and ionizing intensity of the luminous sources close by.

In the following central ”overlap” phase of reionization, the neighboring H II regions merge, and every point within their common boundary gets exposed to ionizing photons from both sources, causing the ionizing intensity to rapidly increase within the H II regions. These regions can then expand into high-density gas that had previously recombined quickly enough to stay neutral. The overlap phase is expected to happen fast with a duration less than Hubble time at the overlap redshift due to the acceleration of reionization by bubble merging and giving a phase transition characteristic. The ionizing intensity is increased significantly and becomes more uniform at the end of the ”overlap” phase since most regions in the IGM have multiple unobscured sources. In this stage, a highly ionized and low-density IGM prevails, where ionizing radiation can stream freely except in self-shielded high-density cloud regions, concluding the reionization overlap phase. It occurs due to increased galaxy formation rates predicted by the hierarchical model of structure formation. Some neutral gas persists in high-density structures corresponding to the Lyman limit and damped Lyman-α systems seen in lower redshift absorption. As galaxies continue to form, these regions gradually ionize, increasing the mean ionizing intensity and its uniformity as IGM becomes transparent to more ionizing sources. The ”post-overlap” phase persists since neutral gas is reserved in collapsed objects. In the subsequent sections, some of the earliest probes of the EoR are discussed, such as the Thomson scattering optical depth measurement from the Cosmic Microwave Background and the absorption spectra of high redshift quasars.

1.1 The Cosmic Microwave Background

In the hot Big Bang model of our Universe, a Big Bang afterglow is predicted to fill the entire Universe, which is expected to follow a blackbody spectrum. The **COBE** mission first measured the anisotropies in this background radiation and placed constraints on it (Mather 1994; Wright et al. 1994). These anisotropies represent the primordial density fluctuations that gave rise to the present structures in the Universe that we see today. Its successors, such as **WMAP** and **Planck** (Planck Collaboration, Aghanim, Akrami, Arroja, et al. 2020), improved the measurements further, where higher-resolution maps of cosmic microwave background radiation (CMBR) were produced. In the cosmic history of our Universe, this represents the earliest possible state of the Universe that we have probed. However, the information from the CMBR only tells us a little about the later stages of the evolution of the Universe. For example, analysis from the CMBR data has placed partial constraints on the epoch of reionization. The reionization process releases free electrons with which the CMB photons interact via Thomson scattering. It introduces further anisotropies in the CMBR temperature fluctuations, and detailed analysis by Planck 2018 (Planck Collaboration, Aghanim, Akrami, Arroja, et al. 2020) has constrained the measured Thomson scattering optical depth—this optical depth to reionization for the observed CMB photons can be written as (Griffiths, Barbosa, and Liddle 1999).

$$\tau = n_{\mathrm{p},0}\sigma_{\mathrm{T}}c\int_0^z (1+z')^2\frac{dz'}{H(z')}x_{\mathrm{e}}(z) \tag{1.1}$$

$n_{\mathrm{p},0}$ and σ_{T} represent the proton density at present and the Thomson scattering cross-section. x_{e} is the ionization fraction. In the instantaneous reionization model, if the reionization completely happened at a single redshift z_{reion}, then x_{e} is given as

$$x_{\mathrm{e}}(z) = 0, z > z_{\mathrm{reion}} \tag{1.2}$$

$$= 1, z \leq z_{\mathrm{reion}}. \tag{1.3}$$

In this scenario, the optical depth is estimated over the path length from $z = 0$ to $z = z_{\text{reion}}$, as was done in some previous works (Griffiths, Barbosa, and Liddle 1999; Venkatesan 2000; M. Shull and Venkatesan 2007). The latest Planck 2018 results (Planck Collaboration, Aghanim, Akrami, Arroja, et al. 2020) put constraints on the midpoint of reionization history assuming a tanh model (Lewis 2008), which is given as

$$x_e(y) = \frac{f}{2}\left[1 + \tanh\left(\frac{y - y(z_{\text{re}})}{\Delta y}\right)\right]. \tag{1.4}$$

Here, $y(z_{\text{re}}) = (1 + z_{\text{re}})^{3/2}$ is where $x_e = f/2$. If the reionization of helium is also taken into account, then $f = 1 + f_{\text{He}}$, with $f_{\text{He}} = n_{\text{He}}/n_{\text{H}}$. Using the model of Eq. 1.4, the Planck 2018 results place the value of the midpoint of reionization at $z_{\text{reion}} = 7.68 \pm 0.79$ (Eq. 18 of (Planck Collaboration, Aghanim, Akrami, Arroja, et al. 2020)). However, this constraint is based on a pre-assumed reionization history, which cannot be independently constrained using only the Thomson scattering optical depth.

1.2 High redshift quasar spectra

The IGM is expected to completely absorb the flux of the spectra from quasars, which is blueward of the Lyman-α line transition beyond some specific redshift. This absorption is observed as a Gunn-Peterson trough. In the study of R. H. Becker et al. 2001 Keck spectroscopy of quasars at $z \sim 5.82, 5.99$, and 6.28, the results are presented. It was observed that the Lyman-α absorption evolves significantly with redshift in these quasar spectra. The absorption of the Lyman-α flux is consistent with extrapolations from lower redshifts up to $z \sim 5.7$, but in SDSS J103027.10+052455.0 ($z \sim 6.28$), which is the highest redshift object, the average transmitted flux was observed to be approximately 0.0038 ± 0.0026 times the continuum level over $8450\mathring{A} < \lambda < 8710\mathring{A}$ ($5.95 < z_{\text{abs}} < 6.16$). Consequently, the level of flux decreases more than 150 times and is consistent with zero flux in the Lyman-α forest region blueward of the Lyman-α emission line, compared to a reduction of ~ 10 times at $z_{\text{abs}} \sim 5.3$. They concluded that a complete Gunn-Peterson trough has been detected which is the result of neutral hydrogen presence in the IGM.

Additionally, quasars at $5.7 < z < 6.3$ as identified by SDSS were investigated by Fan et al. 2002 for Lyman series absorption. Semianalytic methods and cosmological simulations were used to mimic the density fluctuations in the IGM at high redshifts, to assess how the ionizing background evolved with redshift. It was discovered that the ionization background is more than 20 times lower in the IGM at $z \sim 6$ than at $z \sim 3$. At $z \sim 3$, the volume-averaged neutral fraction is around 10^{-5}, which increases to more than 10^{-3} at $z \sim 6$. The mass-averaged neutral hydrogen fraction exceeds 1 percent at this redshift, with the mildly overdense regions ($\delta > 3$) remaining mostly neutral and the comoving mean free path of ionizing photons being less than 8 Mpc. By comparing with cosmological reionization simulations, they also determined that the observed characteristics of the IGM at $z \sim 6$ are indicative of the period after the reionization overlap stage when the separate H II regions coalesce.

Nevertheless, recent research suggests that reionization may have concluded at a redshift below 6. A study by G. D. Becker, Bolton, Zhu, et al. 2024 provides evidence indicating that the most extensive and profound Lyman-α trough observed at $z < 6$, in relation to ULAS J0148 + 0600 (J0148), is linked to damping wing absorption. This conclusion is drawn from an area of pronounced Lyman-α transmission at the boundary of the J0148 proximity zone. They demonstrate that the relatively smooth profile of this transmission window is highly improbable to result from resonant absorption alone and aligns with the presence of a damping wing. Additionally, they propose that the damping wing is unlikely to originate from a compact source due to the absence of associated metal lines; it is more likely to stem from an extensive neutral island connected to the large Lyman-α trough.

1.3 Galaxy redshift surveys - Probing our local Universe and beyond

Galaxy redshift surveys have recently advanced to produce more detailed galaxy catalogs. These surveys attempt to map a large area in the sky to probe how luminous objects such as galaxies cluster on large scales. The galaxies at very low redshifts are a typical representation of our local universe since they are observed in their present state at the present cosmic time. Extending the surveys towards higher redshifts allows us to probe what the properties of galaxies were at a much earlier cosmic time and how that has evolved. Some of the earlier attempts at wide-area galaxy surveys are the **2dF Galaxy Redshift Survey** (**2dFGRS**, Colless et al. 2003) and the **6dF Galaxy Survey** (**6dFGS**, Jones et al. 2009). The more recent ones include **WiggleZ** (Drinkwater et al. 2018), **Galaxy And Mass Assembly** survey (**GAMA**, Driver et al. 2022), **Sloan Digital Sky Survey** (**SDSS**, Almeida et al. 2023), and the galaxy survey with the **Dark Energy Spectroscopic Instrument** (**DESI**, DESI Collaboration et al. 2024). However, these galaxy surveys consist of samples from the low redshift Universe. The recent high-redshift galaxy survey consisting of a large number of galaxy samples was done by the **HETDEX** (Davis, Gebhardt, Cooper, Ciardullo, et al. 2023; Davis, Gebhardt, Cooper, W. P. Bowman, et al. 2023; Mentuch Cooper et al. 2023) up to $z \lesssim 3.5$. However, they do not probe galaxies out to the reionization epoch. The current ongoing surveys that are successfully probing the EoR are from instruments, **ALMA** and **JWST**, although the sample size of galaxies is not as large as the low redshift surveys. Some of the recent results from these observations of the EoR are discussed below.

1.3.1 ALMA

The **Atacama Large Millimeter/submillimeter Array (ALMA)**[1] is an advanced telescope designed to observe radiation emitted by extremely cold objects in the Universe such as molecular clouds (Watanabe and Kouchi 2008) via detection in the millimeter and submillimeter bands. Radiation in this band

[1] https://www.eso.org/public/teles-instr/alma/

provides a unique perspective into the mysterious cold Universe. However, this radiation is significantly hindered by the presence of water vapor in the Earth's atmosphere. Therefore, telescopes used for this type of astronomy require construction on elevated and arid locations, such as the Chajnantor plateau, at an altitude of 5000 meters above sea level. ALMA is an innovative telescope consisting of 66 high-precision antennas, with a very high degree of surface precision of rms $< 25\mu m$ for 12-meter antennas and rms $< 20\mu m$ for 7-meter antennas and pointing accuracy of rms $< 0.6''$ (Wootten and A. R. Thompson 2009). It operates in the wavelength range of 0.32 to 3.6 mm. The primary array of the system consists of fifty 12-meter antennas, which collectively function as an interferometer. This is further enhanced by an additional array consisting of four 12-meter antennae and twelve 7-meter antennas. The 66 ALMA antennas can be stacked in various configurations, allowing for a flexible "zoom" capability with a maximum distance between antennas ranging from 150 meters to 16 kilometers. The instrument can probe the Universe utilizing wavelengths in the millimeter and submillimeter ranges with exceptional sensitivity and resolution. Its visual acuity is up to ten times superior to that of the **Hubble Space Telescope (HST)**, and it complements images produced by the **VLT** interferometer.

The ALMA has probed galaxy samples out to the EoR using redshifted line emissions from those samples. A study by Gallerani et al. 2018 detected a sample of star-forming galaxies $5.2 \lesssim z \lesssim 5.7$ using the [C II]$_{158\mu\text{m}}$ line emission with ALMA. The broadwings of the line emission suggest that there is an outflow driven by starbursts in those galaxy samples, with $v_{\text{outfl}} \sim 500$ km s^{-1}, which is obtained at the largest velocity where the flux excess is observed. The $M_{\text{outfl}} = 2.1 \pm 0.9 \times 10^8 M_\odot$ is the total mass of outflowing gas. An outflow rate of $\dot{M} = 54 \pm 23\ M_\odot$ yr^{-1} is inferred and given that the star-formation rate of their sample is $31 \pm 20\ M_\odot$ yr^{-1}, the estimated loading factor $\eta = \dot{M}/\text{SFR} = 1.7 \pm 1.3$. This is in good agreement with the local starbursts galaxies (Heckman et al. 2015).

Zavala et al. 2018 had probed 3 mm continuum sources by performing a blind search while utilizing the ALMA archive, extending the submillimeter-galaxy selection method at high redshifts to identify dusty star-forming galaxies (DSFGs). By excluding the primary targets of the observations, they identified 16 sources exceeding a conservative threshold of 5σ, with a false detection rate expected to be under 5 percent. From these sources, they determined the first number counts of 3 mm sources. Employing a backward evolution model, they found that the data does not support a Universe that is dust-poor, where at $z > 4$, DSFGs contribute minimally to the cosmic star-formation rate (CSFR). The optimal models for the evolving infrared galaxy luminosity function (IRLF) indicate that DSFGs contribute to the total CSFRD at a level of approximately 35 to 85 percent, between $z \sim 4$ and 5. However, at higher redshifts, it is not well understood how much the dust-obscured star formation contributes to the total CSFRD, due to degeneracies in the parameters of the model. The constraints could imply two different scenarios, one of which is that the dust-obscured star formation can contribute to the total CSFRD up to a level of 75 percent, up to $z \sim 6$, after which obscured star formation becomes much rarer. The other scenario could be a significant contribution (≈ 15–65 percent) of the dust-obscured star-formation towards the total CSFRD up to $z \sim 9$, but which is not well understood.

The ALMA-ALPINE [C II]$_{158\mu\mathrm{m}}$ survey (Le Fèvre et al. 2020), examined 118 star-forming galaxies towards the end of the EoR at $4 < z < 6$. The galaxies in this study were chosen based on reliable spectroscopic redshifts that existed already and SED-based SFR predictions for the [C II]$_{158\mu\mathrm{m}}$ flux using the relation from De Looze, Cormier, et al. 2014. The SFR values were chosen so that $L_{\mathrm{CII}} > 1.2{\times}10^{8} L_{\odot}$. The galaxies that were detected in [C II]$_{158\mu\mathrm{m}}$ constituted about 64 percent of the samples with 3.5σ above the noise and 21 percent in the continuum. The galaxy types detected were comprised of 10.7 percent compact, 13.3 percent rotating discs, 20 percent extended and dispersion-dominated, and 40 percent mergers. The remaining 16 percent could not be classified because they were too faint. This variety of types suggests that different physical processes can contribute to mass assembly in these galaxies, particularly galaxy merging. While starbursts above the main sequence, at least up to $z \sim 3$, typically exhibit galaxy merging, at $z \sim 4.7$, mergers in ALPINE samples are predominantly on the main sequence (MS), indicating that for normal SFGs, merging is also a significant process during this period.

On the other hand, the Reionization Era Bright Emission Line Survey program or REBELS with ALMA has identified galaxy samples from the reionization epoch, aiming to investigate substantial samples of luminous interstellar medium (ISM) reservoirs from this time. Additionally, at $z > 6.5$, for the highly luminous star-forming galaxies, it provides the initial characterization. This is achieved in REBELS by investigating 40 brightest galaxies selected in UV, within an area of 7 deg^2 for emission in dust-continuum and prominent [O III]$_{88\mu\mathrm{m}}$ and [C II]$_{158\mu\mathrm{m}}$ lines. Initial findings from the ALMA-REBELS survey were documented by R. J. Bouwens et al. 2022. From observations during the first year, 18 7σ detections of [C II]$_{158\mu\mathrm{m}}$ lines have been obtained, with emission in dust-continuum at 3.3σ in 13 out of the 18 samples detected. In the $z > 6.5$ universe, the number of known bright ISM-cooling lines has more than tripled, bringing the number of redshifts derived by ALMA at this epoch, to compete with those from Lyman-α observations. Analyzing the completeness of the search results in relation to star formation rate (SFR) indicates an approximate 79 percent efficiency in detecting [C II]$_{158\mu\mathrm{m}}$ with SFR$_{\mathrm{UV+IR}}$ being greater than 28 $M_{\odot}$yr^{-1}.

At high redshifts, the transmission of Lyman-α line can be enhanced owing to the shifting of the profile to larger velocities compared to the systemic redshift. Endsley et al. 2022 explore this at $z \sim 7$ using galaxies detected with the ALMA REBELS survey. Eight such galaxies were detected that have $M_{\mathrm{UV}} \sim -22$ and are UV bright at $z \simeq 7$. To study the Lyman-α velocity profiles the systemic redshifts of the [C II]$_{158\mu\mathrm{m}}$ emission have been used and four out of eight samples are detected in Lyman-α. The FWHM of the Lyman-α lines are around 300-650 km s^{-1} and the offset of velocity on average is 223 km s^{-1}, therefore having significant deviation from the systemic redshift. Also, the Lyman-α profiles which are the broadest, are associated with the largest line widths of [C II]$_{158\mu\mathrm{m}}$. This suggests a relation between the FWHM of Lyman-α line and the dynamical mass. The large velocity profiles are found to boost the visibility of Lyman-α line in the reionization-era UV-luminous galaxies.

Sommovigo et al. 2022 estimate the dust temperatures (T_{d}) using a newly developed approach based on concurrent [C II]$_{158\mu\mathrm{m}}$ line and underlying dust continuum observations in the $z \approx 7$ galaxies detected by the ALMA-REBELS survey. They determine that $39 < T_\mathrm{d} < 58$ K, with dust masses ranging narrowly within $M_\mathrm{d} = (0.9–3.6)\times10^7\,M_\odot$. Their findings also indicate warmer dust in sites with more obscuration, as higher levels of obscuration enhance dust heating efficiency. Overall, REBELS galaxies exhibit relatively low opacity, with effective column densities of gas of around $N_\mathrm{H} \simeq (0.03–1)\times10^{21}$ cm^{-2}.

Topping et al. 2022 have studied 40 UV-bright galaxies and report their specific star formation rates at a redshift of $\sim 7-8$ using the ALMA-REBELS survey. The analysis is based on the FIR continuum measurements and spectroscopic redshifts derived from [C II]$_{158\mu\mathrm{m}}$ line, which was required to derive the sSFRs based on stellar masses obtained from SEDs and improved calibration of SFR. The median value of the distribution of the sSFR within the samples is measured to be around 18^{+7}_{-5} Gyr^{-1}, which is found to be significantly higher compared to other measurements, that do constrain the FIR well. This reflects the larger SFRs obscured by dust that is obtained from dust continuum, as compared to the one that is suggested by the SED in the UV+optical regime. The anomalies are suggested to be originating from variations of dust across space among these luminous galaxies, where the components dominating the UV and the FIR are distinct from each other. Topping et al. 2022 have demonstrated that the stellar masses inferred are dependent strongly on the underlying star formation history of the reionization-era galaxies. It is also found that in the largest sSFR systems, the [C II]$_{158\mu\mathrm{m}}$ line width is often very broad, which suggests that the dynamical masses are capable of accommodating an old stellar population, predicted by non-parametric models.

Fudamoto et al. 2022 report that the typical effective radius of [C II]$_{158\mu\mathrm{m}}$ emission at $z \sim 7$ is r_e of 2.2 ± 0.2 kpc. This size is more than twice as large as the dust continuum and the rest-frame UV emission, which aligns with recent measurements for galaxies at $z \lesssim 6$. Furthermore, we compared the average [C II]$_{158\mu\mathrm{m}}$ sizes of galaxies at $4 < z < 6$ from the ALMA-ALPINE survey. By examining [C II]$_{158\mu\mathrm{m}}$ sizes in two redshift bins for these galaxies, they found that the average effective radius is 2.2 ± 0.2 kpc for $z \sim 5.5$ galaxies and 2.5 ± 0.2 kpc for $z \sim 4.5$ galaxies, respectively. These results indicate that star-forming galaxies do not show any significant evolution in the size of [C II]$_{158\mu\mathrm{m}}$ emitting regions within $z \sim 4-7$. This suggests that the morphologies of these galaxies might be predominantly influenced by gas over this extensive redshift range.

Further, using the ALMA REBELS survey, the infrared luminosity function or IRLF was studied based on the galaxy samples selected in the UV band in the EoR by Barrufet, Oesch, R. Bouwens, et al. 2023. 42 galaxies were targeted within redshifts 6.4 to 7.7 using line scans of [C II]$_{158\mu\mathrm{m}}$ emission. The IR luminosity of the galaxies detected ranges from $10^{11.4}L_\odot$ to $10^{12.2}L_\odot$. The Schecter function is found to well represent the IRLFs derived, where the characteristic luminosity L_* is found to be $\log L_*/L_\odot = 11.6^{+0.2}_{-0.1}$. The simulations at $z \sim 7$ also reproduce similar results with agreement with these observations. It is suggested that the IRLFs evolve significantly between the redshifts of 4 to 7, lying significantly below the estimates from lower redshifts. At $z \sim 7$, the contribution towards the CSFD from the IR obscured star formation is estimated to be $\log(\mathrm{SFRD}/M_{\odot}\,\mathrm{yr}^{-1}\,\mathrm{Mpc}^{-3}) = -2.66^{+0.17}_{-0.14}$. Therefore, during the EoR, the presence of dust is already abundant.

A follow up study for three Lyman break galaxies detected in the Subaru Hyper Suprime-Cam survey was done by Harikane et al. 2020 using the ALMA observations that targeted continuum emission in dust, [N II]$_{22\mu\mathrm{m}}$, [O III]$_{88\mu m}$ and [C II]$_{158\mu m}$ line emissions, which were detected within redshifts 6.0293 to 6.2037. At a significance level of 4.3σ to 11.8σ, [C II]$_{158\mu\mathrm{m}}$ and [O III]$_{88\mu\mathrm{m}}$ lines were detected from all galaxies and from two out of the three galaxies, continuum emission from dust was identified in multi-band. It was found that [O III]$_{88\mu\mathrm{m}}$ luminosities are at a comparable level or higher than what is predicted by L_{OIII}-SFR relation at $z \sim 0$. However, the [C II]$_{158\mu\mathrm{m}}$ line luminosity in these samples was found to be lower than dwarf galaxies and is comparable to starburst galaxies in the local Universe. Therefore, the [O III]$_{88\mu\mathrm{m}}$/[C II]$_{158\mu\mathrm{m}}$ ratio is higher than what is found in the local Universe and is similar to other galaxies found in the redshift range of 6 to 9. An analysis using Cloudy shows that an ionization parameter that is higher by 10 to 100 times or low (0-10 percent) covering fractions of photo-dissociation regions (PDR), can cause such properties in the galaxies at redshifts 6 to 9. In the latter scenario, where there is a PDR deficit, these conditions can be reproduced with a density-bounded nebula with a PDR deficiency. This would cause the enhancement of escape of Lyman continuum, Lyman-α and C^{+} ionizing photons, which is found to be consistent with the positive correlation found in the [O III]$_{88\mu m}$/[C II]$_{158\mu m}$ ratio and the equivalent width of Lyman-α, detected at a significance level of 90 percent.

1.3.2 JWST

The **James Webb Space Telescope** or **JWST**[2] is a space-based observatory with a primary mirror with aperture of ~ 6.5 m. It operates within the wavelength range of $\sim 0.6 - 28.5\mu$m, and achieves an angular resolution of ~ 0.1 arcsecond. The Near Infrared Camera (NIRCam)[3], JWST's main imager, covers 0.6 to 5μm wavelength range that falls in the infrared regime. This device is sensitive to the radiation from objects within the Kuiper Belt, young stars located in the Milky Way, stars within the nearby galaxies, and also the earliest luminous sources during stages of formation. Coronagraphs on NIRCam can block light from other brighter sources, facilitating the observation of dimmer surrounding objects. The Near InfraRed Spectrograph (NIRSpec)[4] on JWST, which also operates over the 0.6 to 5μm wavelength range, generates spectra of observed objects and can produce spectra for multiple objects simultaneously. The Mid-Infrared Instrument (MIRI)[5] has a camera and a spectrograph that can operate in the wavelength range from 5 to 28μm. Its sensitive detectors can detect objects in the Kuiper Belt, comets that are faintly visible and redshifted light from far away galaxies. MIRI's spec-

[2] https://science.nasa.gov/mission/webb/fact-sheet/
[3] https://science.nasa.gov/mission/webb/nircam/
[4] https://science.nasa.gov/mission/webb/nirspec/
[5] https://science.nasa.gov/mission/webb/mid-infrared-instrument-miri/

trograph enables medium-resolution spectroscopy, offering new physical insights into distant objects. To obtain images with high quality, the pointing of the JWST has to be precise, which is allowed by the Fine Guidance Sensor (FGS). The Near Infrared Imager and Slitless Spectrograph component of the FGS/NIRISS[6] investigates several scientific objectives: exoplanet transit spectroscopy, exoplanet identification and characterization and detection of first light. The FGS/NIRISS covers a 0.8 to 5.0μm wavelength range with three primary modes, each addressing a specific wavelength range. Below, some of the recent results of JWST from the EoR have been discussed.

Using the "GLASS-JWST-ERS program", Leethochawalit et al. 2023 have analyzed 13 sources that were identified photometrically from the NIRCam data, within $7 < z < 9$. They used the SED-fitting software `Bagpipes` to calculate the stellar masses, SFRs, and mass-weighted ages for these sources. In general, the number density observed aligns well with the predictions of the UV luminosity function from HST observations at this redshift. These galaxies exhibit a broad range of ages weighted by mass, starting from 30 Myr in the smallest galaxy to about 100 to 200 Myr in the larger $10^9 M_\odot$ galaxies. It indicates substantial star formation activity in typical galaxies at redshift $z \gtrsim 11$, although these results depend on the model for the star-formation history (SFH), which is usually the log-normal model.

Further, with the new "GLASS-JWST NIRCam" data, Santini et al. 2023 present the initial examination of mass-to-light ratios and stellar masses for galaxies with redshifts higher than $z > 7$, which directly sample optical light in rest-frame from these galaxies. They demonstrate that JWST can measure the stellar masses of galaxies at $z \gtrsim 7$ accurately, that is 5–10 times better than previous studies requiring exposure time, which is much shorter. The physical conditions within the early galaxies can vary widely, which is indicated by the two orders of magnitude range of the UV mass-luminosity relation observed. They also point out that earlier assumptions of a uniform UV mass-luminosity relation could introduce systematic errors in estimates of the cosmic stellar mass density (SMD) by as much as a factor of ~ 6.

Further, using NIRCam parallel observations from the "GLASS-JWST Early Release Science" program, Nanayakkara et al. 2023 constrained the UV continuum slope of 401 galaxies within a redshift range of 4 to 7. The dust levels were found to be very low ($A\nu_\beta \sim 0.01 \pm 0.33$) and more than 99 percent of the galaxies are blue star-forming. The UV slope was found to be correlated with the stellar mass within the galaxies, whereas galaxies with higher stellar mass had a shallower UV slope. However, no correlation to the UV magnitude or redshift was found that is statistically significant although at higher redshifts, the galaxies had steeper UV slopes for fainter UV magnitudes in general. The stellar population synthesis models used allowed for bluest UV slope values of $\beta \sim -3.1$ for some of the galaxies, which means that Population III contribution, AGN effects, or a higher amount of Lyman continuum leakage are required that can explain the optical and rest-UV properties. This supports the gradual mass + dust buildup model of galaxies with cosmic time that can describe the Universe within

[6] https://science.nasa.gov/mission/webb/fine-guidance-sensor-near-infrared-imager-and-slitless-spectrogra

the age window of $\sim 0.7 - 1.5$ Gyr. The large population of dust-poor UV faint systems may support the model where low-mass galaxies are important in cosmic reionization at $z > 6$.

Moreover, Z. Chen et al. 2023 have utilized JWST/NIRCam imaging, to study how 12 of the brightest galaxies in the EGS field at $z \simeq 6-8$ are composed internally. In the rest-UV, they appear clumpy, and more than half the radiation originates from star-forming complexes of about 107 to $109\, M_{\odot}$ and sizes ranging from 150 to 480 pc. The clumps are generally filled with young stars (median age 36 Myr), although significant differences in clump ages are observed in the galaxies. The [O II]+Hβ equivalent width (EW) varies considerably among galaxies, indicating variations in gas and stellar characteristics while the ionized regions tend to align with the UV-bright complexes. Most of the stellar mass in these luminous galaxies at redshifts 6 to 8, is concentrated in small clumpy star-forming complexes ($\lesssim 150$ pc), indicative of the highly active assembly phase typical for galaxies during the reionization era.

Also, using the "CEERS" program, 30 galaxy samples were detected using high-resolution and very deep imaging with NIRCam, which were very faint such that they could not be probed with the HST. This study has been done by Barrufet, Oesch, Weibel, et al. 2023 and they derive the physical properties of these galaxy samples using 12-band multiwavelength photometry, that also included HST imaging. The galaxies were found to be massive ($10^{10} M_{\odot}$) and are generally obscured by dust heavily ($A_V \sim 2$ mag), where the surface density is obtained to ~ 0.8 arcmin^2. These galaxies are an important contributor to the population of massive galaxies from $z > 3$ up to the EoR and they also contribute to the obscured SFRD of $3.2^{+1.8}_{-1.3} \times 10^{-3}\, M_{\odot}$ yr^{-1} Mpc^{-3} at a redshift of ~ 7, that suggests the probable presence of dust in the EoR. Overall, this demonstrates the capability of JWST to uncover the missing population of galaxies and provide a comprehensive census of galaxies in the EoR.

Mascia, Pentericci, Calabrò, Treu, et al. 2023 perform a detailed characterization of a set of LyC leakers in the EoR by combining data from JWST-NIRSpec and NIRCam to determine their physical and spectroscopic attributes. Analyzing 29 gravitationally lensed galaxy samples within the redshift range $4.5 \leq z \leq 8$ from the Abell 2744 cluster field, they observe that these galaxies have high [O III]/[O II] flux ratios, compact sizes ($r_{\mathrm{e}} \sim 0.3 - 0.5$ kpc), blue UV spectral slopes ($\beta \sim -2.1$) and low masses ($\log(M_{*}) \sim 8.5$). These characteristics are similar to Lyman continuum leakers at low redshifts. Estimating the escape fraction of ionizing photons indirectly, it is found that over 80 percent of the galaxies are predicted to have f_{esc} values greater than 0.05, categorizing them as leakers. The sample's f_{esc} has an average value of 0.12, suggesting that at $z \geq 6$, galaxies with similar properties have significantly contributed to cosmic reionization.

One of the key challenges in understanding the properties of the galaxies is to measure the fraction of Lyman continuum photons (f_{esc}) that can escape the galaxies and into the IGM. This is difficult to achieve because the IGM is opaque and it is necessary to measure f_{esc}, to understand the role and nature of cosmic reionizers. However, at intermediate and low redshifts efforts have been made to predict f_{esc}, based on measurable indirect indicators in galaxies at high redshifts. Mascia, Pentericci, Calabrò, Santini, et al. 2024 has analyzed spectroscopically confirmed galaxies from "CEERS" survey which are about 62 in number, at redshifts between 6 to 9, and are star-forming. It was discovered that, on average, these galaxies have a predicted value of 0.13 for $f_{\rm esc}$ and are blue sources (UV-$\beta \sim -2.17$), along with being compact in the rest-frame UV with $r_{\rm e} \sim 0.4$ kpc. It is also concluded that most likely, galaxies which is currently not characterized by JWST and are fainter than $M_{1500} = -18$, contributed significantly to the ionizing photon budget of reionization.

Umeda et al. 2024 analyze the spectra from JWST/NIRSpec, from the "CEERS", "GO-1433", "DDT-2750", and "JADES" programs, compiling a sample of 27 galaxies that are bright in UV-continuum ($M_{\rm UV} < -18.5$ mag) within the redshift range of 7 to 12. This analysis aids in determining the volume-averaged fractions of neutral hydrogen, $x_{\rm v;HI}$ and radii of ionized bubble $R_{\rm b}$ based on Ly-α damping wing absorption of these galaxies during the EoR. They estimate Ly-α damping wing absorption using realistic templates that include absorptions in the circumgalactic medium and emission in Ly-α. Under the assumption that the reionization model is "inside-out", with a radius $R_{\rm b}$, for ionized bubble around a galaxy within the intergalactic medium, they derive $x_{\rm v;HI}$ ($R_{\rm b}$) values that increase (decrease) from $x_{\rm v;HI} = 0.53^{+0.18}_{-0.47}$ to $0.92^{+0.08}_{-0.10}$ ($\log R_{\rm b} = 1.67^{+0.14}_{-0.16}$ to $0.69^{+0.89}_{-0.24}$ comoving Mpc) for the redshift interval $z = 7.12^{+0.06}_{-0.08}$ to $9.91^{+1.49}_{-1.15}$. The evolution of $x_{\rm v;HI}$ with redshift indicates a reionization timeline that is moderately late, which has consistency with prior findings from cosmic microwave background electron scattering and UV luminosity function evolution, suggesting $f_{\rm esc} \sim 0.2$. The $R_{\rm b}$ values suggest that compared to the average cosmic value calculated for a given $x_{\rm v;HI}$, the bubble sizes could be a few orders of magnitude larger while being roughly comparable to values of ionized bubbles around bright galaxies that have merged, as have been predicted by simulations recently.

Saxena et al. 2024 describe the characteristics of 17 weak LAEs at $z > 5.8$ from the spectroscopic data of "Hubble Ultra Deep Field/GOODS-S JWST Advanced Deep Extragalactic Survey (JADES)". These LAEs' Lyman-α equivalent width is $\approx$ 250−3500 nm, the UV magnitude range is $M_{\rm UV} \approx -17$ to -20.6 and the redshift range is from 5.8 to 8.0. The general galaxy population at $z > 6$ is composed of metal-poor systems with high ionization characteristics, such as these dim LAEs. The study supported model prediction by finding an anti-correlation between Lyman-α escape fraction and velocity offset arising out of systemic redshift, supporting model predictions. The decrease in Lyman-α escape fractions with redshift suggests that at high redshifts, the ionized bubbles around LAEs are smaller. Across the observed Lyman-α equivalent width, the LAEs' output of ionizing photons into the IGM remains constant, while at higher redshifts and fainter UV magnitudes, it can slightly increase. They suggest that the correlations between LAEs' ionizing photon output, UV magnitudes, Lyman-α strengths, and redshifts can be utilized to determine LAEs' contribution to cosmic reionization at $z > 6$.

Muñoz et al. 2024 recently argued that the JWST observations, revealing early galaxies as prolific ionizing photon producers, created tension among reionization probes. These new observations suggest high ionizing photon production efficiency and a greater abundance of early ($z \gtrsim 9$) galaxies, significantly increasing ionizing photon production at high z. At the same time, recent studies at low-z forecast considerable f_{esc} for faint galaxies during the reionization-era. Muñoz et al. 2024 indicate that the directly observed galaxies ($M_{\text{UV}} < -15$) not only drive reionization but would terminate it prematurely, leading to ionizing photons present in an excess abundance and a reionization process conflicting with the Lyman-α forest and cosmic microwave background (CMB) observations. They suggest solutions like biased calibration of ionizing photon production efficiency, low f_{esc} values, UVLF turnover or flattening, and uncertainties in recombination modeling. Conversely, F. Melia 2024 argue that this tension stems from flawed assumptions in background cosmology (ΛCDM) and propose an $R_{\text{h}} = ct$ cosmology (F. Melia and Shevchuk 2012) as an alternative solution, addressing other cosmological issues such as horizon problems related to the CMB temperature and the electroweak phase transition (F. Melia 2013; Fulvio Melia 2018), the cosmic entropy anomaly (Fulvio Melia 2021), violation of the strong energy condition by inflation in general relativity (Fulvio Melia 2023a), and the monopole problem (Fulvio Melia 2023b) among others.

1.4 Line intensity mapping

Although observations with **ALMA** and **JWST** have pushed the observation of galaxies out to the epoch of reionization, they are generally limited by the small field of view. It means that the number of galaxy samples is also significantly lower than what would usually be required to probe large-scale structures. This drawback comes at the cost of the high resolution of these instruments to resolve the galaxies and conduct detailed studies. One proposed way to overcome this problem is targeting specific bright line emissions from the galaxies and accumulating the aggregate emission within a minimal sky volume. This small volume will have dimensions in the plane of the sky and along the frequency (or redshift) axis and constitutes a voxel. Therefore, the whole observed volume is reconstructed by combining multiple voxels spanning over it. These voxels represent the specific intensity of the targeted line emission resulting from the aggregate flux of the numerous detected sources. This process of detecting the cumulative flux of luminous sources is known as line-intensity mapping (LIM). It trades off high angular resolution compared to the point-source detections to achieve extensive coverage of cosmological volumes spanning hundreds of Mpc, depending on the targeted redshift. This volume coverage would be otherwise impractical to achieve with the current galaxy surveys like **ALMA** and **JWST** probing the epoch of reionization. However, line-intensity mapping can survey large cosmological volumes in a reasonable amount of observational hours compared to point-source detections.

The LIM targets the fluctuations in the specific intensity of the targeted bright line emissions from the galaxies. Numerous luminous sources might reside within a given voxel, each having different luminosities. Let the ith line emitter have a luminosity of L within that voxel. Then the luminosity density within that voxel can be written as $\rho_L(\boldsymbol{x}) = \sum L_i/\Delta V$, where ΔV is the volume of the voxel. It will have an associated flux volume density, f_L, related to ρ_L by $f_L = \rho_L/4\pi D_L^2$. If we convert the volume element to angular coordinates and frequency resolution of the LIM observation, then the flux volume density can be converted to the specific intensity. This can be written as follows:

$$I(\boldsymbol{x}, z) = f_L \frac{\mathrm{d}A}{\mathrm{d}\Omega} \frac{\mathrm{d}\chi}{\mathrm{d}\nu_{\text{obs}}}, \tag{1.5}$$

with dA being the sky area of the voxel, $d\Omega$ being the solid angle subtended by the voxel to the observer, χ being the co-moving distance to the voxel and ν_{obs} being the frequency at which the signal is observed. It can be shown that $dA/d\Omega = D_{\text{A}}^2$, with D_{A} being the angular-diameter distance and $d\chi/d\nu_{\text{obs}} = \lambda_{\text{obs}}(1+z)/H(z)$. Therefore, the specific intensity can be written as

$$I(\boldsymbol{x}, z) = \rho_L(\boldsymbol{x}, z) \frac{\lambda_{\text{rest}}}{4\pi H(z)}, \tag{1.6}$$

or represented as brightness temperature with,

$$T(\boldsymbol{x}, z) = \rho_L(\boldsymbol{x}, z) \frac{\lambda_{\text{rest}}^3 (1+z)^2}{8\pi k_{\text{B}} H(z)}, \tag{1.7}$$

if we invoke the Raleigh-Jeans limit for the specific intensity. If we know the mean number density of the line emitters, we can estimate the mean specific intensity of the corresponding LIM signal. This can be obtained from the mean luminosity density given as follows,

$$\langle I(z) \rangle = \langle \rho_L \rangle \frac{\lambda_{\text{rest}}}{4\pi H(z)} = \frac{\lambda_{\text{rest}}}{4\pi H(z)} \int L \frac{\mathrm{d}n}{\mathrm{d}L}(L, z) \mathrm{d}L, \tag{1.8}$$

where $\mathrm{d}n(L, z)/\mathrm{d}L$ is the mean number density of line emitters.

LIM aims to target the line emissions from galaxies which are comparatively brighter than the continuum emission. Some bright galaxy line emissions are the $[\text{C II}]_{158\mu\text{m}}$, CO, Lyman-α, $[\text{O III}]_{88\mu\text{m}}$, etc., and are potential candidates for tracers to conduct LIM experiments. They are expected to probe different aspects of the properties of galaxies and let us understand the process of galaxy formation and evolution. Additionally, the $[\text{H I}]_{21\text{cm}}$ signal originating from the IGM can also probe cosmic reionization, giving insights into how the IGM has evolved during this period. In this thesis, we have focused on a few line emissions, such as the CO, $[\text{C II}]_{158\mu\text{m}}$, emissions from the galaxies, and the $[\text{H I}]_{21\text{cm}}$ signal from the IGM.

1.4.1 CII 158μm line emission

The $[\text{C II}]_{158\mu\text{m}}$ line emission originates due to radiative decay between the fine structure states ${}^2P_{3/2} \rightarrow {}^2P_{1/2}$. The fine structure state in the [C II] ions can be excited by either radiative processes (e.g., CMB photons) or collisional excitation by electrons, atoms, or molecules. In (Gong, Cooray, M. Silva, et al. 2012) it has been argued that collisional processes dominate the excitation of [C II] ions over radiative processes when the density of electrons or atoms/molecules is higher than a certain critical threshold. The critical density for electrons to collisionally excite [C II] ions is lower than 100 cm^{-3}, whereas for neutral hydrogen this value is close to 10^3 to 10^4 cm^{-3} (S. Malhotra et al. 2001). This means that electrons will dominantly collide with the [C II] ions and excite them (Lehner, Wakker, and Savage 2004; M. Suginohara, T. Suginohara, and Spergel 1999), especially in ionized gas. Compared to neutral hydrogen, the [C II] ions have a low ionization potential of 11.2 eV. Therefore, [C II] ions can be abundantly found in various environments.

The [C II]$_{158\mu\text{m}}$ emission can originate primarily from the photodissociation regions (PDRs) of the galaxies, although a significant portion of the emission can also arise from cold neutral regions, warm ionized regions, and CO dark clouds (De Looze, Baes, et al. 2011; Olsen, Thomas R. Greve, Narayanan, R. Thompson, Toft, et al. 2015). This line emission is also one of the major cooling channels in the ISM, which is conducive to star formation. The PDRs are the regions that separate the H II regions and the molecular clouds, and as argued by De Looze, Baes, et al. 2011, FUV radiation from young hot stars can impinge on the boundary of the H II regions and the PDRs, and via a photoelectric effect on the dust grains, it can heat the gas. Therefore, this can act as an excitation mechanism for the emission of the [C II]$_{158\mu\text{m}}$ line. However, the [C II]$_{158\mu\text{m}}$ line emission might not be directly related to star formation in galaxies. Rather, this emission traces the cold ISM, which is related to star formation via the Schmidt-Kennicutt law (Kennicutt 1998). The Schmidt-Kennicutt law relates the observable surface densities of molecular gas and star formation via a relation of the form $\Sigma_{\text{SFR}} \propto \Sigma_{\text{H}_2}^N$. Here, Σ_{H_2} and Σ_{gas} are the surface densities of SFR and molecular gas, respectively. This was first proposed by Schmidt 1959, which was later tested by Kennicutt 1998 over a much larger range of galaxy types and gas densities. The most reported values of N usually lie close to $N \sim 1.4$.

Pineda, Velusamy, et al. 2010 find that the [C II]$_{158\mu\text{m}}$ line emission is associated with low-density regions in the galaxies, and modest FUV radiation fields. De Looze, Cormier, et al. 2014 further investigate the applicability of the [C II]$_{158\mu\text{m}}$ line emission to reliably trace star formation in different types of galaxies such as metal-poor dwarf galaxies, starburst galaxies, AGNs, ultraluminous infrared galaxies (ULIRGs), and high redshift objects. They find that in all cases [C II]$_{158\mu\text{m}}$ line emission is well correlated with star formation rate. Using the ALMA-ALPINE survey, Schaerer et al. 2020 study whether for the high redshift galaxies at $4 \lesssim z \lesssim 6$, the L_{CII}–SFR relation is different than what has been found in the local Universe. The ALPINE galaxies, identified in both [C II]$_{158\mu\text{m}}$ emissions and dust continuum, exhibit a strong correlation with the low-z L_{CII}-SFR relationship when the total SFR (UV+IR) is considered. After integrating dust-obscured star formation, derived from two distinct stacking methods and SED fitting, the ALPINE galaxies demonstrate an L_{CII}-SFR relationship similar to that observed locally. When [C II]$_{158\mu\text{m}}$ non-detections are included, the slope could be slightly steeper at high-z, though this remains somewhat ambiguous. When evaluated homogenously, the $z > 6$ [C II]$_{158\mu\text{m}}$ measurements (including both detections and upper limits) show no significant deviation from the $z \sim 4$–6 data. The empirical relation between the [C II]$_{158\mu\text{m}}$ luminosity and the star formation rate that is usually followed is of the form

$$\log\left(\frac{L_{\text{CII}}(M,z)}{L_\odot}\right) = a\times\log\left(\frac{\text{SFR}(M,z)}{M_\odot\text{yr}^{-1}}\right)+b, \tag{1.9}$$

where a and b are parameters and can depend on redshift.

1.4.2 CO line emission

The CO line transitions arise from the rotational transition states and have low excitation of ~ 5 K for the first excitation state. The orbital angular momentum of these states L is $L = nh/(2\pi)$ (Townes and Schawlow 1975), where h is the Planck's constant and the corresponding energy levels are $E_{\text{rot}} = J(J+1)h^2/(8\pi^2 I)$, I being the moment of inertia. Therefore, the energy difference between the levels J and $J-1$ is $\Delta E_{\text{rot}} = [J(J+1)-(J-1)J]\,(h^2/8\pi^2 I) = J\times(h^2/(4\pi^2 I))$.

The excitation of other tracer molecules, such as CO, largely depends on the collision frequency with H_2 molecules, given their high abundance, significant mass, and large cross-section. The collisional rates are determined by the kinetic temperature of the H_2 molecules, T_{kin}, which in turn is determined by the velocity distribution of the molecules described by the Maxwell-Boltzmann distribution. It is commonly assumed that, at high densities, this kinetic gas temperature matches the dust temperature. However, the cooling and heating mechanisms of the dust and molecular gas phases differ significantly.

The distribution of molecular levels is governed by the excitation temperature following the Boltzmann distribution. By assuming local thermodynamic equilibrium (LTE), this excitation temperature matches the gas's kinetic temperature. In thermal excitation, the levels' populations adhere to the Boltzmann distribution. Excitation is said to be subthermal when the higher levels have populations lower than expected from the gas's kinetic temperature, a scenario typical in low-density regions where collisional excitation does not offset spontaneous emission rates.

One of the assumed models for modeling the excitation in the CO molecules is the large velocity gradient (LVG) method (Young and Scoville 1991). The model determines, for a specified velocity gradient $\mathrm{d}v/\mathrm{d}r$, CO abundance (CO/H_2), H_2 density and temperature T_{kin}, how the different CO levels are filled through collisions with H_2. Due to the CO emission being optically dense (especially in the low-J transitions), it faces challenges escaping the cloud. Hence, a velocity gradient is included in the model to describe the number of photons escaping the clouds eventually. This gradient is justified because the molecular medium is, in reality, turbulent, allowing CO photons to escape their parental clouds. The LVG method also includes the redshift of the source, which is required to estimate the temperature of the CMB. After calculating the occupation numbers for the various levels, the method derives the optical depths τ_{CO} for the transitions, as well as the Raleigh-Jeans brightness temperatures T_{b} (which remain constant in LTE) and the corresponding line intensities.

In the context of LIM, the CO luminosities are modeled empirically via correlation with the far-infrared (FIR) luminosities of the galaxies. Molecular hydrogen is required for star formation, and since this is also required for exciting the CO molecules, a correlation is expected between CO line emission and the star formation rate. A relation of the following form is usually assumed:

$$\log L_{\mathrm{FIR}} = \alpha_J \log L'_{\mathrm{CO}(J\to J-1)} + \beta_J \tag{1.10}$$

where $L'_{\mathrm{CO}(J\to J-1)}$ is the CO luminosity expressed via the (areal) integrated source brightness temperature in units of $\mathrm{K\,km\,s^{-1}\,pc^2}$. This can be converted to CO luminosity in $L_\odot$ units following $L_{\mathrm{CO}}/L_\odot = 4.9\times10^{-5} J^3 (L'_{\mathrm{CO}(J\to J-1)}/\mathrm{K\,km\,s^{-1}\,pc^2})$ (Bernal and E. D. Kovetz 2022).

1.4.3 HI 21cm line emission

Besides the galaxies, the IGM can also be probed via detection of the redshifted $[\mathrm{H\,I}]_{21\mathrm{cm}}$ signal emitted by the neutral hydrogen. The origin of this line emission is due to the spin-flip transition between the hyperfine states of the hydrogen atom, which has a rest-frame wavelength of approximately 21cm. The excitation mechanism of the hydrogen atoms between these hyperfine states can be radiative processes or via collisional excitations. Depending on the cosmic time, the dominant excitation mechanism can vary. During the early stages of cosmic evolution, the radiation coupling from CMB photons dominated the primary excitation mechanism over collisional excitation for neutral hydrogen in the IGM. However, during the Cosmic Dawn and afterward, as the first luminous sources began to form, the Lyman-α radiation started to couple the spin temperature of neutral hydrogen to the kinetic temperature of the gas. The dominant excitation mechanism, in this case, is via the Wouthuysen-Field effect (Wouthuysen 1952; Field 1958; Madau, Meiksin, and Rees 1997) by the Lyman-α photons.

The $[\mathrm{H\,I}]_{21\mathrm{cm}}$ line emission is observed against the CMB background, and a differential brightness temperature is defined to estimate the strength of this line emission. The $[\mathrm{H\,I}]_{21\mathrm{cm}}$ differential brightness temperature δT_{b} is given as (Somnath Bharadwaj and Ali 2004)

$$\delta T_{\mathrm{b}}(z) = \frac{T_{\mathrm{s}}(z) - T_\gamma(z)}{1+z} \exp\left(-\tau_{21\mathrm{cm}}\right), \tag{1.11}$$

where $\tau_{21\mathrm{cm}}$ is the optical depth of the $[\mathrm{H\,I}]_{21\mathrm{cm}}$ line emission. The optical depth, $\tau_{21\mathrm{cm}}$, will be much less than 1 during cosmic reionization, and it is assumed that the spin temperature will be much higher than the CMB temperature. Under these assumptions, one can write the $[\mathrm{H\,I}]_{21\mathrm{cm}}$ differential brightness temperature as (Somnath Bharadwaj and Ali 2005)

$$\delta T_{\mathrm{b}}(\boldsymbol{x}, z) \approx 4\mathrm{mK}\, x_{\mathrm{HI}}(\boldsymbol{x}, z)(1+\delta_{\mathrm{H}}(\boldsymbol{x}, z))\sqrt{\frac{1+z}{\Omega_{\mathrm{m}}}}\left(\frac{\Omega_{\mathrm{b}}h^2}{0.02}\right)\left(\frac{0.7}{h}\right)\left(1 - \frac{1+z}{H(z)}\frac{\partial v_\parallel}{\partial r_\parallel}\right). \tag{1.12}$$

The terms $x_{\mathrm{HI}}(\boldsymbol{x}, z)$, $\delta_{\mathrm{H}}(\boldsymbol{x}, z)$ and $\partial v_\parallel/\partial r_\parallel$ are the neutral fraction of the IGM, the baryon overdensity and the rate of change of parallel component of peculiar velocity of H I clouds with respect to comoving distance. It can be seen that the $\delta T_b(\boldsymbol{x}, z)$ is a direct probe of the neutral fraction ($x_{HI}(\boldsymbol{x}, z)$) field, modulated by the baryon overdensity ($\delta_H(\boldsymbol{x}, z)$), and therefore, it is a probe of the cosmic reionization as well.

The neutral fraction field is defined as $x_{HI}(\boldsymbol{x}, z) = \rho_{HI}(\boldsymbol{x}, z)/\rho_H(\boldsymbol{x}, z)$, where $\rho_{HI}(\boldsymbol{x}, z)$ is the neutral hydrogen density and $\rho_H(\boldsymbol{x}, z)$ is the total hydrogen (neutral + ionized) density. Overall, the neutral fraction field is determined by the distribution of fully neutral, partially ionized, and fully ionized regions in the IGM, which in turn is affected by the distribution and properties of the luminous sources emitting ionizing radiation (Kim et al. 2013). For example, the presence of minihalos can play an important role in shaping the morphology of the fully ionized H II regions (McQuinn et al. 2007) and consequently affect the [H I]$_{21cm}$ signal (Bin Yue et al. 2009). Similarly, the different sources of reionization also affect the neutral fraction field in different ways, which is captured in the [H I]$_{21cm}$ signal (Majumdar, Jensen, et al. 2016; Noble et al. 2024). Therefore, probing the tomographic view of the early Universe using the [H I]$_{21cm}$ signal during the epoch of reionization can shed light on the reionization process and the luminous sources responsible for driving reionization. It is expected that the upcoming radio interferometers, such as the Square Kilometre Array (SKA), will be capable of producing such tomographic observations with this signal (Mellema, Leon Koopmans, et al. 2015; Y. Wang et al. 2015). However, tomographic observations can suffer from certain drawbacks, for example, being unable to break degeneracies in the IGM temperature and ionization state (Raghunath Ghara, Sambit K. Giri, et al. 2021).

As mentioned earlier, one of the usual assumptions is that the spin temperature $T_s(x, z)$ of the neutral hydrogen gas in the IGM is much higher than the CMB temperature, which allows us to neglect the factor $(1 - T_\gamma(x, z)/T_s(x, z))$, which would otherwise play a role in determining $\delta T_b(x, z)$, since $\delta T_b(x, z) \propto (1 - T_\gamma(x, z)/T_s(x, z))$. A study by Fialkov, Barkana, and Visbal 2014 has shown that this can be the case if one considers a realistic hard X-ray spectrum from X-ray binaries, whose energy content peaks at around 3 keV. The photons with energy above a critical threshold of 1 keV have longer mean free paths, and most of these photons have not been absorbed by the start of reionization. Those photons that are absorbed in the IGM come from distant sources and have been dimmed by the cosmological expansion of the Universe. Therefore, due to late heating from X-ray photons, the IGM temperature could be comparable to the CMB temperature and therefore $\delta T_b(x, z)$ can be sensitive to the fluctuations in $T_s(x, z)$. In the simulation setup used to predict the [H I]$_{21cm}$ signal in this thesis, the population of X-ray binaries and their spectra is not modeled currently, along with its interaction with the IGM, and therefore the fluctuations in the $T_s(x, z)$ have been neglected for simplicity. However, this is a crucial factor that should be incorporated into our future models of the [H I]$_{21cm}$ LIM signal.

1.4.4 Interlopers and Foregrounds

Although the various bright line emissions from galaxies ($[\mathrm{C\ II}]_{158\mu\mathrm{m}}$, CO, etc.) and the $[\mathrm{H\ I}]_{21\mathrm{cm}}$ line emission from the IGM are potential tracers for probing the EoR with LIM, it is not without its challenges. One of the key problems it faces is the issue of interlopers. Within a specific frequency band of a given instrument, the target signal is expected to be observed, which is redshifted to this frequency band. On the other hand, certain LIM signals other than the targeted one can originate from a different cosmic time (redshift) but fall in the same observed band as the targeted signal. This will create confusion in the detected signal, contaminate it, and hinder any meaningful inference from the targeted signal. These are called interloper line emissions, and their degree of contamination can vary depending on the type of line emission and redshift.

In the context of high redshift $[\mathrm{C\ II}]_{158\mu\mathrm{m}}$ LIM signals from the EoR, significant interlopers to consider are the various CO line emissions from low redshift galaxies. As discussed by G. Sun, Moncelsi, et al. 2018, a mitigation strategy for the $[\mathrm{C\ II}]_{158\mu\mathrm{m}}$ line in a simulated field for the **Tomographic Ionized-carbon Mapping Experiment (TIME)** involves identifying and discarding voxels contaminated with CO lines using galaxy catalogs. This process determines the masking depth through the stellar mass of galaxies, corresponding to a certain CO flux threshold. Unlike simple brightness-based masking, this method leverages spectral information, effectively reducing faint CO contamination. The outcomes suggest a criterion equivalent to K-band magnitudes of $m_{\mathrm{AB}} \lesssim 22$ and an achievable $[\mathrm{C\ II}]_{158\mu\mathrm{m}}$/CO power ratio of $\gtrsim 10$, though at the expense of an 8 percent loss in survey volume.

To address the continuum emission from dust within the galaxies, contributing to the fluctuations in the cosmic infrared background (CIB), Van Cuyck et al. 2023 has compared two methods: the asymmetric re-weighted penalized least-squares (arPLS, Baek et al. 2015) and the principal component analysis (PCA). The approach adopted to deal with the interlopers for the $[\mathrm{C\ II}]_{158\mu\mathrm{m}}$ line emission is to mask the galaxies at low redshift utilizing external catalogs and the beam profile of the instrument. Lacking CO observations or sufficiently deep classical CO proxies (like LIR), they utilized the COSMOS stellar mass catalog, which they validate as a reliable proxy of CO, for masking. For assessing the angular power spectrum of the masked data, they modified the P of K EstimatoR (POKER, Ponthieu, Grain, and G. Lagache 2011) typically used in studies of the CIB and discussed its application to data from LIM. The technique of arPLS can reduce the CIB fluctuations by a factor greater than 70 compared to the baseline model for $[\mathrm{C\ II}]_{158\mu\mathrm{m}}$ emission considered, and therefore, compared to the $[\mathrm{C\ II}]_{158\mu\mathrm{m}}$ power spectrum, it is subdominant at the redshift of 7. However, the PCA method can only reduce the fluctuations to a factor of 0.7 at this given redshift. The undetected faint sources might not be clustered around the sources that are either detected or masked, leading to this residual level of contamination. With a survey area loss of 22 percent, the $[\mathrm{C\ II}]_{158\mu\mathrm{m}}$ signal was forecasted to be detected with a $[\mathrm{C\ II}]_{158\mu\mathrm{m}}$/(residual interlopers) power ratio of 62 ± 32 at a redshift of 5.2, for the $[\mathrm{C\ II}]_{158\mu\mathrm{m}}$ emission model assumed in Van Cuyck et al. 2023. However, due to the reduced contrast between the

[C II]$_{158\mu m}$ emission and the residual line contamination, the power ratio is only about 2.0 ± 1.4 at a redshift of 7. It was also demonstrated that for redshifts between 5.2 and 7, the amplitude of the power spectrum of line residuals varies within $12 - 15$ percent, and this is smaller than the field-to-field variance affecting the power spectrum of [C II]$_{158\mu m}$ emission (Gkogkou et al. 2023). The primary obstacle in detecting the [H I]$_{21cm}$ LIM signal in radio frequencies is the foreground contamination caused by extragalactic sources and galactic synchrotron emission (Di Matteo et al. 2002; Oh and Mack 2003; Mário G. Santos, Cooray, and Knox 2005; Ali, Somnath Bharadwaj, and Chengalur 2008). Kerrigan et al. 2018 presents a hybrid approach to addressing foreground contamination for the [H I]$_{21cm}$ signal, combining the filtering of the noise power spectrum in Fourier space with foreground models being subtracted in real space. This method improved significantly over filtering alone when applied to data from PAPER and MWA. When compared to filtering only, the improvement at the band center of MWA is only $\sim 10^9\,\mathrm{mK}^2(h^{-1}\,\mathrm{Mpc})^3$, while this can be expected to be $\sim 10^{12}$–$10^{13}\,\mathrm{mK}^2(h^{-1}\,\mathrm{Mpc})^3$ at the band edges of MWA. Calibration and other systematic errors can still prevail, even when the foreground contamination has been addressed via subtraction and avoidance techniques. The Gaussian Process Regression or GPR technique was presented by F. G. Mertens, A. Ghosh, and L. V. E. Koopmans 2018 to statistically eliminate the contribution to the [H I]$_{21cm}$ power spectrum from these stochastic errors. At specific scales of $k = 0.07$–$3\,h\,\mathrm{Mpc}^{-1}$, this method was shown to recover the power spectrum using simulated LOFAR-EoR data. When the signal rms is $\sigma_{21\mathrm{cm}} > 0.1\sigma_{\mathrm{noise}}$ and at frequency scales of $\gtrsim 3$ MHz, there is a correlation in the foregrounds, this technique is most effective. The sensitivity improves by a factor of 3 as compared to foreground avoidance methods.

Section 1.5 has been adapted from: **Murmu, C. S.**, Ghara, R., Majumdar, S., & Datta, K. K. (2022). Probing the epoch of reionization using synergies of line intensity mapping. *Journal of Astrophysics and Astronomy*, 43(2), DOI: 10.1007/s12036-022-09882-z, arXiv: 2210.09612 (**Review article**)

1.5 Experiments/Instruments for line intensity mapping

Some of the LIM observations targeting various line emissions from the galaxies and IGM out to the epoch of reionization are ongoing or upcoming in the future. In the following, we discuss some of them, mainly targeting the [C II]$_{158\mu m}$, CO, [H I]$_{21cm}$, and other line emissions.

- **CONCERTO**: The CarbON CII line in the post-rEionization and ReionizaTiOn (CONCERTO) instrument, installed on the APEX telescope, is designed to quickly map large sky volumes by targeting [C II]$_{158\mu m}$ line emissions from the EoR and post-EoR. As a 12m class telescope, it is anticipated to complement interferometers like ALMA with its extensive field of view and higher mapping speeds. Covering a frequency range of approximately $\sim 130 - 310$ GHz, it is ideal for line intensity mapping of [C II]$_{158\mu m}$ emission (CONCERTO Collaboration et al. 2020).

The star-forming galaxies emit multiple spectral lines, among which the [C II]$_{158\mu\mathrm{m}}$ line is one of the brightest. On a global scale, this is also an effective tracer of star formation. CONCERTO will trace the [C II]$_{158\mu\mathrm{m}}$ line intensity fluctuations in three dimensions from the reionization and post-reionization epochs ($z \gtrsim 5$), aiming to answer how early galaxy evolution can be affected by star formation and whether [C II]$_{158\mu\mathrm{m}}$-emitters significantly impact cosmic reionization. It will provide a data cube containing a mapping of the line emission intensity over sky position and frequency, and analyze 3D fluctuations of the LIM signal with the power spectrum in Fourier space. Additionally, CONCERTO will also capture the CO intensity fluctuations from galaxies at redshifts between 0.3 and 2, revealing the spatial distribution and abundance of molecular gas across cosmic time. CONCERTO Collaboration et al. 2020 predict sensitivities for CONCERTO at various redshifts and estimate detectability of the power spectrum of [C II]$_{158\mu\mathrm{m}}$ emission using models from Serra, Doré, and Guilaine Lagache 2016. The survey is projected to last approximately ~ 1200 hours, with a redshift width of approximately $\Delta z \sim 0.6$, corresponding to a 20 GHz bandwidth at $z = 6.1$. In the most pessimistic scenario, the SNR varies between $1.1 - 4.3$ at $z = 6.2$.

- **FYST**: The Fred Young Submillimetre Telescope (FYST CCAT-Prime Collaboration et al. 2023) with an aperture of 6 m and expansive field-of-view design, is located on Cerro Chajnantor in northern Chile, at 5600 m altitude (Parshley, Kronshage, et al. 2018; Parshley, M. Niemack, et al. 2018). Combined with Prime-Cam (Vavagiakis et al. 2018), it is exceptionally suited for a variety of scientific purposes. The telescope's aperture allows for imaging, which is diffraction-limited, with a beam size suitable for studies of B-mode polarization of CMB and LIM probes at sub-megaparsec scales. Utilizing FYST's wide field of view, Prime-Cam imaging arrays achieve mapping speeds more than ten times faster than current and upcoming facilities. The FYST has a field of view of 8° in diameter, and the Prime-Cam will cover the central 4.9° (M. D. Niemack 2016; Parshley, Kronshage, et al. 2018). Seven independent instrument modules occupy the field, with a central module surrounded by six modules compactly. The modules are separated by 1.8° and are within a cryostat with a diameter of 1.8 m, and each module covers a field of 1.3° in diameter. While the external designs of the modules are nearly identical, their internals are independently optimized for their specific scientific programs. There are two imaging spectrometers in the Prime-Cam module that uses Fabry-Perot interferometers (FPIs) for LIM that will target the frequency range of 210 - 420 GHz. The Prime-Cam module also has five broadband modules, which are polarization-sensitive and observe at five different frequencies (220, 280, 350, 410, and 850 GHz; Choi et al. 2020). Each module is housed in a cylindrical shell of approximately 1.6 m in length and 45 cm in diameter (Vavagiakis et al. 2018). The Epoch of Reionization Spectrometer (EoR-Spec) modules, dedicated for LIM, have been optimized to probe the [C II]$_{158\mu\mathrm{m}}$ line emission fluctuations, covering a range of redshift between $3.5 \lesssim z \lesssim 8.05$, that encompasses the EoR. The [C II]$_{158\mu\mathrm{m}}$ line emission will be probed over wide fields (Cothard et al. 2020) within this redshift interval using spectrometers based on cryogenic imaging FPI. As the [C II]$_{158\mu m}$line tracks star formation (Stacey, Geis, et al. 1991; Stacey, Hailey-Dunsheath, et al. 2010), it will probe the first stars and galaxies and their evolution, which were responsible for reionization. Recent analysis by Clarke et al. 2024 suggest that the expected lower limits for [C II]$_{158\mu m}$power spectrum with EoR-Spec are $\Delta^2(k = 1\,\text{Mpc}^{-1}, 5.34 < z < 6.31) = 9.8 \times 10^5\,(\text{Jy/sr})^2$ and $\Delta^2(k = 1\,\text{Mpc}^{-1}, 6.75 < z < 8.27) = 2.77 \times 10^5\,(\text{Jy/sr})^2$. However, the predicted SNR for their fiducial [C II]$_{158\mu m}$models assumed and the redshift ranges considered are barely favorable, hinting at a significant challenge for signal detection. The scenario improves when they incorporate galaxy stellar mass functions from Weaver et al. 2023 and use wider k-bins for power spectrum estimation, which results in significantly better SNR.

- **TIME**: The Tomographic Intensity Mapping Experiment (TIME) is an imaging spectrometer array having a wide bandwidth that aims to probe the fluctuations in [C II]$_{158\mu m}$ line intensity between redshifts of 6 to 9 (Hunacek et al. 2018; Cheng, Tzu-Ching Chang, and J. J. Bock 2020). Within this band, it will also detect the galaxies at comparatively low redshifts (0.5$\lesssim$z $\lesssim$2) in CO line emission. The instrument started operation in 2021, and 1000 hours of observation time is planned initially. This is based on the 12 m ALMA prototype antenna located at the Arizona Radio Observatory in Kitt Peak, Arizona. G. Sun, T. C. Chang, et al. 2021 has forecasted that from the EoR, a measurement of the power spectrum of the [C II]$_{158\mu m}$line emission with SNR> 5 is possible with TIME.

- **COMAP**: The CO Mapping Array Project is focused on detecting CO emissions from the early Universe. The Pathfinder instrument is a spectrometer receiver with 19 feeds, mounted on a dish that is 10.4 m in diameter. It is situated at the Owens Valley Radio Observatory and is designed to operate in the 26 - 34 GHz band. Observations began in 2019, targeting CO(1-0) emission from the cosmic noon ($z \sim 2.4 - 3.4$) and CO(2-1) emission reaching out to the EoR ($z \sim 5.8 - 7.8$). Consequently, the CO(1-0) emission acts as a natural interloper for the EoR CO(2-1) signal. The COMAP-EoR instrument will operate in the 12 - 20 GHz band, enabling the detection of CO(1-0) emission reaching out to the EoR, which can be used for cross-correlation with the CO(2-1) signal. Currently, 12 square degrees of the sky are being observed, which is part of the 5-year survey plan, using the COMAP pathfinder.

  The COMAP pathfinder also serves to validate existing technologies, develop new methodologies, understand systematics, and devise new observational strategies (Dongwoo T. Chung et al. 2022; Breysse, Dongwoo T. Chung, et al. 2022; Håvard T. Ihle et al. 2022). It has been predicted by the COMAP team that the CO power spectrum will be detected with an SNR of 9-17 after five years of survey. However, a 2σ upper limit on the CO(1-0) clustering power spectrum has been placed by Cleary et al. 2022, using the first 13 months of observation data, with an upper limit of $P_{\text{CO}}(k) = -2.7 \pm 1.7 \times 10^4 \mu\text{K}^2\,\text{Mpc}^3$ at k scales of 0.051 - 0.62 Mpc^{-1}. Recently, updated results from the COMAP survey have been presented by Stutzer et al. 2024 at redshifts of $z \sim 3$, using feed-group pseudo power spectrum or FGPXS, which improves on the methodology by being more resilient to systematic effects. The measurements span across $0.09 < k < 0.73$ Mpc^{-1}, and in the individual bins, a power spectrum value of $kP_{\rm CO}(k) < 2400 - 4900\,\mu$K^2 Mpc^2 is constrained with a confidence level of 95 percent. D. T. Chung et al. 2024 have also constrained the CO tracer bias to $\langle Tb \rangle < 4.8\mu$K using the COMAP season 2 results. The challenging CO(2-1) LIM signal from $z \gtrsim 6$ is expected to be addressed in the near future.

- **SPHEREx**: The deep spectro-imaging survey from the Spectro-Photometer for the History of the Universe, Epoch of Reionization and Ices Explorer, or SPHEREx, offers a dataset that is ideal for comprehensive tomographic mapping of large-scale structures, particularly focusing on galactic emission lines. As an all-sky spectrometer and space-based mission, it operates within the $0.75 - 5.00\,\mu$m wavelength range, enabling investigation of the EoR through emissions such as [O III], [O II], Lyman-α, etc. The galaxy clustering at large scales is traced by these line emissions, which offer 3D redshift data, unlike 2D continuum measurements. SPHEREx's spectral line intensity cubes effectively trace the evolution of galaxies. SPHEREx detects various lines with high SNR at low redshifts; the primary lines include Hα for $0.1 < z < 5$, Hβ for $0.5 < z < 2$, and [O III] for $0.5 < z < 3$. The Lyman-α line serves as a proxy to study the EoR galaxy formation and evolution, which can be probed by SPHEREx at high redshifts ($5.2 \leq z \leq 8$). Traditionally, Hα post dust extinction correction can reliably trace the cosmic star-formation rate. Although low redshift [O III] and Hβ lines can cause line confusion in observations, this can be tackled by cross-correlation using spectral lines from different bands. For instance, the 2.62μm band will detect the Hα line fluctuations at $z = 3$, while the 2.00μm band will detect the [O III] line fluctuations from the same redshift. Therefore, the galaxies will be traced by a cross-correlation between these two bands at that redshift, without requiring masking, and will mitigate line contaminations in either band. High-redshift intensity mapping with these lines will probe the reionization (Visbal and Loeb 2010; Gong, Cooray, M. B. Silva, et al. 2011; Lidz, Furlanetto, et al. 2011; Gong, Cooray, and Mario G. Santos 2013; M. B. Silva et al. 2013; Pullen, Doré, and J. Bock 2014) in addition to the [H I]$_{\rm 21cm}$ signal. Furthermore, LIM can capture the integrated emission from the dwarf galaxies, thereby complementing JWST surveys that resolve higher luminosity galaxies individually. Spectral masking of the sources of foreground is needed to avoid line confusion whereas for the Lyman-α studies of the EoR, deep region sensitivity might be sufficient to mitigate the dominant H contaminants (Pullen, Doré, and J. Bock 2014).

- **GMRT**: The Giant Metrewave Radio Telescope (GMRT) is sensitive within the frequency band that ranges from 50 - 1420 MHz and this instrument is located in western India. The diameter of each dish is around 45 m and there are 30 such dishes in the array, which is distributed in a Y-shaped pattern and covers an area of radius of approximately 25 km. For post-EoR studies, the 325 and 610 MHz receivers are frequently utilized, while for EoR research, the 150 MHz receiver is utilized. The field of view at 150 MHz is approximately $3.8°$. Initial investigations by S. Bharadwaj and S. K. Sethi 2001; Somnath Bharadwaj and Ali 2005; Ali, Somnath Bharadwaj, and Chengalur 2008 were conducted using GMRT data, into the visibility correlations and angular modes of the $[\mathrm{H\ I}]_{21\mathrm{cm}}$ signal. This research paved the way for further exploration into Multi-frequency Angular Power Spectrum (MAPS, Datta, T. Roy Choudhury, and Somnath Bharadwaj 2007). Abhik Ghosh, Somnath Bharadwaj, et al. 2011a was the pioneer in using GMRT observations to measure the $[\mathrm{H\ I}]_{21\mathrm{cm}}$ signal fluctuations at $\nu_{\mathrm{obs}} = 610$ MHz ($z \sim 1.32$) using a fourth-order polynomial-based foreground removal technique combined with MAPS formalism. Enhancements to the foreground removal process, including sidelobe reduction and primary beam tapering, were subsequently reported by Abhik Ghosh, Somnath Bharadwaj, et al. 2011b. Later, Abhik Ghosh, J. Prasad, et al. 2012 had applied similar analyses at $\nu_{\mathrm{obs}} = 150$ MHz for $z = 8.1$ with GMRT observations. Optimization of power spectrum estimators, like the Tapered Gridded Estimator (TGE) and the Bare Estimator, based on visibility correlations, was later introduced and examined by Choudhuri, Somnath Bharadwaj, Abhik Ghosh, et al. 2014; Choudhuri, Somnath Bharadwaj, S. Chatterjee, et al. 2016; Somnath Bharadwaj, Pal, et al. 2019. At a redshift of 8.6 the first upper limit on the power spectrum of $[\mathrm{H\ I}]_{21\mathrm{cm}}$ signal was reported by Paciga, T.-C. Chang, et al. 2011, based on 50 hours of GMRT observations, presenting a value of 70^2 mK^2 at 2σ confidence level for $k = 0.65\,h$ Mpc^{-1}. An updated upper limit of $(248\,\mathrm{mK})^2$ for $k \sim 0.5\,h\,\mathrm{Mpc}^{-1}$ was later provided by Paciga, Albert, et al. 2013, accounting for loss of signal caused by a previously employed piecewise-linear foreground subtraction method. More recently, Chakraborty et al. 2021 utilized the foreground avoidance technique to estimate the power spectrum upper limits of the $[\mathrm{H\ I}]_{21\mathrm{cm}}$ signal for $z = 1.96, 2.19, 2.62,$ and 3.58 as $(58.87\,\mathrm{mK})^2$, $(61.49\,\mathrm{mK})^2$, $(60.89\,\mathrm{mK})^2$, and $(105.85\,\mathrm{mK})^2$ respectively, at $k \sim 1.0\,h\,\mathrm{Mpc}^{-1}$.

- **LOFAR**: The LOw Frequency ARray (LOFAR) radio interferometer is located in the Netherlands and consists of 38 stations. Out of these, 24 stations are arranged within a core region with a radius of 3 km, whereas up to roughly 100 km, the remaining stations are dispersed. There are also 14 international stations in LOFAR, although they are not utilized for investigations related to the EoR. There are two different types of antennas in the stations: (1) High-Band Antennas (HBA), operating between 120–240 MHz, and (2) Low-Band Antennas (LBA), functioning within the 30–90 MHz range. Each station spans approximately 30 meters in diameter, and at 150 MHz, it has a 3° FoV. The LOFAR EoR Key Science Project team is dedicated to modeling and removing the foreground contaminants from 21-cm observations. Their efforts include developing data analysis methodologies (e.g., Kazemi et al. 2011; Yatawatta 2015), techniques for mitigating foreground interference (e.g., Harker et al. 2009; Chapman et al. 2013; F. G. Mertens, A. Ghosh, and L. V. E. Koopmans 2018; Hothi et al. 2021), and investigating systematic errors (e.g., Mevius et al. 2022), among other approaches. The initial findings on EoR [H

I]$_{21cm}$ fluctuations from LOFAR were reported by Patil et al. 2017, establishing upper limits on the power spectrum of the [H I]$_{21cm}$ signal for redshifts between 9.6 and 10.6 based on 13 hours of LOFAR-HBA data. Gehlot et al. 2019 has placed upper limits at $20 \leq z \leq 25$ on the [H I]$_{21cm}$ power spectrum using only 14 hours of observation data from the LOFAR-LBA. F. G. Mertens, Mevius, et al. 2020 has given a more stringent upper limit of 2σ confidence at $k = 0.075\, h\,\mathrm{Mpc}^{-1}$ with a value of $\Delta^2(k) = 73^2\,\mathrm{mK}^2$ at $z \approx 9.1$, which was obtained from 141 hours of observation using LOFAR-HBA. While earlier limits could not exclude standard EoR and CD scenarios, the new constraints provided by F. G. Mertens, Mevius, et al. 2020 begin to rule out reionization scenarios that are extreme and place restrictions on the nature of sources and the IGM at $z \approx 9.1$ (R. Ghara, S. K. Giri, et al. 2020; R. Mondal et al. 2020; Greig et al. 2021).

- **MWA**: The Murchison Widefield Array (MWA) can observe within the frequency range of 80-200 MHz and therefore measure the [H I]$_{21cm}$ signal fluctuations within the redshift range of $6.1 \lesssim z \lesssim 16.75$. This interferometer consists of 256 stations, divided into two groups: 128 stations with long baselines, part of the Extended Array, and 128 stations with short baselines, including two 36-station subarrays, part of the Compact Array. The Compact Array is dedicated primarily to observe the EoR using the [H I]$_{21cm}$ signal. Compared to a LOFAR station, each MWA station is roughly six times smaller and has a FoV which can range from 15 to 50 degrees at 200 MHz. The analysis of data from MWA utilizes delay transform primarily to obtain the 2D power spectrum of the signal in the $k_\perp$ and $k_\parallel$ space. In this space, the 'EoR Window' portion is not expected to be contaminated by external factors, such as inaccurate calibration, leakage of foreground, etc. The preliminary attempts by the team developed methods to calibrate the data and subtract sources using the Real-Time System (Mitchell et al. 2008), Fast Holographic Deconvolution (Sullivan et al. 2012), power spectra estimator pipelines like CHIPS (C. M. Trott et al. 2016) and εppsilon (Barry, Beardsley, et al. 2019) for the MWA EoR data analysis. Barry, Wilensky, et al. 2019; W. Li et al. 2019 presented the first upper limit results for the EoR [H I]$_{21cm}$ signal, while Ewall-Wice et al. 2016 reported the inaugural upper limits for the [H I]$_{21cm}$ signal from the Cosmic Dawn in the $12 \leq z \leq 18$ redshift range. Cathryn M. Trott et al. 2020 have placed a 2σ upper limit at $k = 0.14\, h\,\mathrm{Mpc}^{-1}$, with a value of $\Delta^2_{21\mathrm{cm}}(k) \approx 43^2\,\mathrm{mK}^2$, which utilized 110 hours of observations in the high-band targeting the EoR0 field at a redshift of $z = 6.5$. Although the study encompassed six different redshifts within the range of $6.5 \leq z \leq 8.8$, the upper limits weakened at the higher redshift end. Subsequently, attempts were made to improve this (Rahimi et al. 2021) by mitigating systematics, that can arise from various factors such as instrument, observation, and analysis. However, the 2σ upper limit of $\Delta^2_{21\mathrm{cm}}(k) \approx 73.78^2\,\mathrm{mK}^2$ at $k = 0.13\, h\,\mathrm{Mpc}^{-1}$ reported in (Rahimi et al. 2021) is higher than that in Cathryn M. Trott et al. 2020 because only 14 hours of observation data were analyzed. Later studies by Greig et al. 2021; Raghunath Ghara, Sambit K. Giri, et al. 2021 have done follow-up work on the upper limits given by Cathryn M. Trott et al. 2020 to discard EoR scenarios which are disfavored, and concluded that by redshift $z = 6.5$, the IGM should have been heated by X-rays from X-ray luminous sources, which rules out a completely neutral and cold IGM at that epoch.

- **HERA**: The HERA radio interferometer is located in the Karoo desert, South Africa, and is designed to detect fluctuations in the [H I]$_{21\mathrm{cm}}$ signal from both the CD and EoR. Phase I features around 350 fixed, zenith-pointing dishes in a hexagonal arrangement within a 300m area, each dish being 14 meters in diameter. It has a FoV of 9°. Phase I of HERA utilizes a correlator and feeds from the preceding [H I]$_{21\mathrm{cm}}$ experiment PAPER. It primarily aims to measure the [H I]$_{21\mathrm{cm}}$ power spectrum accurately from redshifts $6 \lesssim z \lesssim 12$, while the HERA phase II will be capable of probing redshifts $12 \lesssim z \lesssim 35$. The development of calibration pipelines, understanding of systematics, power spectrum estimation, and error propagation was done in preliminary attempts by the HERA team (Dillon et al. 2020; Kern, Parsons, et al. 2020; Kern, Dillon, et al. 2020). HERA's data analysis mainly aims to mitigate spectral systematics to maintain a largely uncontaminated EoR window. Upper limits on the [H I]$_{21\mathrm{cm}}$ power spectrum have been obtained by Abdurashidova et al. 2022, which have used 50 HERA antennas and 36 hours of observation time. At 2σ confidence, an upper limit of $(30.76\,\mathrm{mK})^2$ at $k = 0.190\,h$ Mpc^{-1}, $z = 7.9$ and $(95.74\,\mathrm{mK})^2$ at $k = 0.256\,h$ Mpc^{-1}, $z = 10.4$ were placed using HERA. This has also indicated that by $z = 8$, the temperature of the IGM should exceed that of the adiabatic cooling threshold. The results also constrain the value of the soft X-ray luminosities per star formation rate at 1σ level to a value of $[10^{40.2}, 10^{41.9}]$ erg/s/($M_\odot$/yr).

- **SKA**: The Square Kilometre Array (SKA) is planned to have two different kinds of arrays covering different frequency bands. The SKA-Mid will cover a frequency range of 350 MHz - 15.3 GHz. It will be located in the Karoo desert, South Africa. On the other hand, the SKA-Low will have a frequency range of 50 - 350 MHz, which will target a redshift range of $3 < z < 27.4$. This configuration will be achieved in phase I, consisting of 512 stations, with 212 stations present in a tight core with a radius of ~ 600 m. The remaining stations will be distributed on three spiral arms. These arms can extend up to 65 km from the core region. The SKA-Low is planned to be built in Western Australia. The SKA-Low is expected to supersede LOFAR in terms of sensitivity ($10\times$ better) and allow the generation of tomographic images (e.g., R. Ghara, T. R. Choudhury, et al. 2017) besides conventional statistical measures of [H I]$_{21\mathrm{cm}}$ signal like the power spectrum. Methods such as Minkowski functionals (e.g., Kapahtia et al. 2021), Euler characteristic (see e.g., Sambit K. Giri and Mellema 2021), Bubble size distributions (Sambit K. Giri, Mellema, and Raghunath Ghara 2018; Raghunath Ghara and T. Roy Choudhury 2020), Fractal dimensions (e.g., Bandyopadhyay, T. Roy Choudhury, and Seshadri 2017), and Convolutional neural networks (e.g., Gillet et al. 2019) are being worked on that will be able to make inferences about CD and EoR from the tomographic images from SKA. These methods can characterize the statistical features in these images.

1.6 The observable summary statistics

The line-intensity mapping experiments essentially map and measure the fluctuations of the specific intensity of the probed line emissions. These fluctuations in the specific intensity can be represented as $\delta I(\boldsymbol{x}) = (I(\boldsymbol{x}) - \overline{I})/\overline{I}$, where $\boldsymbol{x}$ is the position in the cosmological volume where the specific intensity is measured. In cosmology, we are interested in knowing the relation of these fluctuations as a function of various length scales. Generally, the length scale dependence of these signal fluctuations is investigated in the Fourier domain, where $\delta I(\boldsymbol{x})$ is Fourier transformed and expressed as a function of k, where $k = 2\pi/\lambda$ and λ is the length scale.

1.6.1 Power spectrum

The lowest-order statistic that captures this length scale information is the power spectrum, which is defined as

$$\langle \delta\tilde{I}(\boldsymbol{k})\delta\tilde{I}^*(\boldsymbol{k'})\rangle = V\delta_{k,k'}P(k). \tag{1.13}$$

The fluctuations in the specific intensity in the Fourier domain, $\delta\tilde{I}(\boldsymbol{k})$, are obtained by Fourier transforming the fluctuations ($\delta I(\boldsymbol{x})$) in real space. This essentially captures the information on the strength of signal fluctuations for different length scales. In the case of the cosmological [H I]$_{21\mathrm{cm}}$ signal whose brightness temperature can be written as $\delta T_\mathrm{b} = T_0\overline{x}_\mathrm{HI}(1+\delta_x)(1+\delta_\rho)$, it can be shown that the power spectrum can be written as (Lidz, Zahn, et al. 2007)

$$\begin{aligned}\Delta^2_{21\mathrm{cm}}(k) =& T_0^2\overline{x}^2_\mathrm{HI}[\Delta^2_{\delta_x,\delta_x}(k) + 2\Delta^2_{\delta_x,\delta_\rho}(k) + \Delta^2_{\delta_\rho,\delta_\rho}(k) + \\ & 2\Delta^2_{\delta_x\delta_\rho,\delta_x}(k) + 2\Delta^2_{\delta_x\delta_\rho,\delta_\rho}(k) + \Delta^2_{\delta_x\delta_\rho,\delta_x\delta_\rho}(k)].\end{aligned} \tag{1.14}$$

Here, $\delta_x = (x_\mathrm{HI} - \overline{x}_\mathrm{HI})/\overline{x}_\mathrm{HI}$ is the fractional fluctuation in the fraction of neutral hydrogen and $\delta_\rho = (\rho - \overline{\rho})/\overline{\rho}$ is the matter overdensity. $\Delta^2_{21\mathrm{cm}}(k) = k^3P_{21\mathrm{cm}}(k)/(2\pi^2)$ is the normalized [H I]$_{21\mathrm{cm}}$ power spectrum, to which the different cross-terms also contribute. On small scales ($k \gtrsim 1\,h\,\mathrm{Mpc}^{-1}$), it can be demonstrated analytically that the higher-order cross term $P_{\delta_x\delta_\rho,\delta_\rho}(k)$ follows $P_{\delta_\rho,\delta_\rho}(k)\int \mathrm{d}\ln k' \Delta^2_{\delta_x,\delta_\rho}(k')$ (Lidz, Zahn, et al. 2007). The integral over $\Delta^2_{\delta_x,\delta_\rho}(k)$ quantifies how well the overdensities are traced by the ionized regions. This integral can be expressed as $\langle\delta_x\delta_\rho\rangle = -1 + \langle x_\mathrm{HI}\rho\rangle/\langle x_\mathrm{HI}\rangle\langle\rho\rangle$, or in terms of the mass-weighted and volume-weighted ionization fractions, indicated by $x_\mathrm{i;m}$ and $x_\mathrm{i;v}$, respectively, as $\langle\delta_x\delta_\rho\rangle = (x_\mathrm{i;v} - x_\mathrm{i;m})/(1 - x_\mathrm{i;v})$. During reionization, this term is negative in these simulations because the ionizing sources are found in overdense regions and therefore, the surroundings are reionized before the underdense regions. As a result, the mass-weighted ionization fraction is consistently higher than the volume-weighted ionization. Likewise, the term $P_{\delta_x\delta_\rho,\delta_\rho}(k)$ follows $P_{\delta_\rho,\delta_x}(k)\int \mathrm{d}\ln k'\Delta^2_{\delta_x,\delta_\rho}(k')$ and $P_{\delta_x\delta_\rho,\delta_\rho}(k)$. This term is less significant on small scales since $P_{\delta_\rho,\delta_\rho}(k) \gg P_{\delta_\rho,\delta_x}(k)$, although it is not entirely negligible (it contributes around 10 percent on small scales). The term $P_{\delta_x\delta_\rho,\delta_x\delta_\rho}(k)$

roughly follows $P_{\delta_\rho,\delta_\rho}(k)\int d\ln k'\Delta^2_{\delta_x,\delta_x}(k')$ (Lidz, Zahn, et al. 2007). Lidz, Zahn, et al. 2007 discuss that in the small scales the contribution of the higher order terms can be important and they measured the higher-order terms in equation 1.14 separately, using the reionization simulations of Zahn et al. 2007 and McQuinn et al. 2007. They found that the perturbative approach matches reasonably well with the simulations on small scales.

Recently, Georgiev et al. 2022 has investigated these decomposition terms on large scales using simulations spanning volumes of the scale of $\sim 714^3$ Mpc^3. It was found that the auto-correlation term of the matter overdensity ($\Delta^2_{\delta_\rho,\delta_\rho}$) will dominate when the ionized fraction of the IGM is very low (few percent level). In this scenario, at low k modes, the $\Delta^2_{21\text{cm}}$ replicates the matter power spectrum. During the later phases, of reionization ($x_{\text{HII}} \sim 5-10$ percent), the density peaks in the [H I]$_{21\text{cm}}$ signal are removed and this phase becomes more related to the cross-correlation of the ionization field and overdensity field. In this phase the cross-terms in the expansion of the $\Delta^2_{21\text{cm}}$ have similar strength. Thus, the [H I]$_{21\text{cm}}$ power spectrum neither traces the neutral fraction or matter power spectra nor any combination of these and has very low amplitudes at large scales. After this phase is over and towards the end of reionization, $\Delta^2_{21\text{cm}}$ follows the neutral fraction power spectrum ($\Delta^2_{\delta_{\text{HI}},\delta_{\text{HI}}}$), which is also the dominant term except when () briefly dominates. The [H I]$_{21\text{cm}}$ power spectrum shows a non-monotonic shape related to the characteristic scale of the sizes of the ionized bubbles. In the expansion of the $\Delta^2_{21\text{cm}}$, the higher order terms are important only during the phases of equilibrium and the late stages of reionization. When $x_{\text{HII}} \sim 70-80$ percent, the $\Delta^2_{\delta_\rho,\delta_{\text{HI}}}(k)$ term is dominated by $\Delta^2_{\delta_{\text{HI}}\delta_\rho,\delta_{\text{HI}}}(k)$ which then becomes the second most influential term.

The finite travel time of radiation will induce anisotropy along the line-of-sight (LoS) in the observed signal. This phenomenon called the light-cone effect will affect the observable summary statistics as well, which can bias their interpretation. Datta, Mellema, et al. 2012 investigated its impact on the [H I]$_{21\text{cm}}$ power spectrum. In their studied cases, they observed that the spherically averaged power spectrum varies by up to ~ 50 percent within the k range of 0.08 to 9 Mpc^{-1} when using a redshift interval matching the full extent of the simulation volume (163 cMpc) considered in the study. As anticipated, the effect is reduced with smaller redshift bins. Larger scales experience a greater impact, while the effects on smaller scales are minimal. They observed that, generally, the power on larger scales increases while on smaller scales it decreases, except during the final phase of reionization where the power spectrum diminishes across all scales detectable in these simulations. A 'cross-over mode,' $k_{\text{cross}-\text{over}}$ exists, below which the power is enhanced and above which it is suppressed. As reionization progresses, this $k_{\text{cross}-\text{over}}$ shifts to lower modes (larger scales).

Similarly, the [H I]$_{21\text{cm}}$ power spectrum will also be affected by the peculiar velocities of the H I clouds, which will induce redshift space distortion. In the quasi-linear approximation (Mao, Shapiro, et al. 2012), the redshift-space [H I]$_{21\text{cm}}$ power spectrum can be represented as

$$P^{\text{s}}(k,\mu) \simeq T_0^2 \overline{x}_{\text{HI}}^2 (P_{\delta_{\text{HI}},\delta_{\text{HI}}} + 2\mu^2 P_{\delta_{\text{HI}},\delta_\rho} + \mu^4 P_{\delta_\rho,\delta_\rho}) \tag{1.15}$$

which can be further decomposed into an orthonormal basis of Legendre polynomials in the following way:

$$P_l^{\rm s}(k) = \frac{2l+1}{4\pi}\int \mathcal{P}(\mu) P^{\rm s}(k,\mu)\,{\rm d}\Omega. \tag{1.16}$$

$P_0^{\rm s}(k)$ is the spherically averaged power spectrum and the other non-zero higher-order multiples are $P_2^{\rm s}(k)$ and $P_4^{\rm s}$ (Majumdar, Somnath Bharadwaj, and T. Roy Choudhury 2013; Majumdar, Mellema, et al. 2014). Majumdar, Jensen, et al. 2016 has shown that the term $P_2^{\rm s}(k)$ is a linear combination of $P_{\delta_\rho,\delta_\rho}$ and $P_{\delta_{\rm HI},\delta_\rho}$, while $P_4^{\rm s}(k)$ follows $P_{\delta_\rho,\delta_\rho}$. Although $P_2^{\rm s}(k)$ might not be robust enough to distinguish the various reionization scenarios, it can be useful to track the reionization history.

The galaxy line-intensity mapping power spectrum for a line emission i, is modeled as,

$$P_i(k,z) = \langle I_i(z)\rangle^2 \langle b_i(k,z)\rangle^2 P_{\rm m}(k,z) + P_{i;\rm SN}(z), \tag{1.17}$$

where $\langle I_i(z)\rangle$ is the average line intensity as defined in 1.8. $b_i(k,z)$ is the line bias defined as

$$\langle b_i(k,z)\rangle = \frac{\int {\rm d}M \frac{{\rm d}n}{{\rm d}M} L_i(M,z) b_{\rm h}(M,k,z)}{\int {\rm d}M \frac{{\rm d}n}{{\rm d}M} L_i(M,z)}, \tag{1.18}$$

with $b_{\rm h}(M,k,z)$ being the halo bias, defined as $b_h^2(M,k,z) = P_{\rm hh}(M,k,z)/P_{\delta\delta}(k,z)$. $P_{\rm hh}(M,k,z)$ is the halo power spectrum and $P_{\delta\delta}(k,z)$ is the dark-matter power spectrum. $L_i(M,z)$ is the relation between the host halo mass of the galaxy and the line luminosity of the i-th line emission, and ${\rm d}n(M,z)/{\rm d}M$ is the halo-mass function. The $P_{\rm m}(k,z)$ is the matter power spectrum, while $P_{i;\rm SN}(z)$ is the shot-noise power spectrum for the i-th line emission. The first term in equation 1.17 represents the clustering term and arises from the large-scale clustering of the sources emitting the i-th line emission. On a small scale, these sources have a discrete nature. The second term, $P_{i;\rm SN}(z)$ represents the power spectrum arising from the discrete nature of these sources. The power spectrum therefore captures both astrophysical information from the sources as well as cosmological information.

The usual models assume the relation between line luminosity and the host halo mass (i.e. $L_i(M,z)$) to be a perfectly correlated one-to-one relation. However, in the most realistic scenario, this does not hold. Due to complex astrophysical aspects, the line luminosity will not follow a tight correlation with the host halo mass, which will be discussed in subseciton 1.8. This is expected to affect the galaxy line-intensity mapping power spectrum.

As a simple approach, one can assume that the line luminosity $L_i(M,z)$ has a log-normal scatter around some relation with the host halo mass, with a value of σ dex. For simplicity, one might further assume that this σ is independent of the host halo mass, i.e. it is constant across all halo mass ranges. Under this scenario, the probability density of the line luminosity can be written as

$$P(x|\mu,\sigma) = \frac{1}{\sqrt{2\pi}\sigma}\exp\left[-\frac{(x-\mu)^2}{2\sigma^2}\right], \tag{1.19}$$

where $\mu = \log L_i(M,z)$ is logarithm of the mean line strength. It can be shown that the clustering power spectrum with scatter is just a rescaled power spectrum without scatter, where the new mean line strength is $\mu_{\mathrm{n}} = \mu + (\sigma^2 \ln 10)/2$ (Guochao Sun, Hensley, et al. 2019). In this sense, the mean intensity is unaffected by the scatter in the line luminosity with respect to the host halo mass, and so is the large-scale clustering power spectrum since it is $\propto \langle I_i(z)\rangle^2$.

On the other hand, the large-scale LIM power spectrum can also be interpreted differently. The enhancement in the mean intensity can be written as

$$\langle I_i(z)\rangle = \frac{\lambda_{\mathrm{rest}}^3 f_\sigma}{4\pi H(z)} \int \mathrm{d}M \frac{\mathrm{d}n(M,z)}{\mathrm{d}M} L_i(M,z), \tag{1.20}$$

where the f_σ is the enhancement factor given as $f_\sigma = 10^{(\sigma^2 \ln 10)/2}$ and $L_i(M,z)$ is the specific luminosity (Moradinezhad Dizgah and Keating 2019a). Therefore on large scales, the galaxy LIM power spectrum is $\propto f_\sigma^2$. Therefore, in this interpretation, the average line intensity and the large-scale power spectrum can be significantly affected due to scatter in line luminosity. However, under the assumption that the scatter σ is independent of the halo mass, one is free to choose any of the interpretations, although this might not be true when one considers a more realistic halo-mass dependent scatter in the line luminosity.

1.6.2 Cross-power spectrum

The LIM cross-power spectrum for two line emission signals, 1 and 2, can be defined as

$$\langle \delta\tilde{I}_1(\boldsymbol{k}) \delta\tilde{I}_2^*(\boldsymbol{k'})\rangle = V\delta_{k,k'} P_{1\times2}(k). \tag{1.21}$$

Unlike the auto-power spectrum, which does not retain any phase information from the LIM signals, the cross-power spectrum captures the relative phase difference between signals 1 and 2. If one writes the fluctuations in Fourier space in the Eulerian form, with $\delta\tilde{I}_1 = A_1 \exp(-\boldsymbol{i}\phi_1)$ and $\delta\tilde{I}_2 = A_2 \exp(-\boldsymbol{i}\phi_2)$, then $\langle \delta\tilde{I}_1 \delta\tilde{I}_2^* \rangle = \langle A_1 A_2 \exp(-\boldsymbol{i}(\phi_1 - \phi_2))\rangle$. It can be easily seen, that for the auto-power spectrum, when signals 1 and 2 are identical, $\phi_1 - \phi_2 = 0$, and the phase information is completely lost. The cross-correlation coefficient is defined as

$$r_{1\times2}(k,z) = \frac{P_{1\times2}(k,z)}{\sqrt{P_1(k,z)P_2(k,z)}} \tag{1.22}$$

captures this information of the relative phase difference. For example, for the cross-correlation of line emission from galaxies and the $[\mathrm{H\,I}]_{21\mathrm{cm}}$ signal from the EoR tracing the IGM, one can expect the cross-correlation between these signals to evolve as the reionization progresses. When the reionization is at its early stages, the strength of the galaxy line emissions and the $[\mathrm{H\,I}]_{21\mathrm{cm}}$ signal is expected to be strongest in the overdensities, resulting in a positive correlation between these signals. However, as reionization proceeds towards the mid stages, when ionized bubbles have developed around the sources, the [H I]$_{21\text{cm}}$ signal will trace the IGM, except the most overdense regions, in an 'inside-out' reionization scenario. This will lead to an anti-correlation between the signals at large scales.

M. B. Silva et al. 2013 has explored the prospects of cross-correlating the Lyman-α emission from the reionizing sources and the [H I]$_{21\text{cm}}$ signal originating from the IGM. During EoR, the [H I]$_{21\text{cm}}$ signal predominantly comes from the IGM contrary to galaxies, whereas the Lyman-α emission mostly comes from the galaxies for most redshifts. Under this scenario, the cross-correlation between these two signals can be written as,

$$P_{\text{Ly}\alpha\times21\text{cm}}(z,k) = \langle I_{\text{Ly}\alpha-\text{GAL}}(z)\rangle\langle I_{21\text{cm}-\text{IGM}}(z)\rangle \left[P_{\delta\delta}(k,z) - \frac{1}{1-\langle x_{\text{i}}(z)\rangle}P_{x_{\text{i}}\delta}(k,z)\right]. \tag{1.23}$$

Here, $P_{\text{Ly}\alpha\times21\text{cm}}(z,k)$ is Lyman-$\alpha\times$[H I]$_{21\text{cm}}$ cross-power spectrum and $\langle I_{\text{Ly}\alpha-\text{GAL}}\rangle$ and $\langle I_{21\text{cm}-\text{IGM}}\rangle$ are mean intensities of the Lyman-α and [H I]$_{21\text{cm}}$ line emissions respectively. $\langle x_{\text{i}}(z)\rangle$ is the average ionized fraction of gas present in the IGM, and $P_{\delta\delta}$ and $P_{x_{\text{i}}\delta}$ are the matter overdensity auto-power spectrum and the cross-power spectrum of the ionized field and matter overdensity field respectively. A discontinuity in the crosscorrelation is anticipated at a scale related to the mean size of the ionized bubble, thereby reflecting the overall ionization fraction in the universe. The k-mode where $P_{\text{Ly}\alpha\times21\text{cm}}(z,k)$ transitions from negative to positive is defined by the typical size of the ionized bubbles. At smaller scales, the correlation tends to be positive as fluctuations in both line intensities are expected to follow the underlying density variations. Conversely, at larger scales (small k), the correlation becomes negative because the [H I]$_{21\text{cm}}$ line and the Lyman-α line are indicative of neutral and ionized gas respectively. Similarly, Kannan et al. 2022 and Guochao Sun, Mas-Ribas, et al. 2023 discuss cross-correlation with other line emission from the galaxies such as Hα, CO, [C II]$_{158\mu\text{m}}$, and [O III].

1.6.3 Bispectrum

The bispectrum is the 3-pt correlation function in Fourier which is defined as,

$$\hat{B}_m(\boldsymbol{k_1},\boldsymbol{k_2},\boldsymbol{k_3}) = \frac{1}{N_{\text{tri}}V_{\text{box}}} \sum_{[\boldsymbol{k_1}+\boldsymbol{k_2}+\boldsymbol{k_3}=0]\,\in\, m} \tilde{\Delta}T_{\text{b}}(\boldsymbol{k_1})\tilde{\Delta}T_{\text{b}}(\boldsymbol{k_2})\tilde{\Delta}T_{\text{b}}(\boldsymbol{k_3}), \tag{1.24}$$

where $\tilde{\Delta}T_{\text{b}}(\boldsymbol{k})$ is the Fourier transform of the fluctuations in the signal and $\boldsymbol{k_1}$, $\boldsymbol{k_2}$, and $\boldsymbol{k_3}$ are the wave vectors. In order to estimate the bispectrum, the wavevectors have to form a closed triangle. The triangle can lie in the m-th triangle configuration bin for which the product of the signal fluctuations in the Fourier space for these wavevectors is averaged over the number of triangles (N_{tri}) lying within that configuration bin and the volume V_{box} over which the bispectrum is estimated. To fully characterize the bispectrum, one must identify all possible configurations of the bispectrum. We can describe the bispectrum with $n = k_2/k_1$ and $\cos\theta = -\boldsymbol{k_2}\cdot\boldsymbol{k_1}/(k_2k_1)$, and unique triangle configurations can be identified if we label the triangle arms so that $k_1 \geq k_2 \geq k_3$ and conditions $0.5 \leq n, \cos\theta \leq 1.0$ and $n\cos\theta \geq 0.5$ are met. The detailed characterization of this can be found in the reference Somnath Bharadwaj, Mazumdar, and Sarkar 2020.

The bispectrum can capture the non-Gaussianities in the EoR [H I]$_{21\mathrm{cm}}$ signal, which the power spectrum might not adequately capture. It has been studied in detail in the context of the [H I]$_{21\mathrm{cm}}$ LIM signal. The [H I]$_{21\mathrm{cm}}$ signal from the EoR is dependent on both the neutral fraction field (x_{HI}) and the matter overdensity field (δ_{H}), and these can contribute to the non-Gaussianities in the [H I]$_{21\mathrm{cm}}$ signal. It has been investigated by Majumdar, Jonathan R. Pritchard, et al. 2018; Majumdar, Kamran, et al. 2020 to understand how they evolve and can contribute to the non-Gaussianities in the EoR [H I]$_{21\mathrm{cm}}$ signal. Additionally, the [H I]$_{21\mathrm{cm}}$ bispectrum's sign has been demonstrated to distinguish between the dominance of individual non-Gaussian contributions. LoS anisotropy, such as the redshift space distortion (RSD), can impact the [H I]$_{21\mathrm{cm}}$ bispectrum significantly in both the sign and magnitude, as investigated in (Majumdar, Kamran, et al. 2020; Gill et al. 2024). Also, the morphology of the [H I]$_{21\mathrm{cm}}$ signal can affect the [H I]$_{21\mathrm{cm}}$ bispectrum (amplitude and sign) as independently investigated by Hutter, Catherine A. Watkinson, et al. 2020 and Raste et al. 2024. During Cosmic Dawn (CD), RSD and spin temperature fluctuations also impact the [H I]$_{21\mathrm{cm}}$ bispectrum heavily (Kamran et al. 2021). Another type of LoS anisotropy, which is the light-cone effect (Datta, Mellema, et al. 2012; Zawada et al. 2014; Murmu, Majumdar, and Datta 2021), arising from the finite travel time of radiation from the sources, is also known to impact the bispectrum at the squeezed limit configuration, that will surpass the level of cosmic variance (Rajesh Mondal, Mellema, et al. 2021). Therefore, to interpret the bispectrum in the context of the [H I]$_{21\mathrm{cm}}$ LIM signal, these effects must be incorporated in our forward models of this summary statistic.

Section 1.7 has been adapted from: **Murmu, C. S.**, Ghara, R., Majumdar, S., & Datta, K. K. (2022). Probing the epoch of reionization using synergies of line intensity mapping. *Journal of Astrophysics and Astronomy*, 43(2), DOI: 10.1007/s12036-022-09882-z, arXiv: 2210.09612 (**Review article**)

1.7 Synergies with LIM

The various individual tracers, such as galaxy line emissions and the redshifted [H I]$_{21\mathrm{cm}}$ signal originating from the IGM give us a window to investigate the Universe during the EoR and act as independent probes. However, one can combine these individual probes to help us comprehend cosmic reionization in ways that would not be possible using the individual probes and mitigate systematics from the instruments and foregrounds/interlopers. One of the common synergies between multiple tracers is to cross-correlate them. This is expected to be robust against instrumental systematics and foreground/interlopers and boost the signal-to-noise ratio for the detection of cross-correlation signal. Below, various possibilities of synergies with different probes of the Universe are discussed, and how they can help shed light on multiple features.

1.7.1 LIM cross-power spectra

One can estimate the cross-power spectrum of LIM tracers from galaxies and the [H I]$_{21\text{cm}}$ signal from the IGM, to constrain the relevant EoR parameters. In the following, we discuss some cases using the cross-power spectrum to infer useful information from the EoR and constrain the relevant parameters. Dumitru et al. 2019 discuss the case of the cross-power spectrum of the [C II]$_{158\mu\text{m}}$ and [H I]$_{21\text{cm}}$ LIM signal, to constrain various EoR parameters, including the minimum halo mass contributing to reionization. They considered CII LIM experiments such as **CONCERTO** and **FYST**, with 1000/5000 hours of observational time and demonstrated that parameters like M_{esc}, which is the minimum halo mass capable of producing Lyman continuum photons escaping the galaxies, can be constrained with the cross-power spectrum [C II]$_{158\mu\text{m}}$ and [H I]$_{21\text{cm}}$ LIM signal, better than radio interferometric experiments alone by a factor of 3 and 10, respectively. Similarly, G. Sun, T. C. Chang, et al. 2021 also discuss the possibility of using the next-generation TIME experiment (**TIME-NG**) and the **SPHEREx**, for cross-correlating [C II]$_{158\mu\text{m}}$ -Lyman-α signal from the EoR. In addition, Fronenberg and A. Liu 2024 had discussed the detectability of [C II]$_{158\mu\text{m}}$ $\times$[H I]$_{21\text{cm}}$ 2D cross-power spectra considering synergy between **FYST** and **HERA**. In their analysis, they consider instrumental noise, as well as different foreground and interloper contaminations for both the [C II]$_{158\mu\text{m}}$ and the [H I]$_{21\text{cm}}$ signal. They forecast that in the very optimistic scenario, one might achieve a cumulative SNR of 6.79σ and 6.84σ at $z = 6$ and $z = 7$, respectively.

1.7.2 LIM cross-bispectra

Similar to the cross-power spectrum, one can also estimate the cross-bispectrum between different LIM tracers for inference. One such example has been demonstrated by Beane and Lidz 2018, where they consider the cross-bispectrum of [C II]$_{158\mu\text{m}}$ and [H I]$_{21\text{cm}}$ LIM signals, and can be defined as

$$\langle T_{21\text{cm}}(\boldsymbol{k_1}) I_{\text{CII}}(\boldsymbol{k_2}) I_{\text{CII}}(\boldsymbol{k_3})\rangle = (2\pi^3)\delta_{\text{D}}(\boldsymbol{k_1}+\boldsymbol{k_2}+\boldsymbol{k_3}) \times B_{21\text{cm,CII,CII}}(\boldsymbol{k_1},\boldsymbol{k_2},\boldsymbol{k_3}). \tag{1.25}$$

They also define a reduced cross-bispectra as

$$\hat{Q}_{21\text{cm,CII,CII}}(\boldsymbol{k_1},\boldsymbol{k_2},\boldsymbol{k_3}) = B_{21\text{cm,CII,CII}}(\boldsymbol{k_1},\boldsymbol{k_2},\boldsymbol{k_3})/(P_{21\text{cm,CII}}(k_1)P_{21\text{cm,CII}}(k_2) + 2\text{perm.}) \tag{1.26}$$

and show that one can express the reduced cross-bispectra with an arbitrary field X, as $\hat{Q}^{(0)}_{21\text{cm,X,X}} = Q_{\delta,\delta,\delta}/\langle T_{21\text{cm}}\rangle b_{21\text{cm}} + C_{21\text{cm,X,X}}$, where $C_{21\text{cm,X,X}} = b^{(2)}_{21\text{cm}}/(6\langle T_{21\text{cm}}\rangle b^2_{21\text{cm}}) + b^{(2)}_{\text{X}}/(3\langle T_{21\text{cm}}\rangle b_{21\text{cm}} b_{\text{X}})$. Therefore, both $\hat{Q}^{(0)}_{21\text{cm},\delta,\delta}$ and $\hat{Q}^{(0)}_{21\text{cm,CII,CII}}$ follow $\hat{Q}_{\delta,\delta,\delta}$ within a constant offset, and using the fact that $\hat{Q}^{(0)}_{21\text{cm},\delta,\delta}$ can be used as a proxy for $\hat{Q}^{(0)}_{21\text{cm,CII,CII}}$, they demonstrate the effectiveness of extracting

$\langle T_{21\text{cm}} \rangle b_{21\text{cm}}$. The cross-bispectrum is shown to extract this quantity with 5 and 10 percent uncertainty for $\langle x_{\rm i} \rangle < 0.5$ and $\langle x_{\rm i} \rangle > 0.5$, respectively, except for the lower redshift ($z = 6$) explored in Beane and Lidz 2018. The inference from the cross-bispectrum on the bias parameter is also more consistent with that obtained from the cross-correlation of [H I]$_{21\text{cm}}$ and matter density field ($P_{21\text{cm},}$), than when inferred from [H I]$_{21\text{cm}}$ auto-bispectrum ($Q_{21\text{cm},21\text{cm},21\text{cm}}$). However, detecting the [H I]$_{21\text{cm}}$ -[C II]$_{158\mu\text{m}}$ -[C II]$_{158\mu\text{m}}$ cross-bispectrum might be challenging, even with stage II [H I]$_{21\text{cm}}$ experiments (M. Silva et al. 2015), although the idea can be extended to other combinations of line emissions such as Lyman-α. With **SPHEREx** and **HERA**, an overlapping sky coverage of ~ 1440 deg^2 might be achieved (Beane and Lidz 2018), which can improve the detectability of the cross-bispectrum.

1.7.3 LIM and Galaxy-surveys

G. Sun, T. C. Chang, et al. 2021 explores the possibility of an angular cross-correlation between the [C II]$_{158\mu\text{m}}$ line intensity mapping signal with TIME and Lyman-α emitters (LAEs), and analyzes its performance in terms of constraining relevant parameters and the achieved SNR. They considered the halo catalogs from the Simulated Infrared Dusty Extragalactic Sky (SIDES, Béthermin et al. 2017), to generate mock [C II]$_{158\mu\text{m}}$ and Lyman-α line emissions from the halo catalogs using various semi-analytical models. The angular cross-correlation is considered which is defined as

$$\omega_{\text{CII}\times\text{LAE}}(\theta) \equiv \frac{\sum_i^{N(\theta)} (I^i_{\text{CII}(\theta)} - \bar{I}_{\text{CII}})}{N(\theta)} \approx b_{\text{LAE}} b_{\text{CII}} \bar{I}_{\text{CII}} \omega_{\text{DM}}(\theta), \tag{1.27}$$

with

$$\omega(\theta, z) = \int dz' \mathcal{N}(z') \int dz'' \mathcal{N}(z'')\, \xi(r(\theta, z', z''),\, z). \tag{1.28}$$

Here, $N(\theta)$ is the number of LAE-pixel pairs, and $\Delta I^i_{\text{CII}}(\theta) = I^i_{\text{CII}}(\theta) - \bar{I}_{\text{CII}}$ are the [C II]$_{158\mu\text{m}}$ intensity fluctuations. $\mathcal{N}(z)$ and $\xi(r, \theta)$ are the selection function and the spatial correlation function, respectively. $\mathcal{N}(z)$ is assumed to be a top-hat function within redshifts 5.67 to 5.77 and 6.52 to 6.63, that is consistent with the SILVERRUSH survey in the bandwidth of narrow-band filters. $b_{\text{LAE}} \approx 6$ in the LAE distributions generated from the semi-analytical models, consistent with the upper limits of the same survey at $z = 5.7$ and $z = 6.6$. ω_{DM} is defined using the equation 1.28 with $\xi_{\text{DM}}(r, z) = (1/(2\pi^2)) \int \mathrm{d}k\, k^2 P_{\delta\delta}(k, z)(\sin(kr)/(kr))$. According to the redshifts of the LAEs identified with the SUBARU HSC narrowband filter, the [C II]$_{158\mu\text{m}}$ data from the TIME spectral channels are extracted and cross-correlated with the LAEs simulated within the ~ 2 deg^2 field. The TIME has a limited survey area, and therefore marginal detections of the angular correlation function are possible, which still can provide independent cross-check against [C II]$_{158\mu\text{m}}$ autocorrelation analysis. The forecasts for the inferred value of $b_{\text{CII}} \bar{I}_{\text{CII}}$ is around 2700$\pm$3200 Jy sr^{-1} at redshift 5.7 and 2600$\pm$2900 Jy sr^{-1} at redshift 6.6, taking $b_{\text{LAE}} \sim 6$ and the fitting is restricted to linear scales with $r > 10$ Mpc.

Given that galaxy surveys will also probe the EoR (e.g. LAE surveys), this brings the opportunities to synergize these surveys with [H I]$_{21\text{cm}}$ survey. Hutter, Dayal, et al. 2019 had investigated the prospects of using **WFIRST** (now the Nancy Grace Roman Space Telescope) with the SKA survey to constrain various aspects of cosmic reionization. Since the Lyman-α photons are resonantly scattered in the IGM, detecting the LAEs is difficult when the neutral fraction is high. However, the LAEs are expected to be visible when reionization is approximately at the mid-stage. For a reionization scenario, which is usually "inside out", the sources that emit ionizing photons are expected to be hosted in the dense regions of the Universe. Therefore, LAEs are also associated with these regions and are expected to be anti-correlated with the [H I]$_{21\text{cm}}$ signal when reionization has progressed sufficiently. The [H I]$_{21\text{cm}}$ -LAE cross-correlation might also help constrain the reionization morphology. The regions with LAEs and those that do not have LAEs will have a relative difference in the [H I]$_{21\text{cm}}$ brightness temperature that can be measured with this cross-correlation. Higher temperatures are expected for the regions of IGM that are under-dense, assuming the reionization morphology is "inside-out". This same information about the [H I]$_{21\text{cm}}$ brightness temperature difference can be useful to infer the state of the ionization of the IGM. Similarly, Pagano and A. Liu 2021 also forecast that although the number density of LAEs observed and the angular correlation function may not be able to contrast between the various density ionization models for redshift 6.8, at 68 percent credibility, adding [H I]$_{21\text{cm}}$ data from HERA can help rule out uncorrelated and outside-in reionization models at 99 percent credibility.

Zackrisson et al. 2020 investigates a related concept of synergy. Given that SKA1 is capable of identifying ionized bubbles with volumes of $\gtrsim 1000\,\text{cMpc}^3$ with adequate resolution, the chances of detecting galaxies within these regions for galaxy-dominated reionization processes are high. This can be achieved through deep-field observations with instruments like **JWST**, **WFIRST**, **Extremely Large Telescope (ELT)**, etc. As reionization approaches its final stages, spectroscopic methods may uncover galaxies within the smallest detectable ionized bubbles. For higher redshifts $z = 10$, a photometric survey could be performed. Such studies can help determine quantities like the minimum total stellar mass needed within the galaxies to form ionized bubbles and the photon number-weighted average escape fraction $\langle f_{\text{esc}} \rangle$.

1.7.4 Other synergies

There are additional synergies that can be explored by integrating data from the global [H I]$_{21\text{cm}}$ signal, quasar spectra and the CMB. A. Chatterjee, Tirthankar Roy Choudhury, and Mitra 2021 introduced a tool to estimate parameters based on the Markov Chain Monte Carlo (MCMC) method, the `CosmoReionMC`, which is designed to constrain relevant parameters using these data inputs. `CosmoReionMC` is grounded in a semi-analytical approach based on physically motivated models of reionization (Mitra, T. Roy Choudhury, and Andrea Ferrara 2011) and the global [H I]$_{21\text{cm}}$ signal while using modified CAMB code. The package is adaptable for incorporating other data types (e.g., BAO), constraining additional astrophysical parameters, and handling cosmological models beyond the standard ΛCDM model. Integrating quasar spectra data with CMB-only data is found to result in more precise constraints on cosmological parameters (A. Chatterjee, Tirthankar Roy Choudhury, and Mitra 2021).

1.8 Capturing astrophysical information with LIM

The ultraviolet photons from the nearby stars and white dwarfs, along with the associated photoelectrons, heat, excite, and ionize the hot (10^4 K) interstellar gas clouds, from where the spectral line emissions of our interest, such as [C II]$_{158\mu\text{m}}$ and CO, are emitted. These lines are capable of providing essential insights into the properties of galaxies, related to astrophysical factors, such as temperature, star formation rate, gas density, and metallicity (Osterbrock and Gary J. Ferland 2006; Levesque, Kewley, and Larson 2010; Gutkin, Charlot, and Bruzual 2016; Byler et al. 2017). The origin of these line emissions identifies the efficient halos and galaxies that can produce a particular line and, therefore, whether the resulting line intensity map can effectively trace the matter density field based on the shot noise and bias of the halos and galaxies. Understanding how these nebular line emissions originate and their physical nature can be vital to cosmology and shed light on how the line luminosities in the galaxies are correlated to each other.

For [C II]$_{158\mu\text{m}}$ emission, the correlation of other line emissions with SFR becomes important, which is dependent on the state of the ISM (ionization state and density), which affects the correlation of [C II]$_{158\mu\text{m}}$ line emission. The [O I]$_{63\mu\text{m}}$ line emission originates from the dense and warm PDRs, whereas the [O III]$_{88\mu\text{m}}$ comes from regions of ISM that are highly ionized. The line ratios such as [O I]$_{63\mu\text{m}}$/([C II]$_{158\mu\text{m}}$ + [O I]$_{63\mu\text{m}}$) and [O III]$_{88\mu\text{m}}$/([C II]$_{158\mu\text{m}}$ + [O I]$_{63\mu\text{m}}$) can act as a proxy for the correlation of [C II]$_{158\mu\text{m}}$ line emission with SFR. De Looze, Cormier, et al. 2014 has found a good correlation between the strength of these line ratios and the magnitude of scatter in the L_{CII} - SFR relation. For the former one ([O I]$_{63\mu\text{m}}$/([C II]$_{158\mu\text{m}}$ + [O I]$_{63\mu\text{m}}$)), a correlation of $\rho = 0.74$ was found with the scatter in L_{CII} - SFR relation. For higher values of the ratio, the strength of the [C II]$_{158\mu\text{m}}$ emission deviates more towards weaker values for a given value of the SFR. This ratio indicates the relative fraction of the dense and warm gas, present in the ISM, and that in regions where this value is high, the [C II]$_{158\mu\text{m}}$ emission is not a reliable tracer of the SFR. Kaufman, Wolfire, and Hollenbach 2006 has shown using PDR models that this line ratio's value is higher for regions with higher radiation field strength and gas density.

Similarly, for the [O III]$_{88\mu\text{m}}$/([C II]$_{158\mu\text{m}}$ + [O I]$_{63\mu\text{m}}$) line ratio, there is correlation of $\rho = 0.87$ with the magnitude of L_{CII} - SFR scatter, as found by De Looze, Cormier, et al. 2014. This line ratio captures the relative fraction of highly ionized gas within the ISM, as [O III]$_{88\mu\text{m}}$ emission originates from these regions near the young O stars. The interpretation of this line ratio is based on the assumption that [C II]$_{158\mu\text{m}}$ emission traces the PDRs. For these regions, [C II]$_{158\mu\text{m}}$ emission is therefore not a good indicator for star formation. The hard ionization radiation is capable of ionizing O^+ but can doubly ionize carbon, thereby leading to most of the carbon being present in the form of double-ionized carbon.

Therefore, [O III]$_{88\mu\mathrm{m}}$ line emission can affect the correlation of [C II]$_{158\mu\mathrm{m}}$ line emission with SFR where highly ionized gas occupies a significant fraction within the ISM. Therefore, these astrophysical phenomena will play an important role in determining the strength of the line emissions, which will be targeted by the LIM experiments, and one needs to forward model these line emissions to accurately predict the observable summary statistics.

1.9 Outline of thesis

LIM offers the potential to probe large-scale structures of the Universe and extend our understanding of the EoR, which is a poorly known period of cosmic history. The early observations of this cosmic period include the Thomson-scattering optical depth measurements from the CMB observations, constraining the mid-point of reionization (Planck Collaboration, Aghanim, Akrami, Arroja, et al. 2020). High redshift quasar absorption spectra somewhat constrain the end of the EoR (G. D. Becker, Bolton, Zhu, et al. 2024). However, these measurements do not suffice to pinpoint the history of cosmic reionization. These observations also add very little, to the understanding of the nature of the reionizing sources. On the other hand, galaxy surveys with the **ALMA** and **JWST** can help to understand the nature of these early galaxies for a limited number of surveys. Therefore, the ongoing and upcoming LIM observations are expected to complement this by accumulating the aggregate flux from these high redshift sources, including the contribution of the very faint sources, which is otherwise not detected in galaxy surveys. It would give us a more comprehensive picture of the Universe, which is otherwise difficult to obtain with the galaxy surveys alone.

The line emissions from the galaxies and the IGM, which will be targeted by the LIM observations, are determined by various astrophysical phenomena. Therefore, the corresponding LIM signals will capture this information and the observable summary statistics will be sensitive to the underlying astrophysics of these line emissions. In the fiducial models of galaxy line emissions, one assumes a one-to-one scaling relation between the host halo mass of the galaxy and the corresponding line luminosity of the galaxy. The usual approach to follow is to assume a model that predicts the star-formation rate in the galaxies given a particular mass of the host halo. Using this model, one can predict the line luminosity for spectral line emissions assuming the line-emission is correlated with the star-formation rate, and there is a relation between these two. These models are easy to implement in simulations, and generating mock LIM maps is generally computationally cheap. However, astrophysical conditions such as multi-phase state of the ISM in the galaxies will introduce a significant line luminosity scatter in the [C II]$_{158\mu\mathrm{m}}$ line emission from these galaxies. This had been reported observationally by De Looze, Cormier, et al. 2014. Similarly, hydrodynamic simulations such as `SIMBA` (Leung et al. 2020), in combination with `SIGAME` (Olsen, Thomas R. Greve, Narayanan, R. Thompson, Toft, et al. 2015; Olsen, Thomas R. Greve, Brinch, et al. 2016; Olsen, Thomas R. Greve, Narayanan, R. Thompson, Davé, et al. 2017) that tracks the giant molecular cloud phase in the gas fluid elements and introduces sub-grid recipes for post-processing, predict significant scatter in the $L_{\rm CII}$ - $M_{\rm halo}$ relation (see figure 4.1) which has a halo-mass dependence. Some models assume a halo-mass-independent line luminosity scatter in the $L_{\rm CII}$ - $M_{\rm halo}$ relation, where $M_{\rm halo}$ is the mass of the host halo. Different approaches can be undertaken to interpret the power spectrum in the presence of scatter in line luminosity, which has been discussed in section 1.6.1. However, until now, it was not known how valid these interpretations are when one considers a more realistic halo-mass-dependent scatter in the $L_{\rm CII}$ - $M_{\rm halo}$ relation and how this would affect the observable [C II]$_{158\mu m}$ power spectrum.

Also, astrophysical factors that determine SFR in the galaxies, such as varying mass-accretion histories, which happen over longer time scales, and shorter time scale variabilities, such as short time-scale variabilities in the gas accretion rate, and different feedback mechanisms important for lower mass galaxies, can introduce scatter in the SFR. Observationally, the main-sequence stars are known to have scatter in their SFR (Speagle et al. 2014), and this is also predicted by simulations (Dutton, van den Bosch, and Dekel 2010; Peng and Maiolino 2014; Lagos et al. 2018; Matthee and Schaye 2019; Blank et al. 2021). Therefore, it will also introduce a scatter in the number of ionizing photons emitted from the galaxies, which is proportional to the SFR of the galaxies, consequently leaving imprints in the IGM during the EoR. However, in fiducial models of reionization, SFR is assumed to have a one-to-one correlation with the host halo mass, and the astrophysical scatter in the SFR $-$ $M_{\rm halo}$ dispersion relation is usually not taken into account. A previous study by Hassan et al. 2022 has shown that the ionization power spectra are not sensitive to these signatures of astrophysical scatter in the IGM. But the ionization field is not directly observable, unlike the [H I]$_{21\rm cm}$ signal, which is also known to be non-Gaussian. Therefore, a more suitable summary statistic to probe the signatures of astrophysical scatter in the IGM would be higher-order statistics such as the bispectrum, which was not well explored in this context.

On the other hand, probing the CO LIM signal can help us understand the correlation between the far-infrared luminosity and the CO line luminosity inside the galaxies, which serves as a proxy for the correlation between star formation and gas depletion. In the post-EoR, galaxy surveys have characterized this correlation (Carilli and F. Walter 2013; T. R. Greve, Leonidaki, et al. 2014; Sargent et al. 2014; Kamenetzky et al. 2016); however, this is difficult to achieve in the EoR regime, due to limited surveys, and therefore it is not well explored. The LIM surveys will also face challenges in probing the EoR due to instrumental noise, which will contaminate the signal. Therefore, one way of tackling this would be to cross-correlate the CO LIM signal with another survey from the same redshift, such as the [H I]$_{21\rm cm}$ LIM survey. A pilot survey with **AARTFAAC** (P. Prasad et al. 2016) has been assumed here, which will survey the [H I]$_{21\rm cm}$ signal from the EoR and is expected to have a large field-of-view. The prospects for detecting the CO signal from the EoR using cross-correlations of observation with **COMAP** (Breysse, Dongwoo T. Chung, et al. 2022) with this pilot survey have been discussed here for a wide range of models of CO emission determined by the correlation between far-infrared luminosity and the CO luminosity in galaxies. Whether the cross-power spectrum of these

LIM signals can contrast the various far-infrared luminosity and the CO line luminosity correlation models of the galaxies, which determine the CO emission, was not well explored in the EoR.

In this thesis, these broad ranges of astrophysical phenomena have been addressed using various observable summary statistics of the LIM signals that demonstrate how the observable summary statistics of the various LIM signals can capture astrophysical information from the EoR. However, LIM observations can be biased due to line-of-sight (LoS) anisotropies, inherent in observations. Since a finite amount of time is taken by electromagnetic radiation to travel, signals from faraway regions of the Universe will take more time to reach the observer, as compared to regions that are nearby. Therefore, along the line of sight, a continuous time evolution of the signal is present, which introduces anisotropies in a particular direction and apparently violates the principle of statistical isotropy. This light-cone effect will impact the observed signal, introducing bias in the estimated summary statistics. Previously, the impact of the light-cone effect on the spherically averaged $[\mathrm{H\,I}]_{21\mathrm{cm}}$ power spectrum had been quantified in Datta, Mellema, et al. 2012. However, in the context of galaxy LIM surveys with line emission, such as $[\mathrm{C\,II}]_{158\mu\mathrm{m}}$ (one of the primary candidates for conducting LIM experiments), this had not been adequately addressed for summary statistics such as the spherically averaged power spectra. Interestingly, since there are various synergy opportunities to cross-correlate different LIM tracers such as the $[\mathrm{C\,II}]_{158\mu\mathrm{m}}$ emission from galaxies and the $[\mathrm{H\,I}]_{21\mathrm{cm}}$ emission from the IGM, quantifying the impact of the light cone effect on the cross-power spectrum is important, which also had not been investigated previously and had been addressed in this thesis.

Chapter 2

Simulating line-intensity maps

Numerical simulations are useful for generating mock line-intensity maps and building forward models for summary statistics. In this thesis, numerical simulations have been used to simulate line-intensity maps. In one of the approaches, the simulations were done from scratch, where N-body simulations (S. Bharadwaj and Srikant 2004) were run, and their output was post-processed with a Friends-of-Friends (FoF) algorithm (Rajesh Mondal, Somnath Bharadwaj, Majumdar, et al. 2015) to obtain the mock halo catalogs from dark-matter density fields. These were then post-processed with semi-numerical simulations of reionization (Tirthankar Roy Choudhury, Haehnelt, and Regan 2009; Majumdar, Mellema, et al. 2014; Rajesh Mondal, Somnath Bharadwaj, and Majumdar 2017) to generate mock $[\mathrm{H\ I}]_{21\mathrm{cm}}$ maps and also with models of galaxy line-intensity maps to generate $[\mathrm{C\ II}]_{158\mu\mathrm{m}}$ and CO LIM maps. In Chapter 3 and Chapter 5, the simulation approach used consists of N-body simulations done from scratch, coupled with the FoF algorithm and further post-processing as described above. This is discussed in section 2.1, section 2.2 and section 2.3. However, in the other approach, pre-simulated data were used to generate mock line-intensity maps. In Chapter 4, pre-simulated $[\mathrm{C\ II}]_{158\mu\mathrm{m}}$ line-luminosities were used that were obtained from SIMBA hydrodynamic simulation coupled with post-processing from SIGAME (Leung et al. 2020). The $[\mathrm{C\ II}]_{158\mu\mathrm{m}}$ line-luminosities were remapped in a large-scale N-body simulation. This approach is discussed in section 2.3. Chapter 6 used the pre-simulated data of dark-matter density fields, halo catalogs from the CUBEP3M N-body simulation (Harnois-Déraps et al. 2013), and radiative transfer simulation outputs from C^2-RAY (Mellema, Ilian T. Iliev, Alvarez, et al. 2006) for $[\mathrm{H\ I}]_{21\mathrm{cm}}$ signal. Post-processing has been applied to the halo catalogs to obtain the CO signal for cross-correlation with the $[\mathrm{H\ I}]_{21\mathrm{cm}}$ signal. This is discussed in section 6.2.1.

2.1 N-body simulations

The mock line intensity maps generated are based on N-body simulations, that generate a mock dark matter density distribution within a specified volume. It is done by assuming a set of grids, later filled with particles representing dark matter (dark matter particles). The mass of the dark matter particles is set such that it reproduces the critical density of the Universe, $\rho_{\rm c}$, which is given as $\rho_{\rm c} = 3H_0^2/(8\pi G)$, where H_0 represent the Hubble parameter and G represent the gravitational constant. For a fixed comoving volume of the simulations, the size of the grid will then determine how small the mass of the dark matter particles can be or how high the mass resolution of these particles can be. Given that the grid size is L in comoving units, and the side length is N in grid units, the mass of each dark matter particle is $M_{\rm DM} = \rho_{\rm c}\Omega_{\rm m} \times N^3L^3/N_{\rm part}$, with Ω_m being the cosmological density parameter for matter and $N_{\rm part}$ is the total number of dark matter particles in the simulation. A finer mass resolution is desirable if we want to resolve dark matter halos of smaller masses later from the snapshots of the simulations. Typically, we resolve a dark matter particle mass of $\approx 10^8 M_\odot$.

We have used a particle-mesh (PM) N-body simulation (S. Bharadwaj and Srikant 2004), where the grids are populated with dark matter particles, and the gravitational potential is solved for this density grid. The density perturbations are generated with Gaussian random phases based on the power spectrum for these perturbations initialized with the transfer function from Eisenstein and Wayne Hu 1998 and normalized from the present value of σ_8. The initial positions and velocities (initial conditions) are obtained using the Zeldovich approximation (Zel'dovich 1970). The grid-based density is then evolved into the non-linear regime by solving the Poisson equation for the gravitational potentials at the grids and updating the positions and velocities of the dark matter particles. At a predetermined sequence of redshifts, the snapshot of the distribution of the dark matter particles and their velocities is dumped in a file.

The dark matter particle distribution in the simulation snapshot is used to identify the collapsed structures. These dark matter halos are assumed to host the galaxies that emit radiation, including various line emissions. For this, a Friends-of-Friends algorithm is employed (Rajesh Mondal, Somnath Bharadwaj, Majumdar, et al. 2015), which identifies clusters of dark matter particles based on a certain linking length. The center-of-mass positions and velocities of these halos are then written in a catalog, and this information is subsequently used to simulate the line intensity maps for various line emission tracers. Identifying the halos uses information on the position of the particles only and does not include any velocity information of the dark matter particles. Later on, we also use only the position of the halos and not their velocities since we have not taken the redshift-space distortion (Kaiser 1987) into account.

2.2 Semi-numerical simulations of reionization

To simulate the ionization of the IGM using detailed physical models, one needs to solve the cosmological radiative transfer equation for the ionizing radiation traversing through the IGM. It generally takes considerable computational resources to do this, especially if the side length of the simulated volume is a few hundred Mpc. In our case, we follow a semi-numerical approach towards simulating the reionization of the IGM and, consequently, the [H I]$_{\rm 21cm}$ signal that originates from this. The basic idea that is implemented is that within a specific region of radius R, the approach evaluates whether the average number of hydrogen atoms is greater than the average number of ionizing photons in some simulation units. We use the code `ReionYuga`[1] (Tirthankar Roy Choudhury, Haehnelt, and Regan 2009; Majumdar, Mellema, et al. 2014; Rajesh Mondal, Somnath Bharadwaj, and Majumdar 2017) which follows this excursion set formalism (Furlanetto, Zaldarriaga, and Hernquist 2004), to simulate cosmic reionization of the IGM. The density of baryons is not explicitly modeled since the simulation snapshots that we use consist of purely dark matter particles, given that we use dark matter-only simulation and not a hydrodynamical simulation. It is assumed that the gas overdensity perfectly follows the dark matter overdensity. We assume that every collapsed dark matter halo hosts a galaxy that contributes to cosmic reionization to implement the luminous sources. The number of Lyman continuum photons deposited in the IGM, N_γ, at a particular simulation snapshot, is modeled from the corresponding mass of the dark matter halo. In the most simplistic scenario, $N_\gamma \propto M_{\rm h}$, where $M_{\rm h}$ is the dark matter halo mass. However, one can also make use of more sophisticated models, where N_γ is dependent on $M_{\rm h}$ via some power law, or model the dependence via a star-formation rate, which can then depend on $M_{\rm h}$.

The ionization condition for the IGM is fulfilled if $\langle n_\gamma \rangle_R \geq \langle n_{\rm H} \rangle_R$ for a smoothed region of radius R, where $\langle n_{\rm H} \rangle_R$ and $\langle n_\gamma \rangle_R$ are the average number of hydrogen atoms and ionizing photons and within a spherical region of radius R. For smoothing, a spherical top-hat filter is assumed and it is repeated for a range of radii, $R_{\rm min}$ to $R_{\rm max}$, which is traversed in small steps of ΔR. Along with the smoothed fields for $n_\gamma(\boldsymbol{x})$ and $n_{\rm H}(\boldsymbol{x})$, the original un-smoothed fields are also stored in memory as well. If the ionization condition is not satisfied $\big(\langle n_\gamma \rangle_R < \langle n_{\rm H} \rangle_R\big)$ for the smoothed region over radius R, then a partial ionized fraction, $x_{\rm HII} = n_\gamma / n_{\rm H}$, is assigned to the voxel, using information from the original un-smoothed fields. It is implicitly assumed that every ionizing photon present can interact with the hydrogen atoms it encounters. However, recombination can also happen depending on the density of neutral hydrogen, giving off photons. The recombination is not modeled here explicitly, but it can be crucial. In general, the inhomogeneous spatial distribution of recombinations can affect the morphology of reionization, such that it favors the 'outside-in' scenario, where low-density regions ionize first compared to high-density regions without ionizing sources as suggested by Tirthankar Roy Choudhury, Haehnelt, and Regan 2009. This will affect the shape and amplitude of the [H I]$_{\rm 21cm}$ power spectra. Further, Mao, Koda, et al. 2020 has shown that inhomogeneous subgrid clumping, which can boost recombinations, plays a role in the slower expansion of H II regions, and delays reionization history. The large-scale [H I]$_{\rm 21cm}$ power spectra are also suppressed due to inhomogeneous subgrid clumping. The semi-numerical approach also suffers from the problem of photon non-conservation (Paranjape, T. Roy Choudhury, and Padmanabhan 2016). When ionized bubbles overlap, the overlap region is supposed to have more ionizing photons than the neutral hydrogen atoms, which are usually not treated properly. In some simulation tools such as `SCRIPT` (Tirthankar Roy Choudhury and Paranjape 2018), this scenario is handled by redistributing these excess photons to the boundaries of the H II regions. However, in our

[1] https://github.com/rajeshmondal18/ReionYuga

simulation, we do not implement photon conservation. Once the ionization field is obtained, converting it into a differential brightness temperature field using equation 1.12 is straightforward.

2.3 Simulations of galaxy line-intensity maps

The line-intensity maps for the line emissions from galaxies are simulated based on empirical relations that relate some dark-matter halo property and the corresponding line luminosity of the galaxy hosted by that halo. Usually, the host dark-matter halo mass is chosen as a part of these empirical models. As a first step, the SFR of these galaxies is modeled as a function of the host halo mass. Ideally, if the halos' merger histories are available, one can model the star-formation rate of galaxies hosted by the halos using this. However, in these simulations, merger histories are not tracked. It is also assumed that every dark-matter halo hosts a galaxy that can emit various line emissions. However, more accurately, this will follow a halo occupation distribution (Berlind and Weinberg 2002), which tells the number distribution of galaxies hosted by a dark matter halo of mass M_h.

In this empirical approach, the SFR of the galaxies is modeled after M. B. Silva et al. 2013, based on the De Lucia and Blaizot 2007 and Guo et al. 2011 simulated galaxy catalogs. It is given as

$$\begin{aligned}\frac{\mathrm{SFR}\,(M_\mathrm{h},z)}{M_\odot\,\mathrm{yr}^{-1}} &= 2.25\times10^{-26}(1+7.5\times10^{-2}\times(z-7))\\ &\times M_\mathrm{h}^a\left(1+\frac{M_\mathrm{h}}{c_1}\right)^b\left(1+\frac{M_\mathrm{h}}{c_2}\right)^d\left(1+\frac{M_\mathrm{h}}{c_3}\right)^e,\end{aligned} \tag{2.1}$$

with $c_3 = 1\times10^{11}M_\odot$, $c_2 = 7\times10^{9}M_\odot$, $c_1 = 8\times10^{8}M_\odot$, $e = -2.25$, $d = 0.4$, $b = -0.62$ and $a = 2.59$. This model's advantage is that it only depends on the halo mass and redshift, which can be easily provided from the catalogs generated in our halo-finding algorithm. The next step in this approach is empirically relating the SFR to the $[\mathrm{C\,II}]_{158\mu\mathrm{m}}$ line luminosity. It is motivated by the strong correlation between the emission of $[\mathrm{C\,II}]_{158\mu\mathrm{m}}$ line and the SFR observed in the galaxy samples present in the local Universe. We follow the relations from M. Silva et al. 2015, which is of the form given in equation 1.9. In our work, we have followed the model ***m1*** from M. Silva et al. 2015, which corresponds to $a = 0.8475$ and $b = 7.2203$. This produces the brightest $[\mathrm{C\,II}]_{158\mu\mathrm{m}}$ signal and corresponds to the most optimistic model compared to the other three models in M. Silva et al. 2015.

In the other approach of simulating the LIM signal of $[\mathrm{C\,II}]_{158\mu\mathrm{m}}$ emission, we use pre-simulated luminosity data of $[\mathrm{C\,II}]_{158\mu\mathrm{m}}$ emission, based on the work of Leung et al. 2020. It is based on the hydrodynamical simulation run using `SIMBA` (Davé, Anglés-Alcázar, et al. 2019; Leung et al. 2020), later post-processed by `SIGAME` (Olsen, Thomas R. Greve, Narayanan, R. Thompson, Toft, et al. 2015; Olsen, Thomas R. Greve, Brinch, et al. 2016; Olsen, Thomas R. Greve, Narayanan, R. Thompson, Davé, et al. 2017; Leung et al. 2020) to generate $[\mathrm{C\,II}]_{158\mu\mathrm{m}}$ line luminosity. The `SIMBA` simulation considers state-of-the-art feedback modules that produce results with good agreement with low-redshift observables. The SIMBA simulation incorporates advanced feedback mechanisms that yield results closely aligning with low-redshift observations. Leung et al. 2020 considered three different simulation volumes—25, 50, and 100 h^{-1} Mpc, with initial gas mass resolutions of 2.9×10^9, 2.3×10^6 and 1.8×10^7 $M_\odot$, respectively. These volumes were collectively analyzed to achieve a broad dynamic range in the resolved galaxy masses. The small simulated cosmological volumes such as 25 and 50 h^{-1} Mpc might be sufficient to probe small scales, however, these volumes individually might not be large enough to probe the large-scale features of the Universe with line-intensity mapping. However, information from these small volumes can be combined with that from a cosmological simulation of a much larger volume, to achieve an overall better dynamic range of the astrophysics. This is what has been done in Leung et al. 2020, where the line-luminosities of [C II]$_{158\mu\text{m}}$ emitters have been combined from all these volumes to obtain a much more extensive range of host halo masses. This information has been remapped in a large-scale N-body simulation in the work discussed in Chapter 4. SIMBA simulates the supermassive black holes with feedback and growth within galaxies, modeling growth through Bondi accretion of hot gas and torque-limited cold gas accretion (Anglés-Alcázar, Davé, et al. 2017). The feedback processes are represented by X-ray energy injection and bipolar kinetic outflows. The simulation also includes a sub-grid model that simulates dust formation and destruction within the interstellar medium (ISM) by considering channels such as metal condensation, asymptotic giant branch stars, and Type II supernovae. while it is primarily destroyed by consumption by star formation and sputtering (including supernova shocks) (Q. Li, Narayanan, and Davé 2019). SIMBA utilizes models of ejective feedback from star formation similar to MUFASA but with revised scaling based on results of particle tracking from the Feedback in Realistic Environments (FIRE) simulations (Anglés-Alcázar, Faucher-Giguère, et al. 2017), along with slight modifications to improve the modeling of galaxy properties during the EoR (Wu et al. 2020). SIMBA has been extensively compared with a variety of observational data across cosmic time and has shown good agreement, particularly in terms of the mass-metallicity relation and galaxy stellar mass function (GSMF) (Davé, Anglés-Alcázar, et al. 2019), black hole characteristics (Thomas et al. 2019), dust properties (Q. Li, Narayanan, and Davé 2019), galaxy sizes and profiles (Appleby et al. 2020), and the cold gas content, including CO(1-0) luminosity functions from $z = 0 - 2$ (Davé, Crain, et al. 2020). However, there are minor discrepancies, such as an overestimation of the most massive galaxies up to redshift of 2, overly large sizes for quenched galaxies of low mass at redshift up to 1, and an underestimation of the mass function of dust at redshift of $\sim$ 2. Wu et al. 2020 examined SIMBA galaxies' properties during the EoR and assuming a Calzetti 2001 dust model they found strong agreement with the galaxy sizes down to the faintest limits, UV slope measurements, and UV luminosity function, at $z = 6$. Therefore, to explore the properties of the far-infrared line emission in the EoR galaxies, SIMBA offers a reliable framework. To be resolved in the simulations, only galaxies with at least 64 stellar and gas particles are included in Leung et al. 2020. For the 25 h^{-1} Mpc, 50 h^{-1} Mpc and 100 h^{-1} Mpc simulation boxes, the required masses correspond to $M_{\star,\text{min}} = 10^{7.24} M_\odot$, $M_{\star,\text{min}} = 10^{8.15} M_\odot$ and $M_{\star,\text{min}} = 10^{9.05} M_\odot$ respectively.

At a redshift of 6, the number of galaxy samples is around ~ 11137. This is achieved by sampling the cloud mass of giant molecular clouds (GMC) from a mass function using a sub-grid recipe and forming GMCs with a minimum mass of $10^4 M_\odot$. For this, it is ensured that galaxies which have at least $M_{\rm mol} = f_{\rm H2} M_{\rm gas} > 10^5 M_\odot$ gas mass is selected in the simulation.

As described in Leung et al. 2020 `SIGAME` post-processes the `SIMBA` outputs using sub-grid recipes to make predictions for the luminosities of the various line emissions. The gas fluid elements are divided into giant molecular gas (GMC) and diffuse gas phase using sampling of the GMC mass from a galactic GMC mass function over the mass range $10^4 - 10^6\, M_\odot$. The GMC mass is subtracted from the parent fluid element, and the remaining mass is assigned to the gas in the diffuse phase. It is subsequently partitioned into neutral and ionized phases. The neutral phase corresponds to the region where $x_{\rm HI} > 0.5$. `SIGAME` accounts for line emissions by tracking three ISM phases, which are distinct. The photoionization code `CLOUDY` version 17.1 (G. J. Ferland, Chatzikos, et al. 2017) is employed to simulate the thermochemistry in the different ISM phases. The detailed processes considered are cosmic-ray (CR) ionization, dust physics (grain-atom/ion charge transfer), and H_2 photo processes. The luminosities corresponding to various line transitions are obtained by calculating their cooling rates. The abundances of the different metals (e.g., Fe, Ca, S, Si, Mg, Ne, O, N, C, He), can be based on the metallicity value provided as input to `CLOUDY` and then scaled according to solar abundance. However, the abundance of the metals tracked in SIMBA is used, to get the abundance pattern in galaxies differing from the solar abundance.

The galaxy catalog derived from `SIMBA+SIGAME` includes numerous galaxy properties, such as the host dark matter halo mass and the [C II]$_{158\mu{\rm m}}$ line luminosity, despite being limited to approximately 11,000 samples. To acquire a sufficient number of samples, we statistically remapped the [C II]$_{158\mu{\rm m}}$ luminosity onto an N-body simulation run at larger scales, based on the respective halo masses. There is sufficient similarity in the halo-mass ranges in both simulations, that facilitated the reproduction of [C II]$_{158\mu{\rm m}}$ luminosities. From the original pre-simulated data, the [C II]$_{158\mu{\rm m}}$ luminosity distribution is estimated within the bins out of the 20 logarithmic bins, in which the halo-mass range is divided. Subsequently, we generate [C II]$_{158\mu{\rm m}}$ luminosity values that follow the same distribution within each halo-mass bin. A *piecewise constant distribution* has been used to remap the [C II]$_{158\mu{\rm m}}$ line luminosity scatter, that resembles the original distribution from `SIMBA`. Using the information about the histogram of the log $L_{\rm [CII]}$ histogram, such as, for each halo mass bin, the probability densities and boundaries of the bin intervals, a random log $L_{\rm [CII]}$ value is generated that follows a probability density function given as

$$P(\log L_{\rm [CII]} | l_0, ..., l_n, w_0, ..., w_{n-1}) = \frac{w_i}{\sum_{k=0}^{n-1} w_k (l_{k+1} - l_k)}\,. \tag{2.2}$$

In this context, the number of boundaries defining the intervals is $n+1$. Here, l_i represents these boundaries for $0 \le i \le n$, and w_i denotes the corresponding weights or probability densities for $0 \le i < n$. For any given $L_{\rm [CII]}$, the condition $l_i \le \log L_{\rm [CII]} < l_{i+1}$ holds true for $0 \le i < n$.

Consequently, uniform values of $\log L_{[\mathrm{CII}]}$ are produced within a specific bin, with an associated weight, that ensures accurate replication of the overall distribution. The C++ standard library provides an implementation of this procedure which has been used here.

In the case of simulating CO emission from the galaxies, we follow an empirical approach, similar to the empirical approach adopted to simulate the [C II]$_{158\mu\mathrm{m}}$ LIM signal. First, a one-to-one relation between SFR and the host halo mass is assumed, which predicts the SFR for a given halo mass. The SFR is then used to predict the far-infrared luminosity within the galaxy, assuming a proportionality relation. Further, the far-infrared luminosity is used to predict the CO line luminosity in the galaxy. The relations used for simulating the CO emission in galaxies has been further described in subsection 6.2.1.

Chapter 3

C II and HI 21cm line intensity mapping from the EoR: Impact of the light-cone effect on auto and cross-power spectra

This chapter has been adapted from: **Murmu, C. S.**, Majumdar, S., & Datta, K. K. (2021). CII and HI 21-cm line intensity mapping from the EoR: impact of the light-cone effect on auto and cross-power spectra. *Monthly Notices of the Royal Astronomical Society*, 507(2), 2500–2509, DOI: 10.1093/mnras/stab2347, arXiv: 2107.09072

3.1 Introdcution

Understanding the mysterious Epoch of Reionization (EoR) is at the forefront of modern cosmology research. The first light sources appeared in the universe during the EoR and subsequently reionized the neutral intergalactic medium (IGM) with ionizing radiation. The current constraints on the EoR come from, among others, the Gunn-Peterson trough in the very distant quasar spectra (R. H. Becker et al. 2001; G. D. Becker, Bolton, Madau, et al. 2015), the constraint on the Thomson optical depth ($\tau = 0.054 \pm 0.007$) for the instantaneous reionization model (Planck Collaboration, Aghanim, N., et al. 2020) and the claimed detection of the global-averaged [H I]$_{21\text{cm}}$ signal from Cosmic Dawn by EDGES (J. D. Bowman, Rogers, et al. 2018), which is still debated (Bevins et al. 2022). Thus, the pressing question about the EoR, how did the reionization process take place, still remains largely unknown. Critical questions like: How did the reionization history proceed?; what are the properties of the sources responsible for reionization?; can we shed light on the history of structure formation by probing the EoR?; also remain unanswered. We need direct observations that can probe the evolving state of the early IGM and the early reionizing sources during the EoR.

State-of-the-art radio interferometers like LOFAR (F. G. Mertens, Mevius, et al. 2020), MWA (Barry, Wilensky, et al. 2019; Patwa, S. Sethi, and Dwarakanath 2021), PAPER (Kolopanis et al. 2019), HERA (DeBoer et al. 2017), GMRT (Choudhuri, Abhik Ghosh, et al. 2020; Pal et al. 2021) etc. are trying to detect the spatial fluctuations in the [H I]$_{21\mathrm{cm}}$ signal originating from the neutral hydrogen of the early IGM during the EoR. These facilities are also acting as the technology and science precursors or path-finders for the upcoming Square Kilometre Array (SKA)[1], the largest radio telescope to be ever built by humankind. The SKA's contribution via the production of the first high-resolution tomographic images of the [H I]$_{21\mathrm{cm}}$ signal from the EoR will be a significant milestone in this paradigm (L. Koopmans et al. 2015; Mellema, Leon Koopmans, et al. 2015). Although many of the existing radio interferometric experiments have advanced significantly, removing $5-6$ orders of magnitude larger foreground contamination from [H I]$_{21\mathrm{cm}}$ observations remains the major challenge (e.g. Di Matteo et al. 2002; Ali, Somnath Bharadwaj, and Chengalur 2008; Jelić et al. 2008; Abhik Ghosh, J. Prasad, et al. 2012; Procopio et al. 2017) in detecting this signal from the EoR. Thus, ongoing experiments have been able to produce only weak upper limits to the signal power spectrum at a few redshifts (Paciga, Albert, et al. 2013; F. G. Mertens, Mevius, et al. 2020; Barry, Wilensky, et al. 2019; W. Li et al. 2019; Kolopanis et al. 2019; Cathryn M. Trott et al. 2020; Pal et al. 2021). Once the [H I]$_{21\mathrm{cm}}$ power spectrum across different redshifts is detected, one might be able to constrain the IGM physics and reionization history, and, most likely, one can also put some indirect constraints on the reionization source properties. However, the [H I]$_{21\mathrm{cm}}$ observations alone are not enough to get a complete picture of the EoR.

To have a comprehensive understanding of the EoR, one would need to probe the sources of the reionizing photons, i.e., the early galaxies and quasars, etc., along with the state of the IGM. However, the spectroscopic detection of individual galaxies from the EoR is challenging. An ideal choice for doing cosmological large-volume surveys of early sources of the EoR is to use the line intensity mapping technique (Visbal and Loeb 2010; Gong, X. Chen, et al. 2011; Gong, Cooray, M. Silva, et al. 2012; M. B. Silva et al. 2013; M. Silva et al. 2015). In the LIM technique, one does not need to resolve the individual light sources but instead needs to detect the integrated flux from several sources that lie within a pixel or voxel of the 3D volume that is being surveyed by the telescope. It targets a specific atomic or molecular line transition from galaxies and uses it as a tracer to detect them (Fonseca et al. 2016) via this method. The ideal line emission choices are the ones that are bright and can provide valuable information regarding various properties of those galaxies.

The [C II]$_{158\mu\mathrm{m}}$ line is expected to be one of the brightest line emissions from the early galaxies and this line emission also correlates well with the star-formation rate within a galaxy (De Looze, Baes, et al. 2011). The recent spectroscopic surveys have detected galaxies at high redshifts using this line emission. The ALPINE-ALMA [C II]$_{158\mu\mathrm{m}}$ survey has detected star-forming galaxies at $4 < z < 6$ and

[1] https://astronomers.skatelescope.org

was also able to classify them (A2C2S, Le Fèvre et al. 2020). The ALMA Spectroscopic Survey in the Hubble Ultra Deep Field (ASPECS) also searched for potential[C II]$_{158\mu m}$ emitters at $6 < z < 8$. They were able to place upper limits on the [C II]$_{158\mu m}$ luminosity and the cumulative number density of [C II]$_{158\mu m}$ emitters (Uzgil et al. 2021) in that redshift range. These high-redshift detections have further strengthened confidence in the upcoming missions like e.g. CONCERTO (Guilaine Lagache 2017; CONCERTO Collaboration et al. 2020), the CCAT-p (Cothard et al. 2020), and TIME (Crites et al. 2014; G. Sun, T. C. Chang, et al. 2021), which will be conducting [C II]$_{158\mu m}$ LIM and probe the spatial fluctuations in [C II]$_{158\mu m}$ emission from early galaxies at different redshifts.

By measuring the fluctuations in the [C II]$_{158\mu m}$ line intensity maps from the early galaxies one would expect to obtain valuable physical insights about the properties of these sources and their role in reionization. By far, the most common statistic that has been considered for measuring these signal fluctuations is the power spectrum. The power spectrum measures the amplitude of fluctuations in any signal at different length scales. Combining this information, one can constrain the role of early galaxies in reionization. In principle, the [C II]$_{158\mu m}$ power spectrum can tell us about the [C II]$_{158\mu m}$ luminosity function (Yue and Ferrara 2019) and its redshift evolution. Additionally, it can also help us to quantify the clustering properties of the ionizing galaxies. Several recent studies have forecasted that the [C II]$_{158\mu m}$ power spectrum should be detectable with experiments like CONCERTO up to $z = 8$; stage-II experiments similar to CCAT-p can push towards higher redshifts with greater signal-to-noise ratio (SNR) (Dumitru et al. 2019).

On the other hand, the cross-power spectrum of the [C II]$_{158\mu m}$ and [H I]$_{21cm}$ signals from the same redshifts is another statistic of particular interest (Tzu-Ching Chang et al. 2015). Reliable detection of the auto power spectrum of the [H I]$_{21cm}$ or [C II]$_{158\mu m}$ signals depends on the successful removal of the foreground emissions. However, in the cross-power spectrum of the [C II]$_{158\mu m}$ and [H I]$_{21cm}$ signals, foregrounds in the individual maps are expected to be uncorrelated to each other. On the other hand, one would expect the [C II]$_{158\mu m}$ and [H I]$_{21cm}$ signals to be anti-correlated at large length scales and would expect their level of anti-correlation to vary with length scales and the stage of reionization. This essentially makes the detection of both signals via cross-correlation statistics, e.g. the cross-power spectrum, more feasible compared to their auto power spectrum. However, one has to keep in mind that the foregrounds will still contribute to the errors of the signal statistics even when it is detected via cross-correlation. Once detected, one in principle can use the [C II]$_{158\mu m}$ $\times$[H I]$_{21cm}$ cross-power spectrum to constrain the reionization history and the EoR parameters (Dumitru et al. 2019) more precisely.

Any electromagnetic radiation takes a finite amount of time to travel from its point of origin to the observer. When any cosmological signal originating at different distances along the line-of-sight (LoS) of a present-day observer, arrives at the present-day observer at the same time, the signal and its statistics will change along the LoS. This is due to the fact that signals coming from different cosmic distances originated at different cosmic times. This effect is popularly known as the ‘light-cone effect’.

As one can anticipate, such a light-cone effect is expected to have an impact on the estimated signal statistics, such as on the power spectrum and cross-power spectrum, etc. In the context of the EoR, it has been demonstrated that this affects the [H I]$_{21\text{cm}}$ signal two-point correlation function and power spectrum (Datta, Mellema, et al. 2012; Datta, Jensen, et al. 2014; Zawada et al. 2014; Plante et al. 2014; Raghunath Ghara, Datta, and T. Roy Choudhury 2015; Rajesh Mondal, Somnath Bharadwaj, and Datta 2018). One would expect the light-cone effect to have a similar impact on the [C II]$_{158\mu\text{m}}$ power spectrum and the [C II]$_{158\mu\text{m}}$ ×[H I]$_{21\text{cm}}$ cross-power spectrum. However, as per our knowledge, the impact of the light-cone effect on the [C II]$_{158\mu\text{m}}$ power spectrum and the [C II]$_{158\mu\text{m}}$ ×[H I]$_{21\text{cm}}$ cross-power spectrum has not been quantified so far.

In this Chapter, we aim to quantify the light-cone effect on the [C II]$_{158\mu\text{m}}$ power-spectrum and [C II]$_{158\mu\text{m}}$ ×[H I]$_{21\text{cm}}$ cross-power spectrum from the EoR. It is important to quantify this effect on the expected signal, as it can potentially affect the predicted detectability of the signal. Additionally, if this effect is not properly taken into account, it may lead to a wrong interpretation of the observed signal. To quantify this effect, we have first simulated both the [C II]$_{158\mu\text{m}}$ and the [H I]$_{21\text{cm}}$ signals from the EoR. We have used a combination of N-body dark matter only simulation, a Friend-of-Friend halo finder, and a set of semi-numerical prescriptions for simulating the EoR [H I]$_{21\text{cm}}$ and [C II]$_{158\mu\text{m}}$ intensity maps for a series of fixed redshifts (coeval maps). We then constructed light-cone cuboids of the simulated signals from these redshift snapshots. While simulating and constructing the light-cone cuboids for the [H I]$_{21\text{cm}}$ signal, we also consider different reionization histories to have varied light-cone impacts on the simulated signal. We next estimate the spherically averaged auto power spectrum of the [C II]$_{158\mu\text{m}}$ and [H I]$_{21\text{cm}}$ signals from both the coeval cubes and light-cone cubes and compare them to assess the impact of the light-cone effect on these two different signals. Next, we have studied the light-cone effect on the [C II]$_{158\mu\text{m}}$ ×[H I]$_{21\text{cm}}$ cross-power spectrum. Throughout this work, the cosmological parameters that have been adopted are $\Omega_\text{m} = 0.3183, \Omega_\Lambda = 0.6817, h = 0.6704, \Omega_\text{b}h^2 = 0.022032, \sigma_8 = 0.8347, n_\text{s} = 0.9619$, consistent with Planck+WP best-fit values (Planck Collaboration, Ade, P. A. R., et al. 2014).

3.2 The EoR CII and HI 21cm line intensity mapping signals

The [C II]$_{158\mu\text{m}}$ line originates from singly ionized carbon atoms, which results from the fine-structure transition between $^2P_{3/2} \rightarrow^2 P_{1/2}$. Although it is believed that [C II]$_{158\mu\text{m}}$ emission originates from the PDR of galaxies as discussed in section 1.4.1, a significant amount is also generated from the cold neutral medium, warm ionized medium (De Looze, Baes, et al. 2011). However, it is expected that the [C II]$_{158\mu\text{m}}$ emission from the ISM of galaxies to be more intense as compared to the emission from the IGM (Gong, Cooray, M. Silva, et al. 2012), therefore it can be treated as a good tracer of the galaxies and star formation.

The intensity of the [C II]$_{158\mu\text{m}}$ emission can be modeled by assuming [C II]$_{158\mu\text{m}}$ luminosity ($L_{\text{CII}}(M, z)$) for a given halo with mass M at redshift z, residing within a co-moving volume ΔV. Then the [C

II]$_{158\mu m}$ LIM signal can be expressed as (Visbal and Loeb 2010; M. Silva et al. 2015),

$$I_{\rm CII} = \frac{1}{\Delta V} \sum_i \frac{L_{\rm CII}(M_i, z)}{4\pi H(z)} \lambda_{\rm CII}. \tag{3.1}$$

where the summation is over all the [C II]$_{158\mu m}$ emitters residing in the volume element ΔV. The [H I]$_{21\rm cm}$ signal originates from the transition between the hyperfine states of the ground state neutral hydrogen. During the EoR, most of the neutral hydrogen gas is present in the IGM, so the [H I]$_{21\rm cm}$ signal from the EoR essentially traces the diffuse gas density of the early IGM. This signal from the EoR can be detected as an excess brightness temperature relative to the CMBR, as given in Equation 1.12.

3.3 Simulations

The particle-mesh (PM) N-body[2] (S. Bharadwaj and Srikant 2004) code that generates dark matter density fields is run at the required redshifts. The simulation has a volume of 215^3 cMpc^3 with 3072^3 grids and 1536^3 particles. It results in a grid resolution of 0.07 cMpc and particle-mass resolution of $\approx 10^8 M_\odot$. Then the Friends-of-Friends (FoF)[3] (Rajesh Mondal, Somnath Bharadwaj, Majumdar, et al. 2015) algorithm is used to identify collapsed halos. The linking length used for this is 0.2 times the mean interparticle separation in the simulation. The resulting halo-mass resolution is $\approx 10^9 M_\odot$, and snapshots are generated at 13 redshifts between $z = 6$ and 7.2, separated by $\Delta z = 0.1$. Then the [C II]$_{158\mu m}$ and [H I]$_{21\rm cm}$ maps are developed from these simulation snapshots. The grid resolution for these maps is reduced from 3072^3 to 384^3, and the grid separation is raised to 0.56 cMpc.

3.3.1 CII maps

The [C II]$_{158\mu m}$ maps are generated by painting [C II]$_{158\mu m}$ luminosity to the halos identified in the dark matter distribution generated by the N-body simulation. To perform this, a set of parametric relationships have been used to connect the halo mass to the [C II]$_{158\mu m}$ luminosity. First, the halo mass is linked to the star-formation rate (SFR) of that halo using Equation 2.1. Then the [C II]$_{158\mu m}$ luminosity is related to the SFR for that halo using Equation 1.9. Based on this prescription, [C II]$_{158\mu m}$ luminosity distribution is generated from the simulated dark-matter halo distribution. Next, using the Cloud in Cell method, this distribution is converted to a coarse gridded map of [C II]$_{158\mu m}$ luminosity. Then for each point on the grid, we determine the [C II]$_{158\mu m}$ intensity using Equation 3.1. This finally gives us the [C II]$_{158\mu m}$ intensity map for each redshift as shown in the left panel of figure 3.1. The choice of parameters for Equation 1.9 adopted throughout this work, corresponds to the model ***m1*** M. Silva et al. 2015. This choice leads to the highest value of $\langle I_{\rm CII}(z)\rangle$ among the four models. It is assumed

[2]https://github.com/rajeshmondal18/N-body

[3]https://github.com/rajeshmondal18/FoF-Halo-finder

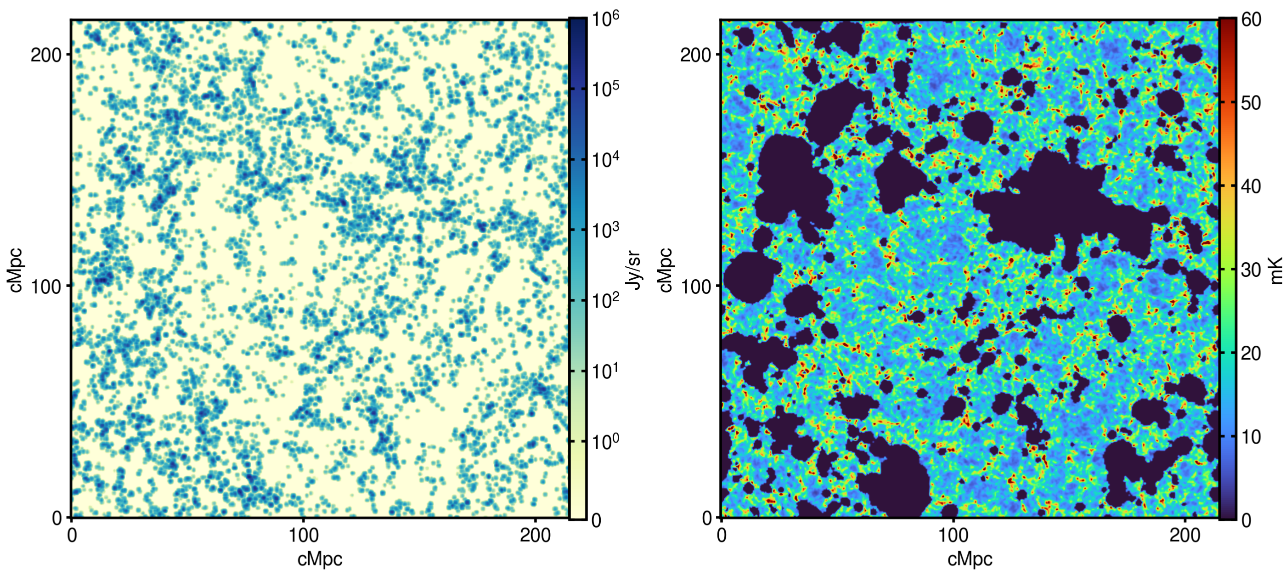

Figure 3.1: This figure shows a slice of [C II]$_{158\mu\mathrm{m}}$ and [H I]$_{21\mathrm{cm}}$ map corresponding to reionization history H1 at $z = 7.2$.

that every halo is an emitter of the [C II]$_{158\mu\mathrm{m}}$ line, which may not be true. This adoption corresponds to the most optimistic scenario, where every halo is an efficient emitter of [C II]$_{158\mu\mathrm{m}}$ line. Due to this, the $\langle I_{\mathrm{CII}}(z)\rangle$ in this work is higher by a factor of ~ 2 compared to that of M. Silva et al. 2015 for the model ***m1***. Nonetheless, the analysis of light-cone remains unaffected without any loss of generality.

3.3.2 HI maps

The [H I]$_{21\mathrm{cm}}$ maps are generated using the semi-numerical code ReionYuga[4] (Tirthankar Roy Choudhury, Haehnelt, and Regan 2009; Majumdar, Mellema, et al. 2014; Rajesh Mondal, Somnath Bharadwaj, Majumdar, et al. 2015), which is based on the excursion-set formalism (Furlanetto, Zaldarriaga, and Hernquist 2004). The [H I]$_{21\mathrm{cm}}$ distribution follows the underlying dark-matter distribution in this simulation. The free parameters used to tune the reionization history are the minimum mass of dark matter halos contributing to reionization ($M_{\mathrm{h,min}}$), ionizing photon-emitting efficiency (N_{ion}), and the mean free path of ionizing photons (R_{mfp}). $M_{\mathrm{h,min}}$ sets the minimum limit of the halo mass below which no halos are considered for the contribution to reionization. The number of ionizing photons emitted by a source is proportional to the halo mass of the halo hosting them in our simulation. The proportionality constant here is N_{ion}. The R_{mfp} is used as the maximum radius to smooth the hydrogen and photon density fields and determine the ionization condition at the grid points. A smoothing radius equal to grid separation is started with and ends at R_{mfp} to check whether at any radius the smoothed photon density exceeds the smoothed neutral hydrogen density at a given grid point. If the condition is met, the point on the grid is considered to be ionized. In the right panel of figure 3.1, an example of the

[4] https://github.com/rajeshmondal18/ReionYuga

simulated $[\mathrm{H\ I}]_{21\mathrm{cm}}$ map corresponding to a particular reionization history has been shown at $z = 7.2$.

By tuning these free parameters, three different reionization histories are generated (H1, H2, H3, figure 3.2), each corresponding to a set of the EoR parameters. These reionization histories differ in the evolution of neutral fraction with redshift, but reionization finishes at $z \sim 6$ in all scenarios. Depending on the reionization history, both the mean and the fluctuations in the $[\mathrm{H\ I}]_{21\mathrm{cm}}$ signal will

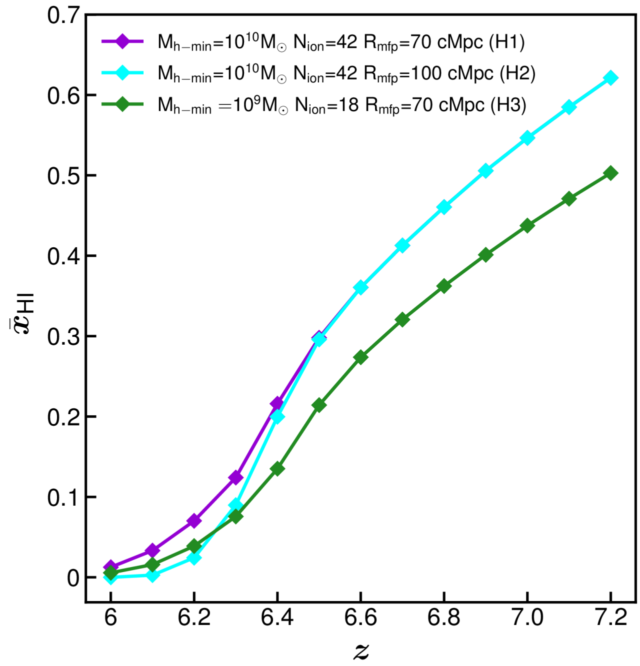

Figure 3.2: Neutral fraction (x_{HI}) vs. Redshift (z) for three different reionization histories.

evolve differently. This means that for different reionization histories, the light-cone effect will affect the $[\mathrm{H\ I}]_{21\mathrm{cm}}$ power spectrum and the $[\mathrm{C\ II}]_{158\mu\mathrm{m}} \times [\mathrm{H\ I}]_{21\mathrm{cm}}$ cross-power spectrum differently. One would expect that in a faster reionization history, the fast-evolving fluctuations will boost the impact of the light-cone effect. For example, in the reionization history H2, having a higher R_{mfp} means that ionized regions will develop faster than H1. In H3, having a lower minimum halo mass for ionizing photon emission means that the reionization gets boosted from these low-mass halos and leads to faster ionization bubble development. These factors play a vital role in determining the evolution of the fluctuations of $[\mathrm{H\ I}]_{21\mathrm{cm}}$ signals, which further contributes to the light-cone effect. In this work, the variation of the impact of the light-cone effect on the $[\mathrm{C\ II}]_{158\mu\mathrm{m}} \times [\mathrm{H\ I}]_{21\mathrm{cm}}$ cross-power spectrum is investigated.

3.3.3 Light-cone maps

We generate light-cone maps using a formalism similar to Datta, Mellema, et al. 2012. The algorithm used here consists of the following basic steps:

1. Given a set of coeval simulations and their redshifts, z_{low} and z_{high} corresponding to the lowest and highest redshifts of the coeval boxes are chosen.

2. If l is the grid spacing of the coeval boxes and L is the co-moving distance between z_{low} and z_{high}, the integer division $N = L/l$ is calculated. A redshift list $\mathbb{Z}$ with N entries $z_1, z_2, z_3, ..., z_N(z_1 < z_2 < z_3... < z_N)$ is prepared, such that each redshift in the entry is separated by a co-moving distance l.

3. If the number of slices in the coeval outputs is M and we want to construct the pth slice of light-cone, the remainder q of the integer division p/M is computed. The qth slice is then taken of all the coeval outputs and using Steffen's interpolation (Steffen 1990), construct the pth slice of light-cone at z_p ($z_p \in \mathbb{Z}$).

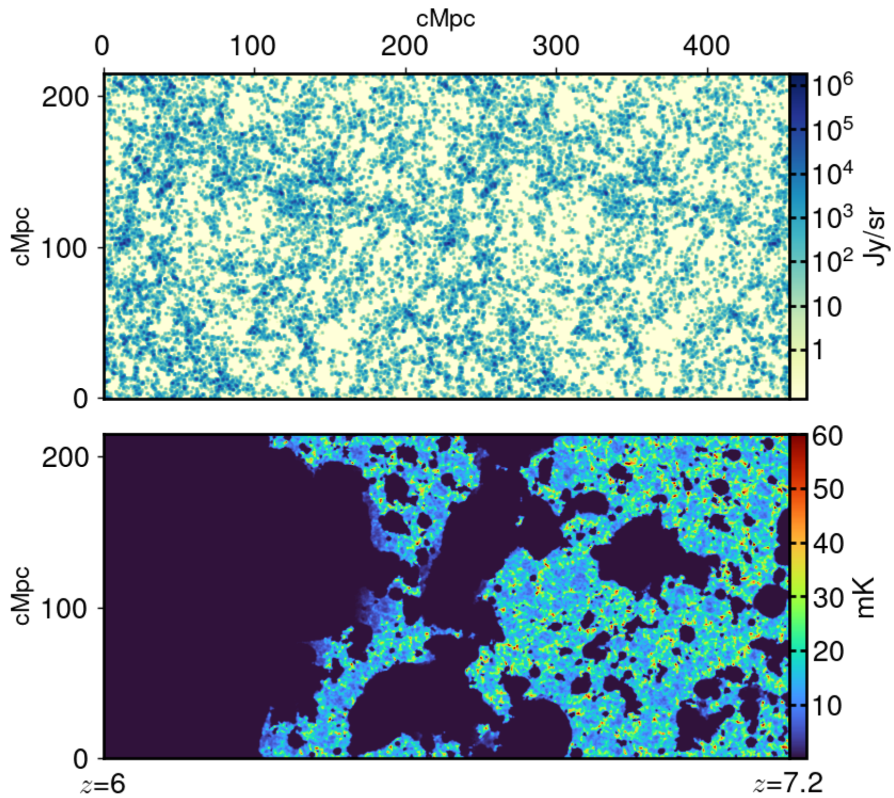

Figure 3.3: Light-cone slices for [C II]$_{158\mu\text{m}}$ (top panel) and [H I]$_{21\text{cm}}$ signal (bottom panel). The reionization history shown here is for model H1.

This algorithm is applied to generate both [C II]$_{158\mu\text{m}}$ and [H I]$_{21\text{cm}}$ light-cone volumes. Slices of light cones are shown in Fig. 3.3. Our redshift range for coeval maps is $z = 6$ to 7.2, so light-cone volumes also have the same redshift extent. The light-cone volumes have a full co-moving extent longer than the size of our coeval cubes. It leads to periodicity effects in the light-cone volumes, and in some cases, structures get repeated (e.g., see the [C II]$_{158\mu\text{m}}$ light-cone in Fig. 3.3). For this reason, light-cone chunks of identical volume as the coeval cubes are cut out, and their statistics are compared. In some cases, the slices of light-cone volumes are rotated to eliminate periodicity effects (see Zawada et al. 2014). Here, this prescription is not followed. This method usually works with light-cone volumes of galaxies or discrete emitters, but not with the diffused gas, e.g., [H I]$_{21\text{cm}}$ light-cone maps. Since one of the principal goals here is to study the cross-power spectrum, the method for generating the light-cone volumes needs to be identical for both signals. In terms of the statistics, since light-cone chunks of the exact size as the coeval cubes are cut out, the periodicity problem is not encountered, and therefore the corrective rotation step is not required. The percentage change in power-spectrum and cross-power spectrum of the signals in the light-cone is estimated with respect to the corresponding summary statistics calculated from coeval volume, i.e. $\Delta(\%) = (\text{lc} - \text{cc}) \times 100/\text{cc}$, where Δ is the percentage change, lc corresponds to light-cone chunk power or the cross-power spectrum and cc corresponds to the coeval cube. We show our light-cone analysis for the [C II]$_{158\mu\text{m}}$ and [H I]$_{21\text{cm}}$ power spectrum and the [C II]$_{158\mu\text{m}}$ $\times$[H I]$_{21\text{cm}}$ cross-power spectrum in the next section.

3.4 Results

Here, the results of the impact of the light-cone effect on the auto-power spectrum and cross-power spectrum of the [C II]$_{158\mu\text{m}}$ and [H I]$_{21\text{cm}}$ signals from the EoR are discussed. The power spectrum and cross-power spectrum are estimated according to Equations 1.13 and 1.21. The cross-correlation coefficient is estimated from Equation 1.22.

3.4.1 CII power spectrum

The [C II]$_{158\mu\text{m}}$ power spectrum for both coeval and light-cone cubes is estimated. The coeval power spectrum is first compared with M. Silva et al. 2015 for consistency check. To have a quantitative estimate of how they compare, a power law of the form $\Delta^2(k) = Ak^n$ is fitted to both M. Silva et al. 2015 and the present results. It is found that, for the M. Silva et al. 2015 ***m1*** model, $A = 3.86 \times 10^6$ and $n = 1.67$, while for this work $A = 1.41 \times 10^7$ and $n = 1.74$. The relative difference in the spectral index in these two results is around ~ 4 percent. This difference is most likely due to the differences in the underlying population abundance of [C II]$_{158\mu\text{m}}$ emitters. Since the number of low-mass halos is high, a higher number of low-mass [C II]$_{158\mu\text{m}}$ emitters would contribute more power to the larger k-modes than higher-mass halos to the lower k-modes. This means that a steeper slope (higher n) can be expected in the present results. The higher population abundance in this case also contributes to a higher magnitude of the power spectrum. Next, the impact of the light-cone effect on the [C II]$_{158\mu\text{m}}$ power spectrum is discussed. Fig. 3.4 shows the [C II]$_{158\mu\text{m}}$ power spectrum (top panel) and the percentage change in the light cone effect relative to the coeval power spectrum (bottom panel). The error bars in the power spectra are estimated from the sample variance in each k-mode bin. The power

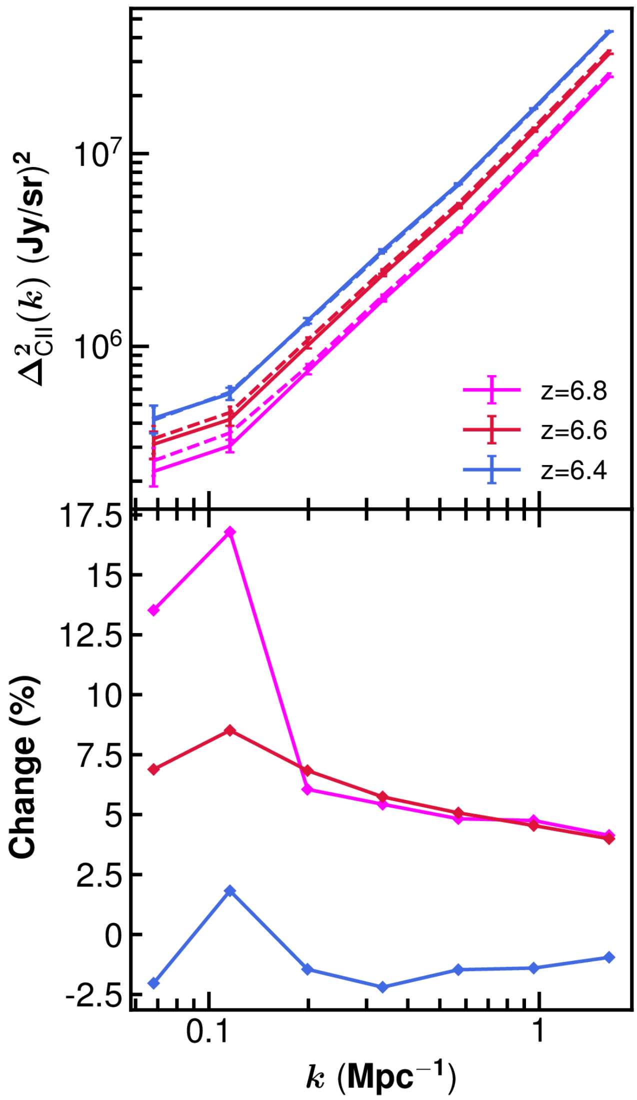

Figure 3.4: [C II]$_{158\mu\rm m}$ power-spectrum is shown in the top panel (solid lines represent coeval and dashed lines represent light-cone power-spectrum). Bottom panel shows the percentage change in power-spectrum due to light-cone effect.

spectra at three redshifts $z = 6.8, 6.6,$ and 6.4 are compared for the coeval and light-cone cubes. The analysis is limited by the extent of LoS of the light-cone volume, in this case, it is such that it was not possible to go beyond $z = 6.4$ and 6.8, although it is important to look at more redshifts beyond this limit. While comparing the light-cone power spectrum with the coeval power spectrum, the redshift of the center of the light-cone chunk is chosen as the reference coeval redshift.

It is observed that at $z = 6.6$ and 6.8, the change in the power spectrum is very much similar across all k-modes, except for $k \lesssim 0.1\,\rm Mpc^{-1}$. At $k \sim 0.1\,\rm Mpc^{-1}$, the light-cone effect is the most pronounced compared to the other k-modes. This is expected as the light-cone effect is a large-scale effect (i.e. small k effect in Fourier space). This can be understood in the following manner. To estimate the spherically averaged power spectrum of a signal if one increases the extent of the observed volume along the LoS (i.e. probing larger length scales along the LoS), one would be effectively combining signals from more distinctly different cosmic times, thus will see more pronounced impact of the light-cone effect in small k power spectrum.

Therefore, at larger scales, the behavior of the light-cone effect becomes interesting and needs to be explored. Our coeval volume is limited to $(215\,\mathrm{Mpc})^3$, and to investigate the light-cone effect on the $[\mathrm{C\,II}]_{158\mu\mathrm{m}}$ power spectrum for k-modes well below ~ 0.1 Mpc^{-1} with higher statistical significance, we will need to simulate the signal at even larger comoving volumes. It is observed that there is a systematic behavior in the change of light-cone effect at $k \sim 0.1$ Mpc^{-1} (Fig. 3.4, bottom panel). The impact of the light-cone effect at this k-mode drops with decreasing redshifts. The fluctuations in the $[\mathrm{C\,II}]_{158\mu\mathrm{m}}$ LIM signal trace the underlying structures. The rate of growth of structures is comparatively rapid at higher redshifts and slows down significantly at lower redshifts. Thus, the difference in structures between a coeval map and a light-cone map at lower redshifts is significantly small, thus, the impact of the light-cone effect on the $[\mathrm{C\,II}]_{158\mu\mathrm{m}}$ power spectrum is also relatively small compared to the scenarios at higher redshifts. This causes the impact of the light-cone effect on the $[\mathrm{C\,II}]_{158\mu\mathrm{m}}$ power spectrum to reduce systematically with decreasing redshifts. The maximum change in power due to the light-cone exceeds 15 percent at $z = 6.8$ at this k-mode; this shows that the impact of light-cone on the $[\mathrm{C\,II}]_{158\mu\mathrm{m}}$ power spectrum is significant.

The light-cone cubes are labeled with z_c, which is the redshift at the center of that volume. As discussed earlier, we compare the power spectrum of this cube with a coeval cube of redshift z_c. The properties of the fluctuations in the $[\mathrm{C\,II}]_{158\mu\mathrm{m}}$ signal will be different in the central part of the light-cone cube compared to the front (lower z) and the far (higher z) end. The $[\mathrm{C\,II}]_{158\mu\mathrm{m}}$ LIM signal essentially follows a biased distribution of the underlying dark matter density distribution, thus the signal coming from the far end of the light-cone volume will have less fluctuations than the front end (as structures are more clustered). Thus the relative difference in the power spectrum amplitude between z_c (central portion) and these sections will be different. When z_c is lower, the relative difference drops by unequal amounts. Compared to the far end of the light-cone volume, the power spectrum from the front part becomes more saturated (as the formation and clustering of structures also saturate and the overall evolution of structures slows down). Thus, the relative difference in power from the front portion and the central portion drops more, and we see that the impact of the light-cone effect drops with decreasing z_c.

3.4.2 HI power spectrum

The main focus here is to quantify the light-cone effect on the $[\mathrm{C\,II}]_{158\mu\mathrm{m}}$ power spectrum and the $[\mathrm{C\,II}]_{158\mu\mathrm{m}} \times [\mathrm{H\,I}]_{21\mathrm{cm}}$ cross-power spectrum. However, we discuss the light-cone effect on the $[\mathrm{H\,I}]_{21\mathrm{cm}}$ power spectrum, which has been studied extensively earlier, in this section for consistency checks and also as a prerequisite to the cross-power spectrum. Unlike the [C II]$_{158\mu\mathrm{m}}$ power spectrum, the [H I]$_{21\mathrm{cm}}$ power spectrum is dependent on the state of the IGM or the reionization history, as the [H I]$_{21\mathrm{cm}}$ signal fluctuations is affected by the ionization field. Thus one would expect that the impact of the light-cone effect will be different in the case of this signal compared to the [C II]$_{158\mu\mathrm{m}}$ signal. The impact of the light-cone effect will vary depending on the reionization history. A faster reionization history is expected to exhibit a more drastic impact due to the light-cone effect. The top panel of Fig. 3.5 shows

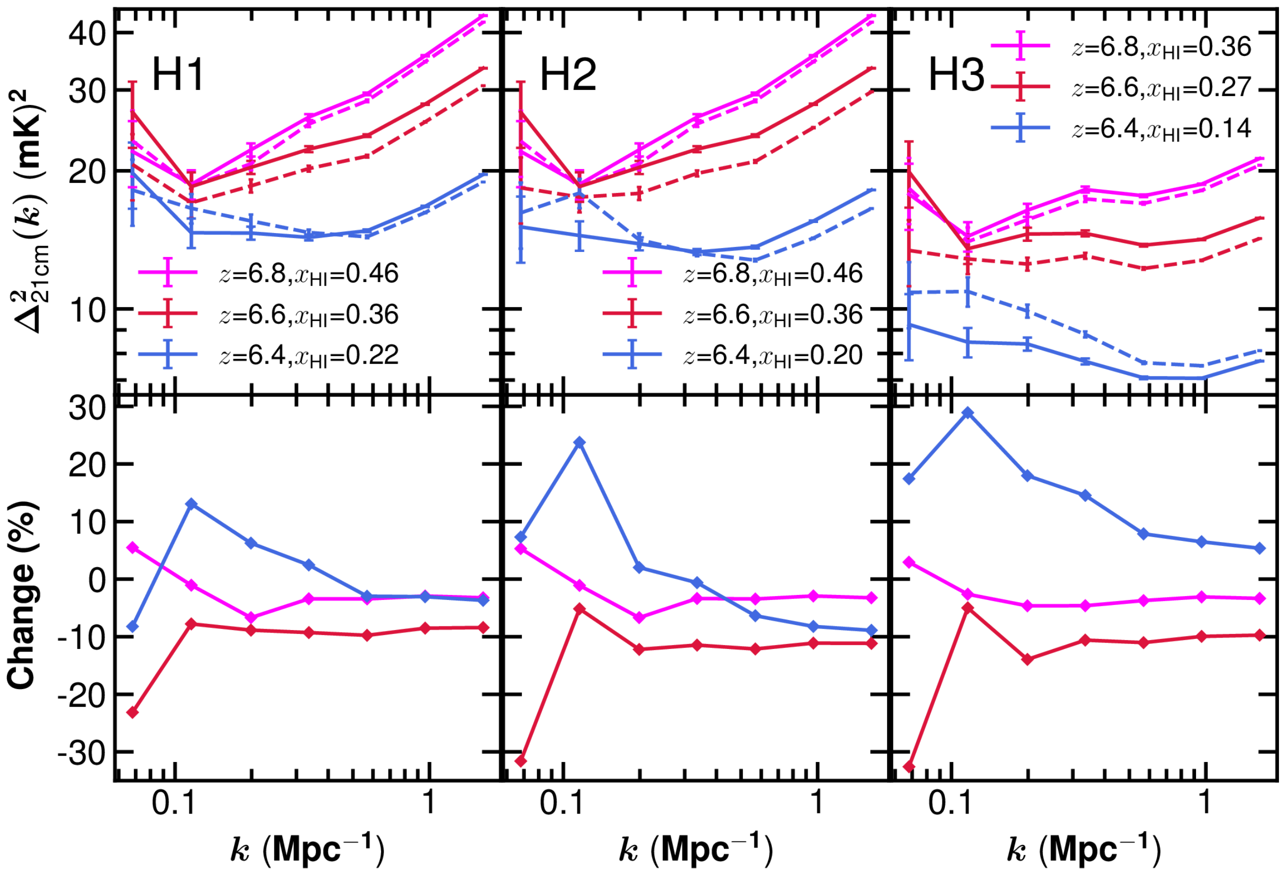

Figure 3.5: Top panel shows the coeval (solid) and light-cone (dashed) [H I]$_{21\mathrm{cm}}$ power spectrum for different neutral fractions ($\langle x_{\rm HI}\rangle$). The bottom panel shows the impact of the light-cone on the power spectrum in percentage. Panels from left to right (H1, H2, and H3) correspond to the different reionization histories.

the coeval and light-cone power spectrum of the [H I]$_{21\mathrm{cm}}$ signal. The bottom panel shows the impact of the light-cone effect in percentage. The [H I]$_{21\mathrm{cm}}$ power spectrum does not have a constant slope in the $\Delta^2(k) - k$ space, unlike the [C II]$_{158\mu\mathrm{m}}$ power spectrum, which is almost featureless. It is found that the [H I]$_{21\mathrm{cm}}$ power spectrum in our work is consistent with Datta, Mellema, et al. 2012 but not exactly similar. The differences in the power spectra can be ascribed to the difference in the reionization history, source model, and the method of simulating the EoR [H I]$_{21\mathrm{cm}}$ signal in Datta, Mellema, et al. 2012 and this work. In the simulations used by Datta, Mellema, et al. 2012, the reionization ends before $z = 8$ and these simulations are based on a full radiative-transfer technique. Even if we compare our [H I]$_{21\text{cm}}$ power spectra at the level of the same mass-averaged IGM neutral fraction with that of the Datta, Mellema, et al. 2012, we still find a significant difference in their amplitude. This is because, as in Datta, Mellema, et al. 2012, the same IGM neutral fraction is reached at a higher redshift, thus the nature of the ionizing sources is different than that of our simulations. This is because the source model in both simulations is strongly dependent on the underlying halo mass function, which will be significantly different at two, far-apart cosmological redshifts.

The light-cone [H I]$_{21\text{cm}}$ power spectrum varies across the three reionization histories that we have considered here. At $z = 6.6$, which roughly represents the redshift mid-point for all three reionization histories, the light-cone power spectrum has different amplitudes for reionization histories H1 and H2. It is observed that the [H I]$_{21\text{cm}}$ power spectrum for H2 is more suppressed (Fig. 3.5, top panels) compared to that of H1, though they have the same mass-averaged neutral fraction at this redshift. The amplitude of the H3 light-cone power spectrum is suppressed at this redshift at a level similar to H2, for all k-modes except at $k \sim 0.2$ Mpc^{-1}. If we compare the light-cone power spectra in these three reionization histories with their respective coeval power spectra, an overall decrease in amplitude is seen due to the light-cone effect by ≈ 10 percent or more in all k-modes for $z = 6.6$. As one goes to the lower redshifts, e.g. $z = 6.4$, a change in the nature of the light-cone effect can be noticed. The light-cone power spectrum amplitude gets boosted compared to the coeval power spectrum, specifically for large length scales, i.e., small k-modes. This impact is maximum for the reionization history H3. For the H3 history, the power spectrum amplitude gets a boosting of around ≈ 20 percent or more. This is consistent with Datta, Mellema, et al. 2012. As the light-cone effect in the EoR [H I]$_{21\text{cm}}$ signal is dependent on the reionization history, we observe a stronger impact when the neutral fraction evolves more rapidly with redshift, e.g., the history H3. Since the [C II]$_{158\mu\text{m}}$ $\times$[H I]$_{21\text{cm}}$ cross-power spectrum has a contribution from the [H I]$_{21\text{cm}}$ signal fluctuations, we expect some of the behavior to reflect in the cross-power spectrum as well, e.g., the variation of the impact of the light-cone with reionization history.

3.4.3 CII-21cm cross-power spectrum

One of the main focuses here is investigating the impact of the light-cone effect on the [C II]$_{158\mu\text{m}}$ $\times$[H I]$_{21\text{cm}}$ cross-power spectrum. The fluctuations in both the [C II]$_{158\mu\text{m}}$ and [H I]$_{21\text{cm}}$ signals contribute to the cross-power spectrum. It implies that the impact of the light-cone effect on the cross-power spectrum will vary with the reionization history under consideration, as it does in the case of the [H I]$_{21\text{cm}}$ power spectrum. Fig. 3.6 shows the [C II]$_{158\mu\text{m}}$ $\times$[H I]$_{21\text{cm}}$ cross-power spectrum, along with the cross-correlation coefficient and the percentage change in the light-cone cross power spectrum with respect to the coeval cross-power spectrum. During the EoR, most of the neutral hydrogen lives in the form of diffused gas within the IGM. In a typical inside-out reionization scenario (as in case of our simulations

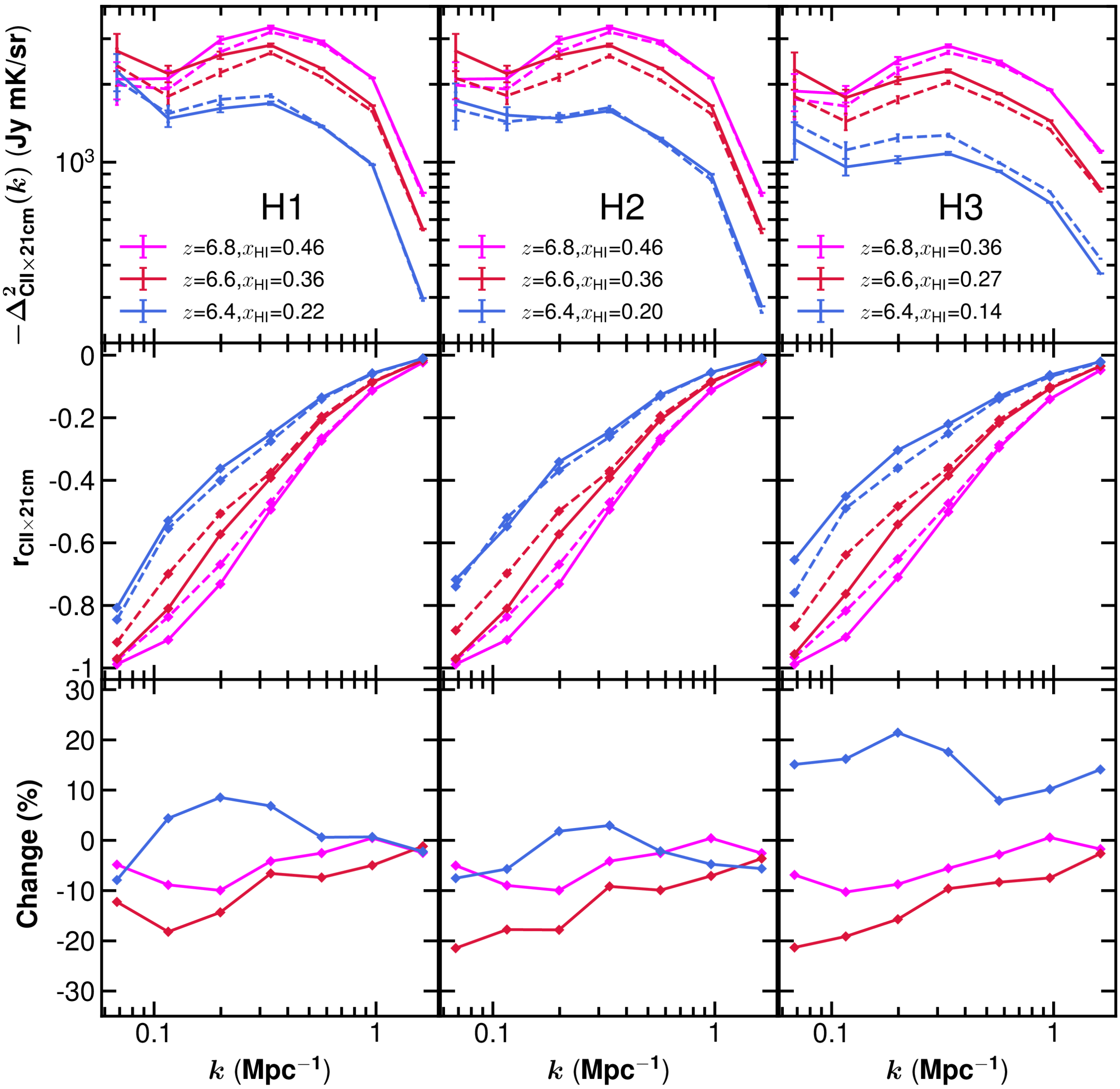

Figure 3.6: The $[\mathrm{C\ II}]_{158\mu\mathrm{m}} \times [\mathrm{H\ I}]_{21\mathrm{cm}}$ cross-power spectrum (top panel), along with cross-correlation coefficient (middle panel) and change in cross power due to light-cone effect (bottom panel) is shown here. Panels from left to right (H1, H2 and H3) correspond to different reionization histories. In the top and middle panel, solid and dashed lines represent coeval and light-cone cross-power spectrum respectively.

here), the ionizing photons released by the reionization sources first ionize their local IGM and then spread out to far-away regions. As discussed earlier, one would expect the $[\mathrm{C\ II}]_{158\mu\mathrm{m}}$ LIM observations to probe the distribution and clustering pattern of these ionizing sources. During the early and middle stages of the EoR, one would expect the ionized regions to form around the sources of ionization, and there will be no $[\mathrm{H\ I}]_{21\mathrm{cm}}$ signal in these regions. This implies that one should expect a strong anti-correlation between the [C II]$_{158\mu m}$ intensity maps (tracing the sources) and [H I]$_{21cm}$ maps (tracing the neutral hydrogen) at these stages. A visual inspection of the simulated light-cone maps of the [H I]$_{21cm}$ and [C II]$_{158\mu m}$ signal shown in figure 3.3 confirms this expectation. It is quite apparent from this figure that most of the [C II]$_{158\mu m}$ emission is coming from locations where the IGM is ionized or there is no [H I]$_{21cm}$ signal. Next, the cross-power spectrum and the cross-correlation coefficients are shown in figure 3.6. For all three reionization histories considered here, there is a strong anti-correlation, marked by the negative value of the cross-power spectrum and the cross-correlation coefficient (see top and middle panels of figure 3.6) between these two signals in the k-mode range $0.07 \leq k \leq 0.5$ Mpc^{-1}, when the reionization is half-way through i.e. $z = 6.8$. The degree of anti-correlation gradually decreases with the progress of reionization for all three reionization histories.

The impact of the light-cone effect on the cross-power spectrum at higher redshifts ($z = 6.8$) i.e. during the early and middle stages of the EoR is similar to that on the [H I]$_{21cm}$ power spectrum. There is an overall suppression in the cross-power spectrum amplitude during these stages of the EoR for all three reionization histories. The level of suppression in the cross-power amplitude is ~ 10 percent or less for smaller k-modes. The light-cone effect effectively reduces the amount of anti-correlation between these two signals at this stage. At the later stages of the EoR ($z = 6.6$) the light-cone effect continues to suppress the cross-power spectrum amplitude further. For histories H2 and H3, where reionization runs faster at later stages, the suppression in the cross-power due to the light-cone effect at large length scales can be as large as ~ 20 percent. The impact on the H1 case for this statistic at this stage is comparatively less relative to H2 and H3. During the very late stages of the EoR ($z = 6.4$) the nature of impact due to the light-cone effect on the cross-power spectrum changes and instead of suppressing the power it enhances the amplitude of the cross-power spectrum significantly. The impact is maximum in case of the reionization history H3. We observe more than 20 percent enhancement in cross-power for smaller k-modes in this scenario. In case of H1, the enhancement in power for small k-modes lies somewhere in between $5 - 10$ percent, whereas for H2 it is less than or equal to ~ 5 percent. The difference in the impact of light-cone effect can be ascribed to the nature of evolution of the reionization history in these three cases.

3.5 Discussion & Conclusion

In this work, the impact of the light-cone effect on the auto and cross-power spectra of the EoR [C II]$_{158\mu m}$ and [H I]$_{21cm}$ line intensity mapping signals is investigated. Using an N-body simulation, an FoF halo finding scheme and semi-numerical schemes to generate [C II]$_{158\mu m}$ and [H I]$_{21cm}$ intensity maps, we have built the light-cone cuboids for [C II]$_{158\mu m}$ and [H I]$_{21cm}$ signals from the EoR. By performing a relative comparison between the auto and cross-power spectra estimated from the coeval and light-cone maps of these two signals, the impact of the light-cone effect on these statistics is quantified. This is the first effort to quantify the impact of the light-cone effect on the [C II]$_{158\mu m}$ power spectrum and the

[C II]$_{158\mu\mathrm{m}}$ $\times$[H I]$_{21\mathrm{cm}}$ cross-power spectrum from the EoR. The key findings of this work is summarised below:

- The light-cone effect has a significant impact on the [C II]$_{158\mu\mathrm{m}}$ power spectrum, and it is most pronounced at large length scales i.e. $k \sim 0.1$ Mpc^{-1}. This effect can introduce a change in power by ~ 15 percent (at $z = 6.8$).
- The impact of light-cone effect on the [C II]$_{158\mu\mathrm{m}}$ power spectrum decreases with decreasing redshift and by $z = 6.4$ it leads to a suppression of the amplitude of the [C II]$_{158\mu\mathrm{m}}$ power spectrum in most of the k-modes by a small amount (~ 2 percent).
- The reduction in the impact of the light-cone effect on the [C II]$_{158\mu\mathrm{m}}$ power spectrum with decreasing redshift can be understood in the following manner: The [C II]$_{158\mu\mathrm{m}}$ power spectrum follows the underlying halo distribution which is a manifestation of the underlying structures. The rate of growth of structures is relatively rapid with redshift at earlier cosmic times. This growth rate slows down significantly as the lower redshifts are approached. Thus, the difference in structures between a coeval map and a light-cone map at lower redshifts is significantly low. Thus, the impact of the light-cone effect on the [C II]$_{158\mu\mathrm{m}}$ power spectrum is also relatively small when compared with the scenarios at higher redshifts.
- The impact of the light-cone effect on the [C II]$_{158\mu\mathrm{m}}$ $\times$[H I]$_{21\mathrm{cm}}$ cross-power spectrum is significant, with the maximum change in cross-power amplitude reaching up to 20 percent.
- For the [C II]$_{158\mu\mathrm{m}}$ $\times$[H I]$_{21\mathrm{cm}}$ cross-power spectrum, the impact of the light-cone effect strongly depends on the reionization history. A rapid evolution in the mass-averaged neutral fraction with redshift results in a stronger light-cone effect on the cross-power spectrum.
- The nature of the impact of the light-cone effect, translated in terms of either suppression or enhancement of the cross-power spectrum amplitude, depends on the stage of reionization that the light-cone volume under consideration is capturing. If the light-cone volume is sampled from the early or middle stages of the EoR, it results in suppression of the cross-power amplitude. However, when the light-cone volume represents a very late stage of the EoR, it results in an enhancement of the cross-power amplitude.

This analysis suggests that the light-cone effect has a significant impact on the amplitude of the [C II]$_{158\mu\mathrm{m}}$ intensity map power spectra as well as the [C II]$_{158\mu\mathrm{m}}$ $\times$[H I]$_{21\mathrm{cm}}$ cross-power spectrum from the EoR. It is therefore essential to take the light-cone effect into account while modeling the signal and estimating the reionization parameters from observations.

Chapter 4

Revisiting the CII line-intensity mapping power spectrum from the EoR using non-uniform line-luminosity scatter

This chapter has been adapted from: **Murmu, C. S.**, Olsen, K. P., Greve, T. R., Majumdar, S., Datta, K. K., Scott, B. R., Leung, T. K. D., Davé, R., Popping, G., Ochoa, R. O., Vizgan, D., & Narayanan, D. (2022). Revisiting the [C II]158μm line-intensity mapping power spectrum from the EoR using non-uniform line luminosity scatter. *Monthly Notices of the Royal Astronomical Society*, 518(2), 3074–3082, DOI: 10.1093/mnras/stac3304, arXiv: 2110.10687

4.1 Introduction

Probing the early galaxies from the Epoch of Reionization (EoR) is challenging, demanding very high resolution and sensitivities from the instruments trying to probe these galaxies. Observations with **Hubble Space Telescope** (HST, Robertson et al. 2015), **Atacama Large Millimetre Array** (ALMA, Le Fèvre et al. 2020), **SUBARU** (Kashikawa, Shimasaku, Malkan, et al. 2006; Kashikawa, Shimasaku, Matsuda, et al. 2011; Kashikawa, Ishizaki, et al. 2015; Itoh et al. 2018; Matsuoka et al. 2018), **LAGER** (Zheng et al. 2017; Weida Hu, J. Wang, Zheng, Sangeeta Malhotra, Infante, et al. 2017; Weida Hu, J. Wang, Zheng, Sangeeta Malhotra, Rhoads, et al. 2019; Harish et al. 2022; Wold et al. 2022) have detected them in small numbers. Instruments like **JWST** (Steinhardt, Jespersen, and Linzer 2021) **are** further detecting these early galaxies. However, point-source detections through spectroscopy or photometry consume a significant amount of observational time and are thus expensive.

LIM survey of galaxies (Visbal and Loeb 2010; Gong, Cooray, M. B. Silva, et al. 2011) is a possible solution for this, by which one can detect the integrated flux of atomic or molecular line emissions from numerous sources at once, without resolving them individually and with reduced sensitivity requirements. Moreover, it will significantly cut down the observational hours required to map large volumes of the sky and probe numerous galaxy samples, to infer about its properties. Line emission candidates promising for LIM experiments include [C II]$_{158\mu\mathrm{m}}$ (Gong, Cooray, M. Silva, et al. 2012; M. Silva et al. 2015; Dumitru et al. 2019; Yue and Ferrara 2019; G. Sun, T. C. Chang, et al. 2021; Murmu, Majumdar, and Datta 2021), CO (Gong, X. Chen, et al. 2011; Lidz, Furlanetto, et al. 2011; M. Silva et al. 2015; T. Y. Li et al. 2016; Breysse and Rahman 2017; Breysse and Alexandroff 2019; H. T. Ihle et al. 2019; Moradinezhad Dizgah and Keating 2019b; Moradinezhad Dizgah, Nikakhtar, et al. 2022), Ly-α (Visbal and McQuinn 2018; Heneka and Cooray 2021) etc. Instruments like **CONCERTO** (Guilaine Lagache 2017; CONCERTO Collaboration et al. 2020), **TIME** (Crites et al. 2014; G. Sun, T. C. Chang, et al. 2021), **FYST** (Cothard et al. 2020; CCAT-Prime Collaboration et al. 2023), **TIM** (Vieira et al. 2020) will be targeting the [C II]$_{158\mu\mathrm{m}}$ line. On the other hand, we have detections of the CO signal with **COPSS** (Keating, Bower, et al. 2015; Keating, Marrone, Bower, Leitch, et al. 2016), **COMAP** (H. T. Ihle et al. 2019; Dongwoo T. Chung et al. 2022; Cleary et al. 2022; Håvard T. Ihle et al. 2022) and **mmIME** (Breysse, Dongwoo T. Chung, et al. 2022). Future phases of the **COMAP** experiment will target the CO line to probe the EoR (Breysse, Dongwoo T. Chung, et al. 2022). Similarly, **SPHEREx** (Visbal and McQuinn 2018; Heneka and Cooray 2021; Cox, Jacobs, and Murray 2022) and **CDIM** (Visbal and McQuinn 2018; Cooray et al. 2019; Heneka and Cooray 2021) will be mapping the universe with Ly-α detections. These experiments will be capturing the sky-fluctuations of the LIM signal, enabling us to estimate statistics, e.g., the power spectrum. It will aid us in understanding the large-scale distribution and the astrophysical properties of the ionizing sources from the EoR.

The presence of line luminosity scatter will introduce a correction to the LIM power spectrum. Under line luminosity scatter, one can model or interpret the change in the power spectrum in the following ways. One of the widely used ways is to interpret against the mean luminosity-halo mass ($\langle L(M_\mathrm{h}, z)\rangle$) correlation function (T. Y. Li et al. 2016; Schaan and White 2021; Yang et al. 2022). In this approach, the mean intensity of the LIM signal is preserved under line luminosity scatter. Therefore, there is no change in the clustering (large-scale) power spectrum component, and only the shot-noise power is enhanced. The other approach (followed by Moradinezhad Dizgah and Keating 2019b; Moradinezhad Dizgah, Nikakhtar, et al. 2022) is to use a $L(M_\mathrm{h}, z)$ correlation fit such that there is a change in the mean intensity and consequently in the clustering power. The deviation in the power spectrum at small k-modes under scatter can be modeled in terms of the scatter parameter σ. We can utilize both models as long as we interpret the power spectrum accordingly. It can be done with scatter, modeled via a semi-analytical approach with a single scatter parameter uniform across halo-mass bins.

In this study, various model-frameworks have been revisited that can be used to interpret the impact of scatter on the 2-point statistic. line luminosity scatter of the [C II]$_{158\mu\mathrm{m}}$ line emission has been used, obtained from simulated data of cosmological hydrodynamic simulation SIMBA (Davé, Anglés-Alcázar, et al. 2019; Leung et al. 2020). The outputs were post-processed with CLOUDY (G. J. Ferland, Porter, et al. 2013; G. J. Ferland, Chatzikos, et al. 2017) and SIGAME (Olsen, Thomas R. Greve, Narayanan, R. Thompson, Toft, et al. 2015; Olsen, Thomas R. Greve, Brinch, et al. 2016; Olsen, Thomas R. Greve, Narayanan, R. Thompson, Davé, et al. 2017; Leung et al. 2020). The scatter emerges naturally from the astrophysics implemented within this sophisticated simulation framework, such as the multi-phase state of the ISM inside galaxies (see section 4.2), and its statistical properties have halo-mass variation, making it non-uniform in nature. Our primary focus had been to explore whether all models can interpret the power spectrum under a more generalized and realistic line luminosity scatter in a consistent and robust fashion. Here, it is demonstrated that a most-probable fit can robustly interpret the LIM signal's mean intensity and power spectrum. Throughout this work, cosmological parameters $\Omega_\mathrm{m} = 0.3183\,, \Omega_\Lambda = 0.6817\,, h = 0.6704\,, \Omega_\mathrm{b}h^2 = 0.022032\,, \sigma_8 = 0.8347\,, n_\mathrm{s} = 0.9619$, have been adopted, consistent with Planck+WP best-fit values (Planck Collaboration, Ade, P. A. R., et al. 2014).

4.2 CII line luminosity scatter

The $[\mathrm{C\ II}]_{158\mu\mathrm{m}}$ line luminosity scatter originates from the collective dependence of L_CII on various astrophysical factors such as star formation, metal enrichment, and different phases of the interstellar medium (ISM). The SIGAME simulations by Leung et al. 2020 handle three ISM phases (ionized, atomic, and molecular), all of which emit $[\mathrm{C\ II}]_{158\mu\mathrm{m}}$. The molecular phase, which makes up no more than ~ 30 percent of the total ISM mass in the simulations, typically contributes by more than 50 per cent to the total $[\mathrm{C\ II}]_{158\mu\mathrm{m}}$ emission, especially in massive galaxies (Accurso et al. 2017; Vizgan et al. 2022). Observationally, constraints on the contribution to the total $[\mathrm{C\ II}]_{158\mu\mathrm{m}}$ emission from the molecular phase come from a survey of our Galaxy, which suggests that the combined dense PDR gas and CO-dark molecular gas make up ~ 50 percent of the total emission (Pineda, Langer, and Goldsmith 2014). Simulations also indicate that the contribution to the $[\mathrm{C\ II}]_{158\mu\mathrm{m}}$ emission from the ionized and atomic gas can be up to 50 percent but decreases with increasing stellar mass and metallicity (Accurso et al. 2017). Although one would expect the $[\mathrm{C\ II}]_{158\mu\mathrm{m}}$ emission to decrease with lower metallicities, this effect is negligible compared to the increase in CO photo-dissociation rate (and thus the available C^+ ions) that comes with lower metallicities (Accurso et al. 2017). The scatter in the L_CII versus M_halo correlation, therefore, primarily comes from the scatter in the relative mass distributions of the ISM phases, which are set by the specific star formation rate and metallicity. Although L_CII is correlated to the host halo-mass, one would expect that, in reality, it is not perfectly correlated. In the following subsections, the method of simulating the $[\mathrm{C\ II}]_{158\mu\mathrm{m}}$ emission from galaxies and obtaining a one-to-one L_CII versus M_halo fit to the L_CII scatter is discussed.

4.2.1 Simulations of CII emission

This work builds on the analysis of snapshots taken from the SIGAME suite of cosmological galaxy formation simulations, which themselves were evolved using the meshless finite mass hydrodynamics technique of GIZMO (Hopkins 2015; Hopkins 2017; Davé, Anglés-Alcázar, et al. 2019). The SIGAME simulation set consists of three cubical volumes, 25, 50, and 100 h^{-1} Mpc ($h = 0.678$) on each side, all of which are used in this work to search for galaxies at $z \sim 6$. For each volume, a total of 1024^3 gas elements and 1024^3 dark matter particles are evolved from $z = 249$. The galaxy properties in SIGAME have been compared to various observations across cosmic time (Thomas et al. 2019; Appleby et al. 2020), including the epoch of reionization (Wu et al. 2020; Leung et al. 2020), and are in reasonable agreement. The sample of galaxies used here is taken from (Leung et al. 2020) and consists of 11,125 galaxies, with derived [C II]$_{158\mu m}$ luminosities from $10^{3.82}$ to $10^{8.91}$ $L_\odot$.

In order to derive the [C II]$_{158\mu m}$ emission, the galaxy samples were post-processed with version 2 of the SIGAME module (Olsen, Thomas R. Greve, Narayanan, R. Thompson, Davé, et al. 2017).[1] It uses the spectral synthesis code CLOUDY (v17.01; G. J. Ferland, Porter, et al. 2013; G. J. Ferland, Chatzikos, et al. 2017) to model the line emission from the multi-phased ISM within each simulated galaxy. As input to CLOUDY, SIGAME uses physically motivated prescriptions to calculate the local interstellar radiation field (ISRF) spectrum, the cosmic ray (CR) ionization rate, and the gas density distribution of the ionized, atomic and molecular ISM phases (see Davé, Anglés-Alcázar, et al. 2019; Leung et al. 2020, for details on the SIMBA simulation and implementation of SIGAME, respectively).

4.2.2 Fitting the CII line luminosity scatter

The halo [C II]$_{158\mu m}$ luminosities are derived from the central galaxies' [C II]$_{158\mu m}$ luminosity; these central galaxies are identified in the SIMBA simulation. The [C II]$_{158\mu m}$ line luminosity scatter is fitted with a one-to-one $L_{\rm CII}$-$M_{\rm h}$ model; this fit is used to interpret the impact of the [C II]$_{158\mu m}$ line luminosity scatter on the power spectrum. Data from simulation SIMBA were used to obtain the fit. The scatter is fitted with multiple approaches. One of the ways in which it was done was by using all the individual samples from the scatter data and applying least-squares minimization. The sample numbers were low enough ($\sim$10,000) to allow for an all-sample fit in this case, although it is not a versatile and reliable approach in general. One should resort to binned statistics, especially when dealing with large sample numbers.

The other way of fitting is to use binned data. In this case, halo mass bins at a logarithmic interval of ~ 0.17 dex is chosen. Binned statistics such as the arithmetic mean and mode within each halo bin were estimated. To make the results more statistically significant, it is ensured that at least 200 samples are present from the lower and higher ends of the halo-mass bins. The halo bins with insufficient samples are removed from the analysis (gray dots, figure 4.1). The least-squares minimization method is applied

[1] https://kpolsen.github.io/SIGAME/index.html

Table 4.1: Parameters and reduced chi-square for various fits: Most-probable, mean and all-sample are listed here.

Fits	A	B	χ^2/dof
Most-probable	-4.19 ± 0.76	1.04 ± 0.07	0.15
Mean	-4.53 ± 0.61	1.08 ± 0.06	0.08
All-sample	-3.95 ± 0.07	1.02 ± 0.01	1.14

to the binned values (mean or modes) to obtain the correlation fits. Within the logarithmic halo mass intervals, the arithmetic mean of $L_{\rm CII}$ is estimated, and with these bin values, a mean correlation fit is obtained. Histograms of the $\log L$ distribution (figure 4.2, top panel) have been used for each halo mass bin of interest to evaluate the mode. From each halo-mass bin, the peak of the histogram is identified as the corresponding discretized mode, representing the most likely occurrence of $\log L$ in that bin. These modes are used in a least-squares minimization procedure to obtain the corresponding most-probable fit.

Initially, the scaling relation from Leung et al. 2020 is used to obtain the fits. This is given as

$$\log\left(\frac{L_{\rm [CII]}}{L_\odot}\right) = C + a\log\left(\frac{M_{\rm h}}{M_a}\right) + b\log\left(1+\frac{M_{\rm h}}{M_b}\right), \tag{4.1}$$

which corresponds to a double power law. The parameters for this model are C, a, M_a, b, and M_b. However, given the simulation data that encompasses a particular halo-mass range (10^9–10^{12}), a robust fit is not obtained using the relationship from Leung et al. 2020. The fits obtained are non-convergent, given an initial guess of parameters, and the errors on the parameters are either unrealistically small or large. Instead, a simpler power law model is used, which has only two parameters. It is given as

$$\log\left(\frac{L_{\rm CII}}{L_\odot}\right) = A + B\log\left(\frac{M_{\rm h}}{M_\odot}\right), \tag{4.2}$$

with parameters A and B. Three fits with this model are obtained, and the corresponding parameters are tabulated in Table 4.1. The mean and the most-probable fits are found to be convergent, given an initial guess for parameter values.

In figure 4.3, the halo-mass variation of the scatter parameter is shown. The *green* line shows the average value of the parameter (σ). As mentioned earlier, the dataset from the `SIMBA` simulation consists of three different volumes, and consequently, the scatter parameter might have abrupt variations in the halo bins, where any two individual volumes overlap. Due to this, it is a bit difficult to ascertain the halo-mass versus scatter parameter trend. Nevertheless, within the individual volumes, one might find an overall variation. In the first couple of points, which lie within the smallest volume of the `SIMBA` simulation, one can see the σ increasing. For the intermediate volume, this trend starts to fall off, and towards the end, no trend is seen other than the fluctuations around the mean. Although this might not be the most accurate representation, a general scenario of how there might be

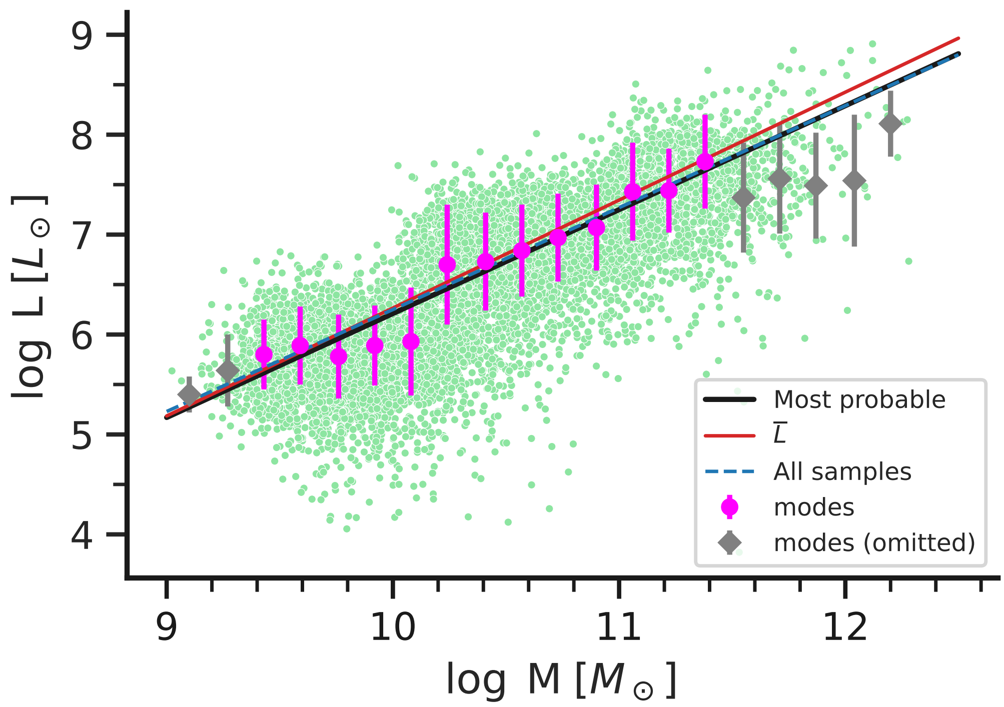

Figure 4.1: L_{CII} vs. M_{halo} scatter from SIMBA simulation is shown here in *green* dots, for $z = 6$. The *magenta* points are the most probable values or *modes* of the L_{CII} distribution in each halo-mass bin. The error bars are representative of the line luminosity scatter in that halo-mass bin. The *black solid, red solid, and blue-dashed* lines represent the fits obtained in this work. The *grey* points are excluded in the fitting analysis due to poor sample numbers.

a halo-mass-dependent variation of statistical properties of the scatter is presented, as inferred from a hydrodynamic simulation. The following section describes the methods for estimating the [C II]$_{158\mu\mathrm{m}}$ LIM power spectrum.

4.3 CII LIM power spectrum with scatter

The simulation volumes in Leung et al. 2020 are not large enough to estimate the [C II]$_{158\mu\mathrm{m}}$ power spectrum with good statistical significance. Furthermore, the number of galaxies in individual volumes is not high enough. To deal with these problems, the scatter generated in the simulation suite of Leung et al. 2020 was reproduced in a N-body (Somnath Bharadwaj and Ali 2004) dark matter-only simulation with a volume of 215^3 Mpc^3. The collapsed halos in the N-body simulation were identified with an FoF algorithm (Rajesh Mondal, Somnath Bharadwaj, Majumdar, et al. 2015), with a halo-mass resolution of $\approx 10^9 M_\odot$. The range of halo-mass in both simulations is similar, which eased this exercise of reproducing the scatter. The distribution of the [C II]$_{158\mu\mathrm{m}}$ luminosity scatter was reproduced using the method described in Section 2.3. The histograms of the reproduced scatter are shown in green

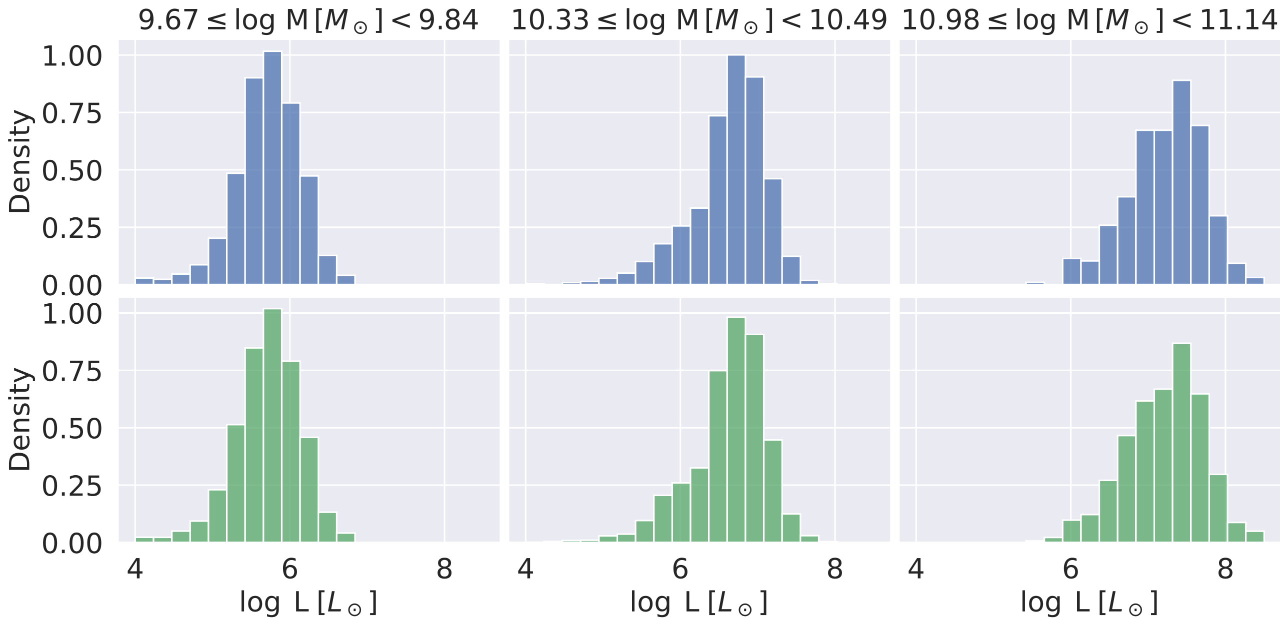

Figure 4.2: *Top*: $L_{[\mathrm{CII}]}$ distribution from `SIMBA` *Bottom*: $L_{[\mathrm{CII}]}$ distribution reproduced in N-body simulation from `SIMBA` data is shown.

in the bottom panels of figure 4.2, corresponding to the method of Equation 2.2. One can see subtle differences between the original histogram (top panels of figure 4.2) and the one reproduced, although they are mostly similar.

Using this method, the actual scatter distribution present in the original simulation by Leung et al. 2020 was reproduced, in the N-body simulation. 1000 different realizations of such scatter distributions were also generated, and eventually that many number of [C II]$_{158\mu\mathrm{m}}$ intensity maps were also developed. Figure 4.4 represents a snapshot of one such realization map. Finally, the power spectra were computed for each of these intensity maps and averaged over, for the case with L_{CII} scatter. The spatial distribution of the [C II]$_{158\mu m}$ line emitters in the N-body simulation volume is directly sampled to estimate the power spectrum.

4.4 Results

4.4.1 Intensity of the CII LIM signal

The mean intensity of the LIM signal is estimated with and without scatter. The no-scatter LIM maps are generated by painting the halos with correlation functions obtained from different fitting approaches. The results are tabulated in Table 4.2. There is an enhancement of 1.7 in the mean intensity of the LIM signal with scatter compared to the most probable fit. For a given halo-mass bin, the

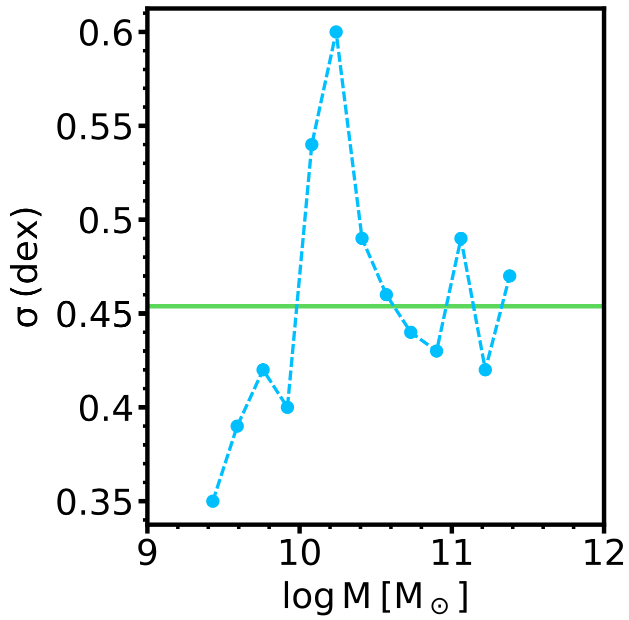

Figure 4.3: Fluctuations in scatter parameter (σ) for the [C II]$_{158\mu\mathrm{m}}$ luminosity is shown across halo-mass bins. The horizontal *green* line is the average value of the scatter parameter (σ_{avg}).

Table 4.2: Mean intensities for each of the following specific cases at $z = 6$ is tabulated.

Case	Mean Intensity (10^2 Jy/sr)
Scatter	5.25
Most probable fit	3.07
Mean fit	3.55
All sample fit	3.45

average luminosity with log scatter is

$$\langle L\rangle = \int_{-\infty}^{\infty} \mathrm{d}(\log L) L \times \frac{1}{\sqrt{2\pi}\sigma} \exp\left[-\frac{(\log L - \log \hat{L})^2}{2\sigma^2}\right], \tag{4.3}$$

which one can rewrite as

$$\frac{\langle L(\sigma)\rangle}{\langle L_{\sigma=0}\rangle} = \int_{-\infty}^{\infty} \mathrm{d}x \frac{10^{\sqrt{2}\sigma x}}{\sqrt{\pi}} \exp\left(-x^2\right) = 10^{\sigma^2 \ln(10)/2} \tag{4.4}$$

(see Moradinezhad Dizgah and Keating 2019b), with $\langle L_{\sigma=0}\rangle = \hat{L}$ being the average of L for $\sigma = 0$ (no scatter), and $\hat{L}$ is the average of L in log-space. It is found that the average σ for the halo-mass bins considered in the fitting, from the SIMBA + SIGMAE results, is 0.45 dex which, when put in Equation 4.4, yields an approximate enhancement factor in the mean intensity of ~ 1.7, in agreement with our simulation result. Therefore, using this simple model, one can interpret the mean intensity of the [C II]$_{158\mu\mathrm{m}}$ maps with log-normal line luminosity scatter.

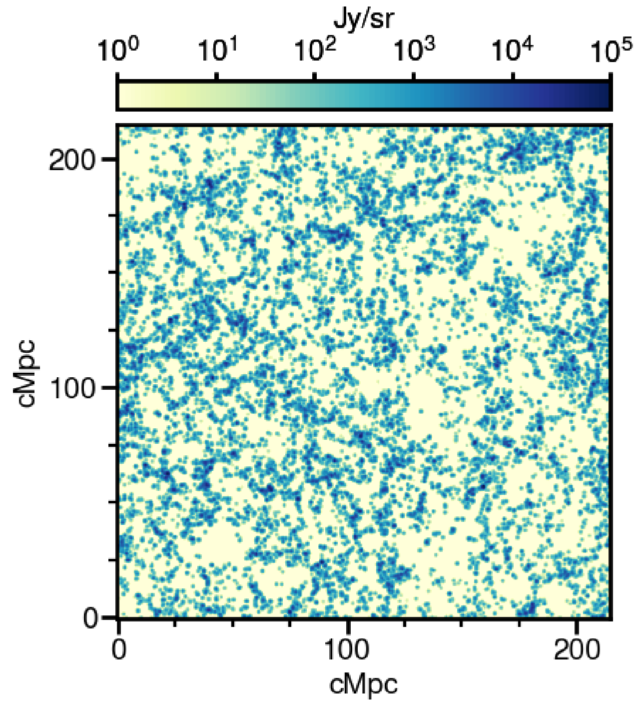

Figure 4.4: A snapshot of the [C II]$_{158\mu\text{m}}$ intensity map with line luminosity scatter at $z = 6$.

If the scatter were implemented with a semi-analytic model, one might have expected the mean intensity to remain preserved compared to this mean fit (see appendix A). However, it is not straightforward in the presence of non-uniform scatter. In this case, the mean intensity changes by ~ 48 percent compared to the mean correlation fit. This change is difficult to interpret and model. A change of ~ 52 percent in the mean intensity is obtained with the all-samples fit. However, the drawback of using this fit is that it lacks statistical interpretation, unlike the others. Moreover, as mentioned earlier, this fit is not expected to be versatile (e.g., for large sample numbers) and reliable, especially since it lacks an underlying statistical model.

4.4.2 CII power spectrum

The dimensionless power spectrum $\Delta^2(k) = k^3P(k)/2\pi^2$ is shown in figure. 4.5. The large-scale power spectrum with line luminosity scatter is enhanced by a factor of $2.3 - 2.1$, compared to the most probable fit. However, since the clustering power spectrum is expected to go as

$$P^{\text{clus}}_{\text{CII}}(k, z) \propto \langle I_{\text{CII}}(z)\rangle^2 \langle b_{\text{CII}}(z)\rangle^2, \tag{4.5}$$

with $\langle I_{\text{CII}}\rangle^2$ and $\langle b_{\text{CII}}\rangle^2$ being the mean [C II]$_{158\mu\text{m}}$ intensity and bias, one should have expected an enhancement close to $1.7^2 \approx 2.9$. In subsection 4.4.3, this discrepancy is attempted to be reconciled.

It is seen that the impact of the scatter on the power spectrum (figure 4.5) for the mean and most-

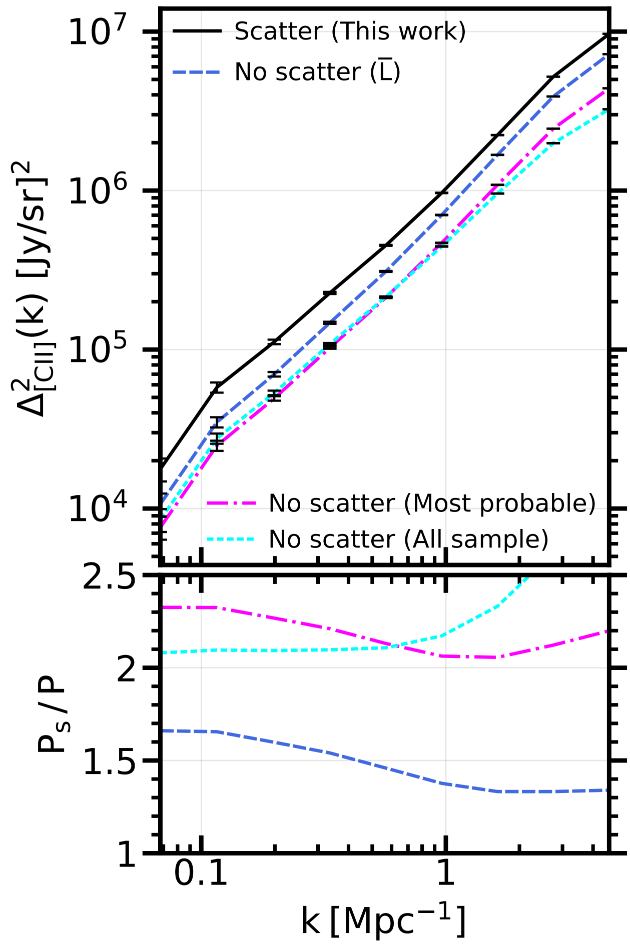

Figure 4.5: *Top*: [C II]$_{158\mu m}$ power spectrum at $z = 6$ with and without L_{CII} scatter. *Bottom*: The ratio of the power spectrum with scatter compared to the no-scatter case is shown.

probable fits varies in a fashion which is different from what would be the case for scatter implemented with a semi-analytic approach. For reference, the impact of scatter when implemented using a semi-analytic method, as in Equation A.1, is shown in figure 4.6. The model of Equation 4.2 with a $\sigma = 0.45$ is used. Within the range of k-modes explored (0.1 to 4 Mpc^{-1}), it is seen that the impact is initially almost constant, but then starts to rise rapidly afterward. The enhancement in the clustering power spectrum at low k-modes is less than the shot-noise power at large k-modes. It can be modeled with

$$f_{n,\sigma} = \int_{-\infty}^{\infty} dx \frac{10^{\sqrt{2}n\sigma x}}{\sqrt{\pi}} \exp\left(-x^2\right) = 10^{n^2\sigma^2 \ln(10)/2} \tag{4.6}$$

(Moradinezhad Dizgah and Keating 2019b). $f^2_{1,\sigma}$ represents the enhancement in the clustering power spectrum, while $f_{2,\sigma}$ is the enhancement in the shot-noise component. However, this well-behaved enhancement for non-uniform scatter within the k-mode range explored is not obtained, which has varying scatter strength for halo-mass bins, in contrast to the semi-analytic case. The impact of shot-noise

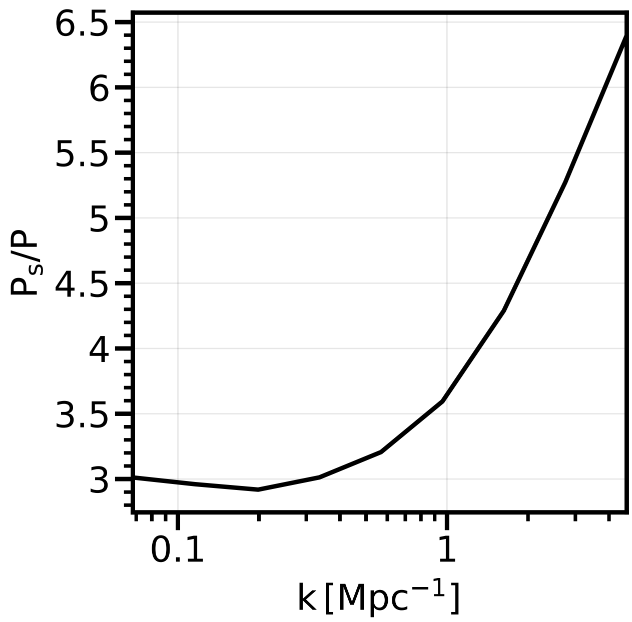

Figure 4.6: The impact of semi-analytic scatter on the power spectrum using model 4.2 and parameters from the most-probable fit is shown here.

might dominate beyond the k-range probed here for these cases. The impact on the power spectrum behaves similarly to the semi-analytic case for the all-sample fit. However, the fit is not expected to be versatile and reliable.

4.4.3 Luminosity-weighted halo bias

A plausible reason for the slight mismatch in power spectrum enhancement is the slight diminishing of the luminosity bias under non-uniform line luminosity scatter. From Equation 4.5, one can follow that this decrement will suppress the maximum enhancement in the clustering power. The linear [C II]$_{158\mu\mathrm{m}}$ luminosity bias can be written as

$$\langle b_{\mathrm{CII}}(z)\rangle = \frac{\int \mathrm{d}M \frac{\mathrm{d}n}{\mathrm{d}M} L_{\mathrm{CII}}(M,z) b(M,z)}{\int \mathrm{d}M \frac{\mathrm{d}n}{\mathrm{d}M} L_{\mathrm{CII}}(M,z)}, \tag{4.7}$$

with $b(M,z)$ being the halo bias. When there is a non-uniform scatter, the binned average luminosity has stochastic fluctuations across halo-mass bins and does not follow any correlation function tightly (see appendix A). It can thus introduce an overall decorrelation between the luminosity and the halo bias across the halo-mass bins and, therefore, decrease the luminosity-weighted halo bias slightly. The luminosity bias is estimated using the relation

$$P_{\delta_{\rho_L}\delta_{\rho_L}}(k,z) = b_{\mathrm{L}}^2(k,z) P_{\delta\delta}(k,z), \tag{4.8}$$

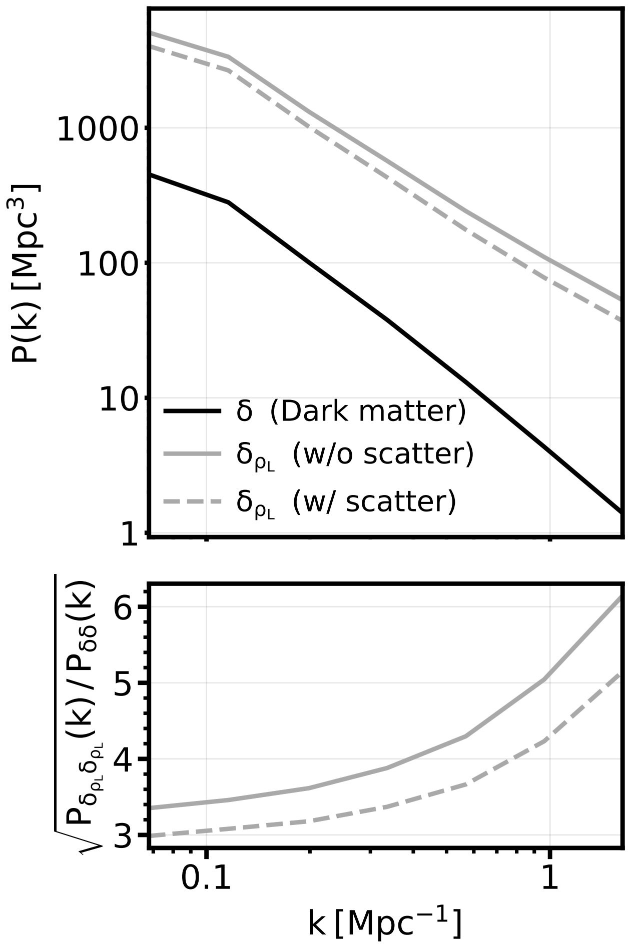

Figure 4.7: *Top panel*: Dark matter and luminosity fluctuations are shown for $z = 6$. *Bottom panel*: The estimated luminosity bias is shown.

to test this. Here, the δ_{ρ_L} represents fluctuations in the luminosity density defined as $\rho_L = \overline{\rho}_L(1+\delta_{\rho_L})$. $P_{\delta_{\rho_L}\delta_{\rho_L}}$ and $P_{\delta\delta}$ represent the power spectrum for the fluctuations corresponding to luminosity and dark matter. $b_{\rm L}$ is the luminosity bias. Figure 4.7 shows the power spectrum for dark matter and luminosity fluctuations, corresponding to the scatter and no-scatter case. The corresponding bias is shown in the bottom panel, and a change of around $\sim 16 - 11$ percent is seen. Although this is not a very large and statistically significant change, it remains a possibility. Further studies are required to confirm this effect. When this is reconciled with the power spectrum, it matches the enhancement factor within $2.3 - 2.1$.

4.5 Summary

The impact of line luminosity scatter on the [C II]$_{158\mu\rm m}$ LIM power spectrum has been revisited in this study. line luminosity scatter from a hydrodynamic simulation is considered, which differs from a simple semi-analytic one in its non-uniform nature (variation of statistical properties across halo-mass bins). Under this scenario, the robustness of various correlation fits has been tested, which can meaningfully interpret the impact of line luminosity scatter. A simple power law model has been used to fit the [C II]$_{158\mu\mathrm{m}}$ line luminosity scatter. The mean intensity for the all-sample fit differs from the scatter case by 52 percent. However, the fit obtained is not expected to be versatile and reliable, since it lacks a meaningful statistical interpretation. It is found that the mean correlation fit produces a mean intensity, which deviates from the scatter one by a large margin (48 percent), although this should not be the case if one deals with semi-analytic scatter (see appendix A). Therefore, modeling the power spectrum with this fit becomes unreliable under non-uniform scatter. However, it is found that the approach presented by (Moradinezhad Dizgah and Keating 2019b) (recognized here as the most-probable fit) provides a robust interpretation of the mean intensity (Equation 4.4) and power spectrum, even under the generalized and realistic non-uniform line luminosity scatter. This work demonstrates one example that the most-probable fit might be the most reliable way to interpret the impact of line luminosity scatter on the LIM signal statistics (e.g., mean intensity and power spectrum) compared to the other correlation fits considered.

Chapter 5

Impact of astrophysical scatter on the Epoch of Reionization HI 21cm bispectrum

---

This chapter has been adapted from: **Murmu, C. S.**, Datta, K. K., Majumdar, S., & Greve, T. R. (2024). Impact of astrophysical scatter on the epoch of reionization [H I] 21cm bispectrum. *Journal of Cosmology and Astroparticle Physics*, 2024(08), 032, DOI: 10.1088/1475-7516/2024/08/032, arXiv: 2311.17062

5.1 Introduction

Modeling observable summary statistics for line-intensity mapping (LIM) signal is one of the key steps to understand the poorly constrained epoch of reionization (EoR). Line emissions from either the IGM or the galaxies provide us the opportunity to map the Universe and its cosmic evolution. The LIM signal corresponding to the redshifted $[\mathrm{H\,I}]_{21\mathrm{cm}}$ emissions from the diffuse IGM (Wouthuysen 1952; Field 1958; Madau, Meiksin, and Rees 1997) has been proposed as an excellent probe to track the epoch of reionization. On the other hand, independent and complementary probes using bright line emissions from the galaxies such as $[\mathrm{C\,II}]_{158\mu\mathrm{m}}$ (Gong, Cooray, M. Silva, et al. 2012; M. Silva et al. 2015; Padmanabhan 2019; Yue and Ferrara 2019; Murmu, Majumdar, and Datta 2021; Murmu, Raghunath Ghara, et al. 2022; Karoumpis et al. 2022), CO (Lidz, Furlanetto, et al. 2011; T. Y. Li et al. 2016; Yang et al. 2022; Moradinezhad Dizgah, Bellini, and Keating 2024; Roy et al. 2023), Ly-α (Peterson and Suarez 2012; M. B. Silva et al. 2013; Pullen, Doré, and J. Bock 2014; Mas-Ribas and Tzu-Ching Chang 2020), $[\mathrm{O\,III}]_{88\mu\mathrm{m}}$ (Padmanabhan 2023) etc. have also been proposed for studying the EoR. In that process, one can use suitable summary statistics to infer useful astrophysical and cosmological information from these LIM probes. Fourier-based statistics, such as the power spectrum, provide information on signal fluctuations at different length scales. Higher-order statistics, such as the [H

I]$_{21\mathrm{cm}}$ bispectrum, can reveal non-Gaussian features present in the signal at multiple length scales.

These statistics are sensitive to various phenomena such as source properties, star formation rate, line-of-sight effects, astrophysical processes of line emissions, etc. Appropriate inferences of various information require these signal statistics to be modeled accurately. One of the usual approaches in this modeling is to connect the galaxy line emissions to their host halo mass using various scaling relations and predict LIM signals. This approach offers flexibility in simulating LIM signals at large (cosmological) scales relatively quickly, as opposed to more accurate hydro-simulations. Normally, these models assume a one-to-one correspondence between the host halo mass and the line luminosity of interest (Gong, X. Chen, et al. 2011; Lidz, Furlanetto, et al. 2011; M. B. Silva et al. 2013; Breysse, E. D. Kovetz, and Kamionkowski 2014; Pullen, Doré, and J. Bock 2014). However, in reality, the line luminosity from galaxies can vary due to various astrophysical reasons even if the host halo mass is similar. This affects the summary statistics. The effect of this astrophysical scatter has been explored in the context of galaxy LIM signals, which is shown to enhance the power spectrum at small scales (T. Y. Li et al. 2016; Schaan and White 2021; Yang et al. 2022). A more generalized non-uniform line luminosity scatter affects the large-scale power spectrum as well (Moradinezhad Dizgah, Nikakhtar, et al. 2022; Murmu, Olsen, et al. 2023).

A similar effect of astrophysical scatter can also be present in the star-formation rates (SFR) of reionizing galaxies. There can be variations in the SFR, even if the host halo mass of a given galaxy is similar. Assuming that the emission rate of ionizing photons from the galaxies is correlated with their SFR, the halo-to-halo scatter in the SFR will affect the number distribution of UV ionizing photons emitted. These photons, in turn, ionize the neutral IGM, and therefore, the scatter would leave imprints on the ionization fluctuations. Consequently, it will affect the cosmological [H I]$_{21\mathrm{cm}}$ signal emerging from the IGM during the EoR. A study by Hassan et al. 2022 explored the role of this astrophysical scatter for the first time in the context of cosmic reionization, using the ionization power spectrum. It was found that the ionization power spectra are mostly unaffected by the presence of scatter. However, the role of this scatter is not well investigated in the context of the observable [H I]$_{21\mathrm{cm}}$ signal from the EoR. This signal is known to have non-Gaussian features, and the astrophysical scatter might introduce additional non-Gaussianity, which the power spectrum might not capture adequately. On the other hand, one-point statistics such as skewness and kurtosis can capture non-Gaussian signatures in the [H I]$_{21\mathrm{cm}}$ signal at a particular length scale (Harker et al. 2009; Shimabukuro et al. 2015; C. A. Watkinson and J. R. Pritchard 2014; C. A. Watkinson and J. R. Pritchard 2015; Kubota et al. 2016; Ross et al. 2021). However, these one-point statistics cannot capture the correlation between multiple-length scales. To characterize the presence of non-Gaussianity in the correlation between different length scales, one needs to resort to higher-order Fourier statistics, such as the bispectrum.

The bispectrum is the 3-pt correlation function in Fourier space and correlates three different $\boldsymbol{k}$ vectors, which form a closed loop in the Fourier domain. Therefore, different triangle configurations of the $\boldsymbol{k}$ vectors can capture the correlation between different length scales, which the power spectrum fails to do. The [H I]$_{21\text{cm}}$ signal bispectrum is sensitive to non-Gaussian features in the signal and, suitable for analyzing features. Studies by Majumdar, Jonathan R. Pritchard, et al. 2018; Majumdar, Kamran, et al. 2020; Hutter, Catherine A. Watkinson, et al. 2020; Gill et al. 2024; Raste et al. 2024 have demonstrated that the [H I]$_{21\text{cm}}$ signal bispectrum can characterize the features of non-Gaussianity and topology, which otherwise would be difficult to do with the power spectrum.

In this work, the impact of the astrophysical scatter on the [H I]$_{21\text{cm}}$ bispectrum is investigated. Since the variation in the SFR for a given host halo mass is stochastic, multiple independent realizations of the [H I]$_{21\text{cm}}$ maps are simulated, at a fixed neutral fraction, by varying the seed of the randomness for the scatter. This is useful in quantifying the statistical significance of the changes in the bispectrum when astrophysical scatter is taken into account. The bispectrum for all unique triangle configurations is estimated and for an extensive range of length scales (k_1 values). The length scales and regions of the [H I]$_{21\text{cm}}$ bispectrum configuration space that are sensitive to the changes introduced by the astrophysical scatter are investigated. These changes are also compared with the changes in the power spectrum, which is also computed for the [H I]$_{21\text{cm}}$ maps with scatter. Finally, the possibility of detecting the bispectrum, at length scales where the changes due to astrophysical scatter are found to be significant is explored, considering the planned SKA1-Low baseline configurations and for various observational scenarios. Throughout this work, the cosmological parameters that have been adopted are $\Omega_\text{m} = 0.3183, \Omega_\Lambda = 0.6817, h = 0.6704, \Omega_\text{b}h^2 = 0.022032, \sigma_8 = 0.8347, n_\text{s} = 0.9619$, consistent with Planck+WP best-fit values (Planck Collaboration, Ade, P. A. R., et al. 2014).

5.2 Astrophysical scatter

The typical approach for modeling ionizing-photon emission from the galaxies is to model their star-formation rates. This is a reasonable approach because star-forming galaxies mainly drive the reionization process. A simple way to model the galaxy SFR is to relate it to the host halo mass. It has been used primarily in the [H I]$_{21\text{cm}}$ literature to model the reionization process. If we assume N_γ to be the total number of ionizing photons deposited in the IGM from the instantaneous star formation in a galaxy, then a common model is to assume $N_\gamma \propto M_\text{h}^\alpha$. Here, the star formation rate is modeled as a power law of the halo mass, with α being the power law index. Other variants of this model can be a complicated function of the halo mass, usually with different power laws at different mass ranges with multiple parameters. We have used one such model in this work, given in Equation 2.1.

However, the stochasticity in these SFR models is usually left out while modeling the cosmic reionization of the IGM and the emanating [H I]$_{21\text{cm}}$ signal. Observationally, it is found that the SFR of galaxies obeys a tight correlation with the stellar mass. Speagle et al. 2014 compile data from earlier works (Daddi, Dickinson, et al. 2007; Noeske et al. 2007; G. E. Magdis et al. 2010; Whitaker et al. 2012), which used different methods to determine the main-sequence (MS) relation and its dispersion. These were brought to a standard calibration by Speagle et al. 2014 to obtain the relation between

$\log\psi$ – $\log M_\star$ and the dispersion around it, with ψ being the SFR and $M_\star$ being the stellar mass of the galaxy. For details, interested readers are referred to Speagle et al. 2014. They find that the true intrinsic scatter is around 0.2 dexes, with 0.3 dexes being the upper limit considering observational uncertainties.

Various analytical modeling and numerical simulations have studied the origin of this dispersion in the relation. It is understood that the main driver for this scatter is the varying mass accretion history over time (Dutton, van den Bosch, and Dekel 2010; Peng and Maiolino 2014; Matthee and Schaye 2019; Blank et al. 2021), which occurs over longer time scales. Shorter time-scale variabilities, such as short time-scale variabilities in the gas accretion rate, and different feedback mechanisms also contribute and are essential for lower-mass galaxies. Various numerical simulations have reproduced the dispersion in the main sequence within a similar range of $0.2-0.3$ dexes (Lagos et al. 2018; Matthee and Schaye 2019; Blank et al. 2021). Therefore, the fiducial value of $\sigma = 0.3$ is adopted, as described in Section 5.4. It is assumed that this scatter also applies to the high-redshift Universe and that the stellar mass follows a tight correlation with the underlying dark-matter (DM) halo mass.

5.3 The HI 21cm bispectrum

The redshifted $[\mathrm{H\,I}]_{21\mathrm{cm}}$ signal arises from the neutral hydrogen atoms (HI) of the Universe via a hyperfine spin-flip transition. It is a promising probe of the IGM and the reionization process as it allows us to track the evolution of the Universe through cosmic time. One of the primary goals is to measure the power spectrum corresponding to the fluctuations in the $[\mathrm{H\,I}]_{21\mathrm{cm}}$ signal. However, it fails to capture all the information in the signal, specifically if the fluctuations in the signal are not Gaussian-random. The reionization process is non-linear, and the nature of the corresponding fluctuations it introduces in the surroundings will be non-Gaussian (Somnath Bharadwaj and Pandey 2005; I. T. Iliev et al. 2006; Mellema, Ilian T. Iliev, Pen, et al. 2006; Rajesh Mondal, Somnath Bharadwaj, Majumdar, et al. 2015). As demonstrated by Mellema, Leon Koopmans, et al. 2015, if we consider a realistic $[\mathrm{H\,I}]_{21\mathrm{cm}}$ map derived from a numerical simulation and an artificial $[\mathrm{H\,I}]_{21\mathrm{cm}}$ map with Gaussian-random fluctuations, the power spectrum might fail to distinguish between these two scenarios.

Given a fixed halo mass, there will be a log-normal distribution in the number of ionizing photons contributed from those haloes of identical masses. This additional source of non-Gaussianity in the number distribution of ionizing photons is expected to affect the spatial distribution of the hydrogen neutral fraction, $x_{\mathrm{HI}}(\boldsymbol{x}, z)$. Keeping the underlying gas density fixed, these induced non-Gaussian fluctuations in $x_{\mathrm{HI}}(\boldsymbol{x}, z)$ will reflect in the differential brightness temperature of the $[\mathrm{H\,I}]_{21\mathrm{cm}}$ signal, $\delta T_{\mathrm{b}}(\boldsymbol{x}, z)$, since $x_{\mathrm{HI}}(\boldsymbol{x}, z) \propto \delta T_{\mathrm{b}}(\boldsymbol{x}, z)$. Therefore, in such a scenario, the power spectrum is not expected to completely capture the impact of scatter on the $[\mathrm{H\,I}]_{21\mathrm{cm}}$ signal, and the bispectrum can be a much more suitable statistic.

5.4 Simulating the HI 21cm maps

A combination of N-body dark-matter only simulation (Somnath Bharadwaj and Ali 2004) and a semi-numerical prescription to model reionization (Tirthankar Roy Choudhury, Haehnelt, and Regan 2009; Majumdar, Mellema, et al. 2014; Rajesh Mondal, Somnath Bharadwaj, and Majumdar 2017) has been used here. The side length of the DM simulation box is 215 Mpc in size, with a total grid number of 3072^3 and a particle number of 1536^3. A FoF algorithm (Rajesh Mondal, Somnath Bharadwaj, Majumdar, et al. 2015) is run to identify collapsed haloes from the dark-matter distribution snapshots, which are assumed to be the sources of ionizing photons. The emission of ionizing photons is modeled as being proportional to the SFR for a given halo. To introduce scatter, a log-normal distribution for the SFR is assumed and implemented as follows:

$$\log \mathrm{SFR}^{\mathrm{scatter}} = \left(\log \overline{\mathrm{SFR}} - \frac{1}{2}\sigma^2 \ln(10) \right) + \mathcal{N}(0, \sigma^2), \tag{5.1}$$

with $\mathcal{N}(0, \sigma^2)$ being the normal distribution with zero mean and standard deviation σ. Therefore $\mathrm{SFR}_{\mathrm{scatter}}$ has a spread of σ dex across the halo mass range. The value of σ is fixed to 0.3 dex for the entire exercise. The number of ionizing photons emitted in the scatter scenario from a given halo is then $N_\gamma^{\mathrm{scatter}} \propto \mathrm{SFR}^{\mathrm{scatter}}$.

The reionization process is simulated over a coarse-gridded box of 384^3 grids, resulting in a grid resolution of 0.56 Mpc. $[\mathrm{H\,I}]_{21\mathrm{cm}}$ maps are generated using excursion set formalism (Furlanetto, Zaldarriaga, and Hernquist 2004), and as described in Section 2.2. This semi-numerical approach of simulating the reionization does not consider density-dependent recombination and we also note that this model is not photon conserving (Tirthankar Roy Choudhury and Paranjape 2018). The impact of photon conservation on the $[\mathrm{H\,I}]_{21\mathrm{cm}}$ bispectrum has not been studied. However, it has been shown that photon conservation boosts the $[\mathrm{H\,I}]_{21\mathrm{cm}}$ power spectrum in all scales (without significant change in its shape) and results in a comparatively rapid reionization (Tirthankar Roy Choudhury and Paranjape 2018). The density-dependent recombination is expected to introduce an additional scatter in the $[\mathrm{H\,I}]_{21\mathrm{cm}}$ signal topology. Both of these may have a significant impact on the $[\mathrm{H\,I}]_{21\mathrm{cm}}$ bispectrum but their study is beyond the scope of this work. This investigation can be followed up in future work.

The $[\mathrm{H\,I}]_{21\mathrm{cm}}$ maps are generated across an extensive neutral fraction range of $\langle x_{\mathrm{HI}} \rangle$ = [0.53, 0.62, 0.72, 0.81, 0.9, 0.95] at $z = 7.4$. As argued by Hassan et al. 2022, the presence of ionized bubbles of sufficient size and a significant number will wash away any signatures of scatter. Therefore at high neutral fractions, any signatures of the scatter are investigated as captured by the bispectrum. Since scatter will impact only the $x_{\mathrm{HI}}(\boldsymbol{x}, z)$ field and non-Gaussianity contributions come from $\delta_{\mathrm{H}}(\boldsymbol{x}, z)$ as well, we fix the redshift for all the neutral fractions to exclusively study the impact of scatter on the bispectrum by removing the contribution of $\delta_{\mathrm{H}}(\boldsymbol{x}, z)$ to non-Gaussian features. We have simulated ~ 50 statistically independent realizations of $[\mathrm{H\,I}]_{21\mathrm{cm}}$ maps by using ~ 50 different seeds of randomness for the scatter at $z = 7.4$ for each of the six neutral fractions to estimate the bispectrum. According to the latest results of Planck 2018 Planck Collaboration, Aghanim, Akrami, Ashdown, et al. 2020, the constraint on the mid-point of reionization is $z_{\rm reion} = 7.68 \pm 0.79$ (Equation 18 of Planck Collaboration, Aghanim, Akrami, Ashdown, et al. 2020) under the assumption of a reionization history that follows a tanh model. Given the uncertainty on the value $z_{\rm reion}$, it may be possible to have large neutral fraction values at $z = 7.4$, as explored in this study. Nevertheless, a different scenario is also considered where the neutral fraction is $\langle x_{\rm HI} \rangle \approx 0.8$ at a higher redshift of $z = 10$, which can be safely regarded as consistent with the Planck 2018 constraints. In this case, we also use the same set of ~ 50 random seeds to generate multiple realizations of the scatter scenario and estimate the impact of the astrophysical scatter and its corresponding statistical significance. Therefore a total of ~ 350 simulations of the [H I]$_{21\rm cm}$ maps combining all scenarios were done, which consumed a significant amount of computational time. It will affect how much ionizing flux a given halo will generate under this stochastic model from realization to realization. It helps to asses any given statistic's variance under the scatter model across the realizations.

5.5 Results

A direct estimator of the bispectrum has been used here as described in Rajesh Mondal, Mellema, et al. 2021. The bispectrum is estimated at a fixed neutral fraction for each realization and then averaged over all realizations. This exercise is repeated for all the neutral fractions considered in this study. $\langle B_{\rm scatter} \rangle$ represents the mean bispectrum estimated from all realizations of [H I]$_{21\rm cm}$ maps with astrophysical scatter, for a given neutral fraction. The impact of astrophysical scatter is quantified by calculating $\langle \Delta B \rangle = \langle B_{\rm scatter} \rangle - B_{\rm no-scatter}$ and the modulus of the ratio between $\langle \Delta B \rangle$ and $B_{\rm no-scatter}$, i.e. $|\langle \Delta B \rangle / B_{\rm no-scatter}|$, where $B_{\rm no-scatter}$ is the bispectrum of the [H I]$_{21\rm cm}$ map without any scatter. This tells how much the bispectrum, averaged over multiple realizations of astrophysical scatter, deviates from the original bispectrum without the impact of scatter. In figure 5.1, the averaged bispectrum (averaged over 50 statistically independent realizations of the scatter at each neutral fraction) is shown for the [H I]$_{21\rm cm}$ maps with scatter. The mean neutral fraction is fixed along the row (labeled on the left), and the k_1 value (mentioned on the top) is fixed along the column. Since the k_1 value changes along the row, plots along a row reflect the effect due to the changing size of the bispectrum triangle configuration. The shape of the configuration is parametrized by $\cos\theta$ and k_2/k_1 ratio for a given k_1. Therefore, k_1 represents the overall length scales over which the correlation occurs between the different $\boldsymbol{k}$ vectors. The results on the impact of scatter on the bispectrum are presented in Subsection 5.5.1. In Subsection 5.5.2, it is discussed on what scales the impact on the [H I]$_{21\rm cm}$ bispectrum is sufficiently high in magnitude and statistically significant. In subsection 5.5.4, the impact of scatter on the power spectrum, which is a more common statistic, is compared to that on the [H I]$_{21\rm cm}$ bispectrum. Finally, various scenarios are explored for detecting the equilateral [H I]$_{21\rm cm}$ bispectrum, which is one of the

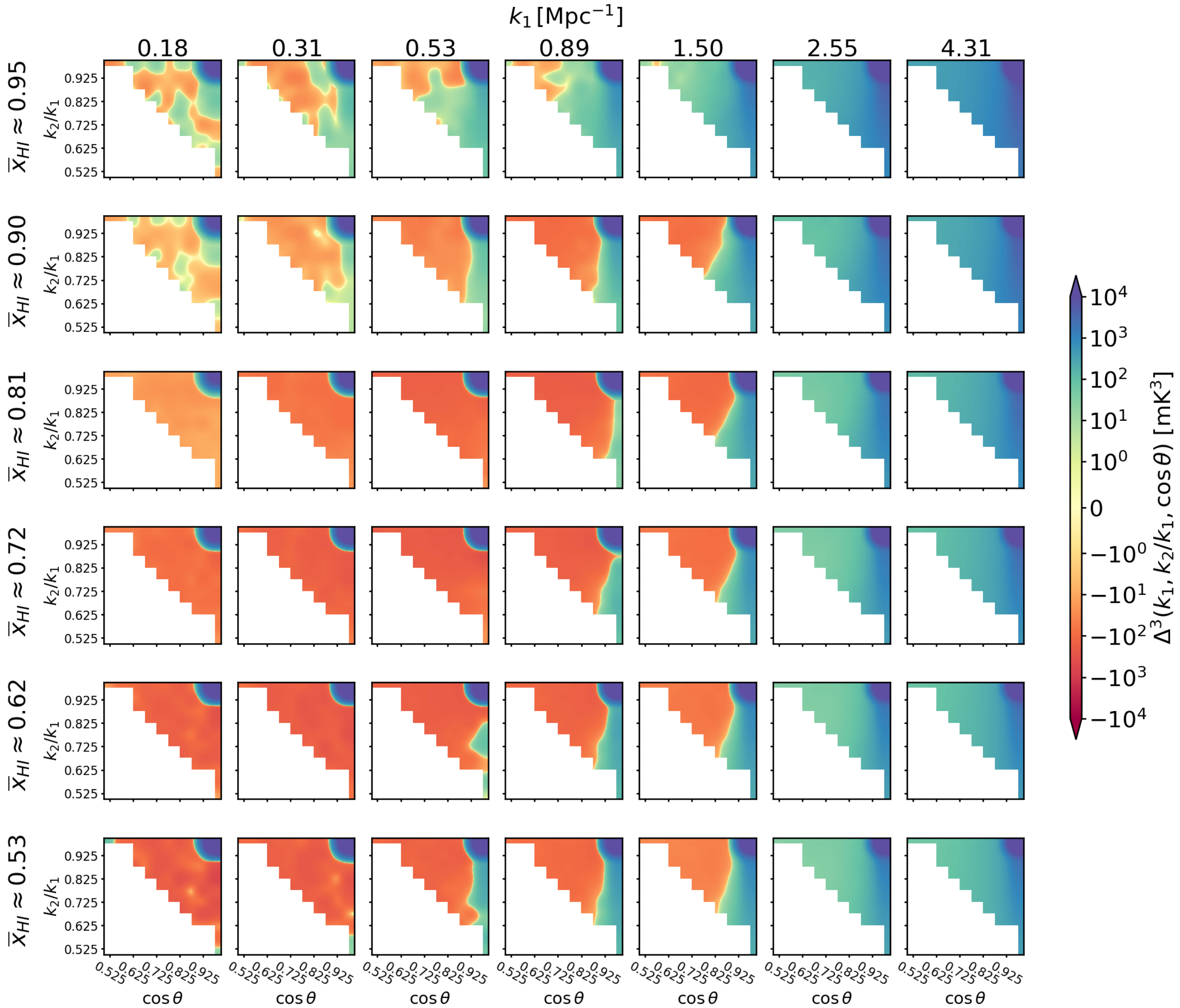

Figure 5.1: This figure shows the [H I]$_{21\mathrm{cm}}$ auto-bispectrum for all unique triangle configurations and averaged over all realizations of astrophysical scatter at $z = 7.4$. This is shown for the full set of neutral fraction range that has been considered here.

triangle configurations expected to capture the signatures of scatter, with the planned SKA1-Low, in subsection 5.5.5.

5.5.1 Impact of scatter on the bispectrum for all unique triangles

The results on the impact of scatter on the [H I]$_{21\mathrm{cm}}$ bispectrum are presented in figure 5.2. The labels in figure 5.2 are identical to those of figure 5.1. The quantity plotted in figure 5.2 is the ratio, $|\langle \Delta B \rangle / B_{\mathrm{no-scatter}}|$, which quantifies the deviation in bispectrum arising from the astrophysical scatter being taken into account in our reionization model. It is seen that across the extensive range of length scales investigated (k_1 values), the impact due to the scatter varies within a large dynamic range of magnitude. The regions of the bispectrum configuration space where the impact is seen to be high in magnitude are randomly spread for $k_1 \lesssim 1.5$ Mpc^{-1}, without any consistent pattern. Here, one can suspect that these random patterns arise mostly due to the statistical variance of the astrophysical scatter in the bispectrum. The magnitude of the impact can be more than a factor of 10 as well for some of the bispectrum triangle configurations. However, as quantified in the following subsection, most of the changes are not statistically significant for k_1 modes up to 1.5 Mpc^{-1} and can vary substantially from realizations to realizations.

At scales $k_1 \sim 2.55$ Mpc^{-1}, it is seen that most of the $\cos\theta$ - k_2/k_1 bispectrum configuration space is sensitive to the astrophysical scatter, and these additional changes follow a consistent pattern across all the neutral fractions, unlike the intermediate and large scales. The ratio $|\langle \Delta B \rangle / B_{\text{no-scatter}}|$ is ~ 0.2 at $\langle x_{\text{HI}} \rangle \approx 0.53$, for a significant region of the bispectrum configuration space. At $\langle x_{\text{HI}} \rangle \approx 0.81$, the ratio goes up to ~ 1, which then declines to $0.2 \lesssim |\langle \Delta B \rangle / B_{\text{no-scatter}}| \lesssim 1.0$ again at $\langle x_{\text{HI}} \rangle \approx 0.95$. The region of the $\cos\theta$ - k_2/k_1 configuration space sensitive to the signatures of astrophysical scatter gradually grows, as we go to higher neutral fractions, and saturation appears at the highest neutral fraction, where the magnitude of the impact is more uniform. In this case, at $\langle x_{\text{HI}} \rangle > 0.8$, enough number of ionized bubbles might not have been formed in the [H I]$_{\text{21cm}}$ maps that would reflect the signatures of astrophysical scatter. In the next subsection (subsection 5.5.2) and figure 5.6, it is argued that the signatures of astrophysical scatter stem from the variations in sizes of small ionized bubbles across the multiple realizations. At higher neutral fractions, a lack of sufficient ionized bubbles will reduce the signatures of astrophysical scatter as compared to the lower neutral fractions. Therefore, the impact is seen to peak somewhere at an intermediate neutral fraction.

The impact of the scatter at $z = 10$ is also estimated assuming $\langle x_{\text{HI}} \rangle \approx 0.8$, which is shown in figure 5.3. Similar to the case at $z = 7.4$, it is found that the impact of scatter is significantly high at $k_1 \sim 2.55$ Mpc^{-1}. At $z = 10$, the magnitude of the impact is much higher compared to that at $z = 7.4$ for the same neutral fraction. At higher redshifts, one should expect the number of ionizing sources to be lesser than that at lower redshifts. This means that the number of ionized bubbles will also be less at higher redshifts, and therefore slightly larger than at lower redshifts when compared at the same neutral fraction. This causes the impact of scatter to be more prominent at higher redshifts.

5.5.2 Statistical significance

Since the astrophysical scatter is a stochastic phenomenon, any statistic used to quantify the impact due to scatter will have an associated variance arising from the stochasticity. Thus, it is important to investigate the statistical significance of the impact of the astrophysical scatter discussed in the previous subsection 5.5.1 and figure 5.2. The realization-to-realization variance arising from the astrophysical scatter is estimated for the bispectrum as $\sigma^2_{\Delta B} = \sum_{\text{R}} (\Delta B_{\text{R}} - \langle \Delta B \rangle)^2 / N$, with $N = 50$ being the number of independent realizations of the scatter. $\Delta B_{\text{R}} = B_{\text{R}} - B_{\text{no-scatter}}$ represents the deviation in the

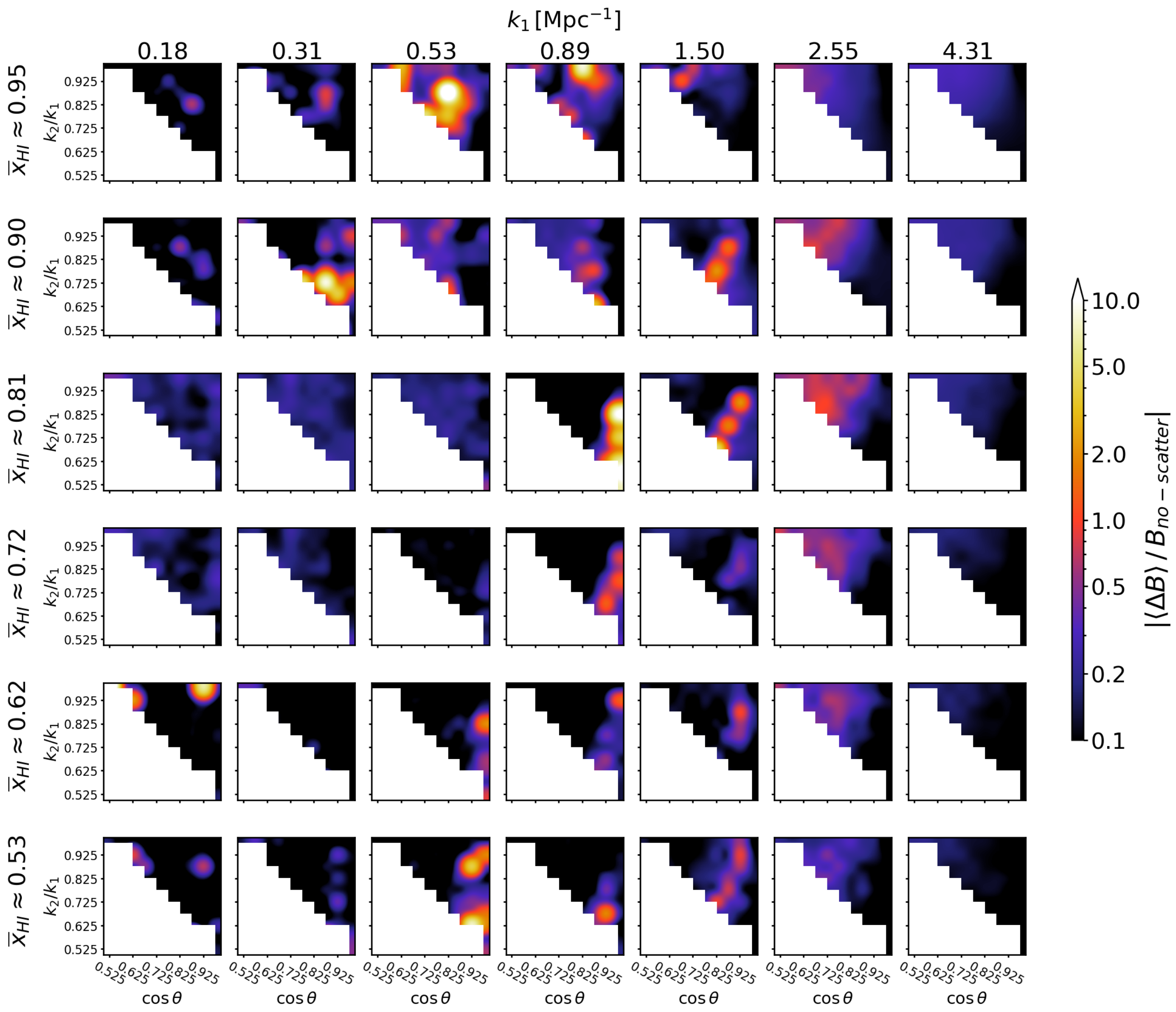

Figure 5.2: Impact on bispectrum due to the astrophysical scatter is shown here at $z = 7.4$. The rows represent the average neutral fractions for a given averaged realization. The columns represent k_1 modes for the bispectrum. The color bar scale represent the change ($\langle B \rangle$) compared to the bispectrum for the no-scatter case ($B_{\text{no-scatter}}$).

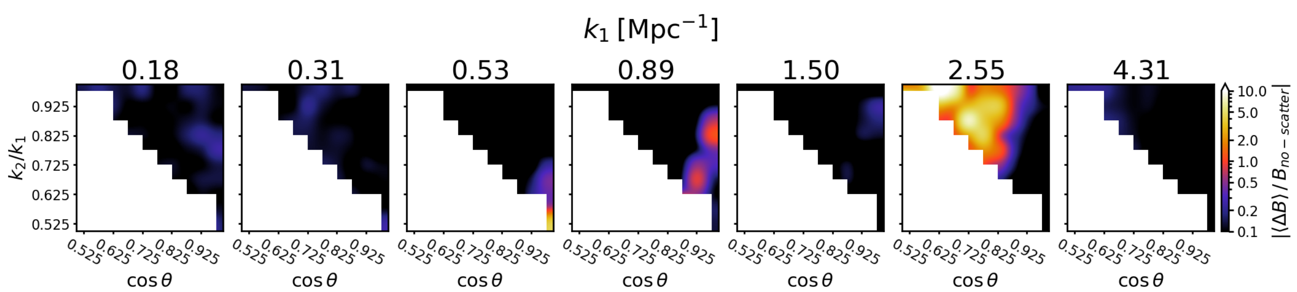

Figure 5.3: This figure shows the impact of astrophysical scatter for the case at $z = 10$ and $\langle x_{\text{HI}} \rangle \approx 0.8$.

bispectrum for a single realization, arising from the astrophysical scatter, compared to the bispectrum without the impact of the scatter, at a fixed neutral fraction. The quantity $|\langle \Delta B \rangle / \sigma_{\Delta B}|$ is used to estimate the statistical significance of the impact of the scatter.

In figure 5.4, it is seen that at large and intermediate scales up to $k_1 \lesssim 1$ Mpc^{-1}, $|\langle \Delta B \rangle / \sigma_{\Delta B}| \sim 1$, meaning that the impact is not statistically significant. At these scales, there are occasional occurrences of 2σ statistical significance at $\langle x_{\rm HI} \rangle \gtrsim 0.81$. These results suggest that the changes in the bispectrum due to astrophysical scatter are not statistically significant at large and intermediate scales. However, at $k_1 \gtrsim 2.55$ Mpc^{-1}, one can see that the changes arising from the astrophysical scatter are statistically significant with more than 3σ significance at $\langle x_{\rm HI} \rangle \approx 0.53$, for almost all $\cos\theta$ - k_2/k_1 bispectrum configurations. The statistical significance becomes $\gtrsim 5\sigma$ for $\langle x_{\rm HI} \rangle \gtrsim 0.81$, and increases further for higher neutral fractions. We notice that at $\langle x_{\rm HI} \rangle \sim 0.7$, a comparatively smaller area in the bispectrum configuration space is statistically significant; however, the exact reason for this behavior is not clearly known. More detailed investigation is required on this, which is deferred for future work.

The impact of the astrophysical scatter that is dominant at the small scales compared to the large scales, can be visually understood. It is found that large ionized bubbles remain very similar in different realizations of astrophysical scatter. This can be seen in figure 5.5, which shows $[\mathrm{H\,I}]_{21\mathrm{cm}}$ maps for 10 different realizations of the scatter, whereas the underlying dark-matter field and halo list are fixed. One can see that the largest ionized bubble in different maps remains largely unaffected. However, the sizes of small ionized bubbles vary considerably in different realizations. This is clearer in figure 5.6, which shows a zoomed-in version of a particular region of figure 5.5, focusing on a small ionized bubble. Small ionized bubbles encompass a few low-mass dark-matter halos, and the number of ionizing photons emitted by them varies in different realizations due to the astrophysical scatter. This results in the size of small ionized bubbles to vary considerably across realizations. This is not the case for larger bubbles, which encompass many more dark-matter halos, and the collective number of ionizing photons contributed by many reionizing sources does not vary much across realizations. Therefore, the impact of scatter is more prominent in the small ionized bubble size distribution, whereas it is largely negligible and washed away in large ionized bubbles. In the absence of large ionized bubbles in a highly neutral IGM, at the early stages of reionization, the signatures of astrophysical scatter are retained and captured in the $[\mathrm{H\,I}]_{21\mathrm{cm}}$ bispectrum at the small scales, with high statistical significance. In contrast, the signatures of astrophysical scatter are not visible at comparatively larger scales, at the later stages of EoR.

The statistical significance for the impact of astrophysical scatter for $z = 10$ and $\langle x_{\rm HI} \rangle \approx 0.8$ is shown in figure 5.7. At $k_1 \sim 2.55$ Mpc^{-1}, where the impact is found to be high, the statistical significance of the impact is around $\sim 3\sigma$. This is lesser than that found at $z = 7.4$, where the statistical significance was around 5σ at the same neutral fraction of $\langle x_{\rm HI} \rangle \approx 0.8$. It is noted that since the number of ionized bubbles is lower at higher redshifts, this might somewhat reduce the overall statistical significance of the impact. However, this impact is still statistically significant at a level of 3σ.

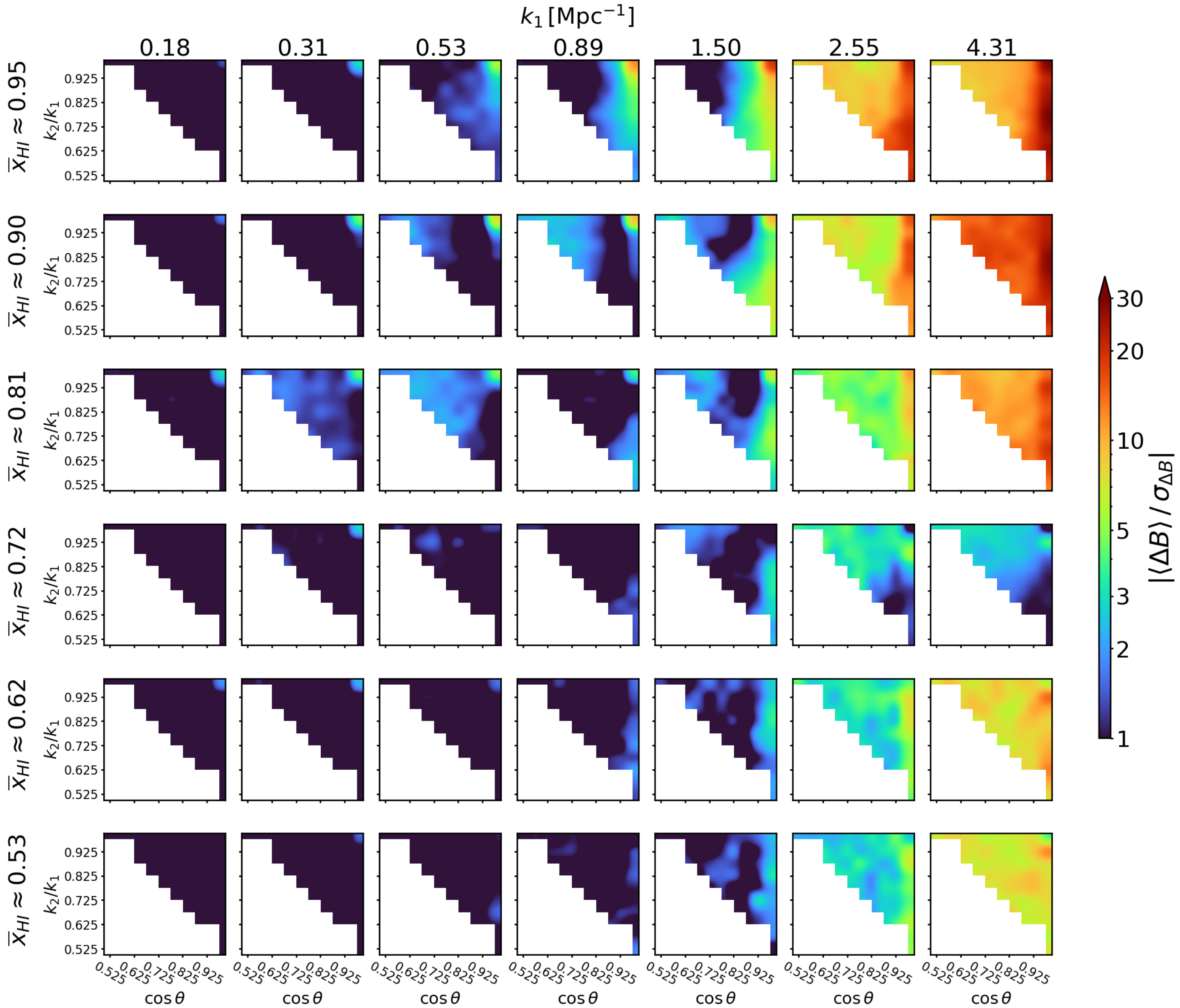

Figure 5.4: Statistical significance of the impact of scatter on the bispectrum is shown here at $z = 7.4$, with rows representing average neutral fraction $\langle x_{\rm HI} \rangle$ and columns representing k_1 mode of the bispectrum.

5.5.3 Sign flip of the HI 21cm bispectrum

The possibility of a sign flip in the bispectrum induced by the impact of astrophysical scatter is discussed here. Whether the condition $B_{\rm scatter}/B_{\rm no-scatter} < 0$ is satisfied in each cell of the $k_1/k_2 - \cos\theta$ space is examined to check the occurrence of sign flip in the bispectrum. It is repeated for all 50 realizations of the astrophysical scatter for the multiple neutral fractions at $z = 7.4$ and $\langle x_{\rm HI} \rangle \approx 0.8$ at $z = 10$. The occurrence of the sign flip in the $[\mathrm{H\ I}]_{21\rm cm}$ bispectrum is counted in all $\sim$50 realizations and the total number of occurrences of this sign flip in each cell of the $k_1/k_2 - \cos\theta$ space is estimated as a percentage. Therefore, a 100 percent would mean that sign flips in $[\mathrm{H\ I}]_{21\rm cm}$ bispectrum occur in a particular cell in $k_1/k_2 - \cos\theta$ space in every realization of astrophysical scatter. In figure 5.8,

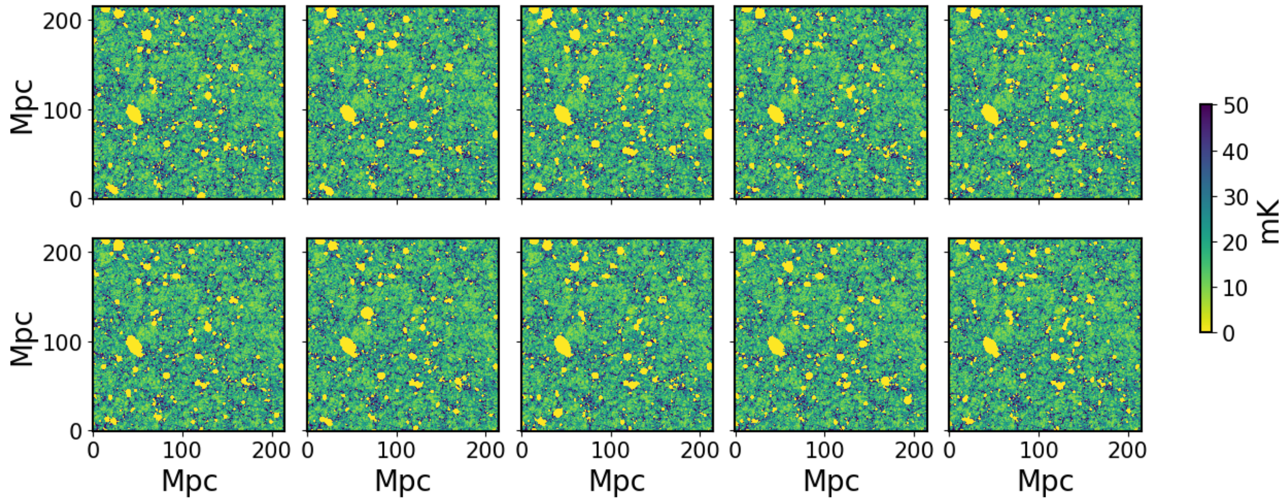

Figure 5.5: Different scatter realizations of the full $215\,\mathrm{Mpc} \times 215\,\mathrm{Mpc}$ slice is shown for $z = 7.4$ at a fixed neutral fraction of $\langle x_{\mathrm{HI}} \rangle \approx 0.81$.

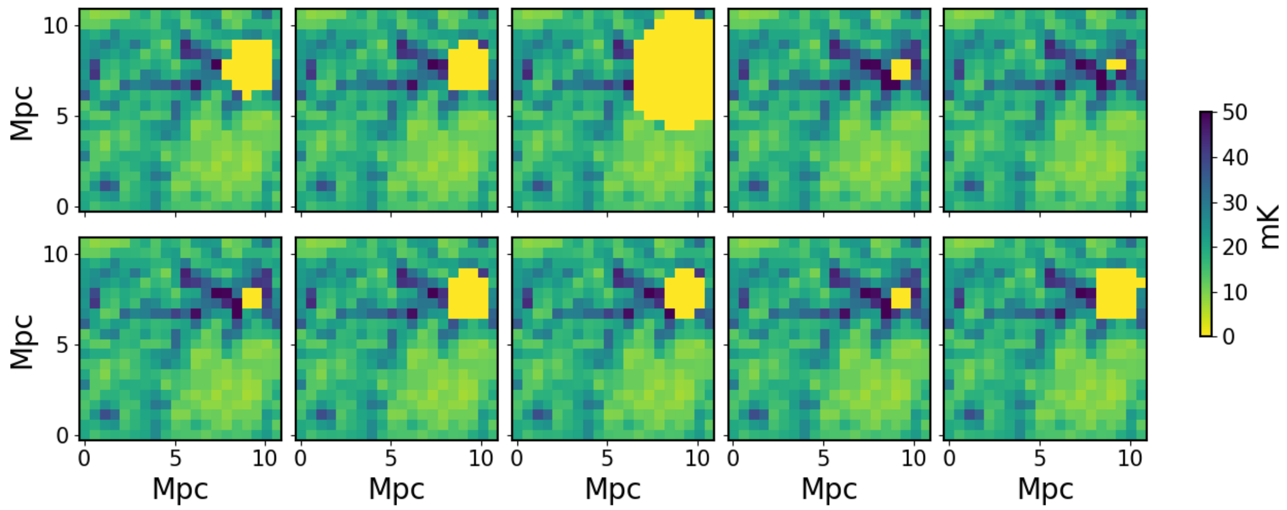

Figure 5.6: Realization to Realization fluctuation of a particular ionized bubble is shown here on a scale of $\approx 10\,\mathrm{Mpc} \times 10\,\mathrm{Mpc}$ for $z = 7.4$ at a fixed neutral fraction of $\langle x_{\mathrm{HI}} \rangle \approx 0.81$.

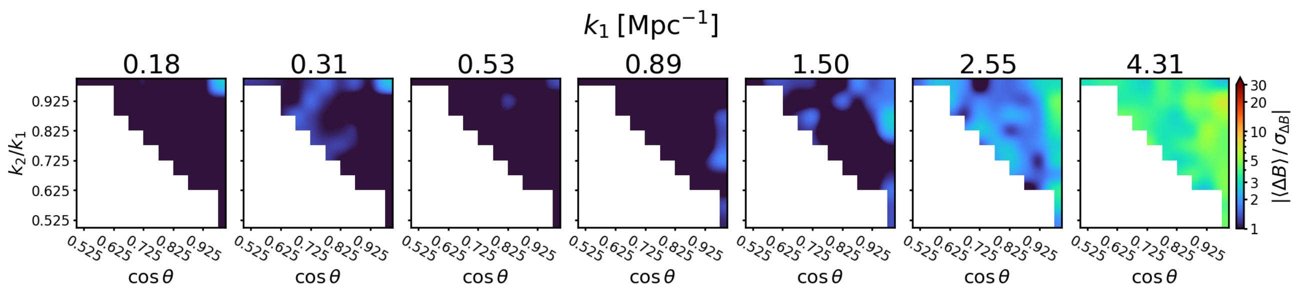

Figure 5.7: This figure shows the statistical significance of the impact of astrophysical scatter at $z = 10$ and $\langle x_{\mathrm{HI}} \rangle \approx 0.8$.

the sign flip due to scatter for $z = 7.4$ is shown for multiple neutral fractions and length scales. It is

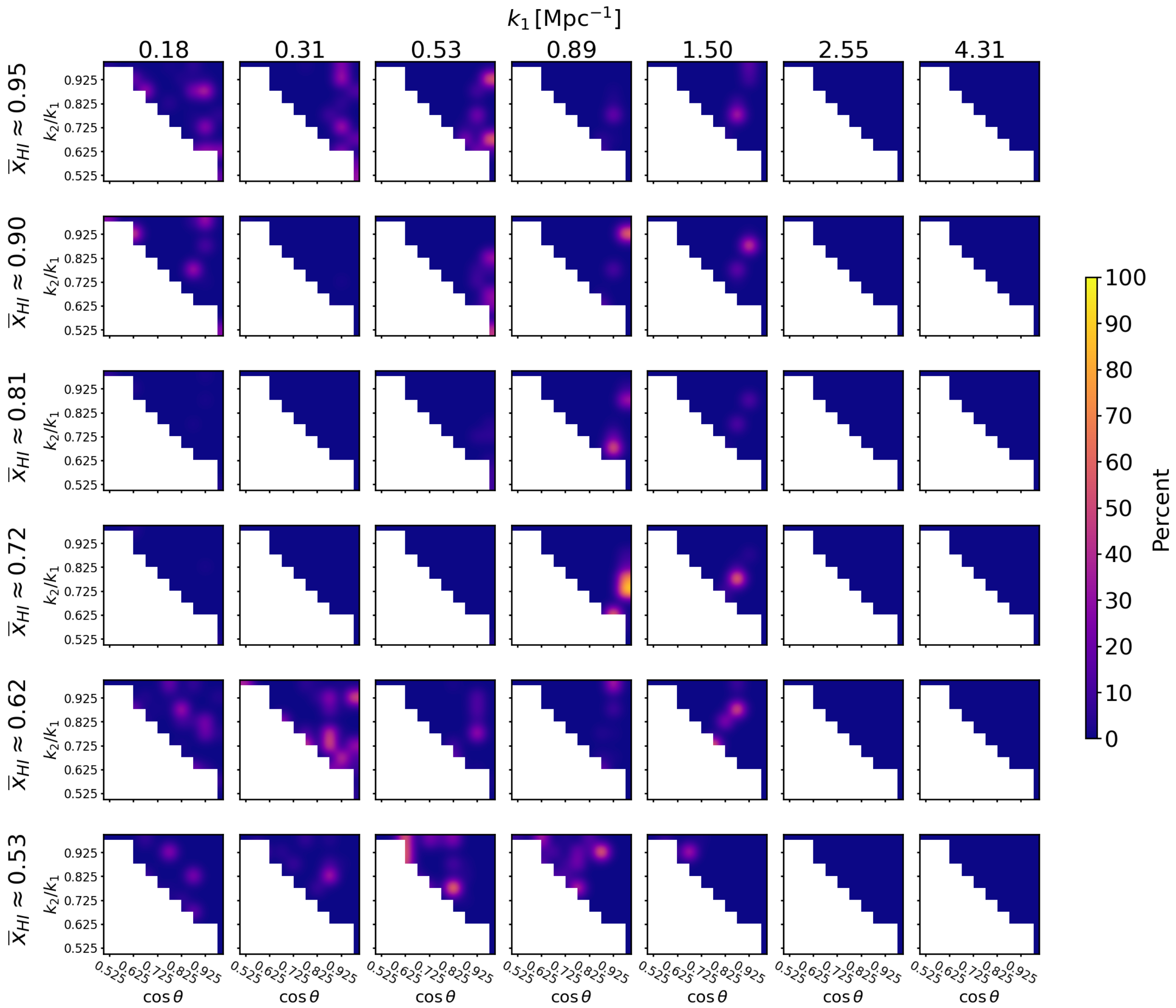

Figure 5.8: This figure shows the sign flip induced by astrophysical scatter at $z = 7.4$ for multiple neutral fractions.

found that for $z = 7.4$ at specific triangle configurations, the frequency of sign flip occurrence is much less than 50 percent in the [H I]$_{21\mathrm{cm}}$ bispectrum, across multiple neutral fractions and for length scales $k_1 \lesssim 1.5$ Mpc^{-1}. It means that for most of the scenarios, there is no sign-flip in the bispectrum, and the fiducial no-scatter model falls in the majority category. For $z = 10$ at $\langle x_{\mathrm{HI}} \rangle \approx 0.8$, a significant area in the bispectrum triangle configuration space at $k_1 \sim 2.55$ Mpc^{-1} shows sign flip occurrence with frequency significantly greater than 50 percent as can be seen in figure 5.9. Therefore, in this case, for most scenarios, the [H I]$_{21\mathrm{cm}}$ bispectrum can change sign and the fiducial no-scatter model falls in the minority category.

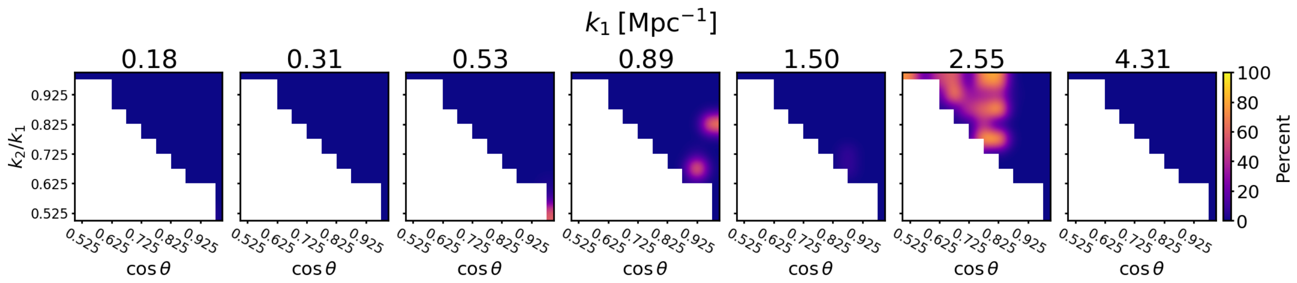

Figure 5.9: This figure shows the frequency of occurrence of sign flip in the [H I]$_{21\mathrm{cm}}$ bispectrum for $z = 10$ at $\langle x_{\mathrm{HI}} \rangle \approx 0.8$ arising from astrophysical scatter.

5.5.4 Comparison with the power spectrum

In this section, a similar analysis of the impact of astrophysical scatter on the power spectrum is done, as is done with the bispectrum (as described in previous sections), and compared with the latter to understand how the bispectrum can capture information that the power spectrum might fail to do. The power spectrum for the no-scatter scenario and all of the ~ 300 realizations of astrophysical scatter is estimated, with ~ 50 realizations for each neutral fraction at $z = 7.4$. In figure 5.10, top panel, the power spectrum for the scenario with astrophysical scatter, averaged over all realizations (red-dashed line) is compared with that when the scatter is not taken into account (black-solid line). It is noted

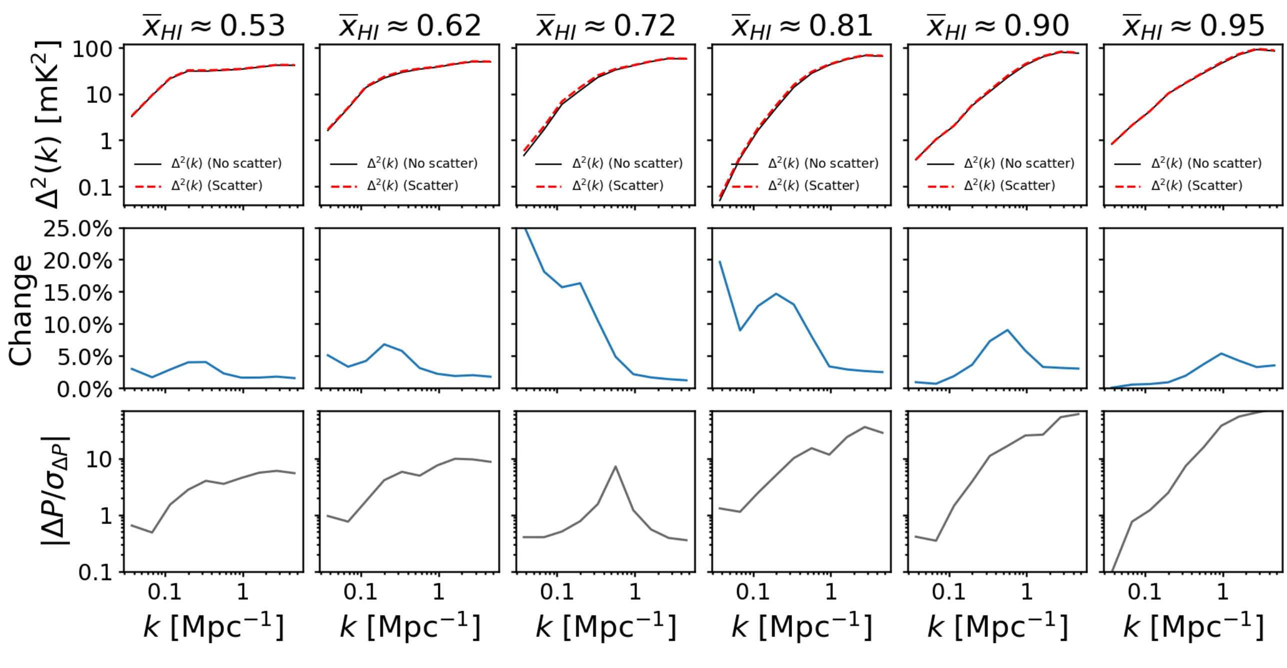

Figure 5.10: Impact on the power spectrum due to the astrophysical scatter is shown here, along with the statistical significance for multiple neutral fractions at $z = 7.4$.

that at $\langle x_{\mathrm{HI}} \rangle \sim 0.8$ the large-scale power spectra exhibit a dip compared to the other neutral fractions. Although the density fluctuations are constant (since the redshift is kept fixed), the cross-correlation between the density of the neutral hydrogen and the total overdensity will vary with different neutral fractions. The cross-power spectrum of these two fields is negative when reionization is in its early stage since the overdense regions (preferred location of ionizing sources) get ionized first in our inside-out reionization model. This cross-term contributes to the [H I]$_{21\mathrm{cm}}$ signal power spectrum and suppresses it at large scales compared to the higher neutral fractions. However, when the ionized bubbles are sufficiently large and numerous at a particular reionization stage, this cross-correlation becomes weaker, and its contribution to the [H I]$_{21\mathrm{cm}}$ power spectrum goes down. However, the contribution of the neutral hydrogen power spectra to [H I]$_{21\mathrm{cm}}$ signal power spectra will dominate over this cross-correlation. It will cause the large-scale power spectra to increase. Therefore, at a particular neutral fraction stage, the large-scale power spectra shows a dip. This phenomenon is consistent with several earlier studies of reionization with radiative transfer and semi-numerical simulations (Lidz, Zahn, et al. 2007; Mao, Shapiro, et al. 2012; Majumdar, Somnath Bharadwaj, and T. Roy Choudhury 2013; Majumdar, Jensen, et al. 2016). In the middle panel, we present the percentage change in the power spectrum due to scatter and the corresponding statistical significance of the impact in the bottom panel.

For the neutral fractions, $\langle x_{\mathrm{HI}} \rangle = 0.53 - 0.81$, the magnitude of the impact ranges from $5 - 15$ percent, with statistical significance ranging from $4\sigma - 5\sigma$. At $\langle x_{\mathrm{HI}} \rangle = 0.90$ and $\langle x_{\mathrm{HI}} \rangle = 0.95$, the statistical significance is very high (10σ and 14σ respectively), where the magnitude of the impact of astrophysical scatter reaches its peak. However, the magnitude of this impact is less (~ 10 percent and ~ 5 percent respectively) compared to the magnitude of the impact at $\langle x_{\mathrm{HI}} \rangle = 0.81$. Unlike the bispectrum, the impact on the power spectrum is at a single-length scale, with the maximum magnitude of the impact at $k \sim 0.2$ Mpc^{-1} being $\lesssim 15$ percent for $\langle x_{\mathrm{HI}} \rangle = 0.81$. The maximum magnitude of the impact declines and shifts to smaller scales for the higher neutral fractions. The maximum magnitude of the impact we find for the neutral fractions considered is broadly consistent with the findings of Hassan et al. 2022. However, they present their results based on the ionization power spectrum (which is different from the power spectrum of the brightness temperature fluctuations). They also do not include a corresponding statistical significance of the changes in the power spectrum that they find, arising from the astrophysical scatter.

On the other hand, the bispectrum, being a 3-pt Fourier statistic, captures the impact of scatter on the correlations between different length scales. This impact consistently exceeds 20 percent across all neutral fractions ($\langle x_{\mathrm{HI}} \rangle \gtrsim 0.53$) at $k \sim 2.55$ Mpc^{-1}, with statistical significance consistently equal to or higher than 3σ, at those scales. At $\langle x_{\mathrm{HI}} \rangle = 0.81$, the impact of astrophysical scatter reaches ~ 100 percent for a significant region of the bispectrum triangle configuration space at 5σ statistical significance. It suggests that the impact of the astrophysical scatter on the [H I]$_{21\mathrm{cm}}$ signal is captured and characterized in a more detailed manner with the bispectrum as opposed to the power spectrum, which misses out on the signatures of the impact of scatter at the relevant neutral fractions and length-scales, with sufficient magnitude.

5.5.5 Detectability of the HI 21cm auto-bispectrum

Here, the possibility of detecting the impact of the scatter on the $[\mathrm{H\ I}]_{21\mathrm{cm}}$ bispectrum considering observations with the planned SKA1-Low is considered. As a test case, the current analysis is limited to only the equilateral triangle configurations of the bispectrum, which correspond to the top-left corner of the bispectrum configuration space shown in the previous figures. The equilateral bispectrum is expected to be most affected by system noise. Although it has been shown in previous studies (Rajesh Mondal, Mellema, et al. 2021), that the squeezed limit bispectrum has the best signal-to-noise ratio for detection, it is found that this bispectrum triangle configuration is not likely to be affected by astrophysical scatter. The bispectrum for the equilateral triangle configuration is found to be significantly affected by scatter. Therefore, we focus on the prospects for the detectability of the equilateral bispectrum. In figure 5.11, the equilateral bispectrum is shown without (dashed lines) and with (solid lines) the astrophysical scatter, along with the corresponding impact and the statistical significance of the impact, for various neutral fractions at $z = 7.4$. It is seen that, except for $\langle x_{\mathrm{HI}} \rangle \sim 0.5$, the impact on the equilateral bispectrum is statistically significant with $|\langle \Delta B \rangle / \sigma_{\Delta B}| \gtrsim 3\sigma$ for $k_1 \sim 2.55\ \mathrm{Mpc}^{-1}$.

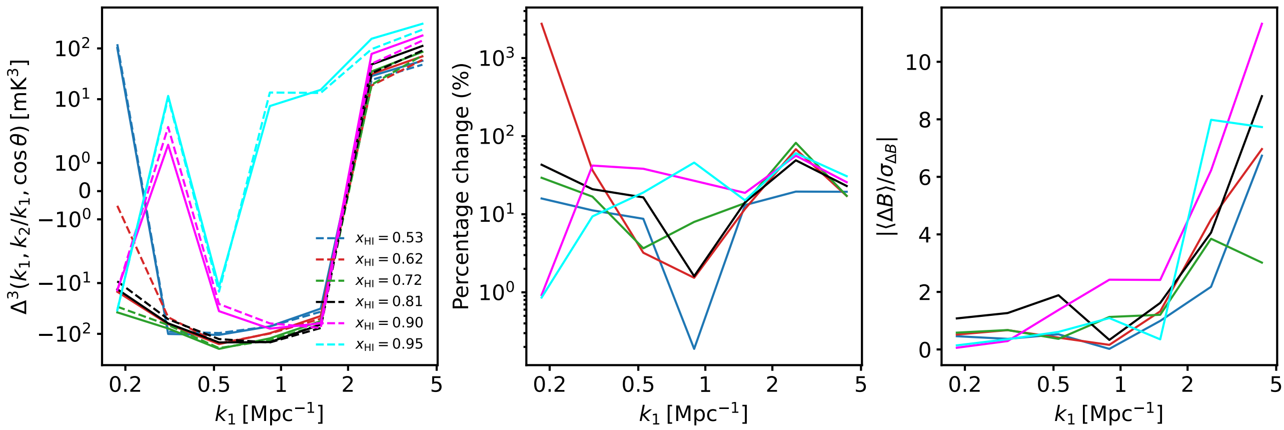

Figure 5.11: Left panel: The equilateral bispectrum without (dashed lines) and with (solid lines) the astrophysical scatter is shown here for multiple neutral fractions at $z = 7.4$. Middle panel: The impact due to scatter on the equilateral bispectrum is shown here. Right panel: The corresponding statistical significance of the impact of scatter is shown here.

The variance in the bispectrum ($\sigma_{\mathrm{N}}^2(B)$) due to system noise is computed following (Scoccimarro, Sefusatti, and Zaldarriaga 2004; Liguori et al. 2010):

$$\sigma_{\mathrm{N}}^2(B) \approx s_B \frac{V_f}{V_B} P_{\mathrm{N}}(k_1, z) P_{\mathrm{N}}(k_2, z) P_{\mathrm{N}}(k_3, z) \tag{5.2}$$

Here, $V_f = (2\pi)^3/V_s$ is the volume of the fundamental cell in the Fourier domain, with V_s being the survey volume, and $P_{\mathrm{N}}(k, z)$ is the noise power spectrum contributed by the system noise. In equation 5.2, $s_B = 6$ for equilateral triangles, and $V_B \approx 8\pi^2 k_1 k_2 k_3 \Delta k_1 \Delta k_2 \Delta k_3$. The noise power spectrum due to the system noise in radio interferometric experiment is given by (Bull et al. 2015; Obuljen et al. 2018):

$$P_{\rm N}(k,z)=\frac{T^2_{\rm sys}(z)\chi^2(z)r_\nu(z)\lambda^4(z)}{A^2_{\rm eff}t_{\rm obs}n_{\rm pol}n(\boldsymbol{u},z)\nu_{21\rm cm}}. \tag{5.3}$$

$\chi(z)$ is the comoving distance to redshift z, and $r_\nu = (c/H(z))(1+z)^2$. $\lambda(z) = 21 \times (1+z)$ cm and $\nu_{21\rm cm} = 1420$ MHz are the redshifted wavelength and the rest frame frequency of the [H I]$_{21\rm cm}$emission, respectively. The number of polarization ($n_{\rm pol}$) is assumed to be 2 and $n(\boldsymbol{u},z) = N_{\rm a}^2/(2\pi u^2_{\rm max})$ is the baseline density which is assumed to be constant within the core radius. $N_{\rm a}$ is the total number of antennae in the experiment and $u_{\rm max}$ is the maximum baseline in units of $\lambda(z)$. The system temperature $T_{\rm sys}$ is modeled as $T_{\rm sys}(\nu) = 100 + 300(150\,{\rm MHz}/\nu)^{2.55}$ K following Mellema, Léon V. E. Koopmans, et al. 2013. $A_{\rm eff}$ is the effective collecting area of each antenna which is modeled as, $A_{\rm eff} = A_{\rm eff}(\nu_{\rm crit}) \times \epsilon(\nu)$ (Bull et al. 2015), where $\epsilon(\nu)$ is defined as

$$\epsilon(\nu)=\begin{cases}(\nu_{\rm crit}/\nu)^2, & \nu>\nu_{\rm crit}\\ 1, & \nu\le\nu_{\rm crit}.\end{cases} \tag{5.4}$$

$A_{\rm eff}(\nu_{\rm crit})$ is taken to be 962 m^2 at $\nu_{\rm crit} = 110$ MHz (Sambit K. Giri, Mellema, and Raghunath Ghara 2018). We take $N_{\rm a} = 296$ within a core radius of $R_{\rm max} = 2$ Km (Mazumder et al. 2022). The relative k-bin size is taken as $\Delta k/k \sim 1$. Different scenarios are assumed, where the bandwidth is kept fixed at 16 MHz and the observational duration $t_{\rm obs}$ is varied, to estimate the detectability of the equilateral bispectrum for the signal model considered here. Three scenarios are considered, with the first being to observe for a total of 1000 hours. In the other two scenarios, we assume that the observation takes 1000 hours per year after SKA1-Low is operational, and the observational campaign is carried out for the next couple of years. It is assumed that this campaign lasts five and ten years, with the total observational time accumulated to 5000 and 10000 hours, respectively. This exercise is restricted to only the scales of our interest, where the impact of the scatter is statistically significant and of sufficient magnitude, i.e., $k_1 \sim 2.55$ Mpc^{-1}. In figure 5.12, the resulting signal-to-noise ratio is shown, considering these three scenarios of observational duration for various neutral fractions that have been explored in this study.

In the first scenario, it is seen that with a total of 1000 hours of observation (grey-dashed line), the equilateral bispectrum is not detectable with a sufficient signal-to-noise ratio. In the case, where the observational campaign lasts for five years with 1000 hours per year (orange-dotted line), the signal-to-noise ratio cross the 1σ detection limit at $\langle x_{\rm HI}\rangle \sim 0.8$ and it reaches 3σ for $\langle x_{\rm HI}\rangle \sim 0.9$. However, if we adopt a more optimistic case, where the campaign lasts ten years with 1000 hours of observation time per year (blue-solid line), then the equilateral bispectrum is above the 1σ detection limit for all the neutral fractions at $k_1 \sim 2.55$ Mpc^{-1}, starting from $\sim 2\sigma$ detection significance at $\langle x_{\rm HI}\rangle \sim 0.5$. However, at $\langle x_{\rm HI}\rangle \sim 0.8$ and 0.9, the detection significance is $\sim 3\sigma$ and $\sim 5\sigma$ respectively.

The results for the detectability that have been presented here are for a single redshift ($z = 7.4$).

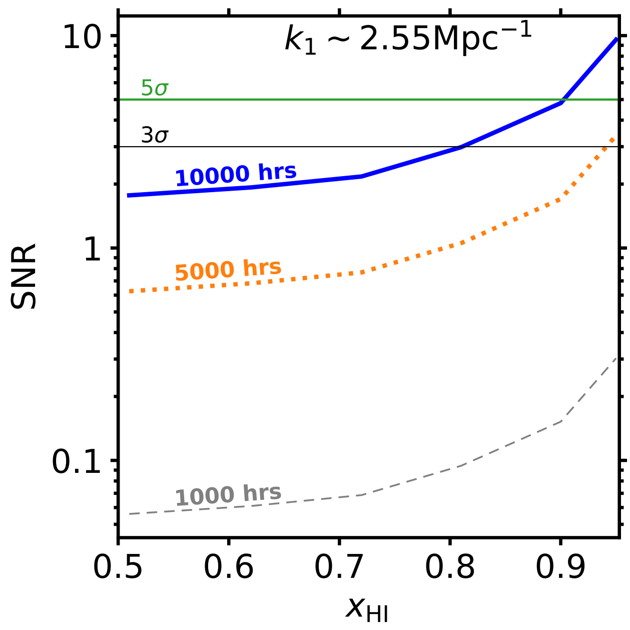

Figure 5.12: The signal-to-noise ratio of the detection of the equilateral bispectrum at $z = 7.4$ is shown, for the scales where the impact of scatter is expected to be significant ($k_1 \sim 2.55$ Mpc^{-1}) and considering observations with SKA1-Low for various durations of observational time. The horizontal solid black and solid green line denotes the threshold for 3σ and 5σ detection significance, respectively.

However, at higher redshifts, one can expect that the signal-to-noise ratio will be further degraded, due to increased system noise temperature T_{sys}. We estimated the signal-to-noise ratio of the detectability of the bispectrum for $z = 10$ at $\langle x_{\mathrm{HI}} \rangle \approx 0.8$, which was done for the triangle configurations near the vicinity of the equilateral triangles, where statistical significance is high. The signal-to-noise ratio is far below the unity even for $t_{\mathrm{obs}} = 10000$ hours.

For higher-order Fourier statistics such as bispectrum, the contributions of cosmic variance to the total bispectrum uncertainty can be significant at large scales. In Rajesh Mondal, Mellema, et al. 2021, the contribution of the cosmic variance to the total bispectrum uncertainty budget has been studied thoroughly for a range of length scales. The uncertainty contributed by cosmic variance decreases with decreasing length-scale and this is true for the equilateral bispectrum as well, as found by Rajesh Mondal, Mellema, et al. 2021. They studied a case with roughly 1000 hours of observation with SKA1-Low. They found that the contribution from the cosmic variance to the total uncertainty budget dominated at $k_1 \lesssim 0.5$ Mpc^{-1} in this case. However, one might expect that cosmic variance in the bispectrum can still contribute to the total signal-to-noise ratio budget down to the scales at $k_1 \sim 2.55$ Mpc^{-1} to some extent, and affect the signal-to-noise ratio of the detection at those scales. Also, the estimation of the signal-to-noise ratio of the detection of the equilateral bispectrum, presented here, is analytic, and a full numerical approach (Rajesh Mondal, Mellema, et al. 2021) is needed for a more thorough investigation. Therefore, one needs to simulate multiple independent realizations of the underlying dark-matter distribution to estimate the uncertainty contribution from cosmic variance in the bispectrum and multiple realizations of [H I]$_{21\text{cm}}$ noise maps (telescope noise) for a full numerical approach. This thorough approach is a more computationally challenging task and is beyond the scope of the current article. This exercise can be taken up in future follow-up work.

5.6 Summary

The [H I]$_{21\text{cm}}$ signal is a promising probe of the Universe during the EoR and can be used to track the evolution of the early IGM and the reionization process. Although the power spectrum can shed light on many important issues, it cannot capture the entire information content in the [H I]$_{21\text{cm}}$ signal because it is highly non-Gaussian. The variation in the ionizing photon emission rates for host halos of a given mass which is referred to as astrophysical scatter, can introduce an additional non-Gaussianity into the [H I]$_{21\text{cm}}$ signal. In Hassan et al. 2022, the effects of this astrophysical scatter had been studied in the context of cosmic reionization of the IGM, using power spectra of the ionization field. They found that the power spectra are mostly unaffected by the presence of astrophysical scatter. However, the statistical significance of the impact of astrophysical scatter on the power spectrum has not been thoroughly studied, and the ionization field is not observable, unlike the [H I]$_{21\text{cm}}$ signal. However, bispectra can capture some aspects of the non-Gaussian [H I]$_{21\text{cm}}$ signal. In this work, the impact of the astrophysical scatter on the [H I]$_{21\text{cm}}$ bispectra during the EoR has been investigated. [H I]$_{21\text{cm}}$ maps had been simulated using a semi-numerical prescription that also incorporates astrophysical scatter and then estimated the fractional change in the bispectra $|\langle \Delta B \rangle / B_{\text{no-scatter}}|$ of the maps due to the scatter. 50 independent realizations of the astrophysical scatter were generated for each of the six neutral fractions that were considered to quantify the statistical significance of the impact of scatter. The statistical significance of the impact is quantified by $|\langle \Delta B \rangle / \sigma_{\Delta B}|$, where $\sigma^2_{\Delta B}$ is the variance in ΔB, arising from the independent realizations of the astrophysical scatter, for each of the neutral fractions. Here, the analysis is presented for all unique triangle configurations of the bispectrum, for a range of neutral fractions, at a fixed redshift of $z = 7.4$ and for $z = 10$ at $\langle x_{\text{HI}} \rangle \approx 0.8$. The equilateral bispectrum is one of the triangle configurations, where a significant impact of the scatter is expected. The prospects of detecting the small-scale ($k_1 \sim 2.55$) Mpc^{-1} bispectrum with the planned SKA1-Low were also explored. The key findings of this work are:

- The large and intermediate scales in the [H I]$_{21\text{cm}}$ maps ($k_1 \lesssim 1.5$ Mpc^{-1}) are largely unaffected due to astrophysical scatter, as captured by the bispectrum. Although, the magnitude of the fractional change in the bispectrum, $|\langle \Delta B \rangle / B_{\text{no-scatter}}|$, is more than a factor of ~ 10 in some regions of the $\cos\theta - k_2/k_1$ configuration space of the bispectrum for these length scales, this impact is found to be non-significant, and are a result of statistical noise.

- At the small scales ($k_1 \sim 2.55$ Mpc^{-1}), we find that the impact of astrophysical scatter on the bispectrum is significant. We find that $|\langle \Delta B \rangle / B_{\text{no-scatter}}| \gtrsim 20$ percent at neutral fractions $\langle x_{\text{HI}} \rangle \gtrsim 0.81$ at $z = 7.4$ and a significant region of the $\cos\theta - k_2/k_1$ configuration space of the bispectrum, the impact of the astrophysical scatter is maximum, where $|\langle \Delta B \rangle / B_{\text{no-scatter}}| \sim 100$ percent. For $z = 10$ at $\langle x_{\text{HI}} \rangle \approx 0.8$, the impact due to scatter is more prominent ($|\langle \Delta B \rangle / B_{\text{no-scatter}}| \gtrsim 10$), although the statistical significance is somewhat less ($\sim 3\sigma$) as compared to the same neutral fraction at $z = 7.4$.

- The presence of astrophysical scatter primarily affects the small ionized regions of the IGM the most. On the other hand, large ionized bubbles would be formed due to ionization from the cumulative photon from multiple sources, thus averaging out the signatures of astrophysical scatter, as similarly argued in Hassan et al. 2022. Therefore large-length scales would be primarily unaffected by the presence of scatter in the number distribution of the ionizing photons. At higher redshifts, we expect fewer ionizing sources, and hence fewer ionized bubbles, which would be larger compared to the case at lower redshifts at the same neutral fraction. This might result in the impact of scatter being more prominent, however, due to the lower number of ionized bubbles, the statistical significance of the impact of scatter can be reduced compared to lower redshifts.

- The astrophysical scatter is not found to induce any significant sign flip occurrence in the [H I]$_{21\text{cm}}$ bispectrum at $z = 7.4$. For $z = 10$ at $\langle x_{\text{HI}} \rangle \approx 0.8$, the bispectrum is seen to have a significant occurrence of sign flip for a few specific triangle configurations at $k_1 \sim 2.55$ Mpc^{-1}. However, most of the triangle configurations do not show a significant occurrence of sign flip.

- In the case of the power spectrum, the magnitude of the impact of scatter is not high enough ($\lesssim 10$ percent) for most of the neutral fractions and length scales. Occasionally, the magnitude of the impact is high ($\gtrsim 15$ percent), however, this is not statistically significant. On the other hand, wherever the impact is statistically significant, the magnitude of the impact is not sufficient enough ($\lesssim 15$ percent). Therefore, the power spectrum does not capture the signatures of astrophysical scatter adequately at the small scales, unlike the bispectrum.

- The equilateral bispectra for $z = 7.4$ at the small scales could be detected with $\sim 3\sigma/5\sigma$ detection significance at $\langle x_{\text{HI}} \rangle \sim 0.8/0.9$ if we consider a very optimistic scenario of observing for 1000 hours per year with the SKA1-Low and this observational campaign lasts for ten years. However, at high redshifts, such as $z = 10$, the signal-to-noise ratio for the detectability of the [H I]$_{21\text{cm}}$ bispectrum for triangle configurations in the vicinity of the equilateral triangle is far below unity, at $k_1 \sim 2.55$ Mpc^{-1}. The increased system temperature (T_{sys}) of the interferometer at higher redshifts can be a contributing factor for the low signal-to-noise ratio. One might note that cosmic variance can significantly contribute to the total uncertainty budget of the bispectrum at large scales, as investigated in Rajesh Mondal, Mellema, et al. 2021. However, it remains to be seen how much it might contribute to the total uncertainty budget and affect the detection significance at the small scales ($k_1 \sim 2.55$ Mpc^{-1}), where the impact of astrophysical scatter is found to be significant. This exercise is left to future work.

Chapter 6

Forecasting the CO-21cm cross-power spectrum from the EoR with line-intensity mapping surveys

6.1 Introduction

One of the essential tracers of the molecular gas in galaxies is the emission of the CO line, which is predominantly excited by collisional excitation from the gas (Draine 2011). Therefore, the far-infrared surveys at the millimeter wavelengths are suitable probes for the molecular gas content in these galaxies. On the other hand, star formation in galaxies is known to follow a strong correlation with the gas content in galaxies, including H_2, via the well-known Schmidt-Kennicut relation (Kennicutt 1998). Understanding how star formation is related to the molecular gas content of galaxies is essential since this is related to the efficiency with which gas is depleted to form stars, which can ultimately affect galaxy formation and evolution (Carilli and F. Walter 2013). Usually, this is studied through the proxies of molecular gas content and star formation. One of the proxies used for molecular gas content and star formation is the CO line luminosity (L'_{CO}) and infrared luminosity (L_{FIR}) of the galaxies. Therefore, the correlation in the $L_{\mathrm{FIR}} - L'_{\mathrm{CO}}$ relation can be used as an observable to understand the relationship between gas depletion in galaxies and the SFR.

As discussed earlier, these galaxy surveys are typically limited by the number of samples detected and the redshifts out to which they are detected. These limitations are complemented by LIM surveys, which detect integrated flux of numerous line-emitting sources (E. D. Kovetz et al. 2017; E. Kovetz et al. 2019; Bernal and E. D. Kovetz 2022) from a large survey volume. Typically, bright-line emissions such as [C II]$_{158\mu\mathrm{m}}$, Ly-α, [O III] from the galaxies are expected to be good tracers for LIM, along with the CO line emission, out to the EoR era. CO intensity mapping was proposed by Carilli 2011 to probe the EoR and one of the early attempts for intensity mapping with the CO line emission was done using the CO Power Spectrum Survey (**COPSS**, Keating, Bower, et al. 2015; Keating, Marrone, Bower, Leitch, et al. 2016) at around $z \sim 3$. Using theoretical estimates, they constrained the molecular gas density $\rho_{\mathrm{H}_2} \sim 1.1^{+0.7}_{-0.4} \times 10^8 M_\odot$ Mpc^{-3}. Later, interferometric CO intensity mapping experiment with a pair of 3 mm data sets, from the **ALMA Spectroscopic Survey in the Hubble Ultra Deep Field (ASPECS)**, and the series of **Atacama Compact Array (ACA)** observations conducted between 2016 and 2018, targeting the COSMOS field were considered by Keating, Marrone, Bower, and Keenan 2020. The inferred molecular gas density at $z = 1 - 3$ was consistent with the **COPSS** results. In addition, CO intensity mapping was performed with the Millimetre-wave Intensity Mapping Experiment (**mmIME**, Breysse, Yang, et al. 2022), which suggested that careful modeling efforts are required while using semi-analytic approaches. The latest endeavor in CO intensity mapping is taken up by the CO Mapping Array Project (**COMAP**, Breysse, Dongwoo T. Chung, et al. 2022; Dongwoo T. Chung et al. 2022; Cleary et al. 2022; Håvard T. Ihle et al. 2022; Lamb et al. 2022; D. T. Chung et al. 2024; Stutzer et al. 2024). Given the multiple CO line transitions, the **COMAP-pathfinder** with its 30 GHz dishes and the **COMAP-EoR** with its 16 GHz dish can target CO emission from the epoch of stellar build-up ($z \sim 3$) up to the EoR ($z \gtrsim 6$).

However, the LIM surveys are expected to be challenged because the presence of the instrumental noise will contaminate the observed signal. This will bias any observable summary statistics, particularly the auto-correlation signal. One of the ways to tackle this challenge is to cross-correlate the targeted signal with other line-emission probes of the Universe originating from similar cosmic time or redshift. In the context of **COMAP**, this has been discussed by Breysse, Dongwoo T. Chung, et al. 2022 and Dongwoo T. Chung 2023, where the cross-correlation between the 16 GHz and 30 GHz bands were considered, essentially cross-correlating the CO$(1-0)$ and CO$(2-1)$ LIM signals, both of them originating from the EoR ($z \gtrsim 6$). One can also consider cross-correlations of the CO LIM signal with a different tracer such as the [H I]$_{21\mathrm{cm}}$ signal from the neutral IGM during EoR. In the context of CO emission, cross-correlation with [H I]$_{21\mathrm{cm}}$ signal was earlier proposed by Gong, Cooray, M. B. Silva, et al. 2011; Lidz, Furlanetto, et al. 2011, where Lidz, Furlanetto, et al. 2011 consider cross-correlation between early generation **MWA** (J. D. Bowman, Morales, and Hewitt 2006) and a hypothetical CO LIM experiment to forecast the detectability of the cross-power spectrum.

In this work, the possibility of cross-correlating observations from **COMAP** has been considered with that of the observations from **AARTFAAC** (P. Prasad et al. 2016; Kuiack et al. 2019). **AARTFAAC** is an all-sky radio survey that utilizes data from the LOFAR antennae but post-processes them independently. It has a moderate resolution and sensitivity, but a much wider field-of-view (typically all-sky), high availability, and autonomous calibration and imaging in near real-time (P. Prasad et al. 2016). The other notable examples of this class of telescopes are the **Long Wavelength Array** (**LWA,** Ellingson et al. 2013) and the **MWA** (Tingay et al. 2013). Therefore, the **AARTFAAC** can conduct a pilot survey for cross-correlation with **COMAP** observations, having a good possibility of overlap in the survey areas.

The outputs from a large-scale N-body simulation have been considered here, and the identified halos were post-processed to produce the mock $\mathrm{CO}(2-1)$ and $\mathrm{CO}(1-0)$ signal. The density fields and halos were also used to develop the mock [H I]$_{21\mathrm{cm}}$ signal to cross-correlate with the CO signals. The CO signals were generated by considering different correlation parameters of the $L_{\mathrm{FIR}} - L'_{\mathrm{CO}}$ relation. In earlier works, Breysse, Dongwoo T. Chung, et al. 2022 consider a set of CO models from various references which are related to the host halo mass via a set of parametric relations to forecast cross-correlation of the $\mathrm{CO}(2-1)$ and $\mathrm{CO}(1-0)$ signals from the EoR. The approach undertaken by Dongwoo T. Chung 2023 tries to motivate their models using more detailed physical factors such as the CO column density and the temperature of the ISM in one of their semi-analytic models. In the other model, they employed the non-LTE radiative transfer code `Radex` (van der Tak et al. 2007), that self-consistently models the CO spectral line energy distributions (SLEDs), which is used to predict the CO luminosities, assuming some scaling relations for the CO column density and molecular gas density as inputs to `Radex`. Using this, cross-correlation between the $\mathrm{CO}(1-0)$, $\mathrm{CO}(2-1)$ and the $\mathrm{CO}(3-2)$ signals were predicted. Here, a somewhat different approach to modeling the CO signals have been followed for cross-correlation in the sense that it deals only with the $L_{\mathrm{FIR}} - L'_{\mathrm{CO}}$ correlation, which is of the form $\log L_{\mathrm{FIR}} = \alpha \log L'_{\mathrm{CO}} + \beta$. According to T. R. Greve, Leonidaki, et al. 2014, the slope α of this correlation provides insights into how molecular gas plays a role in star formation. The super-linear relationship between L_{FIR} and L'_{CO} luminosities suggests that dense molecular gas acts as the primary fuel for star formation across all galaxies, maintaining a consistent star-forming efficiency. The ratio $f_{\mathrm{dense,X}} = M_{\mathrm{dense}}/M_{\mathrm{X}}$ varies within galaxy samples, where X might represent the total H_2 gas mass indicated by CO $J = 1$–0 and $J = 2$–1 lines, with $\mathrm{d}(f_{\mathrm{dense}})/\mathrm{d}L_{\mathrm{FIR}} > 0$. This phenomenon is linked to mergers and starbursts, which dominate the high-L_{FIR} spectrum and exhibit a higher dense-to-total fraction of gas mass when compared to isolated disks with lower-L_{FIR} (e.g., Gao and Philip M. Solomon 2004; García-Burillo et al. 2012). The $\mathrm{d}(f_{\mathrm{dense}})/\mathrm{d}L_{\mathrm{FIR}}$ value is higher when the gas phase X is further away from the dense, star-forming phase in terms of physical conditions and relevance to star formation. It will result in a super-linear slope of $L_{\mathrm{FIR}} - L'_{\mathrm{CO}}$ correlation. Additionally, the normalization factor β may provide information about the regulation of star formation through feedback from radiation pressure due to dust grains, which absorb and scatter FUV light (T. R. Greve, Leonidaki, et al. 2014). Here, a few such combinations of the $L_{\mathrm{FIR}} - L'_{\mathrm{CO}}$ correlation parameters, α and β have been considered as reported in observations, as well as a continuously varying set of α values (which is related to the variation in β), to predict various CO emission models and their detectability in the cross-correlation signal. Throughout, the work, flat ΛCDM cosmology has been assumed, with cosmological parameters: $\Omega_{\mathrm{m}} = 0.27$, $\Omega_{\mathrm{b}} = 0.044$, $h = 0.7$, $n_{\mathrm{s}} = 0.96$, $\sigma_8 = 0.8$ which is consistent with the WMAP (Hinshaw et al. 2013) and Planck observations (Planck Collaboration, Ade, P. A. R., et al. 2014), have been adopted.

6.2 Modeling mock observation

6.2.1 Mock signals

The mock [H I]$_{21\mathrm{cm}}$and CO signals are based on the outputs of large-scale N-body simulations. We used the pre-simulated density field outputs of the N-body code `CUBEP3M` (Harnois-Déraps et al. 2013), with a grid size of 13824^3, resulting in a simulation box size of ~ 714 Mpc on one side, and the number of particles is 6912^3. The halos were identified with a spherical overdensity halo-finder algorithm (Watson et al. 2013), with at least 25 particles, resulting in a minimum halo mass of $\sim 10^9 M_\odot$. These outputs were post-processed using the radiative transfer code C^2-RAY (Mellema, Ilian T. Iliev, Alvarez, et al. 2006) to assign ionizing luminosity to host halos and simulate the ionization maps of IGM (Sambit K. Giri, Mellema, Aldheimer, et al. 2019; Rajesh Mondal, Shaw, et al. 2020), on a gridded box of 300^3 cells. These simulations were performed as part of the PRACE (Partnership for Advanced Computing in Europe) project, PRACE4LOFAR.

For the radiative transfer simulations, the ionizing luminosity of the haloes was assigned based on their masses. The total ionizing photon production rate within the volume was determined by multiplying the halo growth rate by a constant ionizing efficiency ζ, then distributing it across individual haloes, under the assumption that between the halo mass and the ionizing luminosity a linear relationship exists. In this source model, up to a specific redshift, the total number of ionizing photons generated is proportional to the fraction of matter that is bound in dark-matter haloes at that redshift. More details on this approach are available in Sambit K. Giri and Mellema 2021. For our purpose, we chose an output of the simulation available at a redshift of $z \sim 7.2$.

To develop the CO LIM maps, we follow the prescription as mentioned in Equation 1.10, to relate the CO luminosity to the FIR luminosity of that halo. We follow Kennicutt 1998, to obtain the relation $\mathrm{SFR}(M_\mathrm{h}, z) = \delta_\mathrm{MF} \times 10^{-10} L_\mathrm{FIR}$. The value of δ_MF is set to 1, as in Behroozi, Wechsler, and Conroy 2013; T. Y. Li et al. 2016. The halo mass is connected to the SFR using Equation 2.1 from M. B. Silva et al. 2013. Four different models for α_{1-0} and β_{1-0} are chosen that relate $L'_{\mathrm{CO}(1-0)}$ to L_FIR following Carilli and F. Walter 2013; Sargent et al. 2014; T. R. Greve, Leonidaki, et al. 2014; Kamenetzky et al. 2016. Carilli and F. Walter 2013 derived the values of α_{1-0} and β_{1-0} based on a sample of low, intermediate ($0.2 < z < 1$) and high-redshift galaxies ($z > 1$), which comprised of spirals, quasi-stellar objects (QSOs), ultra-luminous infrared galaxies (ULIRGs), sub-millimitre galaxies (SMGs), galaxies selected in the 24-μm band, Lyman-break galaxies (LBGs), color-selected galaxies (CSGs), star-forming radio galaxies (SFRGs) and radio galaxies (RG). They find that for the entire distribution, $\alpha_{1-0} = 1.37 \pm 0.04$ and $\beta_{1-0} = -1.74 \pm 0.40$, where the slope is consistent with the power law found for nearby galaxies only, considering integrated properties (including ULIRGs, Kennicutt 1998).

On the other hand, Sargent et al. 2014 chose a sample of 131 main-sequence (MS) galaxies with CO detections and a particular cut-off stellar mass ($M_* \geq 10^{10} M_\odot$), of which 46 percent were low-

Model	α_{1-0}	β_{1-0}
Carilli and F. Walter 2013	1.37 ± 0.04	-1.74 ± 0.40
Sargent et al. 2014	1.23 ± 0.05	-0.67 ± 0.05
T. R. Greve, Leonidaki, et al. 2014	0.99 ± 0.04	1.90 ± 0.40
Kamenetzky et al. 2016	1.27 ± 0.04	-1.00 ± 0.40

Table 6.1: The correlation parameters α_{1-0} and β_{1-0} for $L_{\rm FIR} - L'_{\rm CO(1-0)}$ are tabulated here for various models.

redshift systems ($z < 0.1$) and the remaining 54 percent had redshifts within $0.1 < z < 3.2$. Low redshift samples were detected in the HERA CO Line Extragalactic Survey (**HERACLES**, Leroy, Fabian Walter, Brinks, et al. 2008; Leroy, Fabian Walter, Bigiel, et al. 2009; Leroy, Fabian Walter, Sandstrom, et al. 2013), targeted by the IRAM 30m telescope, which was also augmented by the **COLD GASS** survey (Saintonge et al. 2011). Galaxies beyond $z > 0.1$, were compiled from Geach et al. 2011 ($z \sim 0.4$), Daddi, Elbaz, et al. 2010 ($z \sim 0.5$ and 1.5), the **PHIBSS** survey (Tacconi et al. 2013, $z \sim 1.2$ and 2.3), Georgios E. Magdis et al. 2012 ($z \sim 3$), where all have used the IRAM Plateau de Bure interferometer—and from the **EGNoG** survey (Bauermeister et al. 2013, $0.06 \lesssim z \lesssim 0.3$). Except for Geach et al. 2011 and Bauermeister et al. 2013, the other detections were done using the higher CO transitions, where suitable excitation corrections/line-ratios were used to estimate the CO$(1-0)$ line luminosity. They were able to obtain fitted values of $\alpha_{1-0} = 1.23 \pm 0.05$ and $\beta_{1-0} = -0.67 \pm 0.05$.

Further, T. R. Greve, Leonidaki, et al. 2014 present a set of local ULIRGs ($z < 0.1$) and both lensed ($\mu > 1$) and un-lensed high-redshift ($1.0 \leq z \leq 6.3$) dusty star-forming galaxies (DSFGs), detected in CO emission and derive the correlation between $L_{\rm FIR}$ and $L_{\rm CO}$. The ULIRG data were compiled from the Herschel Comprehensive (U)LIRG Emission Survey (**HerCULES**, van der Werf et al. 2010) and from Papadopoulos et al. 2010. The DSFGs were taken from studies by P. M. Solomon and Vanden Bout 2005; Carilli and F. Walter 2013 and the published CO detections of large-sample DSFGs (T. R. Greve, Bertoldi, et al. 2005; Bothwell et al. 2013). From these samples, T. R. Greve, Leonidaki, et al. 2014 were able to derive $\alpha_{1-0} = 0.99 \pm 0.04$ and $\beta_{1-0} = 1.90 \pm 0.40$.

Finally, Kamenetzky et al. 2016 analysed a combination of galaxies detected from earlier literature such as T. R. Greve, Leonidaki, et al. 2014; Lu et al. 2014; D. Liu et al. 2015 and also used measurements from the Arizona Radio Observatory[1] (**ARO**) and obtain fitted values of $\alpha_{1-0} = 1.27 \pm 0.04$ and $\beta_{1-0} = -1.0 \pm 0.4$. The values of all sets of parameters α_{1-0} and β_{1-0} considered here, are presented in Table 6.1.

[1] https://aro.as.arizona.edu/

6.2.2 Noise

The variance in the cross-correlation signal is given as

$$\mathrm{var}\left[P_{\times}(k)\right] = \frac{1}{2}\left[\frac{P_{\times}^{2}(k) + (P_{\rm CO}(k) + P_{\rm N;CO}(k))(P_{21\rm cm}(k) + P_{\rm N;21cm}(k))}{N_{\rm modes}(k)}\right], \tag{6.1}$$

where we have not taken into account the foregrounds and interlopers for the CO and $[\mathrm{H\,I}]_{21\mathrm{cm}}$ LIM signals. $P_{\times}(k)$ is the CO$\times[\mathrm{H\,I}]_{21\mathrm{cm}}$ cross-power spectrum and $P_{\rm CO}(k)$ and $P_{21\rm cm}(k)$ represent the auto-power spectrum for the CO and the $[\mathrm{H\,I}]_{21\mathrm{cm}}$ signal. $P_{\rm N;CO}(k)$ and $P_{\rm N;21cm}(k)$ are the corresponding noise power spectrum for the CO and the $[\mathrm{H\,I}]_{21\mathrm{cm}}$ survey. The noise power spectrum $P_{\rm N;21cm}(k)$, for the $[\mathrm{H\,I}]_{21\mathrm{cm}}$ observation with **AARTFAAC** is obtained using the tool `ps_eor`[2] (Florent G. Mertens, Bobin, and Carucci 2024). It is assumed that for the **COMAP** survey a total of $12\ \mathrm{deg}^2$ of sky patch will be observed (Breysse, Dongwoo T. Chung, et al. 2022), and for the same area, overlap with the **AARTFAAC** survey is assumed. For the same survey area, and within the frequency band of $169 - 175$ MHz the $[\mathrm{H\,I}]_{21\mathrm{cm}}$ noise power spectrum is simulated assuming a system equivalent flux density (SEFD) of 72 kJy. The $u_{\rm min}$ and $u_{\rm max}$ are kept at 5 and 160 respectively, where $u = b/\lambda_{\rm obs}$ and b is the length of the baseline. The number of k-modes $N_{\rm modes}(k)$ is also obtained from the `ps_eor`. The mock observation is assumed to happen for 6 hours per night, continuing for 200 days in the first scenario accumulating a total of 1200 hours of observation time on **AARTFAAC**. In the second scenario, this is extended to a total of 400 days, thus accumulating a total of 2400 hours with **AARTFAAC**.

The noise power spectrum for the **COMAP** signal is given as

$$P_{\rm N;CO} = \sigma_{\rm N}^{2} V_{\rm vox}, \tag{6.2}$$

where $\sigma_{\rm N}$ is the noise level in a voxel given as $\sigma_{\rm N} = T_{\rm sys}/\sqrt{N_{\rm feeds} n_{\rm pol} \delta\nu t_{\rm pix}}$. $T_{\rm sys}$ is the system temperature for **COMAP**, $N_{\rm feeds}$ is the number of feeds for the dish under consideration. $\delta\nu$ and $t_{\rm pix}$ are the frequency channel width and the effective time per sky pixel, respectively. As described in Breysse, Dongwoo T. Chung, et al. 2022, there **is** expected to be three dishes in the 30 GHz band, one being the pathfinder dish, and the other two will be deployed later. The pathfinder dish is assumed to have a $T_{\rm sys}$ of 44 K, while the newer 30 GHz dishes are expected to have $T_{\rm sys} = 34$ K. The improved $T_{\rm sys}$ is reconciled in terms of an effective observing time, $t_{\rm obs}^{\rm eff}$, by noting that $\sigma_{\rm N} \propto T_{\rm sys}/\sqrt{t_{\rm obs}}$. Therefore, if $t_{\rm obs}^{\rm PF}$ and $t_{\rm obs}^{\rm new}$ are the observation time allocated to the pathfinder and the new 30 GHz dishes, then the effective observation time, $t_{\rm obs}^{\rm eff}$, can be written as (Breysse, Dongwoo T. Chung, et al. 2022)

$$t_{\rm obs}^{\rm eff} = t_{\rm obs}^{\rm PF} + 2\left(\frac{44\mathrm{K}}{34\mathrm{K}}\right)^{2} t_{\rm obs}^{\rm new}. \tag{6.3}$$

[2] https://gitlab.com/flomertens/ps_eor

The contribution from $t_{\text{obs}}^{\text{new}}$ is rescaled according to the improved T_{sys} of 34 K, according to Equation 6.3. Given this, the observation time per sky pixel, t_{pix}, can be written as $t_{\text{pix}} = t_{\text{obs}}^{\text{eff}}(\sigma_{\text{beam}}^2/\Omega_{\text{field}})$, where $\sigma_{\text{beam}}^2 = \theta_{\text{FWHM}}/\sqrt{8\ln 2}$ is the beam size of the instrument and Ω_{field} is the area of the survey which is observed with duration, $t_{\text{obs}}^{\text{eff}}$. V_{vox} is the volume of a voxel, which is assumed to be of width σ_{beam} on one side and with a depth of a single frequency channel, $\delta\nu$.

Following Breysse, Dongwoo T. Chung, et al. 2022, we assume that in the first scenario, the pathfinder campaign accumulates 12000 hours on the old pathfinder dish and 5000 hours on each of the newer 30 GHz dishes, giving approximately $t_{\text{obs}}^{\text{eff}} \approx 29000$ hours, per field, where each field is $\Omega_{\text{field}} \approx 4$ deg^2 with a total of 3 fields. The CO$(2-1)$ signal has a rest frequency of ≈ 230.5 GHz, which can be observed in the 28 GHz band at $z \sim 7.2$. At this frequency, the beam width θ_{FWHM} is assumed to be 4.5 arcmin. $T_{\text{sys}} = 44$ K for this case, since the contribution of the improved system temperature is already taken into account in $t_{\text{obs}}^{\text{eff}}$. $N_{\text{feeds}} = 19$ and $n_{\text{pol}} = 1$ is the number of polarizations for the pathfinder instrument. In the second scenario (COMAP-EoR campaign), we also consider the 16 GHz dish, which will detect the CO$(1-0)$ signal from $z \sim 7.2$ in the 14 GHz band. It has a much lower system temperature of $T_{\text{sys}} = 20$ K and dual polarization feeds, with $N_{\text{feeds}} = 19$ and $n_{\text{pol}} = 2$. The **COMAP-EoR** campaign is assumed to accumulate a total of 7000 dish hours. The frequency channel width is set to $\delta\nu = 2$ MHz, in both the **COMAP-pathfinder** and the **COMAP-EoR** campaigns.

6.3 Results

This section discusses the mock auto and cross-power spectrum for the CO and [H I]$_{21\text{cm}}$LIM signals. In figure 6.1, we show the simulated [H I]$_{21\text{cm}}$signal at $z \sim 7.2$ and $x_{\text{HI}} \sim 0.3$, and also the corresponding signal-to-noise ratio (SNR) with **AARTFAAC** for the two scenarios of 1200 hours (solid) and 2400 hours (dotted) of observation time. It is noted that within the k range of $0.12 - 0.62$ Mpc^{-1}, the maximum SNR is achieved at $k \sim 0.12$ Mpc^{-1} for both scenarios. While at $k \sim 0.12$ Mpc^{-1}, an SNR of $\sim 3.5\sigma$ is achieved with 1200 hours of observation time, this is improved to $\sim 6\sigma$ when the integration time is doubled to 2400 hours. In figure 6.2, the CO$(2-1)$ auto-power spectrum and the CO$(2-1)\times$[H I]$_{21\text{cm}}$ cross-power spectrum are shown along with their corresponding SNR, for various $L_{\text{FIR}} - L'_{\text{CO}(1-0)}$ correlation models, assuming observation with the **COMAP** 30 GHz dishes. In all these models, a constant value of excitation correction ($r_{21} = L_{\text{CO}(2-1)}/L_{\text{CO}(1-0)}$) is used with $r_{21} = 0.76$ (Daddi, Dannerbauer, et al. 2015). We see that for the Sargent et al. 2014; Kamenetzky et al. 2016 models, the SNR is $\sim 4\sigma$ at $k \sim 0.12$ Mpc^{-1}, while it is around $\sim 2.5\sigma$ for Carilli and F. Walter 2013. However, the weakest power spectrum comes from the T. R. Greve, Leonidaki, et al. 2014 model, where the signal has an SNR < 1 and is therefore not detectable in the k ranges considered here. In the cross-power spectrum considering the scenario with 1200 hours of **AARTFAAC** observation time, the SNR for the Sargent et al. 2014; Kamenetzky et al. 2016 models diminishes slightly to $\sim 3.5\sigma$ at $k \sim 0.12$ Mpc^{-1}, while for Carilli and F. Walter 2013, it is slightly improved to $\sim 3\sigma$. However,

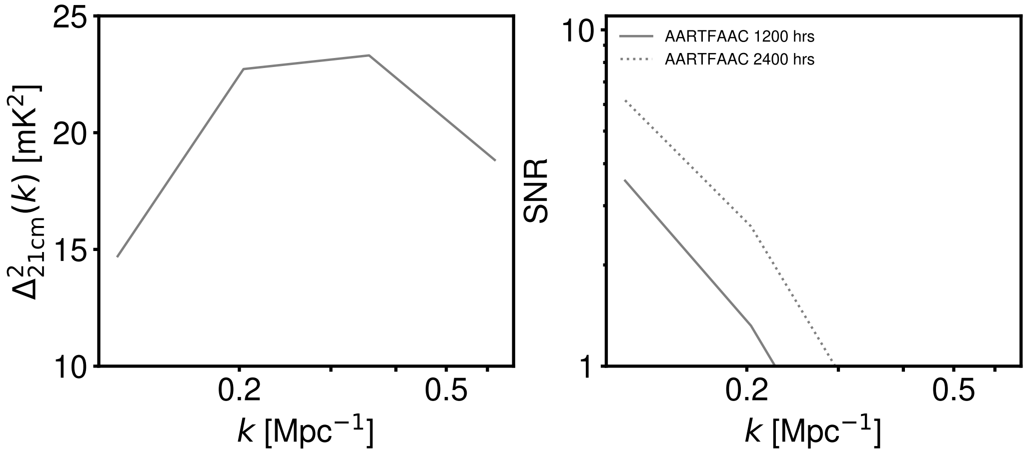

Figure 6.1: Left panel: The [H I]$_{21\rm cm}$ power spectrum is shown at $z \sim 7.2$ and $x_{\rm HI} \sim 0.3$. Right panel: The signal-to-noise ratio (SNR) is shown for 1200 hours (solid) and 2400 hours (dotted) of observation time with **AARTFAAC**.

the notable fact here is that the T. R. Greve, Leonidaki, et al. 2014 model is now detectable with a $\sim 1.5\sigma$ significance in cross-correlation, which is only barely detectable and an improvement over the previous case. This scenario improves further when the T. R. Greve, Leonidaki, et al. 2014 model is detectable with $\sim 2\sigma$ significance when cross-correlation is considered with 2400 hrs of **AARTFAAC** observation time. The rest of the models are detectable within $\sim 4\sigma$ significance for this scenario, for the same k value. This suggests that, for some models, cross-correlation can improve detectability against contamination from instrumental noise.

In figure 6.3 the observation of the $\mathrm{CO}(1-0)$ signal is considered with the **COMAP** 16 GHz dishes (**COMAP-EoR**). The scenario for the $\mathrm{CO}(1-0)$ auto-power spectrum is somewhat similar to that of the $\mathrm{CO}(2-1)$ in the aspect, that the T. R. Greve, Leonidaki, et al. 2014 model is barely detectable with SNR $\sim 1\sigma$. The Carilli and F. Walter 2013 model is detectable with a SNR of $\gtrsim 4\sigma$, while Sargent et al. 2014; Kamenetzky et al. 2016 models are detectable with $\sim 6\sigma$ significance. In the cross-power spectrum, the T. R. Greve, Leonidaki, et al. 2014 model is detectable with at least $\sim 2\sigma$ significance for cross-correlation with 1200 hours of **AARTFAAC** observation and is improved to $\sim 2.5\sigma$ with 2400 hours of **AARTFAAC** observation time at $k \sim 0.12$ Mpc^{-1}. The Carilli and F. Walter 2013 and the Sargent et al. 2014; Kamenetzky et al. 2016 models are detectable with $\sim 4-4.5\sigma$ significance for 1200 hours of **AARTFAAC** observation time, while it improves to $\sim 5\sigma$ for 2400 hours with **AARTFAAC** at $k \sim 0.12$ Mpc^{-1}.

It is noted that the **COMAP-EoR** scenario yields better prospects for detecting the CO signal over the **COMAP-pathfinder**. Overall, the cross-correlation scenario with 2400 hours of observation time with **AARTFAAC**, slightly improves the detectability in most cases over the 1200 hours of observation time with **AARTFAAC**. In cross-correlation, the weakest model, which is the T. R. Greve, Leonidaki, et al. 2014 scenario, is significantly improved over the auto-correlation scenario, where it is barely

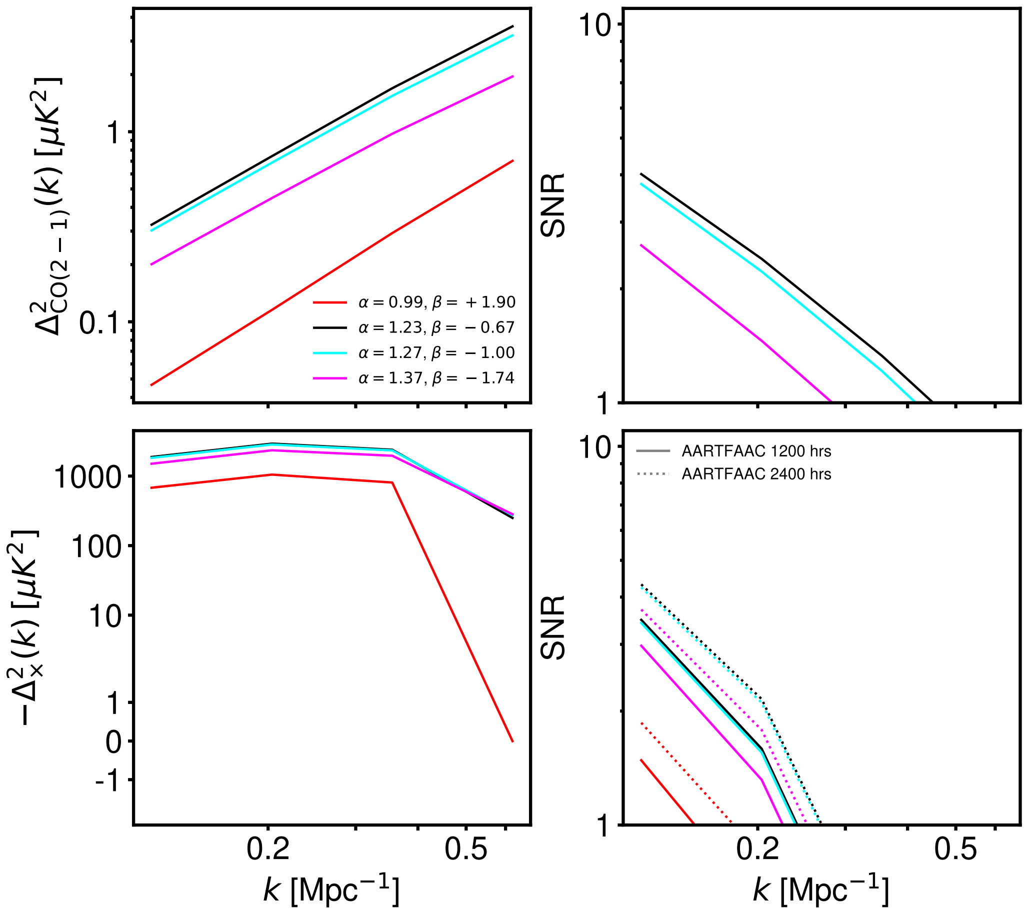

Figure 6.2: Top panel: The $\mathrm{CO}(2-1)$ auto-power spectrum is shown with the corresponding SNR on the right for various $L_{\mathrm{FIR}} - L'_{\mathrm{CO}(1-0)}$ correlation models. Bottom panel: The $\mathrm{CO}(2-1) \times [\mathrm{H\,I}]_{21\mathrm{cm}}$ cross-power spectrum is shown along with the corresponding SNR on the right. The solid and dotted lines on the bottom right panel correspond to the SNR for 1200 hours and 2400 hours of the **AARTFAAC** observation time.

detectable. It is also noted that the various parameter values for α_{1-0} and β_{1-0} considered here are not completely independent of each other. As explained in T. R. Greve, Leonidaki, et al. 2014, both the correlation parameters, α_{1-0} and β_{1-0} are related to f_{dense}. For α_{1-0}, this has been discussed earlier. In the case of β_{1-0}, the f_{dense} plays a role by setting the factor by which β_{1-0} is lower than its Eddington limit set value, in normal star-forming spirals. They argue that the offset $\Delta\beta$, in the $L_{\mathrm{FIR}} - L'_{\mathrm{CO}(1-0)}$ correlation roughly follows, $\Delta\beta \sim \log(f_{\mathrm{dense},2}/f_{\mathrm{dense},1})$, for two different population of galaxies which has varying f_{dense}, $f_{\mathrm{dense},1}$ and $f_{\mathrm{dense},2}$. Therefore, the super-linear slopes of the $L_{\mathrm{FIR}} - L'_{\mathrm{CO}(1-0)}$ correlation due to increasing $f_{\mathrm{dense}}(L_{\mathrm{IR}})$ function, is actually a varying $\beta(L_{\mathrm{IR}})$ function, and there is an anticorrelation between these parameters. In figure 6.4, it is seen that these parameters are anticorrelated with each other. To obtain a correlation fit between these parameters, the `scipy.odr` tool is used from the `SciPy` python package, which deals with uncertainties in both α_{1-0} and β_{1-0}. Assuming a correlation fit of the form $\beta_{1-0} = m\alpha_{1-0} + c$, the values obtained for the fit parameters are $m = -9.85 \pm 0.64$ and

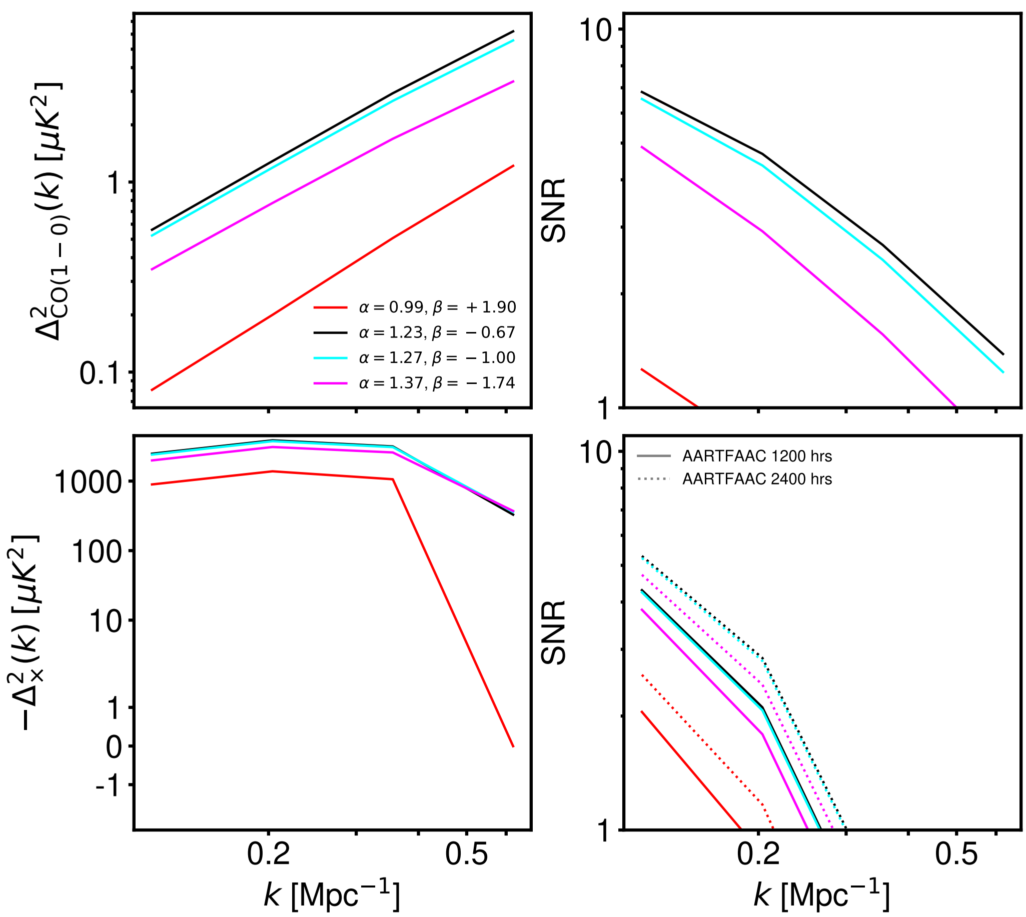

Figure 6.3: Top panel: The $\mathrm{CO}(1-0)$ auto-power spectrum is shown with the corresponding SNR on the right for various $L_{\mathrm{FIR}} - L'_{\mathrm{CO}(1-0)}$ correlation models. Bottom panel: The $\mathrm{CO}(1-0)\times$[H I]$_{21\mathrm{cm}}$ cross-power spectrum is shown along with the corresponding SNR on the right. The solid and dotted lines on the bottom right panel correspond to the SNR for 1200 and 2400 hours of the **AARTFAAC** observation time.

$c = 11.58 \pm 0.78$. Using this relation, we vary α_{1-0} within the range $0.90 - 1.37$ and obtain the corresponding values of β_{1-0}. The goal is to obtain a set of cross-power spectrum for the $\mathrm{CO}(1-0)\times$[H I]$_{21\mathrm{cm}}$ signal, and to estimate the SNR at $k \sim 0.12$ Mpc^{-1} with varying values of α_{1-0}. It will give an idea of the observation scenarios that can rule out certain models of the $L_{\mathrm{FIR}} - L'_{\mathrm{CO}(1-0)}$ correlation. The value of k is fixed at 0.12 Mpc^{-1}, as within the k range $0.12 - 0.62$ Mpc^{-1}, the maximum SNR is obtained in this k mode.

In figure 6.5, the variation of the SNR for the $\mathrm{CO}(1-0)$ power spectrum and the $\mathrm{CO}(1-0)\times$[H I]$_{21\mathrm{cm}}$ cross power spectrum, with continuous variation in α_{1-0} is shown. The variation in SNR vs. α_{1-0} is much steeper in the case of $\mathrm{CO}(1-0)$ power spectrum than the cross-power power spectrum. They intersect at SNR $\sim 3\sigma$ for the $\mathrm{CO}(1-0)$ power spectrum and the $\mathrm{CO}(1-0)\times$[H I]$_{21\mathrm{cm}}$ cross-power spectrum with 1200 hours of **AARTFAAC** observation, which occurs at a α_{1-0} value of ~ 1.12. Above the 3σ level, the $\mathrm{CO}(1-0)$ power spectrum has better SNR, than the $\mathrm{CO}(1-0)\times$[H I]$_{21\mathrm{cm}}$

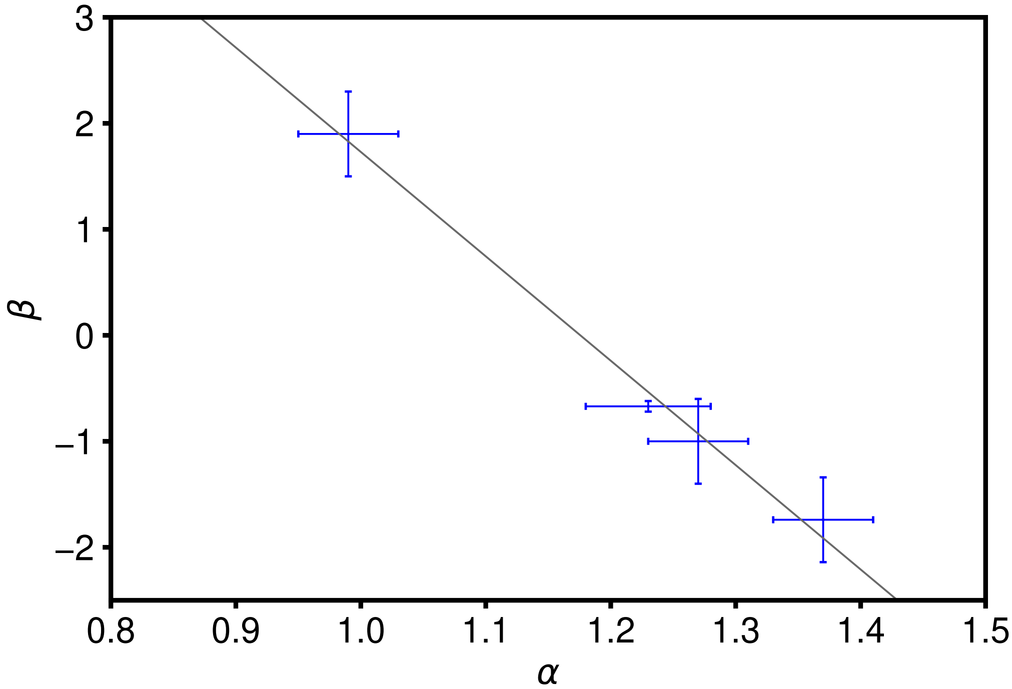

Figure 6.4: The $L_{\mathrm{FIR}} - L'_{\mathrm{CO}(1-0)}$ correlation parameters, α_{1-0} and β_{1-0} are shown here for the various models that have been considered here, along with their uncertainties. The gray line is the correlation fit obtained for these parameters.

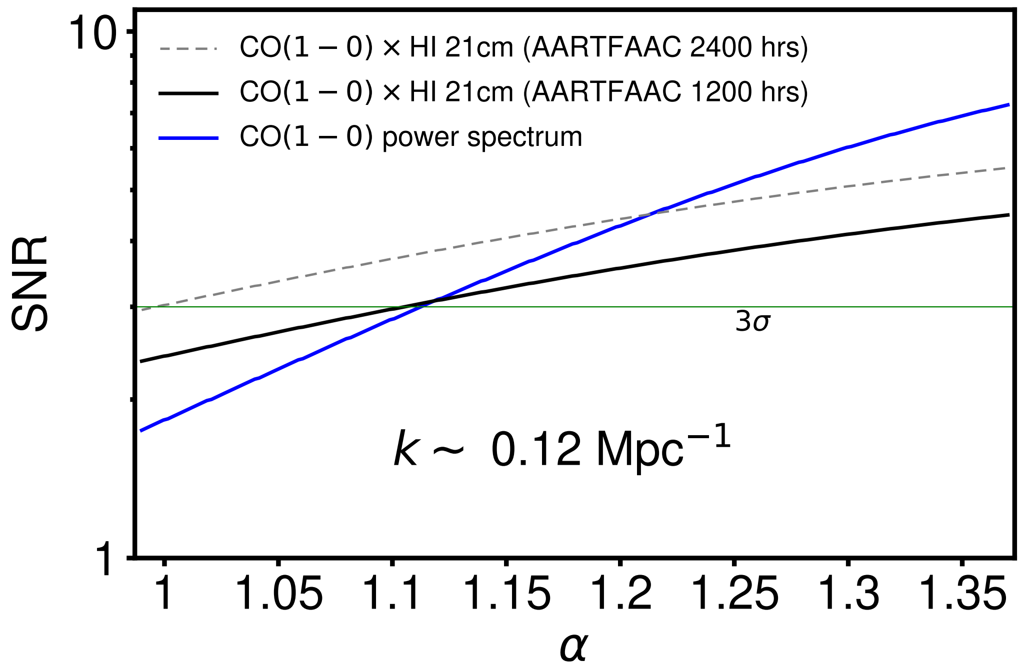

Figure 6.5: This plot shows the SNR of $\mathrm{CO}(1-0)$ auto-power and cross-power spectrum at $k \sim 0.12$ Mpc^{-1} for continuously varying slope (α_{1-0}) of the $L_{\mathrm{FIR}} - L'_{\mathrm{CO}(1-0)}$ correlation.

cross-power spectrum with 1200 hours of **AARTFAAC** observation. Therefore, both can rule out the $L_{\mathrm{FIR}} - L'_{\mathrm{CO}(1-0)}$ correlation models for $\alpha_{1-0} \lesssim 1.2$ at SNR $\gtrsim 3\sigma$. The CO$(1-0)\times$[H I]$_{21\mathrm{cm}}$ cross-power spectrum with 2400 hours of **AARTFAAC** observation is much more sensitive for the lower α_{1-0} values. Therefore, at similar sensitivities of 3σ, it can detect a wider set of $L_{\mathrm{FIR}} - L'_{\mathrm{CO}(1-0)}$ correlations, and it can rule out models with $\alpha_{1-0} \lesssim 0.99$ at SNR $\gtrsim 3\sigma$. Above the 4.5σ significance, the CO$(1-0)$ power spectrum becomes more sensitive than the CO$(1-0)\times$[H I]$_{21\mathrm{cm}}$ cross-power spectrum with 2400 hours of **AARTFAAC** observation and at $\gtrsim 5\sigma$ significance, the power spectrum can rule out models with $\alpha_{1-0} \lesssim 1.24$.

6.4 Discussion & Conclusion

In the post-EoR era, galaxy surveys detected CO emitters and characterized the correlation of the L_{IR} and L'_{CO}. LIM surveys can complement the galaxy surveys in probing the high redshift Universe out to the EoR. With **COMAP**, one can expect the detection of the CO signal in the EoR to shed light on the properties of the early galaxies. However, instrumental noise will challenge the detection of the LIM signal up to EoR. One possible way of tackling this is cross-correlation with another signal, such as the redshift [H I]$_{21\mathrm{cm}}$ signal, originating from a similar cosmic time or redshift. The noise from different instruments is expected to not correlate with each other and, therefore, be subdominant to the cross-correlation signal. A pilot survey with **AARTFAAC** has been considered, which has a wide field of view suitable for cross-correlation with other LIM signals, such as the **COMAP** survey. The detectability of the CO$\times$[H I]$_{21\mathrm{cm}}$ signal is analyzed for different scenarios of **AARTFAAC** and **COMAP** observation, assuming an overlap of 12 deg^2. It is found that for k range $0.12 - 0.62$ Mpc^{-1}, the highest SNR occurs at $k \sim 0.12$ Mpc^{-1} for both auto-power and cross-power spectrum for the CO signals. For the Sargent et al. 2014; Kamenetzky et al. 2016 models, the detectability of the CO$(2-1)$ signal diminishes slightly from $\sim 4\sigma$ to $\sim 3.5\sigma$ significance when considering the cross-power spectrum over the auto-power spectrum with 1200 hours of **AARTFAAC** observation, while the detectability for the Carilli and F. Walter 2013 model slightly improved from $\sim 2.5\sigma$ to $\sim 3\sigma$. With 2400 hours of **AARTFAAC** observation, these three models are detectable with $\sim 4\sigma$ significance in the cross-power spectrum for $k \sim 0.12$ Mpc^{-1}. The prospects for detectability for the CO$(1-0)$ signal are better than for the CO$(2-1)$ signal. The Carilli and F. Walter 2013 model is detectable at $\sim 4\sigma$ while the Sargent et al. 2014; Kamenetzky et al. 2016 models are detectable at $\sim 6\sigma$ in the auto-power spectrum at $k \sim 0.12$ Mpc^{-1}. In cross-correlation, these three models are detectable at $\sim 4\sigma$ and $\sim 5\sigma$ significance for 1200 and 2400 hours of **AARTFAAC** observation.

However, for the weakest model, T. R. Greve, Leonidaki, et al. 2014, the auto power spectrum is not detectable for the CO$(2-1)$ and barely detectable for CO$(1-0)$ signal. This scenario is significantly improved with cross-correlation with **AARTFAAC**, where the CO$(2-1)$ signal is detectable at $\sim 2\sigma$ for 2400 hours of **AARTFAAC** observation. For the CO$(1-0)$ signal, one might achieve $\sim 2\sigma$

and $\sim 2.5\sigma$ detection significance at $k \sim 0.12$ Mpc^{-1}, for 1200 and 2400 hours of **AARTFAAC** observation respectively. It shows that in the worst-case scenario, cross-correlation can increase the detectability of CO LIM signals for the **COMAP** survey.

The α_{1-0} and β_{1-0} are not independent of each other, but rather anticorrelated. A correlation fit is obtained between them, and using this fit, SNR values are obtained for the CO$(1-0)$ power spectrum and cross-power spectrum at $k \sim 0.12$ Mpc^{-1} by continuously varying the α_{1-0} parameter. The CO$(1-0)$ cross-power spectrum has better sensitivity than the power spectrum towards the lower values of α_{1-0} for the $L_{\rm IR}$ and $L'_{\rm CO}$ correlation models. At $\gtrsim 3\sigma$ significance, both the CO$(1-0)$ power spectrum and cross-power spectrum with 1200 hours of **AARTFAAC** observation can rule models with $\alpha_{1-0} \lesssim 1.2$. The CO$(1-0)$ cross-power spectrum with 2400 hours of **AARTFAAC** observation is more sensitive than the power spectrum below 4.5σ detection significance, and above 3σ significance can detect wider range of $L_{\rm IR}$ and $L'_{\rm CO}$ correlation models, with $\alpha \gtrsim 0.99$. However, at $\gtrsim 5\sigma$ significance, the power spectrum has the best sensitivity and can rule out models with $\alpha_{1-0} \lesssim 1.24$.

Chapter 7

Summary

The EoR is one of the most poorly understood epochs of the cosmic evolutionary history. During this epoch, the luminous sources such as galaxies that began to form in the Universe for the first time began to emit copious amounts of Lyman continuum photons, capable of ionizing the neutral hydrogen in the IGM. Understanding the nature of these ionizing sources and the process of cosmic reionization is crucial so that this mysterious epoch can be better comprehended. The earliest probes of cosmic reionization include the measurement of the optical depth of Thomson scattering of the CMB photons, which comes from the scattering of CMB photons from the free electrons released during cosmic reionization. However, the Thomson scattering optical depth is an integrated quantity and does not give an idea about the precise history of reionization. Similarly, analysis of the high redshift quasar absorption spectra and the measurement of the Gunn-Peterson trough have placed constraints on the timing of the end stages of reionization. However, these observations do not give a detailed idea about the EoR, such as the nature of the reionizing sources. Recently, observations with galaxy surveys such as **ALMA** and **JWST** have been able to peer into these early galaxies that drove the cosmic reionization. They have been able to put constraints on quantities like the star-formation rate of these galaxies from a limited number of galaxy samples. However, owing to the small field of view and limited sensitivity thresholds, these surveys are not suitable for probing the large-scale structures of the Universe during the EoR and, therefore, can not provide a complete picture of the EoR.

The LIM is a novel technique that can measure the cumulative flux of the bright spectral line emissions from the individually unresolved galaxies and the diffuse IGM. Therefore, compared to galaxy surveys, it can probe the EoR at large scales with much less observational time, thereby complementing the galaxy surveys. Ongoing/Upcoming LIM experiments, such as **CONCERTO**, **FYST**, and **COMAP**, will essentially map the fluctuations in these spectral line emissions, such as CO and [C II]$_{158\mu\mathrm{m}}$, over the sky, originating from the galaxies. In addition, ongoing/upcoming LIM experiments at radio wavelengths such as **MWA**, **HERA**, and **SKA** will probe the fluctuations in the diffuse [H I]$_{21\mathrm{cm}}$ emission from the EoR originating from the IGM. It is expected to capture astrophysical information about the reionizing sources and the IGM during the EoR and how cosmic reionization has progressed over cosmic time. The multi-phase state of the ISM will introduce scatter in the line luminosity of the emission lines from the galaxies. It can affect the large-scale power spectrum of the LIM signal. Also, varying star-formation histories across the halos will introduce variability in the star-formation rate and halo mass relationship, which can affect the ionizing luminosity of the galaxies. It can leave imprints in the IGM and consequently on the observable [H I]$_{21\mathrm{cm}}$ signal, which might not be adequately probed by the power spectrum but can be probed with the [H I]$_{21\mathrm{cm}}$ bispectrum and is a higher-order statistic. Further, the correlation between far-infrared luminosity and the CO line luminosity in the galaxies, which serves as a good proxy for astrophysical phenomena such as the correlation between the SFR and gas depletion in galaxies, can be probed with CO LIM signals. This is not well explored in the EoR regime. It is also not well explored whether the summary statistic can distinguish between a wide range of far-infrared luminosity and the CO line luminosity correlation models. Therefore, to understand and interpret the LIM observations, one has to forward model the observable LIM summary statistics, which will also be affected by LoS anisotropies and needs to be incorporated in the forward models of the summary statistics, such as the light-cone effect.

Here, an investigation has been done on how the light-cone effect can bias the LIM power spectrum of [C II]$_{158\mu\mathrm{m}}$ line emission from the EoR and also impact the [C II]$_{158\mu\mathrm{m}}$ $\times$[H I]$_{21\mathrm{cm}}$ cross-power spectrum. It is found from the numerical simulations that for a specific redshift, the [C II]$_{158\mu\mathrm{m}}$ power spectrum can be significantly affected ($\gtrsim 15$ percent) by the light-cone effect at the large scales ($k \sim 0.1$ Mpc^{-1}). For the cross-power spectrum of the [C II]$_{158\mu\mathrm{m}}$ and [H I]$_{21\mathrm{cm}}$ LIM signal, the light-cone effect can also significantly bias the summary statistic on similar length scales, reaching up to 20 percent. It is also seen that this impact on the cross-power spectrum changes among the different reionization histories. However, in the [C II]$_{158\mu\mathrm{m}}$ emission model employed here, it is assumed that galaxies hosted in every halo can efficiently emit the [C II]$_{158\mu\mathrm{m}}$ line, whereas one can adopt a more realistic model for the population abundance of galaxies emitting the [C II]$_{158\mu\mathrm{m}}$ line. Although this can cause the estimation of the power spectrum of [C II]$_{158\mu\mathrm{m}}$ emission to be different in comparison to M. Silva et al. 2015, this should negligibly affect the results presented here. There is no redshift dependence in the relation between the [C II]$_{158\mu\mathrm{m}}$ luminosity and the SFR (Equation 1.9) from the M. Silva et al. 2015 model. If this model has a redshift dependence, then the bias introduced on the observed [C II]$_{158\mu\mathrm{m}}$ summary statistics from the light-cone effect can change. In general, the light-cone effect should be incorporated in the forward models of summary statistics.

The [C II]$_{158\mu\mathrm{m}}$ power spectrum can also capture the imprints of line luminosity scatter, which originates from various astrophysical conditions in the ISM. Using results from a pre-simulated hydrodynamical simulation `SIMBA`, which was post-processed with `SIGAME`, it is found that the halo-mass dependent non-uniform scatter in the [C II]$_{158\mu\mathrm{m}}$ luminosity can significantly affect the large-scale power spectrum of [C II]$_{158\mu\mathrm{m}}$ line emission. Using the most probable fit, the large-scale power spectrum can be robustly interpreted, where the scatter has a significant impact. This does not hold for the case using other correlation fits such as the mean fit and the all-sample fit. In this study, the number of galaxy samples from which the line luminosity scatter in the [C II]$_{158\mu\text{m}}$ emission is derived is limited to ∼10,000 however for improved statistical significance of the correlation fits and the conclusions drawn here, a higher sample number is required. Emulation techniques can play a key role in reproducing the line emissions from the galaxies using accurate ISM conditions. It can reduce computational costs to reproduce line emissions for a higher number of galaxy samples. This analysis is also restricted to a single redshift of $z = 6$. The LIM observations might constrain aspects such as the slope of SFR - M_h and L_CII - SFR relations (Karoumpis et al. 2022), using the power spectrum. However, it can be seen from Equation 4.4 that there can arise degeneracy in the power spectrum resulting from different combinations of the L_CII-M_halo relation with varying amplitudes and the value of σ. Therefore, the power spectrum itself might not be enough to infer the magnitude of the scatter, and the bispectrum, a higher-order statistic, might be used to analyze the LIM signal better and constrain the astrophysics underlying it.

Further, it is found that the signatures induced on the [H I]$_{21\text{cm}}$ signal from the EoR by the astrophysical scatter in the SFR of galaxies can be captured using the bispectrum, which is a higher-order Fourier statistic. In this study, a semi-numerical prescription has been used to simulate cosmic reionization and the corresponding [H I]$_{21\text{cm}}$ maps, while taking into account astrophysical scatter in the SFR. Multiple realizations of the scatter are also considered for each neutral fraction in order to evaluate the statistical significance of the impact of this phenomenon, on the summary statistic. The large and intermediate-scale ($k_1 \lesssim 1$ Mpc^{-1}) [H I]$_{21\text{cm}}$ bispectrum is found to be mostly unaffected by the scatter and the impact seen to be present mostly arises from statistical noise in the [H I]$_{21\text{cm}}$ bispectrum. However, at $k_1 \sim 2.55$ Mpc^{-1}, the signatures of variability in the SFR are seen to be significant statistically ($|\Delta B/\sigma_{\Delta B}| \gtrsim 5\sigma$ at $\langle x_\text{HI}\rangle \sim 0.8$) and of high magnitude $0.2 \lesssim |\Delta B/B_{\text{no-scatter}}| \lesssim 1$ for most of the bispectrum triangle configurations at $z = 7$. It can be seen visually, that the impact at the small scales stems from the variation in the ionized bubbles at those scales among the multiple realizations of the scatter. At earlier epochs ($z = 10$), the magnitude of the impact becomes more pronounced $|\Delta B/B_{\text{no-scatter}}| \gtrsim 10$, although less significant statistically ($|\Delta B/\sigma_{\Delta B}| \sim 3\sigma$) for most of the bispectrum triangle configurations at $k_1 \sim 2.55$ Mpc^{-1} for the same neutral fraction of $\langle x_\text{HI}\rangle \sim 0.8$. This is due to the lower number of ionizing sources at the higher redshifts compared to the lower redshifts, which can reduce the statistical significance of the astrophysical scatter. However, the size of the ionized bubbles at higher redshifts for similar neutral fractions is expected to be larger than at the lower redshifts, which can cause the imprints from the astrophysical scatter on the IGM to be more pronounced. It is also found that the imprints from the astrophysical scatter do not cause sign flip in the bispectrum to significantly occur at $z = 7$, except for $z = 10$ at $k_1 \sim 2.55$ Mpc^{-1}, for a substantial part of the triangle configuration space of the bispectrum. At $z = 7$, the prospects of detecting the imprints of astrophysical scatter using the SKA1-Low might be possible with good statistical significance ($3\sigma - 5\sigma$ for $\langle x_\text{HI}\rangle \sim 0.8 - 0.9$), if one assumes a scenario to observe for 1000 hours per year and continue the campaign for 10 years, accumulating a total of 10000 observing hours, which is very optimistic.

However, detection of the lower order statistics such as the CO$\times$[H I]$_{21\mathrm{cm}}$ LIM cross-power spectrum from the EoR can be more promising. Considering the **COMAP** survey for both the Pathfinder and the EoR campaign, the prospects for cross-correlation with a pilot survey by **AARTFAAC** can be useful in detecting the various $L_{\mathrm{FIR}} - L'_{\mathrm{CO}(1-0)}$ correlation models for CO emission signal. Using a combination of radiative transfer output for the [H I]$_{21\mathrm{cm}}$ signal and a semi-analytic prescription for the CO signal, the cross-power spectrum is estimated, and its detectability is calculated for 1200 and 2400 hours of **AARTFAAC** observing time, with the standard **COMAP** campaigns. It is found that given the standard **COMAP** campaigns, the weakest signal in the set of CO emission models considered here can be detected in the cross-correlation signal, which improves on the auto-correlation scenario for both 1200 and 2400 hours of **AARTFAAC** observing time. The CO$(1-0)$ signal has better detection prospects using **COMAP-EoR** campaign than the CO$(2-1)$ signal using the **COMAP-Pathfinder** campaign for the cross-correlation signal. For the CO$(1-0)$ signal, the cross-power spectrum can be detected at $\gtrsim 3\sigma$ significance at $k \sim 0.12\,\mathrm{Mpc}^{-1}$ for a large range of $L_{\mathrm{FIR}} - L'_{\mathrm{CO}(1-0)}$ correlation models for CO emission signal using 2400 hours of **AARTFAAC** observing time. However, for models with $\alpha_{1-0} \gtrsim 1.24$, the CO$(1-0)$ auto-power spectrum has the better prospects for detection, with $\gtrsim 5\sigma$ significance at $k \sim 0.12\,\mathrm{Mpc}^{-1}$.

Overall, the LIM surveys can probe the EoR and help us comprehend the reionizing sources, and the IGM, and how reionization had progressed. To interpret the observable summary statistics, one should consider the LoS anisotropies, such as the light-cone effect, which can significantly impact the cross-power spectrum of [C II]$_{158\mu\mathrm{m}}$and [H I]$_{21\mathrm{cm}}$LIM signal and vary with reionization history. The summary statistics like the power spectrum, can be sensitive to the imprints of the line luminosity scatter, as was found in the case of the LIM signal of [C II]$_{158\mu\mathrm{m}}$ emission. On the other hand, the cosmic [H I]$_{21\mathrm{cm}}$ signal originating from the EoR, which originates from the IGM, is a complementary probe of the EoR in addition to the galaxy LIM surveys and can capture signatures of the astrophysical scatter in the SFR. The detection of the cross-correlation signal in the CO$\times$[H I]$_{21\mathrm{cm}}$cross-power spectrum case looks promising, considering the pilot survey with **AARTFAAC** and the planned survey with **COMAP**. It is expected to improve in future [H I]$_{21\mathrm{cm}}$ surveys with the **SKA**. Therefore, LIM surveys will address critical questions about EoR in the upcoming years.

Chapter 8

Future scope

The studies presented in this thesis are not entirely complete, and further scope exists to extend them in various ways. The models of reionization that have been considered in the investigation of the impact of light-cone on the power spectrum of [C II]$_{158\mu\text{m}}$ LIM signal and the cross-power spectrum of the [C II]$_{158\mu\text{m}}$ and [H I]$_{21\text{cm}}$ LIM signals do not incorporate the effects of density-dependent recombination of ionized hydrogen. When included properly, it will impact the [H I]$_{21\text{cm}}$ morphology and reionization history. It can subsequently affect the light-cone effect on the cross-power spectrum of [C II]$_{158\mu\text{m}}$ and [H I]$_{21\text{cm}}$ LIM signal. For the [C II]$_{158\mu\text{m}}$ LIM signal, the systematics (impact of the interlopers, modeling the foregrounds, and instrumental effects) had not been considered in this study. The emission of the CO line originating from the comparatively low-redshift galaxies (Gong, Cooray, M. Silva, et al. 2012; M. Silva et al. 2015; G. Sun, Moncelsi, et al. 2018) will contaminate the [C II]$_{158\mu\text{m}}$ line emission as interlopers. Similarly, the [H I]$_{21\text{cm}}$ signal will be contaminated by the foregrounds. It has been assumed in this study that the foreground and interloper emissions had been eliminated perfectly from the [H I]$_{21\text{cm}}$ and the [C II]$_{158\mu\text{m}}$ data. However, to achieve this in reality can be a difficult goal. This will contribute to the uncertainties in estimating the observable summary statistics. Finally, the box size of the simulation is restricted to 215 Mpc. The impact of light-cone mostly affects large-scale that has been demonstrated here. For $k \leq 0.1$ Mpc^{-1}, investigating the light-cone effect with improved statistical significance will need a simulation box, with a volume larger than what has been used in the current study. Thus, investigating this for large k-modes with improved statistical significance can be worthwhile. Modeling the light-cone effect analytically is also important, leading to faster evaluation of the impact. These issues can be followed up in future work.

Although the power spectrum of the [C II]$_{158\mu\text{m}}$ LIM signal has been primarily investigated for the impact of non-uniform line luminosity scatter here, using the other line emissions like the [O III]$_{88\mu\text{m}}$, Lyman-α, and CO, a similar analysis can be done. The halo-mass dependence of scatter and how it evolves with redshift would be of interest to study for these line emissions. In this study, the duty cycle of the galaxies has not been considered; the inclusion of which will affect the power spectrum scaling, and the conclusions given here overall will not be affected. The duty cycle is more useful in investigating variation in the scatter, which is time-based. These aspects can be potentially investigated in future follow-up work.

In the analysis of the imprints of variability in the SFR of galaxies on the $[\mathrm{H\ I}]_{21\mathrm{cm}}$ signal, it is assumed that the spin temperature of the neutral hydrogen in the IGM has surpassed the CMB temperature and therefore the term $(1 - T_\gamma(z)/T_\mathrm{s}(\boldsymbol{x}, z))$ (Somnath Bharadwaj and Ali 2005) has achieved saturation. However, as investigated by Fialkov, Barkana, and Visbal 2014, the δT_b fluctuations can be affected by fluctuations in $T_\mathrm{s}(\boldsymbol{x}, z)$, due to late heating of the IGM by X-ray photons from X-ray binaries. Further, these fluctuations can be influenced by the coupling of Lyman-α photons and subsequent heating of the IGM. Ionizing photons from the uniform ionizing background (UIB) contributed by mini-QSOs, or X-ray binaries or AGNs McQuinn 2012; Mesinger, Andrea Ferrara, and Spiegel 2013; Majumdar, Jensen, et al. 2016 can also be incorporated here, besides the ionizing radiation from star-forming galaxies, which is expected to drive the reionization process primarily. In ionized hydrogen, the process of density-dependent recombination can impact the morphology of the cosmic reionization; this has not been taken into account here. Under this collective scenario of all possible ionizing-photon sources, the impact of the astrophysical scatter on the IGM might change in nature. On the other hand, the value of the width of scatter, σ, has been reckoned to be a fixed value throughout the study. The scatter is not well constrained at the EoR redshifts, although here in this study, scatter from the main sequence SFR (Speagle et al. 2014) has been considered. A different value of the width of the scatter, σ, is possible than what has been used in this study if the presence of *bursty* SFR is considered during the EoR, as suggested by recent simulations and observations (Guochao Sun, Mas-Ribas, et al. 2023). Therefore, one can also study how the $[\mathrm{H\ I}]_{21\mathrm{cm}}$ bispectrum can be impacted by astrophysical scatter by using different values of σ, which can also change the nature of the impact. Simulations of $[\mathrm{H\ I}]_{21\mathrm{cm}}$ signal with different σ values and many realizations, that are statistically independent, would be required to understand how varying σ can change this scenario. Furthermore, the inherent LoS anisotropies in the observations, like the light-cone effect and the RSD, have not been incorporated in this particular analysis but can be important for understanding how variability in the SFR can affect the IGM. In the case of $[\mathrm{H\ I}]_{21\mathrm{cm}}$ bispectrum, the impact of light-cone had been analyzed independently (Rajesh Mondal, Mellema, et al. 2021); however, this would be interesting for this analysis as well. The imprints of scatter can affect the small-scale ionized bubbles significantly, and the RSD can distort these ionized bubbles and change the nature of the impact of scatter. As an example, the RSD is known to affect the $[\mathrm{H\ I}]_{21\mathrm{cm}}$ power spectrum significantly ($\gtrsim 40$ percent), when the neutral fraction is high ($\langle x_\mathrm{HI} \rangle \gtrsim 0.8$), as depicted in figure 2 of Mao, Shapiro, et al. 2012. The $[\mathrm{H\ I}]_{21\mathrm{cm}}$ bispectrum is also significantly impacted by RSD (~ 200 percent) at $k_1 \sim 2.37$ Mpc^{-1}, as shown by Majumdar, Kamran, et al. 2020. Therefore, the modulation of the imprints of astrophysical scatter by the LoS anisotropies needs to be investigated further.

The caveats in the detectability analysis of the CO$(1-0)\times[\mathrm{H\ I}]_{21\mathrm{cm}}$ cross-power spectrum is that the foreground and interlopers have not been considered for the $[\mathrm{H\ I}]_{21\mathrm{cm}}$ and CO signal. Recently, Fronenberg and A. Liu 2024 have analyzed the detectability of the [C II]$_{158\mu m}$ $\times$[H I]$_{21cm}$ signal considering **FYST** and **HERA** considering both instrumental noise and foreground and interlopers. In the case of the [H I]$_{21cm}$ signal, it is expected that the foregrounds will dominate by orders of magnitude. For CO emission, the CO$(2-1)$ signal will have the CO$(1-0)$ signal from low redshifts ($z \sim 3$) as an interloper, which is expected to dominate the EoR CO$(2-1)$ signal. However, for the **COMAP-EoR** scenario, we can expect the impact of the interlopers to be less severe than that of the **COMAP-pathfinder**, since for the CO$(1-0)$ signal no other CO lines fall in the 14 GHz band. In cross-correlation, it is expected that the low redshift foregrounds for the [H I]$_{21cm}$ signal will not be correlated with the high redshift CO signal, thus not significantly affecting the cross-correlation signal; however, this should be thoroughly analyzed. It is assumed that the [H I]$_{21cm}$ signal is fixed at a particular neutral fraction for a given redshift. However, uncertainty is expected in the neutral fraction since the reionization history is not well constrained. Therefore, any model variations in the [H I]$_{21cm}$ signal will also correspondingly affect the cross-power spectrum with the CO signal. In turn, it will affect the detectability of the cross-power spectrum for the various correlation models. Here, we have used the pre-simulated mock signal from the radiative transfer output for the [H I]$_{21cm}$ signal, which has a fixed reionization history. Radiative transfer simulations are generally expensive to run, making it difficult to vary the reionization history and source models. However, this can be achieved comparatively less computationally expensively using semi-numerical simulations for the mock [H I]$_{21cm}$ signal. It can allow us to investigate how different reionization scenarios might affect the CO$\times$[H I]$_{21cm}$ cross-power spectrum and its detectability for a given survey scenario, which remains to be seen. Also, the underlying star formation model is assumed to be known and fixed at this high redshift, which is an assumption that can deviate from a more realistic scenario. On the contrary, earlier work such as Breysse, E. D. Kovetz, and Kamionkowski 2016 have considered quite the opposite, where they fix the correlation of the $L_{\rm IR}$ and $L'_{\rm CO}$ to a known value to derive joint constraints on the $\langle T_{\rm CO}\rangle$ and the SFRD. In principle, one can jointly vary the star formation model and the $L_{\rm FIR}$ and $L'_{\rm CO}$ correlation, to investigate the broader prospects of the detectability of the CO LIM signal. Inputs from other independent observations of the high redshift galaxies with **ALMA** and **JWST** might also be valuable to mitigate degeneracies between the star formation models and the $L_{\rm FIR}$ and $L'_{\rm CO}$ correlation in this regard. It will be interesting to see the constraining power of the pilot survey with **AARTFAAC** and the **COMAP** survey with respect to the correlation parameters. As seen from the previous discussion, the correlation parameters can depend on the different types of population of CO emitters (normal galaxies, ULIRGs, etc.) considered. It can be approached with the current survey scenarios using a Fisher analysis. It will provide perspective for future extensions of **COMAP** surveys, such as **COMAP-ERA** (Breysse, Dongwoo T. Chung, et al. 2022), where more dishes will be used for improved detectability. It can be considered in conjunction with future [H I]$_{21cm}$ surveys, such as the **SKA**, where it can be expected that the models for CO emission at EoR can be much better constrained.

Appendix A

Implementation of semi-analytic scatter

This section has been adapted from: **Murmu, C. S.**, Olsen, K. P., Greve, T. R., Majumdar, S., Datta, K. K., Scott, B. R., Leung, T. K. D., Davé, R., Popping, G., Ochoa, R. O., Vizgan, D., & Narayanan, D. (2022). Revisiting the [C II]158μm line-intensity mapping power spectrum from the EoR using non-uniform line-luminosity scatter. *Monthly Notices of the Royal Astronomical Society*, 518(2), 3074–3082, DOI: 10.1093/mnras/stac3304, arXiv: 2110.10687

Here, the comparison between the semi-analytic scatter to that obtained from hydrodynamic simulation is discussed for galaxy LIM. If it is assumed that $L_{\rm m}(M, z)$ is any correlation function between halo-mass and luminosity (corresponding to mode), then the log scatter can be reproduced by

$$\log L = \log L_{\rm m} + \mathcal{N}(0, \sigma^2), \tag{A.1}$$

where $\mathcal{N}(0, \sigma^2)$ represents normal distribution with zero mean and σ^2 variance. The corresponding mean correlation function is then related to $L_{\rm m}$ by

$$\log\langle L\rangle = \log L_{\rm m} + \frac{1}{2}\sigma^2 \ln(10) \tag{A.2}$$

(Guochao Sun, Hensley, et al. 2019; Yang et al. 2022). In this semi-analytic approach, since we use $L_{\rm m}$ as a base for generating scatter, the binned values of modes will lie very close to the correlation function. This is illustrated in figure A.1, using the model from M. Silva et al. 2015 ***m4*** (light-grey curve in figure A.1) as the $L_{\rm m}$. Equation A.1 is used to generate scatter and estimate the binned values of modes (light-blue points in figure A.1), and it is seen that the correlation function almost passes through all the mode values. The same is true for the mean correlation function as well. So when scatter is introduced in this fashion, the binned values will tightly follow the corresponding correlation function. However, the scatter drawn from the hydrodynamic simulation described is different. The

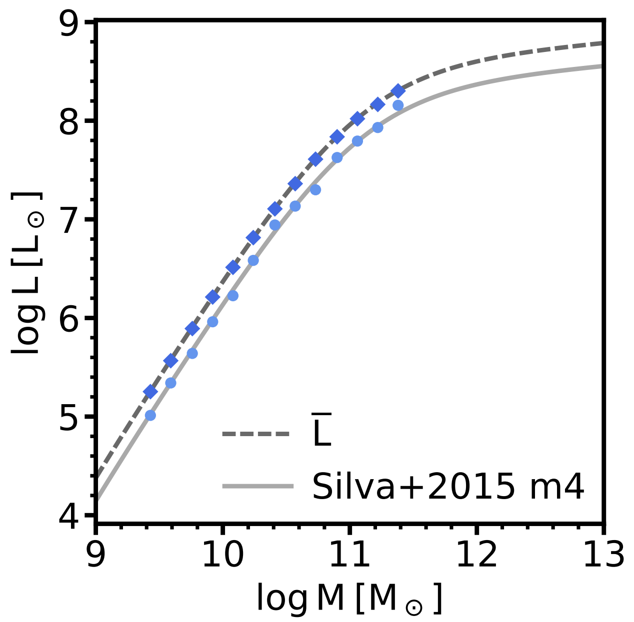

Figure A.1: The solid grey line represents the ***m4*** model (M. Silva et al. 2015) as the most probable fit. The corresponding mean correlation fit is shown in the dashed grey line. The mean fit is obtained by shifting the most probable fit using equation (A.2). The corresponding points are the binned values (modes and arithmetic mean) for the correlation fits derived from the implemented line-luminosity scatter. It is noted that the points tightly follow the respective correlation fits.

origin of this is the more accurate astrophysics implemented in the simulation. The result is that the binned values of modes (or the mean, for that matter) do not follow the correlation function tightly. They fluctuate stochastically, which makes some aspects different. The relation A.2 does not hold necessarily, i.e., if σ_{avg} is the average value of the scatter parameter, then it is possible that

$$\log\langle L\rangle \neq \log L_{\text{m}} + \frac{1}{2}\sigma_{\text{avg}}^2 \ln(10). \tag{A.3}$$

If $\log L_{\text{m}}$ is shifted by $\sigma_{\text{avg}}^2 \ln(10)/2$, it no longer corresponds to the mean correlation function. This is demonstrated by showing that an independently obtained mean correlation function doesn't keep the mean intensity invariant. From this perspective, the most-probable fit is a more robust approach to interpret the mean intensity and power spectrum of the LIM signal, even under non-uniform line-luminosity scatter.

Bibliography

Planck Collaboration, N. Aghanim, Y. Akrami, F. Arroja, et al. (Sept. 2020). "Planck 2018 results. I. Overview and the cosmological legacy of Planck". In: *Astronomy & Astrophysics* 641, A1. DOI: 10.1051/0004-6361/201833880. arXiv: 1807.06205 [astro-ph.CO].

Bennett, C. L. et al. (Oct. 2013). "Nine-year Wilkinson Microwave Anisotropy Probe (WMAP) Observations: Final Maps and Results". In: *The Astrophysical Journal Supplement Series* 208.2, p. 20. DOI: 10.1088/0067-0049/208/2/20. arXiv: 1212.5225 [astro-ph.CO].

Mentuch Cooper, Erin et al. (Feb. 2023). "HETDEX Public Source Catalog 1: 220 K Sources Including Over 50 K Lyα Emitters from an Untargeted Wide-area Spectroscopic Survey". In: *The Astrophysical Journal* 943.2, p. 177. DOI: 10.3847/1538-4357/aca962. arXiv: 2301.01826 [astro-ph.GA].

McQuinn, Matthew (Oct. 2012). "Constraints on X-ray emissions from the reionization era". In: *Monthly Notices of the Royal Astronomical Society* 426.2, pp. 1349–1360. DOI: 10.1111/j.1365-2966.2012.21792.x. arXiv: 1206.1335 [astro-ph.CO].

Mesinger, Andrei, Andrea Ferrara, and David S. Spiegel (May 2013). "Signatures of X-rays in the early Universe". In: *Monthly Notices of the Royal Astronomical Society* 431.1, pp. 621–637. DOI: 10.1093/mnras/stt198. arXiv: 1210.7319 [astro-ph.CO].

Majumdar, Suman, Hannes Jensen, et al. (Feb. 2016). "Effects of the sources of reionization on 21-cm redshift-space distortions". In: *Monthly Notices of the Royal Astronomical Society* 456.2, pp. 2080–2094. DOI: 10.1093/mnras/stv2812. arXiv: 1509.07518 [astro-ph.CO].

Gnedin, Nickolay Y. (June 2000). "Cosmological Reionization by Stellar Sources". In: *The Astrophysical Journal* 535.2, pp. 530–554. DOI: 10.1086/308876. arXiv: astro-ph/9909383 [astro-ph].

Madau, Piero and J. Michael Shull (Feb. 1996). "Cosmic Metal Production and the Contribution of QSO Absorption Systems to the Ionizing Background". In: *The Astrophysical Journal* 457, p. 551. DOI: 10.1086/176751. arXiv: astro-ph/9509136 [astro-ph].

Madau, Piero, Francesco Haardt, and Martin J. Rees (Apr. 1999). "Radiative Transfer in a Clumpy Universe. III. The Nature of Cosmological Ionizing Sources". In: *The Astrophysical Journal* 514.2, pp. 648–659. DOI: 10.1086/306975. arXiv: astro-ph/9809058 [astro-ph].

Loeb, Abraham and Rennan Barkana (Jan. 2001). “The Reionization of the Universe by the First Stars and Quasars”. In: *Annual Review of Astronomy and Astrophysics* 39, pp. 19–66. DOI: 10.1146/annurev.astro.39.1.19. arXiv: astro-ph/0010467 [astro-ph].

Mather, John C. (Mar. 1994). “Infrared measurements from the Cosmic Background Explorer (COBE)”. In: *Infrared Physics and Technology* 35.2-3, pp. 331–336. DOI: 10.1016/1350-4495(94)90091-4.

Wright, E. L. et al. (Jan. 1994). “Interpretation of the COBE FIRAS CMBR Spectrum”. In: *The Astrophysical Journal* 420, p. 450. DOI: 10.1086/173576.

Griffiths, Louise M., Domingos Barbosa, and Andrew R. Liddle (Sept. 1999). “Cosmic microwave background constraints on the epoch of reionization”. In: *Monthly Notices of the Royal Astronomical Society* 308.3, pp. 854–862. DOI: 10.1046/j.1365-8711.1999.02777.x. arXiv: astro-ph/9812125 [astro-ph].

Venkatesan, Aparna (July 2000). “The Optical Depth to Reionization as a Probe of Cosmological and Astrophysical Parameters”. In: *The Astrophysical Journal* 537.1, pp. 55–64. DOI: 10.1086/309033. arXiv: astro-ph/9912401 [astro-ph].

Shull, Michael and Aparna Venkatesan (Feb. 2007). “Optical Depth of the Cosmic Microwave Background and Reionization of the Intergalactic Medium”. In: *arXiv e-prints*, astro-ph/0702323, astro–ph/0702323. DOI: 10.48550/arXiv.astro-ph/0702323. arXiv: astro-ph/0702323 [astro-ph].

Lewis, Antony (July 2008). “Cosmological parameters from WMAP 5-year temperature maps”. In: *Physical Review D* 78.2, 023002, p. 023002. DOI: 10.1103/PhysRevD.78.023002. arXiv: 0804.3865 [astro-ph].

Becker, Robert H. et al. (Dec. 2001). “Evidence for Reionization at z~6: Detection of a Gunn-Peterson Trough in a z=6.28 Quasar”. In: *The Astronomical Journal* 122.6, pp. 2850–2857. DOI: 10.1086/324231. arXiv: astro-ph/0108097 [astro-ph].

Fan, Xiaohui et al. (Mar. 2002). “Evolution of the Ionizing Background and the Epoch of Reionization from the Spectra of z~6 Quasars”. In: *The Astronomical Journal* 123.3, pp. 1247–1257. DOI: 10.1086/339030. arXiv: astro-ph/0111184 [astro-ph].

Becker, George D., James S. Bolton, Yongda Zhu, et al. (Sept. 2024). “Damping wing absorption associated with a giant Ly α trough at z < 6: direct evidence for late-ending reionization”. In: *Monthly Notices of the Royal Astronomical Society* 533.2, pp. 1525–1540. DOI: 10.1093/mnras/stae1918. arXiv: 2405.08885 [astro-ph.CO].

Colless, Matthew et al. (June 2003). “The 2dF Galaxy Redshift Survey: Final Data Release”. In: *arXiv e-prints*, astro-ph/0306581, astro–ph/0306581. DOI: 10.48550/arXiv.astro-ph/0306581. arXiv: astro-ph/0306581 [astro-ph].

Jones, D. Heath et al. (Oct. 2009). “The 6dF Galaxy Survey: final redshift release (DR3) and southern large-scale structures”. In: *Monthly Notices of the Royal Astronomical Society* 399.2, pp. 683–698. DOI: 10.1111/j.1365-2966.2009.15338.x. arXiv: 0903.5451 [astro-ph.CO].

Drinkwater, Michael J. et al. (Mar. 2018). “The WiggleZ Dark Energy Survey: final data release and the metallicity of UV-luminous galaxies”. In: *Monthly Notices of the Royal Astronomical Society* 474.3, pp. 4151–4168. DOI: 10.1093/mnras/stx2963. arXiv: 1910.08284 [astro-ph.GA].

Driver, Simon P. et al. (June 2022). “Galaxy And Mass Assembly (GAMA): Data Release 4 and the $z < 0.1$ total and $z < 0.08$ morphological galaxy stellar mass functions”. In: *Monthly Notices of the Royal Astronomical Society* 513.1, pp. 439–467. DOI: 10.1093/mnras/stac472. arXiv: 2203.08539 [astro-ph.GA].

Almeida, Andrés et al. (Aug. 2023). “The Eighteenth Data Release of the Sloan Digital Sky Surveys: Targeting and First Spectra from SDSS-V”. In: *The Astrophysical Journal Supplement Series* 267.2, p. 44. DOI: 10.3847/1538-4365/acda98. arXiv: 2301.07688 [astro-ph.GA].

DESI Collaboration et al. (Aug. 2024). “The Early Data Release of the Dark Energy Spectroscopic Instrument”. In: *The Astronomical Journal* 168.2, p. 58. DOI: 10.3847/1538-3881/ad3217. arXiv: 2306.06308 [astro-ph.CO].

Davis, Dustin, Karl Gebhardt, Erin Mentuch Cooper, Robin Ciardullo, et al. (Apr. 2023). “The HETDEX Survey Emission-line Exploration and Source Classification”. In: *The Astrophysical Journal* 946.2, p. 86. DOI: 10.3847/1538-4357/acb0ca. arXiv: 2301.01799 [astro-ph.GA].

Davis, Dustin, Karl Gebhardt, Erin Mentuch Cooper, William P. Bowman, et al. (Sept. 2023). “HETDEX Public Source Catalog 1-Stacking 50,000 Lyman Alpha Emitters”. In: *The Astrophysical Journal* 954.2, p. 209. DOI: 10.3847/1538-4357/ace4c2. arXiv: 2307.03096 [astro-ph.GA].

Watanabe, Naoki and Akira Kouchi (Dec. 2008). “Ice surface reactions: A key to chemical evolution in space”. In: *Progress in Surface Science* 83.10–12, pp. 439–489. ISSN: 0079-6816. DOI: 10.1016/j.progsurf.2008.10.001. URL: http://dx.doi.org/10.1016/j.progsurf.2008.10.001.

Wootten, Alwyn and A. Richard Thompson (Aug. 2009). “The Atacama Large Millimeter/Submillimeter Array”. In: *IEEE Proceedings* 97.8, pp. 1463–1471. DOI: 10.1109/JPROC.2009.2020572. arXiv: 0904.3739 [astro-ph.IM].

Gallerani, S. et al. (Jan. 2018). “ALMA suggests outflows in $z \sim 5.5$ galaxies”. In: *Monthly Notices of the Royal Astronomical Society* 473.2, pp. 1909–1917. DOI: 10.1093/mnras/stx2458. arXiv: 1604.05714 [astro-ph.GA].

Heckman, Timothy M. et al. (Aug. 2015). “The Systematic Properties of the Warm Phase of Starburst-Driven Galactic Winds”. In: *The Astrophysical Journal* 809.2, p. 147. DOI: 10.1088/0004-637X/809/2/147. arXiv: 1507.05622 [astro-ph.GA].

Zavala, J. A. et al. (Dec. 2018). “Constraining the Volume Density of Dusty Star-forming Galaxies through the First 3 mm Number Counts from ALMA”. In: *The Astrophysical Journal* 869.1, p. 71. DOI: 10.3847/1538-4357/aaecd2. arXiv: 1810.12300 [astro-ph.GA].

Le Fèvre, O. et al. (Nov. 2020). “The ALPINE-ALMA [CII] survey. Survey strategy, observations, and sample properties of 118 star-forming galaxies at $4 < z < 6$”. In: *Astronomy & Astrophysics* 643, A1. DOI: 10.1051/0004-6361/201936965. arXiv: 1910.09517 [astro-ph.CO].

De Looze, Ilse, Diane Cormier, et al. (Aug. 2014). “The applicability of far-infrared fine-structure lines as star formation rate tracers over wide ranges of metallicities and galaxy types”. In: *Astronomy & Astrophysics* 568, A62. DOI: 10.1051/0004-6361/201322489. arXiv: 1402.4075 [astro-ph.GA].

Bouwens, R. J. et al. (June 2022). “Reionization Era Bright Emission Line Survey: Selection and Characterization of Luminous Interstellar Medium Reservoirs in the z > 6.5 Universe”. In: *The Astrophysical Journal* 931.2, p. 160. DOI: 10.3847/1538-4357/ac5a4a. arXiv: 2106.13719 [astro-ph.GA].

Endsley, Ryan et al. (Dec. 2022). “The REBELS ALMA Survey: efficient Ly α transmission of UV-bright $z \simeq 7$ galaxies from large velocity offsets and broad line widths”. In: *Monthly Notices of the Royal Astronomical Society* 517.4, pp. 5642–5659. DOI: 10.1093/mnras/stac3064. arXiv: 2202.01219 [astro-ph.GA].

Sommovigo, L. et al. (July 2022). “The ALMA REBELS Survey: cosmic dust temperature evolution out to $z \sim 7$”. In: *Monthly Notices of the Royal Astronomical Society* 513.3, pp. 3122–3135. DOI: 10.1093/mnras/stac302. arXiv: 2202.01227 [astro-ph.GA].

Topping, Michael W. et al. (Oct. 2022). “The ALMA REBELS Survey: specific star formation rates in the reionization era”. In: *Monthly Notices of the Royal Astronomical Society* 516.1, pp. 975–991. DOI: 10.1093/mnras/stac2291. arXiv: 2203.07392 [astro-ph.GA].

Fudamoto, Y. et al. (Aug. 2022). “The ALMA REBELS Survey: Average [C II] 158 μm Sizes of Star-forming Galaxies from z 7 to z 4”. In: *The Astrophysical Journal* 934.2, p. 144. DOI: 10.3847/1538-4357/ac7a47. arXiv: 2206.01886 [astro-ph.GA].

Barrufet, L., P. A. Oesch, R. Bouwens, et al. (July 2023). “The ALMA REBELS Survey: the first infrared luminosity function measurement at z $\sim$ 7”. In: *Monthly Notices of the Royal Astronomical Society* 522.3, pp. 3926–3934. DOI: 10.1093/mnras/stad1259. arXiv: 2303.11321 [astro-ph.GA].

Harikane, Yuichi et al. (June 2020). “Large Population of ALMA Galaxies at z > 6 with Very High [O III] 88 μm to [C II] 158 μm Flux Ratios: Evidence of Extremely High Ionization Parameter or PDR Deficit?” In: *The Astrophysical Journal* 896.2, p. 93. DOI: 10.3847/1538-4357/ab94bd. arXiv: 1910.10927 [astro-ph.GA].

Leethochawalit, N. et al. (Jan. 2023). “Early Results from GLASS-JWST. X. Rest-frame UV-optical Properties of Galaxies at 7 < z < 9”. In: *The Astrophysical Journal Letters* 942.2, p. L26. DOI: 10.3847/2041-8213/ac959b. arXiv: 2207.11135 [astro-ph.GA].

Santini, P. et al. (Jan. 2023). “Early Results from GLASS-JWST. XI. Stellar Masses and Mass-to-light Ratio of z > 7 Galaxies”. In: *The Astrophysical Journal Letters* 942.2, p. L27. DOI: 10.3847/2041-8213/ac9586. arXiv: 2207.11379 [astro-ph.GA].

Nanayakkara, Themiya et al. (Apr. 2023). “Early Results from GLASS-JWST. XVI. Discovering a Bluer z 4-7 Universe through UV Slopes”. In: *The Astrophysical Journal Letters* 947.2, p. L26. DOI: 10.3847/2041-8213/acbfb9. arXiv: 2207.13860 [astro-ph.GA].

Chen, Zuyi et al. (Feb. 2023). “JWST/NIRCam observations of stars and H II regions in $z \simeq 6-8$ galaxies: properties of star-forming complexes on 150 pc scales”. In: *Monthly Notices of the Royal Astronomical Society* 518.4, pp. 5607–5619. DOI: 10.1093/mnras/stac3476. arXiv: 2207.12657 [astro-ph.GA].

Barrufet, L., P. A. Oesch, A. Weibel, et al. (June 2023). “Unveiling the nature of infrared bright, optically dark galaxies with early JWST data”. In: *Monthly Notices of the Royal Astronomical Society* 522.1, pp. 449–456. DOI: 10.1093/mnras/stad947. arXiv: 2207.14733 [astro-ph.GA].

Mascia, S., L. Pentericci, A. Calabrò, T. Treu, et al. (Apr. 2023). “Closing in on the sources of cosmic reionization: First results from the GLASS-JWST program”. In: *Astronomy & Astrophysics* 672, A155. DOI: 10.1051/0004-6361/202345866. arXiv: 2301.02816 [astro-ph.GA].

Mascia, S., L. Pentericci, A. Calabrò, P. Santini, et al. (May 2024). “New insight on the nature of cosmic reionizers from the CEERS survey”. In: *Astronomy & Astrophysics* 685, A3. DOI: 10.1051/0004-6361/202347884. arXiv: 2309.02219 [astro-ph.GA].

Umeda, Hiroya et al. (Aug. 2024). “JWST Measurements of Neutral Hydrogen Fractions and Ionized Bubble Sizes at z = 7–12 Obtained with Lyα Damping Wing Absorptions in 27 Bright Continuum Galaxies”. In: *The Astrophysical Journal* 971.2, p. 124. DOI: 10.3847/1538-4357/ad554e. arXiv: 2306.00487 [astro-ph.GA].

Saxena, Aayush et al. (Apr. 2024). “JADES: The production and escape of ionizing photons from faint Lyman-alpha emitters in the epoch of reionization”. In: *Astronomy & Astrophysics* 684, A84. DOI: 10.1051/0004-6361/202347132. arXiv: 2306.04536 [astro-ph.GA].

Muñoz, Julian B. et al. (Apr. 2024). “Reionization after JWST: a photon budget crisis?” In: *arXiv e-prints*, arXiv:2404.07250, arXiv:2404.07250. DOI: 10.48550/arXiv.2404.07250. arXiv: 2404.07250 [astro-ph.CO].

Melia, F. (Sept. 2024). “The cosmic timeline implied by the JWST reionization crisis”. In: *Astronomy & Astrophysics* 689, A10. DOI: 10.1051/0004-6361/202450835. arXiv: 2407.01581 [astro-ph.CO].

Melia, F. and A. S. H. Shevchuk (Jan. 2012). “The R_h=ct universe”. In: *Monthly Notices of the Royal Astronomical Society* 419.3, pp. 2579–2586. DOI: 10.1111/j.1365-2966.2011.19906.x. arXiv: 1109.5189 [astro-ph.CO].

Melia, F. (May 2013). “The R_h = ct universe without inflation”. In: *Astronomy & Astrophysics* 553, A76. DOI: 10.1051/0004-6361/201220447. arXiv: 1206.6527 [astro-ph.CO].

Melia, Fulvio (Dec. 2018). “A comparison of the R_h = ct and ΛCDM cosmologies using the cosmic distance duality relation”. In: *Monthly Notices of the Royal Astronomical Society* 481.4, pp. 4855–4862. DOI: 10.1093/mnras/sty2596. arXiv: 1804.09906 [astro-ph.CO].

— (Mar. 2021). “Thermodynamics of the R_h=c t Universe: a simplification of cosmic entropy”. In: *European Physical Journal C* 81.3, p. 234. DOI: 10.1140/epjc/s10052-021-09028-5. arXiv: 2103.03933 [astro-ph.CO].

— (Sept. 2023a). “Validation of the Numen Field by the Energy Conditions in the Early Universe”. In: *Annalen der Physik* 535.9, p. 2300157. DOI: 10.1002/andp.202300157.

— (Dec. 2023b). “A resolution of the monopole problem in the R_h = ct Universe”. In: *Physics of the Dark Universe* 42, p. 101329. DOI: 10.1016/j.dark.2023.101329. arXiv: 2309.10009 [hep-ph].

Gong, Yan, Asantha Cooray, Marta Silva, et al. (Jan. 2012). “Intensity Mapping of the [C II] Fine Structure Line during the Epoch of Reionization”. In: *The Astrophysical Journal* 745.1, p. 49. DOI: 10.1088/0004-637X/745/1/49. arXiv: 1107.3553 [astro-ph.CO].

Malhotra, S. et al. (Nov. 2001). “Far-Infrared Spectroscopy of Normal Galaxies: Physical Conditions in the Interstellar Medium”. In: *The Astrophysical Journal* 561.2, pp. 766–786. DOI: 10.1086/323046. arXiv: astro-ph/0106485 [astro-ph].

Lehner, N., B. P. Wakker, and B. D. Savage (Nov. 2004). “C II Radiative Cooling of the Diffuse Gas in the Milky Way”. In: *The Astrophysical Journal* 615.2, pp. 767–793. DOI: 10.1086/424730. arXiv: astro-ph/0407363 [astro-ph].

Suginohara, Maki, Tatsushi Suginohara, and David N. Spergel (Feb. 1999). “Detecting z>10 Objects through Carbon, Nitrogen, and Oxygen Emission Lines”. In: *The Astrophysical Journal* 512.2, pp. 547–552. DOI: 10.1086/306787. arXiv: astro-ph/9803236 [astro-ph].

De Looze, Ilse, Maarten Baes, et al. (Oct. 2011). “The reliability of [C II] as an indicator of the star formation rate”. In: *Monthly Notices of the Royal Astronomical Society* 416.4, pp. 2712–2724. DOI: 10.1111/j.1365-2966.2011.19223.x. arXiv: 1106.1643 [astro-ph.CO].

Olsen, Karen P., Thomas R. Greve, Desika Narayanan, Robert Thompson, Sune Toft, et al. (Nov. 2015). “Simulator of Galaxy Millimeter/Submillimeter Emission (SíGAME): The [C ii]-SFR Relationship of Massive $z = 2$ Main Sequence Galaxies”. In: *The Astrophysical Journal* 814.1, p. 76. DOI: 10.1088/0004-637X/814/1/76. arXiv: 1507.00362 [astro-ph.GA].

Kennicutt Robert C., Jr. (May 1998). "The Global Schmidt Law in Star-forming Galaxies". In: *The Astrophysical Journal* 498.2, pp. 541–552. DOI: 10.1086/305588. arXiv: astro-ph/9712213 [astro-ph].

Schmidt, Maarten (Mar. 1959). "The Rate of Star Formation." In: *The Astrophysical Journal* 129, p. 243. DOI: 10.1086/146614.

Pineda, J. L., T. Velusamy, et al. (Oct. 2010). "A sample of [C II] clouds tracing dense clouds in weak FUV fields observed by Herschel". In: *Astronomy & Astrophysics* 521, p. L19. DOI: 10.1051/0004-6361/201015089. arXiv: 1007.5068 [astro-ph.GA].

Schaerer, D. et al. (Nov. 2020). "The ALPINE-ALMA [C II] survey. Little to no evolution in the [C II]-SFR relation over the last 13 Gyr". In: *Astronomy & Astrophysics* 643, A3. DOI: 10.1051/0004-6361/202037617. arXiv: 2002.00979 [astro-ph.GA].

Townes, C.H. and A.L. Schawlow (1975). *Microwave Spectroscopy*. Dover Books on Physics. Dover Publications. ISBN: 9780486617985. URL: https://books.google.co.in/books?id=nI9bSU8hxusC.

Young, J. S. and N. Z. Scoville (Jan. 1991). "Molecular gas in galaxies." In: *Annual Review of Astronomy and Astrophysics* 29, pp. 581–625. DOI: 10.1146/annurev.aa.29.090191.003053.

Bernal, José Luis and Ely D. Kovetz (Dec. 2022). "Line-intensity mapping: theory review with a focus on star-formation lines". In: *The Astronomy and Astrophysics Review* 30.1, p. 5. DOI: 10.1007/s00159-022-00143-0. arXiv: 2206.15377 [astro-ph.CO].

Wouthuysen, S. A. (Jan. 1952). "On the excitation mechanism of the 21-cm (radio-frequency) interstellar hydrogen emission line." In: *The Astronomical Journal* 57, pp. 31–32. DOI: 10.1086/106661.

Field, George B. (Jan. 1958). "Excitation of the Hydrogen 21-CM Line". In: *Proceedings of the IRE* 46, pp. 240–250. DOI: 10.1109/JRPROC.1958.286741.

Madau, Piero, Avery Meiksin, and Martin J. Rees (Feb. 1997). "21 Centimeter Tomography of the Intergalactic Medium at High Redshift". In: *The Astrophysical Journal* 475.2, pp. 429–444. DOI: 10.1086/303549. arXiv: astro-ph/9608010 [astro-ph].

Bharadwaj, Somnath and Sk. Saiyad Ali (July 2004). "The cosmic microwave background radiation fluctuations from HI perturbations prior to reionization". In: *Monthly Notices of the Royal Astronomical Society* 352.1, pp. 142–146. DOI: 10.1111/j.1365-2966.2004.07907.x. arXiv: astro-ph/0401206 [astro-ph].

— (Feb. 2005). "On using visibility correlations to probe the HI distribution from the dark ages to the present epoch - I. Formalism and the expected signal". In: *Monthly Notices of the Royal Astronomical Society* 356.4, pp. 1519–1528. DOI: 10.1111/j.1365-2966.2004.08604.x. arXiv: astro-ph/0406676 [astro-ph].

Kim, Han-Seek et al. (Jan. 2013). "The structure of reionization in hierarchical galaxy formation models". In: *Monthly Notices of the Royal Astronomical Society* 428.3, pp. 2467–2479. DOI: 10.1093/mnras/sts206. arXiv: 1203.3598 [astro-ph.CO].

McQuinn, Matthew et al. (May 2007). “The morphology of HII regions during reionization”. In: *Monthly Notices of the Royal Astronomical Society* 377.3, pp. 1043–1063. DOI: 10.1111/j.1365-2966.2007.11489.x. arXiv: astro-ph/0610094 [astro-ph].

Yue, Bin et al. (Oct. 2009). “The contribution of the IGM and minihaloes to the 21-cm signal of reionization”. In: *Monthly Notices of the Royal Astronomical Society* 398.4, pp. 2122–2133. DOI: 10.1111/j.1365-2966.2009.15261.x. arXiv: 0906.3105 [astro-ph.CO].

Noble, Leon et al. (June 2024). “Impact of the Epoch of Reionization sources on the 21-cm bispectrum”. In: *arXiv e-prints*, arXiv:2406.03118. DOI: 10.48550/arXiv.2406.03118. arXiv: 2406.03118 [astro-ph.CO].

Mellema, Garrelt, Leon Koopmans, et al. (2015). “HI tomographic imaging of the Cosmic Dawn and Epoch of Reionization with SKA”. In: *Proceedings of Advancing Astrophysics with the Square Kilometre Array — PoS(AASKA14)*. Vol. 215, p. 010. DOI: 10.22323/1.215.0010.

Wang, Yougang et al. (2015). “Topology of neutral hydrogen distribution with the Square Kilometre Array”. In: *PoS* AASKA14, p. 033. DOI: 10.22323/1.215.0033.

Ghara, Raghunath, Sambit K. Giri, et al. (May 2021). “Constraining the state of the intergalactic medium during the Epoch of Reionization using MWA 21-cm signal observations”. In: *Monthly Notices of the Royal Astronomical Society* 503.3, pp. 4551–4562. DOI: 10.1093/mnras/stab776. arXiv: 2103.07483 [astro-ph.CO].

Fialkov, Anastasia, Rennan Barkana, and Eli Visbal (Feb. 2014). “The observable signature of late heating of the Universe during cosmic reionization”. In: *Nature* 506.7487, pp. 197–199. DOI: 10.1038/nature12999. arXiv: 1402.0940 [astro-ph.CO].

Sun, G., L. Moncelsi, et al. (Apr. 2018). “A Foreground Masking Strategy for [C II] Intensity Mapping Experiments Using Galaxies Selected by Stellar Mass and Redshift”. In: *The Astrophysical Journal* 856.2, p. 107. DOI: 10.3847/1538-4357/aab3e3. arXiv: 1610.10095 [astro-ph.GA].

Van Cuyck, M. et al. (Aug. 2023). “CONCERTO: Extracting the power spectrum of the [C_{II}] emission line”. In: *Astronomy & Astrophysics* 676, A62. DOI: 10.1051/0004-6361/202346270. arXiv: 2306.01568 [astro-ph.CO].

Baek, Sung-June et al. (Jan. 2015). “Baseline correction using asymmetrically reweighted penalized least squares smoothing”. In: *The Analyst* 140.1, pp. 250–257. DOI: 10.1039/C4AN01061B.

Ponthieu, N., J. Grain, and G. Lagache (Nov. 2011). “POKER: estimating the power spectrum of diffuse emission with complex masks and at high angular resolution”. In: *Astronomy & Astrophysics* 535, A90. DOI: 10.1051/0004-6361/201117098. arXiv: 1111.0766 [astro-ph.CO].

Gkogkou, A. et al. (Feb. 2023). “CONCERTO: Simulating the CO, [CII], and [CI] line emission of galaxies in a 117 deg^2 field and the impact of field-to-field variance”. In: *Astronomy & Astrophysics* 670, A16. DOI: 10.1051/0004-6361/202245151. arXiv: 2212.02235 [astro-ph.CO].

Di Matteo, Tiziana et al. (Jan. 2002). "Radio Foregrounds for the 21 Centimeter Tomography of the Neutral Intergalactic Medium at High Redshifts". In: *The Astrophysical Journal* 564.2, pp. 576–580. DOI: 10.1086/324293. arXiv: astro-ph/0109241 [astro-ph].

Oh, S. Peng and Katherine J. Mack (Dec. 2003). "Foregrounds for 21-cm observations of neutral gas at high redshift". In: *Monthly Notices of the Royal Astronomical Society* 346.3, pp. 871–877. DOI: 10.1111/j.1365-2966.2003.07133.x. arXiv: astro-ph/0302099 [astro-ph].

Santos, Mário G., Asantha Cooray, and Lloyd Knox (June 2005). "Multifrequency Analysis of 21 Centimeter Fluctuations from the Era of Reionization". In: *The Astrophysical Journal* 625.2, pp. 575–587. DOI: 10.1086/429857. arXiv: astro-ph/0408515 [astro-ph].

Ali, Sk. Saiyad, Somnath Bharadwaj, and Jayaram N. Chengalur (Apr. 2008). "Foregrounds for redshifted 21-cm studies of reionization: Giant Meter Wave Radio Telescope 153-MHz observations". In: *Monthly Notices of the Royal Astronomical Society* 385.4, pp. 2166–2174. DOI: 10.1111/j.1365-2966.2008.12984.x. arXiv: 0801.2424 [astro-ph].

Kerrigan, Joshua R. et al. (Sept. 2018). "Improved 21 cm Epoch of Reionization Power Spectrum Measurements with a Hybrid Foreground Subtraction and Avoidance Technique". In: *The Astrophysical Journal* 864.2, p. 131. DOI: 10.3847/1538-4357/aad8bb. arXiv: 1801.00460 [astro-ph.IM].

Mertens, F. G., A. Ghosh, and L. V. E. Koopmans (Aug. 2018). "Statistical 21-cm signal separation via Gaussian Process Regression analysis". In: *Monthly Notices of the Royal Astronomical Society* 478.3, pp. 3640–3652. DOI: 10.1093/mnras/sty1207. arXiv: 1711.10834 [astro-ph.CO].

CONCERTO Collaboration et al. (Oct. 2020). "A wide field-of-view low-resolution spectrometer at APEX: Instrument design and scientific forecast". In: *Astronomy & Astrophysics* 642, A60. DOI: 10.1051/0004-6361/202038456. arXiv: 2007.14246 [astro-ph.IM].

Serra, Paolo, Olivier Doré, and Guilaine Lagache (Dec. 2016). "Dissecting the High-z Interstellar Medium through Intensity Mapping Cross-correlations". In: *The Astrophysical Journal* 833.2, p. 153. DOI: 10.3847/1538-4357/833/2/153. arXiv: 1608.00585 [astro-ph.GA].

CCAT-Prime Collaboration et al. (Jan. 2023). "CCAT-prime Collaboration: Science Goals and Forecasts with Prime-Cam on the Fred Young Submillimeter Telescope". In: *The Astrophysical Journal Supplement Series* 264.1, p. 7. DOI: 10.3847/1538-4365/ac9838. arXiv: 2107.10364 [astro-ph.CO].

Parshley, Stephen C., Jörg Kronshage, et al. (July 2018). "CCAT-prime: a novel telescope for submillimeter astronomy". In: *Ground-based and Airborne Telescopes VII*. Ed. by Heather K. Marshall and Jason Spyromilio. Vol. 10700. Society of Photo-Optical Instrumentation Engineers (SPIE) Conference Series, 107005X, p. 107005X. DOI: 10.1117/12.2314046. arXiv: 1807.06675 [astro-ph.IM].

Parshley, Stephen C., Michael Niemack, et al. (July 2018). "The optical design of the six-meter CCAT-prime and Simons Observatory telescopes". In: *Ground-based and Airborne Telescopes VII*. Ed. by Heather K. Marshall and Jason Spyromilio. Vol. 10700. Society of Photo-Optical Instrumentation

Engineers (SPIE) Conference Series, 1070041, p. 1070041. DOI: 10.1117/12.2314073. arXiv: 1807.06678 [astro-ph.IM].

Vavagiakis, E. M. et al. (July 2018). "Prime-Cam: a first-light instrument for the CCAT-prime telescope". In: *Millimeter, Submillimeter, and Far-Infrared Detectors and Instrumentation for Astronomy IX*. Ed. by Jonas Zmuidzinas and Jian-Rong Gao. Vol. 10708. Society of Photo-Optical Instrumentation Engineers (SPIE) Conference Series, 107081U. DOI: 10.1117/12.2313868. arXiv: 1807.00058 [astro-ph.IM].

Niemack, Michael D. (Mar. 2016). "Designs for a large-aperture telescope to map the CMB 10× faster". In: *Applied Optics* 55.7, p. 1688. DOI: 10.1364/AO.55.001688.

Choi, S. K. et al. (Mar. 2020). "Sensitivity of the Prime-Cam Instrument on the CCAT-Prime Telescope". In: *Journal of Low Temperature Physics* 199.3-4, pp. 1089–1097. DOI: 10.1007/s10909-020-02428-z. arXiv: 1908.10451 [astro-ph.IM].

Cothard, N. F. et al. (Jan. 2020). "The Design of the CCAT-prime Epoch of Reionization Spectrometer Instrument". In: *Journal of Low Temperature Physics* 199.3-4, pp. 898–907. DOI: 10.1007/s10909-019-02297-1. arXiv: 1911.11687 [astro-ph.IM].

Stacey, G. J., N. Geis, et al. (June 1991). "The 158 Micron [C ii] Line: A Measure of Global Star Formation Activity in Galaxies". In: *The Astrophysical Journal* 373, p. 423. DOI: 10.1086/170062.

Stacey, G. J., S. Hailey-Dunsheath, et al. (Dec. 2010). "A 158 μm [C II] Line Survey of Galaxies at z $\sim$1-2: An Indicator of Star Formation in the Early Universe". In: *The Astrophysical Journal* 724.2, pp. 957–974. DOI: 10.1088/0004-637X/724/2/957. arXiv: 1009.4216 [astro-ph.CO].

Clarke, J. et al. (Apr. 2024). "[CII] luminosity models and large-scale image cubes based on COSMOS 2020 and ALPINE-ALMA [CII] data back to the epoch of reionisation". In: *arXiv e-prints*, arXiv:2404.05352, arXiv:2404.05352. DOI: 10.48550/arXiv.2404.05352. arXiv: 2404.05352 [astro-ph.GA].

Weaver, J. R. et al. (Sept. 2023). "COSMOS2020: The galaxy stellar mass function. The assembly and star formation cessation of galaxies at 0.2< z $\leq$ 7.5". In: *Astronomy & Astrophysics* 677, A184. DOI: 10.1051/0004-6361/202245581. arXiv: 2212.02512 [astro-ph.GA].

Hunacek, J. et al. (Dec. 2018). "Hafnium Films and Magnetic Shielding for TIME, A mm-Wavelength Spectrometer Array". In: *Journal of Low Temperature Physics* 193.5-6, pp. 893–900. DOI: 10.1007/s10909-018-1906-3.

Cheng, Yun-Ting, Tzu-Ching Chang, and James J. Bock (Oct. 2020). "Phase-space Spectral Line Deconfusion in Intensity Mapping". In: *The Astrophysical Journal* 901.2, p. 142. DOI: 10.3847/1538-4357/abb023. arXiv: 2005.05341 [astro-ph.CO].

Sun, G., T. C. Chang, et al. (July 2021). "Probing Cosmic Reionization and Molecular Gas Growth with TIME". In: *The Astrophysical Journal* 915.1, p. 33. DOI: 10.3847/1538-4357/abfe62. arXiv: 2012.09160 [astro-ph.GA].

Chung, Dongwoo T. et al. (July 2022). “COMAP Early Science. V. Constraints and Forecasts at $z \sim 3$”. In: *The Astrophysical Journal* 933.2, p. 186. DOI: 10.3847/1538-4357/ac63c7. arXiv: 2111.05931 [astro-ph.CO].

Breysse, Patrick C., Dongwoo T. Chung, et al. (July 2022). “COMAP Early Science. VII. Prospects for CO Intensity Mapping at Reionization”. In: *The Astrophysical Journal* 933.2, p. 188. DOI: 10.3847/1538-4357/ac63c9. arXiv: 2111.05933 [astro-ph.CO].

Ihle, Håvard T. et al. (July 2022). “COMAP Early Science. IV. Power Spectrum Methodology and Results”. In: *The Astrophysical Journal* 933.2, p. 185. DOI: 10.3847/1538-4357/ac63c5. arXiv: 2111.05930 [astro-ph.CO].

Cleary, Kieran A. et al. (July 2022). “COMAP Early Science. I. Overview”. In: *The Astrophysical Journal* 933.2, p. 182. DOI: 10.3847/1538-4357/ac63cc. arXiv: 2111.05927 [astro-ph.CO].

Stutzer, N. -O. et al. (June 2024). “COMAP Pathfinder – Season 2 results II. Updated constraints on the CO(1-0) power spectrum”. In: *arXiv e-prints*, arXiv:2406.07511, arXiv:2406.07511. DOI: 10.48550/arXiv.2406.07511. arXiv: 2406.07511 [astro-ph.CO].

Chung, D. T. et al. (June 2024). “COMAP Pathfinder – Season 2 results III. Implications for cosmic molecular gas content at “Cosmic Half-past Eleven””. In: *arXiv e-prints*, arXiv:2406.07512, arXiv:2406.07512. DOI: 10.48550/arXiv.2406.07512. arXiv: 2406.07512 [astro-ph.CO].

Visbal, Eli and Abraham Loeb (Nov. 2010). “Measuring the 3D clustering of undetected galaxies through cross correlation of their cumulative flux fluctuations from multiple spectral lines”. In: *Journal of Cosmology and Astroparticle Physics* 2010.11, p. 016. DOI: 10.1088/1475-7516/2010/11/016. arXiv: 1008.3178 [astro-ph.CO].

Gong, Yan, Asantha Cooray, Marta B. Silva, et al. (Feb. 2011). “Probing Reionization with Intensity Mapping of Molecular and Fine-structure Lines”. In: *The Astrophysical Journal Letters* 728.2, p. L46. DOI: 10.1088/2041-8205/728/2/L46. arXiv: 1101.2892 [astro-ph.CO].

Lidz, Adam, Steven R. Furlanetto, et al. (Nov. 2011). “Intensity Mapping with Carbon Monoxide Emission Lines and the Redshifted 21 cm Line”. In: *The Astrophysical Journal* 741.2, p. 70. DOI: 10.1088/0004-637X/741/2/70. arXiv: 1104.4800 [astro-ph.CO].

Gong, Yan, Asantha Cooray, and Mario G. Santos (May 2013). “Probing the Pre-reionization Epoch with Molecular Hydrogen Intensity Mapping”. In: *The Astrophysical Journal* 768.2, p. 130. DOI: 10.1088/0004-637X/768/2/130. arXiv: 1212.2964 [astro-ph.CO].

Silva, Marta B. et al. (Feb. 2013). “Intensity Mapping of Lyα Emission during the Epoch of Reionization”. In: *The Astrophysical Journal* 763.2, p. 132. DOI: 10.1088/0004-637X/763/2/132. arXiv: 1205.1493 [astro-ph.CO].

Pullen, Anthony R., Olivier Doré, and Jamie Bock (May 2014). “Intensity Mapping across Cosmic Times with the Lyα Line”. In: *The Astrophysical Journal* 786.2, p. 111. DOI: 10.1088/0004-637X/786/2/111. arXiv: 1309.2295 [astro-ph.CO].

Bharadwaj, S. and S. K. Sethi (Dec. 2001). "HI Fluctuations at Large Redshifts: I–Visibility correlation". In: *Journal of Astrophysics and Astronomy* 22, pp. 293–307. DOI: 10.1007/BF02702273. arXiv: astro-ph/0203269 [astro-ph].

Datta, Kanan K., T. Roy Choudhury, and Somnath Bharadwaj (June 2007). "The multifrequency angular power spectrum of the epoch of reionization 21-cm signal". In: *Monthly Notices of the Royal Astronomical Society* 378.1, pp. 119–128. DOI: 10.1111/j.1365-2966.2007.11747.x. arXiv: astro-ph/0605546 [astro-ph].

Ghosh, Abhik, Somnath Bharadwaj, et al. (Mar. 2011a). "GMRT observation towards detecting the post-reionization 21-cm signal". In: *Monthly Notices of the Royal Astronomical Society* 411.4, pp. 2426–2438. ISSN: 0035-8711. DOI: 10.1111/j.1365-2966.2010.17853.x. eprint: https://academic.oup.com/mnras/article-pdf/411/4/2426/3049477/mnras0411-2426.pdf. URL: https://doi.org/10.1111/j.1365-2966.2010.17853.x.

— (Dec. 2011b). "Improved foreground removal in GMRT 610 MHz observations towards redshifted 21-cm tomography". In: *Monthly Notices of the Royal Astronomical Society* 418.4, pp. 2584–2589. ISSN: 0035-8711. DOI: 10.1111/j.1365-2966.2011.19649.x. eprint: https://academic.oup.com/mnras/article-pdf/418/4/2584/18448274/mnras0418-2584.pdf. URL: https://doi.org/10.1111/j.1365-2966.2011.19649.x.

Ghosh, Abhik, Jayanti Prasad, et al. (Nov. 2012). "Characterizing foreground for redshifted 21 cm radiation: 150 MHz Giant Metrewave Radio Telescope observations". In: *Monthly Notices of the Royal Astronomical Society* 426.4, pp. 3295–3314. DOI: 10.1111/j.1365-2966.2012.21889.x. arXiv: 1208.1617 [astro-ph.CO].

Choudhuri, Samir, Somnath Bharadwaj, Abhik Ghosh, et al. (Dec. 2014). "Visibility-based angular power spectrum estimation in low-frequency radio interferometric observations". In: *Monthly Notices of the Royal Astronomical Society* 445.4, pp. 4351–4365. DOI: 10.1093/mnras/stu2027. arXiv: 1409.7789 [astro-ph.CO].

Choudhuri, Samir, Somnath Bharadwaj, Suman Chatterjee, et al. (Dec. 2016). "The visibility-based tapered gridded estimator (TGE) for the redshifted 21-cm power spectrum". In: *Monthly Notices of the Royal Astronomical Society* 463.4, pp. 4093–4107. DOI: 10.1093/mnras/stw2254. arXiv: 1609.01732 [astro-ph.CO].

Bharadwaj, Somnath, Srijita Pal, et al. (Mar. 2019). "A Tapered Gridded Estimator (TGE) for the multifrequency angular power spectrum (MAPS) and the cosmological H I 21-cm power spectrum". In: *Monthly Notices of the Royal Astronomical Society* 483.4, pp. 5694–5700. DOI: 10.1093/mnras/sty3501. arXiv: 1812.08801 [astro-ph.CO].

Paciga, G., T.-C. Chang, et al. (May 2011). "The GMRT Epoch of Reionization experiment: a new upper limit on the neutral hydrogen power spectrum at z $\tilde{8}$.6". In: *Monthly Notices of the Royal Astronomical Society* 413, pp. 1174–1183. DOI: 10.1111/j.1365-2966.2011.18208.x. arXiv: 1006.1351.

Paciga, G., J. G. Albert, et al. (July 2013). "A simulation-calibrated limit on the H I power spectrum from the GMRT Epoch of Reionization experiment". In: *Monthly Notices of the Royal Astronomical Society* 433, pp. 639–647. DOI: 10.1093/mnras/stt753. arXiv: 1301.5906 [astro-ph.CO].

Chakraborty, Arnab et al. (Jan. 2021). "First Multi-redshift Limits on Post-Epoch of Reionization 21 cm Signal from z = 1.96-3.58 Using uGMRT". In: *The Astrophysical Journal Letters* 907.1, p. L7. DOI: 10.3847/2041-8213/abd17a. arXiv: 2012.04674 [astro-ph.CO].

Kazemi, S. et al. (June 2011). "Radio interferometric calibration using the SAGE algorithm". In: *Monthly Notices of the Royal Astronomical Society* 414.2, pp. 1656–1666. DOI: 10.1111/j.1365-2966.2011.18506.x. arXiv: 1012.1722 [astro-ph.IM].

Yatawatta, Sarod (June 2015). "Distributed radio interferometric calibration". In: *Monthly Notices of the Royal Astronomical Society* 449.4, pp. 4506–4514. DOI: 10.1093/mnras/stv596. arXiv: 1502.00858 [astro-ph.IM].

Harker, Geraint et al. (Aug. 2009). "Non-parametric foreground subtraction for 21-cm epoch of reionization experiments". In: *Monthly Notices of the Royal Astronomical Society* 397.2, pp. 1138–1152. DOI: 10.1111/j.1365-2966.2009.15081.x. arXiv: 0903.2760 [astro-ph.CO].

Chapman, Emma et al. (Feb. 2013). "The scale of the problem: recovering images of reionization with Generalized Morphological Component Analysis". In: *Monthly Notices of the Royal Astronomical Society* 429.1, pp. 165–176. DOI: 10.1093/mnras/sts333. arXiv: 1209.4769 [astro-ph.CO].

Hothi, Ian et al. (Jan. 2021). "Comparing foreground removal techniques for recovery of the LOFAR-EoR 21 cm power spectrum". In: *Monthly Notices of the Royal Astronomical Society* 500.2, pp. 2264–2277. DOI: 10.1093/mnras/staa3446. arXiv: 2011.01284 [astro-ph.CO].

Mevius, M. et al. (Jan. 2022). "A numerical study of 21-cm signal suppression and noise increase in direction-dependent calibration of LOFAR data". In: *Monthly Notices of the Royal Astronomical Society* 509.3, pp. 3693–3702. DOI: 10.1093/mnras/stab3233. arXiv: 2111.02537 [astro-ph.CO].

Patil, A. H. et al. (Mar. 2017). "Upper Limits on the 21 cm Epoch of Reionization Power Spectrum from One Night with LOFAR". In: *The Astrophysical Journal* 838, p. 65. DOI: 10.3847/1538-4357/aa63e7. arXiv: 1702.08679.

Gehlot, B. K. et al. (Sept. 2019). "The first power spectrum limit on the 21-cm signal of neutral hydrogen during the Cosmic Dawn at z = 20-25 from LOFAR". In: *Monthly Notices of the Royal Astronomical Society* 488.3, pp. 4271–4287. DOI: 10.1093/mnras/stz1937. arXiv: 1809.06661 [astro-ph.IM].

Mertens, F. G., M. Mevius, et al. (Apr. 2020). "Improved upper limits on the 21 cm signal power spectrum of neutral hydrogen at $z \approx 9.1$ from LOFAR". In: *Monthly Notices of the Royal Astronomical Society* 493.2, pp. 1662–1685. DOI: 10.1093/mnras/staa327. arXiv: 2002.07196 [astro-ph.CO].

Ghara, R., S. K. Giri, et al. (Apr. 2020). “Constraining the intergalactic medium at $z \approx 9.1$ using LOFAR Epoch of Reionization observations”. In: *Monthly Notices of the Royal Astronomical Society* 493.4, pp. 4728–4747. DOI: 10.1093/mnras/staa487. arXiv: 2002.07195 [astro-ph.CO].

Mondal, R. et al. (Nov. 2020). “Tight constraints on the excess radio background at $z = 9.1$ from LOFAR”. In: *Monthly Notices of the Royal Astronomical Society* 498.3, pp. 4178–4191. DOI: 10.1093/mnras/staa2422. arXiv: 2004.00678 [astro-ph.CO].

Greig, Bradley et al. (Jan. 2021). “Exploring reionization and high-z galaxy observables with recent multiredshift MWA upper limits on the 21-cm signal”. In: *Monthly Notices of the Royal Astronomical Society* 500.4, pp. 5322–5335. DOI: 10.1093/mnras/staa3494. arXiv: 2008.02639 [astro-ph.CO].

Mitchell, Daniel A. et al. (2008). “Real-Time Calibration of the Murchison Widefield Array”. In: *IEEE Journal of Selected Topics in Signal Processing* 2.5, pp. 707–717. DOI: 10.1109/JSTSP.2008.2005327.

Sullivan, I. S. et al. (Nov. 2012). “Fast Holographic Deconvolution: A New Technique for Precision Radio Interferometry”. In: *The Astrophysical Journal* 759.1, p. 17. DOI: 10.1088/0004-637X/759/1/17. arXiv: 1209.1653 [astro-ph.IM].

Trott, C. M. et al. (Feb. 2016). “CHIPS: The Cosmological H I Power Spectrum Estimator”. In: *The Astrophysical Journal* 818.2, p. 139. DOI: 10.3847/0004-637X/818/2/139. arXiv: 1601.02073 [astro-ph.IM].

Barry, N., A. P. Beardsley, et al. (July 2019). “The FHD/ϵppsilon Epoch of Reionisation power spectrum pipeline”. In: *Publications of the Astronomical Society of Australia* 36, e026, e026. DOI: 10.1017/pasa.2019.21. arXiv: 1901.02980 [astro-ph.IM].

Barry, N., M. Wilensky, et al. (Oct. 2019). “Improving the Epoch of Reionization Power Spectrum Results from Murchison Widefield Array Season 1 Observations”. In: *The Astrophysical Journal* 884.1, p. 1. DOI: 10.3847/1538-4357/ab40a8. arXiv: 1909.00561 [astro-ph.IM].

Li, W. et al. (Dec. 2019). “First Season MWA Phase II Epoch of Reionization Power Spectrum Results at Redshift 7”. In: *The Astrophysical Journal* 887.2, p. 141. DOI: 10.3847/1538-4357/ab55e4. arXiv: 1911.10216 [astro-ph.CO].

Ewall-Wice, A. et al. (Aug. 2016). “First limits on the 21 cm power spectrum during the Epoch of X-ray heating”. In: *Monthly Notices of the Royal Astronomical Society* 460.4, pp. 4320–4347. DOI: 10.1093/mnras/stw1022. arXiv: 1605.00016 [astro-ph.CO].

Trott, Cathryn M. et al. (Apr. 2020). “Deep multiredshift limits on Epoch of Reionization 21 cm power spectra from four seasons of Murchison Widefield Array observations”. In: *Monthly Notices of the Royal Astronomical Society* 493.4, pp. 4711–4727. DOI: 10.1093/mnras/staa414. arXiv: 2002.02575 [astro-ph.CO].

Rahimi, M. et al. (Dec. 2021). “Epoch of reionization power spectrum limits from Murchison Widefield Array data targeted at EoR1 field”. In: *Monthly Notices of the Royal Astronomical Society* 508.4, pp. 5954–5971. DOI: 10.1093/mnras/stab2918. arXiv: 2110.03190 [astro-ph.CO].

Dillon, Joshua S. et al. (Dec. 2020). “Redundant-baseline calibration of the hydrogen epoch of reionization array”. In: *Monthly Notices of the Royal Astronomical Society* 499.4, pp. 5840–5861. DOI: 10.1093/mnras/staa3001. arXiv: 2003.08399 [astro-ph.IM].

Kern, Nicholas S., Aaron R. Parsons, et al. (Jan. 2020). “Mitigating Internal Instrument Coupling for 21 cm Cosmology. II. A Method Demonstration with the Hydrogen Epoch of Reionization Array”. In: *The Astrophysical Journal* 888.2, p. 70. DOI: 10.3847/1538-4357/ab5e8a. arXiv: 1909.11733 [astro-ph.IM].

Kern, Nicholas S., Joshua S. Dillon, et al. (Feb. 2020). “Absolute Calibration Strategies for the Hydrogen Epoch of Reionization Array and Their Impact on the 21 cm Power Spectrum”. In: *The Astrophysical Journal* 890.2, p. 122. DOI: 10.3847/1538-4357/ab67bc. arXiv: 1910.12943 [astro-ph.IM].

Abdurashidova, Zara et al. (Feb. 2022). “First Results from HERA Phase I: Upper Limits on the Epoch of Reionization 21 cm Power Spectrum”. In: *The Astrophysical Journal* 925.2, p. 221. DOI: 10.3847/1538-4357/ac1c78. arXiv: 2108.02263 [astro-ph.CO].

Ghara, R., T. R. Choudhury, et al. (Jan. 2017). “Imaging the redshifted 21 cm pattern around the first sources during the cosmic dawn using the SKA”. In: *Monthly Notices of the Royal Astronomical Society* 464, pp. 2234–2248. DOI: 10.1093/mnras/stw2494. arXiv: 1607.02779.

Kapahtia, Akanksha et al. (May 2021). “Prospects of constraining reionization model parameters using Minkowski tensors and Betti numbers”. In: *Journal of Cosmology and Astroparticle Physics* 2021.5, 026, p. 026. DOI: 10.1088/1475-7516/2021/05/026. arXiv: 2101.03962 [astro-ph.CO].

Giri, Sambit K. and Garrelt Mellema (Aug. 2021). “Measuring the topology of reionization with Betti numbers”. In: *Monthly Notices of the Royal Astronomical Society* 505.2, pp. 1863–1877. DOI: 10.1093/mnras/stab1320. arXiv: 2012.12908 [astro-ph.CO].

Giri, Sambit K., Garrelt Mellema, and Raghunath Ghara (Oct. 2018). “Optimal identification of H II regions during reionization in 21-cm observations”. In: *Monthly Notices of the Royal Astronomical Society* 479.4, pp. 5596–5611. DOI: 10.1093/mnras/sty1786. arXiv: 1801.06550 [astro-ph.CO].

Ghara, Raghunath and T. Roy Choudhury (July 2020). “Bayesian approach to constraining the properties of ionized bubbles during reionization”. In: *Monthly Notices of the Royal Astronomical Society* 496.1, pp. 739–753. DOI: 10.1093/mnras/staa1599. arXiv: 1909.12317 [astro-ph.CO].

Bandyopadhyay, Bidisha, T. Roy Choudhury, and T. R. Seshadri (Apr. 2017). “Studying neutral hydrogen structures during the epoch of reionization using fractal dimensions”. In: *Monthly Notices* *of the Royal Astronomical Society* 466.2, pp. 2302–2311. DOI: 10.1093/mnras/stw3347. arXiv: 1611.05554 [astro-ph.CO].

Gillet, Nicolas et al. (Mar. 2019). "Deep learning from 21-cm tomography of the cosmic dawn and reionization". In: *Monthly Notices of the Royal Astronomical Society* 484.1, pp. 282–293. DOI: 10.1093/mnras/stz010. arXiv: 1805.02699 [astro-ph.CO].

Lidz, Adam, Oliver Zahn, et al. (Apr. 2007). "Higher Order Contributions to the 21 cm Power Spectrum". In: *The Astrophysical Journal* 659.2, pp. 865–876. DOI: 10.1086/511670. arXiv: astro-ph/0610054 [astro-ph].

Zahn, Oliver et al. (Jan. 2007). "Simulations and Analytic Calculations of Bubble Growth during Hydrogen Reionization". In: *The Astrophysical Journal* 654.1, pp. 12–26. DOI: 10.1086/509597. arXiv: astro-ph/0604177 [astro-ph].

Georgiev, Ivelin et al. (July 2022). "The large-scale 21-cm power spectrum from reionization". In: *Monthly Notices of the Royal Astronomical Society* 513.4, pp. 5109–5124. DOI: 10.1093/mnras/stac1230. arXiv: 2110.13190 [astro-ph.CO].

Datta, Kanan K., Garrelt Mellema, et al. (Aug. 2012). "Light-cone effect on the reionization 21-cm power spectrum". In: *Monthly Notices of the Royal Astronomical Society* 424.3, pp. 1877–1891. DOI: 10.1111/j.1365-2966.2012.21293.x. arXiv: 1109.1284 [astro-ph.CO].

Mao, Yi, Paul R. Shapiro, et al. (May 2012). "Redshift-space distortion of the 21-cm background from the epoch of reionization - I. Methodology re-examined". In: *Monthly Notices of the Royal Astronomical Society* 422.2, pp. 926–954. DOI: 10.1111/j.1365-2966.2012.20471.x. arXiv: 1104.2094 [astro-ph.CO].

Majumdar, Suman, Somnath Bharadwaj, and T. Roy Choudhury (Sept. 2013). "The effect of peculiar velocities on the epoch of reionization 21-cm signal". In: *Monthly Notices of the Royal Astronomical Society* 434.3, pp. 1978–1988. DOI: 10.1093/mnras/stt1144. arXiv: 1209.4762 [astro-ph.CO].

Majumdar, Suman, Garrelt Mellema, et al. (Oct. 2014). "On the use of seminumerical simulations in predicting the 21-cm signal from the epoch of reionization". In: *Monthly Notices of the Royal Astronomical Society* 443.4, pp. 2843–2861. DOI: 10.1093/mnras/stu1342. arXiv: 1403.0941 [astro-ph.CO].

Sun, Guochao, Brandon S. Hensley, et al. (Dec. 2019). "A Self-consistent Framework for Multiline Modeling in Line Intensity Mapping Experiments". In: *The Astrophysical Journal* 887.2, p. 142. DOI: 10.3847/1538-4357/ab55df. arXiv: 1907.02999 [astro-ph.GA].

Moradinezhad Dizgah, Azadeh and Garrett K. Keating (Feb. 2019a). "Line Intensity Mapping with [C II] and CO(1-0) as Probes of Primordial Non-Gaussianity". In: *The Astrophysical Journal* 872.2, p. 126. DOI: 10.3847/1538-4357/aafd36. arXiv: 1810.02850 [astro-ph.CO].

Kannan, Rahul et al. (Aug. 2022). “The THESAN project: predictions for multitracer line intensity mapping in the epoch of reionization”. In: *Monthly Notices of the Royal Astronomical Society* 514.3, pp. 3857–3878. DOI: 10.1093/mnras/stac1557. arXiv: 2111.02411 [astro-ph.CO].

Sun, Guochao, Lluís Mas-Ribas, et al. (June 2023). “LIMFAST. II. Line Intensity Mapping as a Probe of High-redshift Galaxy Formation”. In: *The Astrophysical Journal* 950.1, p. 40. DOI: 10.3847/1538-4357/acc9b3. arXiv: 2206.14186 [astro-ph.CO].

Bharadwaj, Somnath, Arindam Mazumdar, and Debanjan Sarkar (Mar. 2020). “Quantifying the redshift space distortion of the bispectrum I: primordial non-Gaussianity”. In: *Monthly Notices of the Royal Astronomical Society* 493.1, pp. 594–602. DOI: 10.1093/mnras/staa279. arXiv: 2001.10243 [astro-ph.CO].

Majumdar, Suman, Jonathan R. Pritchard, et al. (May 2018). “Quantifying the non-Gaussianity in the EoR 21-cm signal through bispectrum”. In: *Monthly Notices of the Royal Astronomical Society* 476.3, pp. 4007–4024. DOI: 10.1093/mnras/sty535. arXiv: 1708.08458 [astro-ph.CO].

Majumdar, Suman, Mohd Kamran, et al. (Dec. 2020). “Redshifted 21-cm bispectrum - I. Impact of the redshift space distortions on the signal from the Epoch of Reionization”. In: *Monthly Notices of the Royal Astronomical Society* 499.4, pp. 5090–5106. DOI: 10.1093/mnras/staa3168. arXiv: 2007.06584 [astro-ph.CO].

Gill, Sukhdeep Singh et al. (Jan. 2024). “The monopole and quadrupole moments of the epoch of reionization (EoR) 21-cm bispectrum”. In: *Monthly Notices of the Royal Astronomical Society* 527.1, pp. 1135–1140. DOI: 10.1093/mnras/stad3273. arXiv: 2310.15579 [astro-ph.CO].

Hutter, Anne, Catherine A. Watkinson, et al. (Feb. 2020). “The 21 cm bispectrum during reionization: a tracer of the ionization topology”. In: *Monthly Notices of the Royal Astronomical Society* 492.1, pp. 653–667. DOI: 10.1093/mnras/stz3139. arXiv: 1907.04342 [astro-ph.CO].

Raste, Janakee et al. (Mar. 2024). “The 21-cm bispectrum from neutral hydrogen islands at $z < 6$”. In: *Monthly Notices of the Royal Astronomical Society* 529.1, pp. 129–140. DOI: 10.1093/mnras/stae492. arXiv: 2308.09744 [astro-ph.CO].

Kamran, Mohd et al. (Apr. 2021). “Redshifted 21-cm bispectrum - II. Impact of the spin temperature fluctuations and redshift space distortions on the signal from the Cosmic Dawn”. In: *Monthly Notices of the Royal Astronomical Society* 502.3, pp. 3800–3813. DOI: 10.1093/mnras/stab216. arXiv: 2012.11616 [astro-ph.CO].

Zawada, Karolina et al. (Apr. 2014). “Light-cone anisotropy in the 21 cm signal from the epoch of reionization”. In: *Monthly Notices of the Royal Astronomical Society* 439.2, pp. 1615–1627. DOI: 10.1093/mnras/stu035. arXiv: 1401.1807 [astro-ph.CO].

Murmu, Chandra Shekhar, Suman Majumdar, and Kanan K. Datta (Oct. 2021). “C II and H I 21-cm line intensity mapping from the EoR: impact of the light-cone effect on auto and cross-power spectra”. In: *Monthly Notices of the Royal Astronomical Society* 507.2, pp. 2500–2509. DOI: 10.1093/mnras/stab2347. arXiv: 2107.09072 [astro-ph.CO].

Mondal, Rajesh, Garrelt Mellema, et al. (Dec. 2021). “The Epoch of Reionization 21-cm bispectrum: the impact of light-cone effects and detectability”. In: *Monthly Notices of the Royal Astronomical Society* 508.3, pp. 3848–3859. DOI: 10.1093/mnras/stab2900. arXiv: 2107.02668 [astro-ph.CO].

Dumitru, Sebastian et al. (May 2019). “Predictions and sensitivity forecasts for reionization-era [C II] line intensity mapping”. In: *Monthly Notices of the Royal Astronomical Society* 485.3, pp. 3486–3498. DOI: 10.1093/mnras/stz617. arXiv: 1802.04804 [astro-ph.GA].

Fronenberg, Hannah and Adrian Liu (July 2024). “Forecasts and Statistical Insights for Line Intensity Mapping Cross-Correlations: A Case Study with 21cm x [CII]”. In: *arXiv e-prints*, arXiv:2407.14588, arXiv:2407.14588. DOI: 10.48550/arXiv.2407.14588. arXiv: 2407.14588 [astro-ph.CO].

Beane, Angus and Adam Lidz (Nov. 2018). “Extracting Bias Using the Cross-bispectrum: An EoR and 21 cm-[C II]-[C II] Case Study”. In: *The Astrophysical Journal* 867.1, p. 26. DOI: 10.3847/1538-4357/aae388. arXiv: 1806.02796 [astro-ph.CO].

Silva, Marta et al. (June 2015). “PROSPECTS FOR DETECTING C II EMISSION DURING THE EPOCH OF REIONIZATION”. In: *The Astrophysical Journal* 806.2, p. 209. DOI: 10.1088/0004-637x/806/2/209. URL: https://doi.org/10.1088/0004-637x/806/2/209.

Béthermin, Matthieu et al. (Nov. 2017). “The impact of clustering and angular resolution on far-infrared and millimeter continuum observations”. In: *Astronomy & Astrophysics* 607, A89. DOI: 10.1051/0004-6361/201730866. arXiv: 1703.08795 [astro-ph.GA].

Hutter, Anne, Pratika Dayal, et al. (May 2019). “A proposal to exploit galaxy-21cm synergies to shed light on the Epoch of Reionization”. In: *Bulletin of the American Astronomical Society* 51.3, p. 57. arXiv: 1903.03628 [astro-ph.CO].

Pagano, Michael and Adrian Liu (Dec. 2021). “Lyman-alpha emitters and the 21 cm power spectrum as probes of density-ionization correlation in the epoch of reionization”. In: *Monthly Notices of the Royal Astronomical Society* 508.2, pp. 1915–1928. DOI: 10.1093/mnras/stab2656. arXiv: 2105.03434 [astro-ph.CO].

Zackrisson, Erik et al. (Jan. 2020). “Bubble mapping with the Square Kilometre Array - I. Detecting galaxies with Euclid, JWST, WFIRST, and ELT within ionized bubbles in the intergalactic medium at z > 6”. In: *Monthly Notices of the Royal Astronomical Society* 493.1, pp. 855–870. DOI: 10.1093/mnras/staa098. arXiv: 1905.00437 [astro-ph.GA].

Chatterjee, Atrideb, Tirthankar Roy Choudhury, and Sourav Mitra (Oct. 2021). “CosmoReionMC: a package for estimating cosmological and astrophysical parameters using CMB, Lyman-α absorption, and global 21 cm data”. In: *Monthly Notices of the Royal Astronomical Society* 507.2, pp. 2405–2422. DOI: 10.1093/mnras/stab2316. arXiv: 2101.11088 [astro-ph.CO].

Mitra, Sourav, T. Roy Choudhury, and Andrea Ferrara (May 2011). “Reionization constraints using principal component analysis”. In: *Monthly Notices of the Royal Astronomical Society* 413.3, pp. 1569–1580. ISSN: 0035-8711. DOI: 10.1111/j.1365-2966.2011.18234.x. eprint: https:

//academic.oup.com/mnras/article-pdf/413/3/1569/2863597/mnras0413-1569.pdf. URL: https://doi.org/10.1111/j.1365-2966.2011.18234.x.

Osterbrock, Donald E. and Gary J. Ferland (2006). *Astrophysics of gaseous nebulae and active galactic nuclei*.

Levesque, Emily M., Lisa J. Kewley, and Kirsten L. Larson (Feb. 2010). "Theoretical Modeling of Star-Forming Galaxies. I. Emission-Line Diagnostic Grids for Local and Low-Metallicity Galaxies". In: *The Astronomical Journal* 139.2, pp. 712–727. DOI: 10.1088/0004-6256/139/2/712. arXiv: 0908.0460 [astro-ph.GA].

Gutkin, Julia, Stéphane Charlot, and Gustavo Bruzual (Oct. 2016). "Modelling the nebular emission from primeval to present-day star-forming galaxies". In: *Monthly Notices of the Royal Astronomical Society* 462.2, pp. 1757–1774. DOI: 10.1093/mnras/stw1716. arXiv: 1607.06086 [astro-ph.GA].

Byler, Nell et al. (May 2017). "Nebular Continuum and Line Emission in Stellar Population Synthesis Models". In: *The Astrophysical Journal* 840.1, p. 44. DOI: 10.3847/1538-4357/aa6c66. arXiv: 1611.08305 [astro-ph.GA].

Kaufman, Michael J., Mark. G. Wolfire, and David J. Hollenbach (June 2006). "[Si II], [Fe II], [C II], and H_2 Emission from Massive Star-forming Regions". In: *The Astrophysical Journal* 644.1, pp. 283–299. DOI: 10.1086/503596.

Leung, T. K. Daisy et al. (Dec. 2020). "Predictions of the $L_{[CII]}$-SFR and [CII] Luminosity Function at the Epoch of Reionization". In: *The Astrophysical Journal* 905.2, p. 102. DOI: 10.3847/1538-4357/abc25e. arXiv: 2004.11912 [astro-ph.GA].

Olsen, Karen P., Thomas R. Greve, Christian Brinch, et al. (Apr. 2016). "SImulator of GAlaxy Millimetre/submillimetre Emission (SÍGAME): CO emission from massive $z = 2$ main-sequence galaxies". In: *Monthly Notices of the Royal Astronomical Society* 457.3, pp. 3306–3333. DOI: 10.1093/mnras/stw162. arXiv: 1507.00012 [astro-ph.GA].

Olsen, Karen P., Thomas R. Greve, Desika Narayanan, Robert Thompson, Romeel Davé, et al. (Sept. 2017). "SÍGAME Simulations of the [CII], [OI], and [OIII] Line Emission from Star-forming Galaxies at $z \simeq 6$". In: *The Astrophysical Journal* 846.2, p. 105. DOI: 10.3847/1538-4357/aa86b4. arXiv: 1708.04936 [astro-ph.GA].

Speagle, J. S. et al. (Oct. 2014). "A Highly Consistent Framework for the Evolution of the Star-Forming "Main Sequence" from z $\sim$0-6". In: *The Astrophysical Journal Supplement Series* 214.2, p. 15. DOI: 10.1088/0067-0049/214/2/15. arXiv: 1405.2041 [astro-ph.GA].

Dutton, Aaron A., Frank C. van den Bosch, and Avishai Dekel (July 2010). "On the origin of the galaxy star-formation-rate sequence: evolution and scatter". In: *Monthly Notices of the Royal Astronomical Society* 405.3, pp. 1690–1710. DOI: 10.1111/j.1365-2966.2010.16620.x. arXiv: 0912.2169 [astro-ph.CO].

Peng, Ying-jie and Roberto Maiolino (Oct. 2014). "From haloes to Galaxies - I. The dynamics of the gas regulator model and the implied cosmic sSFR history". In: *Monthly Notices of the Royal Astronomical Society* 443.4, pp. 3643–3664. DOI: 10.1093/mnras/stu1288. arXiv: 1402.5964 [astro-ph.CO].

Lagos, Claudia del P. et al. (Dec. 2018). "Shark: introducing an open source, free, and flexible semi-analytic model of galaxy formation". In: *Monthly Notices of the Royal Astronomical Society* 481.3, pp. 3573–3603. DOI: 10.1093/mnras/sty2440. arXiv: 1807.11180 [astro-ph.GA].

Matthee, Jorryt and Joop Schaye (Mar. 2019). "The origin of scatter in the star formation rate-stellar mass relation". In: *Monthly Notices of the Royal Astronomical Society* 484.1, pp. 915–932. DOI: 10.1093/mnras/stz030. arXiv: 1805.05956 [astro-ph.GA].

Blank, Marvin et al. (Jan. 2021). "NIHAO XXVI: nature versus nurture, the star formation main sequence, and the origin of its scatter". In: *Monthly Notices of the Royal Astronomical Society* 500.1, pp. 1414–1420. DOI: 10.1093/mnras/staa2670. arXiv: 2008.13379 [astro-ph.GA].

Hassan, Sultan et al. (May 2022). "Reionization with SIMBA: How Much Does Astrophysics Matter in Modeling Cosmic Reionization?" In: *The Astrophysical Journal* 931.1, p. 62. DOI: 10.3847/1538-4357/ac69e2. arXiv: 2109.03840 [astro-ph.CO].

Carilli, C. L. and F. Walter (Aug. 2013). "Cool Gas in High-Redshift Galaxies". In: *Annual Review of Astronomy and Astrophysics* 51.1, pp. 105–161. DOI: 10.1146/annurev-astro-082812-140953. arXiv: 1301.0371 [astro-ph.CO].

Greve, T. R., I. Leonidaki, et al. (Oct. 2014). "Star Formation Relations and CO Spectral Line Energy Distributions across the J-ladder and Redshift". In: *The Astrophysical Journal* 794.2, p. 142. DOI: 10.1088/0004-637X/794/2/142. arXiv: 1407.4400 [astro-ph.GA].

Sargent, M. T. et al. (Sept. 2014). "Regularity Underlying Complexity: A Redshift-independent Description of the Continuous Variation of Galaxy-scale Molecular Gas Properties in the Mass-star Formation Rate Plane". In: *The Astrophysical Journal* 793.1, p. 19. DOI: 10.1088/0004-637X/793/1/19. arXiv: 1303.4392 [astro-ph.CO].

Kamenetzky, J. et al. (Oct. 2016). "L□$_{CO}$/L$_{FIR}$ Relations with CO Rotational Ladders of Galaxies Across the Herschel SPIRE Archive". In: *The Astrophysical Journal* 829.2, p. 93. DOI: 10.3847/0004-637X/829/2/93. arXiv: 1508.05102 [astro-ph.GA].

Prasad, Peeyush et al. (Dec. 2016). "The AARTFAAC All-Sky Monitor: System Design and Implementation". In: *Journal of Astronomical Instrumentation* 5.4, p. 1641008. DOI: 10.1142/S2251171716410087. arXiv: 1609.04205 [astro-ph.IM].

Bharadwaj, S. and P. S. Srikant (Mar. 2004). "HI fluctuations at large redshifts: III - Simulating the signal expected at GMRT." In: *Journal of Astrophysics and Astronomy* 25, pp. 67–80. DOI: 10.1007/BF02702289. arXiv: astro-ph/0402262 [astro-ph].

Mondal, Rajesh, Somnath Bharadwaj, Suman Majumdar, et al. (Feb. 2015). "The effect of non-Gaussianity on error predictions for the Epoch of Reionization (EoR) 21-cm power spectrum". In: *Monthly No-*

tices of the Royal Astronomical Society: Letters* 449.1, pp. L41–L45. DOI: 10.1093/mnrasl/slv015. URL: https://doi.org/10.1093%2Fmnrasl%2Fslv015.

Choudhury, Tirthankar Roy, Martin G. Haehnelt, and John Regan (Apr. 2009). "Inside-out or outside-in: the topology of reionization in the photon-starved regime suggested by Lyα forest data". In: *Monthly Notices of the Royal Astronomical Society* 394.2, pp. 960–977. DOI: 10.1111/j.1365-2966.2008.14383.x. arXiv: 0806.1524 [astro-ph].

Mondal, Rajesh, Somnath Bharadwaj, and Suman Majumdar (Jan. 2017). "Statistics of the epoch of reionization (EoR) 21-cm signal - II. The evolution of the power-spectrum error-covariance". In: *Monthly Notices of the Royal Astronomical Society* 464.3, pp. 2992–3004. DOI: 10.1093/mnras/stw2599. arXiv: 1606.03874 [astro-ph.CO].

Harnois-Déraps, Joachim et al. (Nov. 2013). "High-performance P^{3}M N-body code: CUBEP^{3}M". In: *Monthly Notices of the Royal Astronomical Society* 436.1, pp. 540–559. DOI: 10.1093/mnras/stt1591. arXiv: 1208.5098 [astro-ph.CO].

Mellema, Garrelt, Ilian T. Iliev, Marcelo A. Alvarez, et al. (Mar. 2006). "C ^{2}-ray: A new method for photon-conserving transport of ionizing radiation". In: *New Astronomy* 11.5, pp. 374–395. DOI: 10.1016/j.newast.2005.09.004. arXiv: astro-ph/0508416 [astro-ph].

Eisenstein, Daniel J. and Wayne Hu (Mar. 1998). "Baryonic Features in the Matter Transfer Function". In: *The Astrophysical Journal* 496.2, pp. 605–614. DOI: 10.1086/305424. arXiv: astro-ph/9709112 [astro-ph].

Zel'dovich, Ya. B. (Mar. 1970). "Gravitational instability: An approximate theory for large density perturbations." In: *Astronomy & Astrophysics* 5, pp. 84–89.

Kaiser, Nick (July 1987). "Clustering in real space and in redshift space". In: *Monthly Notices of the Royal Astronomical Society* 227, pp. 1–21. DOI: 10.1093/mnras/227.1.1.

Furlanetto, Steven R., Matias Zaldarriaga, and Lars Hernquist (Sept. 2004). "The Growth of H II Regions During Reionization". In: *The Astrophysical Journal* 613.1, pp. 1–15. DOI: 10.1086/423025. arXiv: astro-ph/0403697 [astro-ph].

Mao, Yi, Jun Koda, et al. (Jan. 2020). "The impact of inhomogeneous subgrid clumping on cosmic reionization". In: *Monthly Notices of the Royal Astronomical Society* 491.2, pp. 1600–1621. DOI: 10.1093/mnras/stz2986. arXiv: 1906.02476 [astro-ph.CO].

Paranjape, Aseem, T. Roy Choudhury, and Hamsa Padmanabhan (Aug. 2016). "Photon number conserving models of H II bubbles during reionization". In: *Monthly Notices of the Royal Astronomical Society* 460.2, pp. 1801–1810. DOI: 10.1093/mnras/stw1060. arXiv: 1512.01345 [astro-ph.CO].

Choudhury, Tirthankar Roy and Aseem Paranjape (Dec. 2018). "Photon number conservation and the large-scale 21 cm power spectrum in seminumerical models of reionization". In: *Monthly Notices of the Royal Astronomical Society* 481.3, pp. 3821–3837. DOI: 10.1093/mnras/sty2551. arXiv: 1807.00836 [astro-ph.CO].

Berlind, Andreas A. and David H. Weinberg (Aug. 2002). "The Halo Occupation Distribution: Toward an Empirical Determination of the Relation between Galaxies and Mass". In: *The Astrophysical Journal* 575.2, pp. 587–616. ISSN: 1538-4357. DOI: 10.1086/341469. URL: http://dx.doi.org/10.1086/341469.

De Lucia, Gabriella and Jérémy Blaizot (Feb. 2007). "The hierarchical formation of the brightest cluster galaxies". In: *Monthly Notices of the Royal Astronomical Society* 375.1, pp. 2–14. DOI: 10.1111/j.1365-2966.2006.11287.x. arXiv: astro-ph/0606519 [astro-ph].

Guo, Qi et al. (May 2011). "From dwarf spheroidals to cD galaxies: simulating the galaxy population in a ΛCDM cosmology". In: *Monthly Notices of the Royal Astronomical Society* 413.1, pp. 101–131. DOI: 10.1111/j.1365-2966.2010.18114.x. arXiv: 1006.0106 [astro-ph.CO].

Davé, Romeel, Daniel Anglés-Alcázar, et al. (June 2019). "SIMBA: Cosmological simulations with black hole growth and feedback". In: *Monthly Notices of the Royal Astronomical Society* 486.2, pp. 2827–2849. DOI: 10.1093/mnras/stz937. arXiv: 1901.10203 [astro-ph.GA].

Anglés-Alcázar, Daniel, Romeel Davé, et al. (Jan. 2017). "Gravitational torque-driven black hole growth and feedback in cosmological simulations". In: *Monthly Notices of the Royal Astronomical Society* 464.3, pp. 2840–2853. DOI: 10.1093/mnras/stw2565. arXiv: 1603.08007 [astro-ph.GA].

Li, Qi, Desika Narayanan, and Romeel Davé (Nov. 2019). "The dust-to-gas and dust-to-metal ratio in galaxies from z = 0 to 6". In: *Monthly Notices of the Royal Astronomical Society* 490.1, pp. 1425–1436. DOI: 10.1093/mnras/stz2684. arXiv: 1906.09277 [astro-ph.GA].

Anglés-Alcázar, Daniel, Claude-André Faucher-Giguère, et al. (Oct. 2017). "The cosmic baryon cycle and galaxy mass assembly in the FIRE simulations". In: *Monthly Notices of the Royal Astronomical Society* 470.4, pp. 4698–4719. DOI: 10.1093/mnras/stx1517. arXiv: 1610.08523 [astro-ph.GA].

Wu, Xiaohan et al. (June 2020). "Photometric properties of reionization-epoch galaxies in the SIMBA simulations". In: *Monthly Notices of the Royal Astronomical Society* 494.4, pp. 5636–5651. DOI: 10.1093/mnras/staa1044. arXiv: 1911.06330 [astro-ph.GA].

Thomas, Nicole et al. (Aug. 2019). "Black hole - Galaxy correlations in SIMBA". In: *Monthly Notices of the Royal Astronomical Society* 487.4, pp. 5764–5780. DOI: 10.1093/mnras/stz1703. arXiv: 1905.02741 [astro-ph.GA].

Appleby, Sarah et al. (June 2020). "The impact of quenching on galaxy profiles in the SIMBA simulation". In: *Monthly Notices of the Royal Astronomical Society* 494.4, pp. 6053–6071. DOI: 10.1093/mnras/staa1169. arXiv: 1911.02041 [astro-ph.GA].

Davé, Romeel, Robert A. Crain, et al. (Sept. 2020). "Galaxy cold gas contents in modern cosmological hydrodynamic simulations". In: *Monthly Notices of the Royal Astronomical Society* 497.1, pp. 146–166. DOI: 10.1093/mnras/staa1894. arXiv: 2002.07226 [astro-ph.GA].

Calzetti, Daniela (Dec. 2001). “The Dust Opacity of Star-forming Galaxies”. In: *Publications of the Astronomical Society of the Pacific* 113.790, pp. 1449–1485. DOI: 10.1086/324269. arXiv: astro-ph/0109035 [astro-ph].

Ferland, G. J., M. Chatzikos, et al. (Oct. 2017). “The 2017 Release Cloudy”. In: *Revista Mexicana de Astronomía y Astrofísica* 53, pp. 385–438. DOI: 10.48550/arXiv.1705.10877. arXiv: 1705.10877 [astro-ph.GA].

Becker, George D., James S. Bolton, Piero Madau, et al. (Jan. 2015). “Evidence of patchy hydrogen reionization from an extreme Lyα trough below redshift six”. In: *Monthly Notices of the Royal Astronomical Society* 447.4, pp. 3402–3419. DOI: 10.1093/mnras/stu2646. URL: https://doi.org/10.1093%2Fmnras%2Fstu2646.

Planck Collaboration, Aghanim, N., et al. (2020). “Planck 2018 results - VI. Cosmological parameters”. In: *A&A* 641, A6. DOI: 10.1051/0004-6361/201833910. URL: https://doi.org/10.1051/0004-6361/201833910.

Bowman, Judd D., Alan E. E. Rogers, et al. (Mar. 2018). “An absorption profile centred at 78 megahertz in the sky-averaged spectrum”. In: *Nature* 555.7694, pp. 67–70. DOI: 10.1038/nature25792. URL: https://doi.org/10.1038%2Fnature25792.

Bevins, H. T. J. et al. (Dec. 2022). “Astrophysical constraints from the SARAS 3 non-detection of the cosmic dawn sky-averaged 21-cm signal”. In: *Nature Astronomy* 6, pp. 1473–1483. DOI: 10.1038/s41550-022-01825-6. arXiv: 2212.00464 [astro-ph.CO].

Patwa, Akash Kumar, Shiv Sethi, and K. S. Dwarakanath (June 2021). “Extracting the 21 cm EoR signal using MWA drift scan data”. In: *Monthly Notices of the Royal Astronomical Society* 504.2, pp. 2062–2072. DOI: 10.1093/mnras/stab989. arXiv: 2104.03321 [astro-ph.CO].

Kolopanis, Matthew et al. (Sept. 2019). “A Simplified, Lossless Reanalysis of PAPER-64”. In: *The Astrophysical Journal* 883, p. 133. DOI: 10.3847/1538-4357/ab3e3a.

DeBoer, David R. et al. (Apr. 2017). “Hydrogen Epoch of Reionization Array (HERA)”. In: *Publications of the Astronomical Society of the Pacific* 129, p. 045001. DOI: 10.1088/1538-3873/129/974/045001. arXiv: 1606.07473 [astro-ph.IM].

Choudhuri, Samir, Abhik Ghosh, et al. (Apr. 2020). “All-sky angular power spectrum – I. Estimating brightness temperature fluctuations using the 150-MHz TGSS survey”. In: *Monthly Notices of the Royal Astronomical Society* 494.2, pp. 1936–1945. DOI: 10.1093/mnras/staa762. URL: https://doi.org/10.1093%2Fmnras%2Fstaa762.

Pal, Srijita et al. (Mar. 2021). “Demonstrating the Tapered Gridded Estimator (TGE) for the cosmological H I 21-cm power spectrum using 150-MHz GMRT observations”. In: *Monthly Notices of the Royal Astronomical Society* 501.3, pp. 3378–3391. DOI: 10.1093/mnras/staa3831. arXiv: 2012.04998 [astro-ph.CO].

Koopmans, L. et al. (2015). “The Cosmic Dawn and Epoch of Reionisation with SKA”. In: *Advancing Astrophysics with the Square Kilometre Array (AASKA14)*, 1, p. 1. arXiv: 1505.07568.

Jelić, V. et al. (Sept. 2008). “Foreground simulations for the LOFAR-epoch of reionization experiment”. In: *Monthly Notices of the Royal Astronomical Society* 389, pp. 1319–1335. arXiv: 0804.1130.

Procopio, P. et al. (2017). “A High-Resolution Foreground Model for the MWA EoR1 Field: Model and Implications for EoR Power Spectrum Analysis”. In: *Publications of the Astronomical Society of Australia* 34. DOI: 10.1017/pasa.2017.26. URL: https://doi.org/10.1017%2Fpasa.2017.26.

Gong, Yan, Xuelei Chen, et al. (Oct. 2011). “The OH Line Contamination of 21 cm Intensity Fluctuation Measurements for z = 1-4”. In: *The Astrophysical Journal Letters* 740.1, p. L20. DOI: 10.1088/2041-8205/740/1/L20. arXiv: 1108.0947 [astro-ph.CO].

Fonseca, José et al. (Sept. 2016). “Cosmology with intensity mapping techniques using atomic and molecular lines”. In: *Monthly Notices of the Royal Astronomical Society* 464.2, pp. 1948–1965. DOI: 10.1093/mnras/stw2470. URL: https://doi.org/10.1093%2Fmnras%2Fstw2470.

Uzgil, Bade D. et al. (May 2021). “The ALMA Spectroscopic Survey in the HUDF: A Search for [C ii] Emitters at $6 \leq z \leq 8$”. In: *The Astrophysical Journal* 912.1, p. 67. DOI: 10.3847/1538-4357/abe86b. URL: https://doi.org/10.3847%2F1538-4357%2Fabe86b.

Lagache, Guilaine (2017). “Exploring the dusty star-formation in the early Universe using intensity mapping”. In: *Proceedings of the International Astronomical Union* 12.S333, pp. 228–233. DOI: 10.1017/S1743921318000558.

Crites, A. T. et al. (Aug. 2014). “The TIME-Pilot intensity mapping experiment”. In: *Millimeter, Submillimeter, and Far-Infrared Detectors and Instrumentation for Astronomy VII*. Ed. by Wayne S. Holland and Jonas Zmuidzinas. SPIE. DOI: 10.1117/12.2057207. URL: https://doi.org/10.1117%2F12.2057207.

Yue, B and A Ferrara (Oct. 2019). “Studying high-z galaxies with [C ii] intensity mapping”. In: *Monthly Notices of the Royal Astronomical Society* 490.2, pp. 1928–1943. DOI: 10.1093/mnras/stz2728. URL: https://doi.org/10.1093%2Fmnras%2Fstz2728.

Chang, Tzu-Ching et al. (May 2015). “Synergy of CO/[CII]/Lya Line Intensity Mapping with the SKA”. In: *Proceedings of Advancing Astrophysics with the Square Kilometre Array — PoS(AASKA14)*. Sissa Medialab. DOI: 10.22323/1.215.0004. URL: https://doi.org/10.22323%2F1.215.0004.

Datta, Kanan K., Hannes Jensen, et al. (June 2014). “Light cone effect on the reionization 21-cm signal – II. Evolution, anisotropies and observational implications”. In: *Monthly Notices of the Royal Astronomical Society* 442.2, pp. 1491–1506. DOI: 10.1093/mnras/stu927. URL: https://doi.org/10.1093%2Fmnras%2Fstu927.

Plante, P. La et al. (June 2014). “REIONIZATION ON LARGE SCALES. IV. PREDICTIONS FOR THE 21 cm SIGNAL INCORPORATING THE LIGHT CONE EFFECT”. In: *The Astrophysical*

Journal 789.1, p. 31. DOI: 10.1088/0004-637x/789/1/31. URL: https://doi.org/10.1088%2F0004-637x%2F789%2F1%2F31.

Ghara, Raghunath, Kanan K. Datta, and T. Roy Choudhury (Sept. 2015). “21 cm signal from cosmic dawn – II. Imprints of the light-cone effects”. In: *Monthly Notices of the Royal Astronomical Society* 453.3, pp. 3144–3157. DOI: 10.1093/mnras/stv1855. URL: https://doi.org/10.1093%2Fmnras%2Fstv1855.

Mondal, Rajesh, Somnath Bharadwaj, and Kanan K. Datta (Feb. 2018). “Towards simulating and quantifying the light-cone EoR 21-cm signal”. In: *Monthly Notices of the Royal Astronomical Society* 474.1, pp. 1390–1397. DOI: 10.1093/mnras/stx2888. arXiv: 1706.09449 [astro-ph.CO].

Planck Collaboration, Ade, P. A. R., et al. (2014). “Planck 2013 results. XVI. Cosmological parameters”. In: *A&A* 571, A16. DOI: 10.1051/0004-6361/201321591. URL: https://doi.org/10.1051/0004-6361/201321591.

Steffen, M. (1990). In: *A&A* 239, p. 443.

Robertson, Brant E. et al. (Apr. 2015). “Cosmic Reionization and Early Star-forming Galaxies: A Joint Analysis of New Constraints from Planck and the Hubble Space Telescope”. In: *The Astrophysical Journal Letters* 802.2, p. L19. DOI: 10.1088/2041-8205/802/2/L19. arXiv: 1502.02024 [astro-ph.CO].

Kashikawa, Nobunari, Kazuhiro Shimasaku, Matthew A. Malkan, et al. (Sept. 2006). “The End of the Reionization Epoch Probed by Lyα Emitters at $z = 6.5$ in the Subaru Deep Field”. In: *The Astrophysical Journal* 648.1, pp. 7–22. DOI: 10.1086/504966. arXiv: astro-ph/0604149 [astro-ph].

Kashikawa, Nobunari, Kazuhiro Shimasaku, Yuichi Matsuda, et al. (June 2011). “Completing the Census of Lyα Emitters at the Reionization Epoch”. In: *The Astrophysical Journal* 734.2, p. 119. DOI: 10.1088/0004-637X/734/2/119. arXiv: 1104.2330 [astro-ph.CO].

Kashikawa, Nobunari, Yoshifumi Ishizaki, et al. (Jan. 2015). “The Subaru High-z Quasar Survey: Discovery of Faint z ~6 Quasars”. In: *The Astrophysical Journal* 798.1, p. 28. DOI: 10.1088/0004-637X/798/1/28. arXiv: 1410.7401 [astro-ph.GA].

Itoh, Ryohei et al. (Nov. 2018). “CHORUS. II. Subaru/HSC Determination of the Lyα Luminosity Function at z = 7.0: Constraints on Cosmic Reionization Model Parameter”. In: *The Astrophysical Journal* 867.1, p. 46. DOI: 10.3847/1538-4357/aadfe4. arXiv: 1805.05944 [astro-ph.GA].

Matsuoka, Yoshiki et al. (Dec. 2018). “Subaru High-z Exploration of Low-luminosity Quasars (SHELLQs). V. Quasar Luminosity Function and Contribution to Cosmic Reionization at $z = 6$”. In: *The Astrophysical Journal* 869.2, p. 150. DOI: 10.3847/1538-4357/aaee7a. arXiv: 1811.01963 [astro-ph.GA].

Zheng, Zhen-Ya et al. (June 2017). “First Results from the Lyman Alpha Galaxies in the Epoch of Reionization (LAGER) Survey: Cosmological Reionization at $z \sim 7$”. In: *The Astrophysical Jour-*

nal Letters 842.2, p. L22. DOI: 10.3847/2041-8213/aa794f. arXiv: 1703.02985 [astro-ph.GA].

Hu, Weida, Junxian Wang, Zhen-Ya Zheng, Sangeeta Malhotra, Leopoldo Infante, et al. (Aug. 2017). "First Spectroscopic Confirmations of z $\sim$ 7.0 Lyα Emitting Galaxies in the LAGER Survey". In: *The Astrophysical Journal Letters* 845.2, p. L16. DOI: 10.3847/2041-8213/aa8401. arXiv: 1706.03586 [astro-ph.GA].

Hu, Weida, Junxian Wang, Zhen-Ya Zheng, Sangeeta Malhotra, James E. Rhoads, et al. (Dec. 2019). "The Lyα Luminosity Function and Cosmic Reionization at z $\sim$ 7.0: A Tale of Two LAGER Fields". In: *The Astrophysical Journal* 886.2, p. 90. DOI: 10.3847/1538-4357/ab4cf4. arXiv: 1903.09046 [astro-ph.GA].

Harish, Santosh et al. (Aug. 2022). "New Spectroscopic Confirmations of Lyα Emitters at $z \sim 7$ from the LAGER Survey". In: *The Astrophysical Journal* 934.2, p. 167. DOI: 10.3847/1538-4357/ac7cf1. arXiv: 2111.01173 [astro-ph.GA].

Wold, Isak G. B. et al. (Mar. 2022). "LAGER Lyα Luminosity Function at $z \sim 7$: Implications for Reionization". In: *The Astrophysical Journal* 927.1, p. 36. DOI: 10.3847/1538-4357/ac4997. arXiv: 2105.12191 [astro-ph.GA].

Steinhardt, Charles L., Christian Kragh Jespersen, and Nora B. Linzer (Dec. 2021). "Finding High-redshift Galaxies with JWST". In: *The Astrophysical Journal* 923.1, p. 8. DOI: 10.3847/1538-4357/ac2a2f. URL: https://doi.org/10.3847/1538-4357/ac2a2f.

Li, Tony Y. et al. (Feb. 2016). "Connecting CO Intensity Mapping to Molecular Gas and Star Formation in the Epoch of Galaxy Assembly". In: *The Astrophysical Journal* 817.2, p. 169. DOI: 10.3847/0004-637X/817/2/169. arXiv: 1503.08833 [astro-ph.CO].

Breysse, Patrick C. and Mubdi Rahman (June 2017). "Feeding cosmic star formation: exploring high-redshift molecular gas with CO intensity mapping". In: *Monthly Notices of the Royal Astronomical Society* 468.1, pp. 741–750. DOI: 10.1093/mnras/stx451. arXiv: 1606.07820 [astro-ph.GA].

Breysse, Patrick C. and Rachael M. Alexandroff (Nov. 2019). "Observing AGN feedback with CO intensity mapping". In: *Monthly Notices of the Royal Astronomical Society* 490.1, pp. 260–273. DOI: 10.1093/mnras/stz2534. arXiv: 1904.03197 [astro-ph.GA].

Ihle, H. T. et al. (Jan. 2019). "Joint Power Spectrum and Voxel Intensity Distribution Forecast on the CO Luminosity Function with COMAP". In: *The Astrophysical Journal* 871.1, p. 75. DOI: 10.3847/1538-4357/aaf4bc. arXiv: 1808.07487 [astro-ph.CO].

Moradinezhad Dizgah, Azadeh and Garrett K. Keating (Feb. 2019b). "Line Intensity Mapping with [C II] and CO(1-0) as Probes of Primordial Non-Gaussianity". In: *The Astrophysical Journal* 872.2, p. 126. DOI: 10.3847/1538-4357/aafd36. arXiv: 1810.02850 [astro-ph.CO].

Moradinezhad Dizgah, Azadeh, Farnik Nikakhtar, et al. (Feb. 2022). "Precision tests of CO and [CII] power spectra models against simulated intensity maps". In: *Journal of Cosmology and Astropar-*

ticle Physics 2022.2, p. 026. DOI: 10.1088/1475-7516/2022/02/026. arXiv: 2111.03717 [astro-ph.CO].
Visbal, Eli and Matthew McQuinn (Aug. 2018). "The Impact of Neutral Intergalactic Gas on Lyα Intensity Mapping during Reionization". In: *The Astrophysical Journal Letters* 863.1, p. L6. DOI: 10.3847/2041-8213/aad5e6. arXiv: 1807.03370 [astro-ph.CO].
Heneka, Caroline and Asantha Cooray (Sept. 2021). "Optimal survey parameters: Lyα and Hα intensity mapping for synergy with the 21-cm signal during reionization". In: *Monthly Notices of the Royal Astronomical Society* 506.2, pp. 1573–1584. DOI: 10.1093/mnras/stab1842. arXiv: 2104.12739 [astro-ph.CO].
Vieira, Joaquin et al. (Sept. 2020). "The Terahertz Intensity Mapper (TIM): a Next-Generation Experiment for Galaxy Evolution Studies". In: *arXiv e-prints*, arXiv:2009.14340, arXiv:2009.14340. arXiv: 2009.14340 [astro-ph.IM].
Keating, Garrett K., Geoffrey C. Bower, et al. (Dec. 2015). "First Results from COPSS: The CO Power Spectrum Survey". In: *The Astrophysical Journal* 814.2, p. 140. DOI: 10.1088/0004-637X/814/2/140. arXiv: 1510.06744 [astro-ph.GA].
Keating, Garrett K., Daniel P. Marrone, Geoffrey C. Bower, Erik Leitch, et al. (Oct. 2016). "COPSS II: The Molecular Gas Content of Ten Million Cubic Megaparsecs at Redshift $z \sim 3$". In: *The Astrophysical Journal* 830.1, p. 34. DOI: 10.3847/0004-637X/830/1/34. arXiv: 1605.03971 [astro-ph.GA].
Cox, Tyler A., Daniel C. Jacobs, and Steven G. Murray (May 2022). "Estimating the feasibility of 21cm-Lyα synergies using the hydrogen Epoch of Reionization array". In: *Monthly Notices of the Royal Astronomical Society* 512.1, pp. 792–801. DOI: 10.1093/mnras/stac486. arXiv: 2202.08957 [astro-ph.CO].
Cooray, Asantha et al. (Sept. 2019). "Cosmic Dawn Intensity Mapper". In: *Bulletin of the American Astronomical Society*. Vol. 51, p. 23. arXiv: 1903.03144 [astro-ph.GA].
Schaan, Emmanuel and Martin White (May 2021). "Multi-tracer intensity mapping: cross-correlations, line noise & decorrelation". In: *Journal of Cosmology and Astroparticle Physics* 2021.05, p. 068. DOI: 10.1088/1475-7516/2021/05/068. URL: https://doi.org/10.1088%2F1475-7516%2F2021%2F05%2F068.
Yang, Shengqi et al. (Apr. 2022). "An Empirical Representation of a Physical Model for the ISM [C II], CO, and [C I] Emission at Redshift $1 \leq z \leq 9$". In: *The Astrophysical Journal* 929.2, p. 140. DOI: 10.3847/1538-4357/ac5d57. arXiv: 2108.07716 [astro-ph.GA].
Ferland, G. J., R. L. Porter, et al. (Apr. 2013). "The 2013 Release of Cloudy". In: *Revista Mexicana de Astronomía y Astrofísica* 49, pp. 137–163. arXiv: 1302.4485 [astro-ph.GA].
Accurso, G. et al. (Jan. 2017). "Radiative transfer meets Bayesian statistics: where does a galaxy's [C II] emission come from?" In: *Monthly Notices of the Royal Astronomical Society* 464.3, pp. 3315–3330. DOI: 10.1093/mnras/stw2580. arXiv: 1607.03488 [astro-ph.GA].

Vizgan, D. et al. (Apr. 2022). "Tracing Molecular Gas Mass in $z \simeq 6$ Galaxies with [C II]". In: *The Astrophysical Journal* 929.1, p. 92. DOI: 10.3847/1538-4357/ac5cba.

Pineda, J. L., W. D. Langer, and P. F. Goldsmith (Oct. 2014). "A Herschel [C II] Galactic plane survey. III. [C II] as a tracer of star formation". In: *Astronomy & Astrophysics* 570, A121. DOI: 10.1051/0004-6361/201424054. arXiv: 1409.0537 [astro-ph.GA].

Hopkins, Philip F. (June 2015). "A new class of accurate, mesh-free hydrodynamic simulation methods". In: *Monthly Notices of the Royal Astronomical Society* 450.1, pp. 53–110. DOI: 10.1093/mnras/stv195. arXiv: 1409.7395 [astro-ph.CO].

— (Dec. 2017). "A New Public Release of the GIZMO Code". In: *arXiv e-prints*, arXiv:1712.01294, arXiv:1712.01294. arXiv: 1712.01294 [astro-ph.IM].

Padmanabhan, Hamsa (Sept. 2019). "Constraining the evolution of [C II] intensity through the end stages of reionization". In: *Monthly Notices of the Royal Astronomical Society* 488.3, pp. 3014–3023. DOI: 10.1093/mnras/stz1878. arXiv: 1811.01968 [astro-ph.CO].

Murmu, Chandra Shekhar, Raghunath Ghara, et al. (Dec. 2022). "Probing the epoch of reionization using synergies of line intensity mapping". In: *Journal of Astrophysics and Astronomy* 43.2. ISSN: 0973-7758. DOI: 10.1007/s12036-022-09882-z. arXiv: 2210.09612 [astro-ph.CO]. URL: http://dx.doi.org/10.1007/s12036-022-09882-z.

Karoumpis, C. et al. (Mar. 2022). "[CII] line intensity mapping the epoch of reionization with the Prime-Cam on FYST. I. Line intensity mapping predictions using the Illustris TNG hydrodynamical simulation". In: *Astronomy & Astrophysics* 659, A12. DOI: 10.1051/0004-6361/202141293. arXiv: 2111.12847 [astro-ph.GA].

Moradinezhad Dizgah, Azadeh, Emilio Bellini, and Garrett K. Keating (Apr. 2024). "Probing Dark Energy and Modifications of Gravity with Ground-based millimeter-wavelength Line Intensity Mapping". In: *The Astrophysical Journal* 965.1, p. 19. DOI: 10.3847/1538-4357/ad2078. arXiv: 2304.08471 [astro-ph.CO].

Roy, Anirban et al. (Nov. 2023). "LIMpy: A Semianalytic Approach to Simulating Multiline Intensity Maps at Millimeter Wavelengths". In: *The Astrophysical Journal* 957.2, p. 87. DOI: 10.3847/1538-4357/acf92f. arXiv: 2304.06748 [astro-ph.GA].

Peterson, J. B. and Enrique Suarez (June 2012). "Intensity Mapping with the 21-cm and Lyman Alpha Lines". In: *arXiv e-prints*, arXiv:1206.0143, arXiv:1206.0143. DOI: 10.48550/arXiv.1206.0143. arXiv: 1206.0143 [astro-ph.CO].

Mas-Ribas, Lluís and Tzu-Ching Chang (Apr. 2020). "Lyman-α polarization intensity mapping". In: *Physical Review D* 101.8, p. 083032. DOI: 10.1103/PhysRevD.101.083032. arXiv: 2002.04107 [astro-ph.GA].

Padmanabhan, Hamsa (Aug. 2023). "Synergizing 21 cm and submillimetre surveys during reionization: new empirical insights". In: *Monthly Notices of the Royal Astronomical Society* 523.3, pp. 3503–3515. DOI: 10.1093/mnras/stad1559. arXiv: 2212.08077 [astro-ph.CO].

Breysse, Patrick C., Ely D. Kovetz, and Marc Kamionkowski (Oct. 2014). “Carbon monoxide intensity mapping at moderate redshifts”. In: *Monthly Notices of the Royal Astronomical Society* 443.4, pp. 3506–3512. DOI: 10.1093/mnras/stu1312. arXiv: 1405.0489 [astro-ph.CO].

Murmu, Chandra Shekhar, Karen P. Olsen, et al. (Jan. 2023). “Revisiting the [C II] $_{158\mu m}$ line-intensity mapping power spectrum from the EoR using non-uniform line-luminosity scatter”. In: *Monthly Notices of the Royal Astronomical Society* 518.2, pp. 3074–3082. DOI: 10.1093/mnras/stac3304. arXiv: 2110.10687 [astro-ph.CO].

Shimabukuro, Hayato et al. (July 2015). “Studying 21cm power spectrum with one-point statistics”. In: *Monthly Notices of the Royal Astronomical Society* 451.1, pp. 467–474. DOI: 10.1093/mnras/stv965. arXiv: 1412.3332 [astro-ph.CO].

Watkinson, C. A. and J. R. Pritchard (Oct. 2014). “Distinguishing models of reionization using future radio observations of 21-cm 1-point statistics”. In: *Monthly Notices of the Royal Astronomical Society* 443.4, pp. 3090–3106. DOI: 10.1093/mnras/stu1384. arXiv: 1312.1342 [astro-ph.CO].

— (Dec. 2015). “The impact of spin-temperature fluctuations on the 21-cm moments”. In: *Monthly Notices of the Royal Astronomical Society* 454.2, pp. 1416–1431. DOI: 10.1093/mnras/stv2010. arXiv: 1505.07108 [astro-ph.CO].

Kubota, Kenji et al. (Aug. 2016). “Expected constraints on models of the epoch of reionization with the variance and skewness in redshifted 21 cm-line fluctuations”. In: *Publications of the Astronomical Society of Japan* 68.4, p. 61. DOI: 10.1093/pasj/psw059. arXiv: 1602.02873 [astro-ph.CO].

Ross, Hannah E. et al. (Sept. 2021). “Redshift-space distortions in simulations of the 21-cm signal from the cosmic dawn”. In: *Monthly Notices of the Royal Astronomical Society* 506.3, pp. 3717–3733. DOI: 10.1093/mnras/stab1822. arXiv: 2011.03558 [astro-ph.CO].

Daddi, E., M. Dickinson, et al. (Nov. 2007). “Multiwavelength Study of Massive Galaxies at z$\sim$2. I. Star Formation and Galaxy Growth”. In: *The Astrophysical Journal* 670.1, pp. 156–172. DOI: 10.1086/521818. arXiv: 0705.2831 [astro-ph].

Noeske, K. G. et al. (May 2007). “Star Formation in AEGIS Field Galaxies since z=1.1: The Dominance of Gradually Declining Star Formation, and the Main Sequence of Star-forming Galaxies”. In: *The Astrophysical Journal* 660.1, pp. L43–L46. DOI: 10.1086/517926. arXiv: astro-ph/0701924 [astro-ph].

Magdis, G. E. et al. (Jan. 2010). “On the stellar masses of IRAC detected Lyman Break Galaxies at z $\sim$3”. In: *Monthly Notices of the Royal Astronomical Society* 401.3, pp. 1521–1531. DOI: 10.1111/j.1365-2966.2009.15779.x. arXiv: 0909.3950 [astro-ph.CO].

Whitaker, Katherine E. et al. (Aug. 2012). “The Star Formation Mass Sequence Out to $z = 2.5$”. In: *The Astrophysical Journal Letters* 754.2, p. L29. DOI: 10.1088/2041-8205/754/2/L29. arXiv: 1205.0547 [astro-ph.CO].

Bharadwaj, Somnath and Sanjay K. Pandey (Apr. 2005). “Probing non-Gaussian features in the HI distribution at the epoch of re-ionization”. In: *Monthly Notices of the Royal Astronomical Society* 358.3, pp. 968–976. DOI: 10.1111/j.1365-2966.2005.08836.x. arXiv: astro-ph/0410581 [astro-ph].

Iliev, I. T. et al. (July 2006). “Simulating cosmic reionization at large scales - I. The geometry of reionization”. In: *Monthly Notices of the Royal Astronomical Society* 369.4, pp. 1625–1638. DOI: 10.1111/j.1365-2966.2006.10502.x. arXiv: astro-ph/0512187 [astro-ph].

Mellema, Garrelt, Ilian T. Iliev, Ue-Li Pen, et al. (Oct. 2006). “Simulating cosmic reionization at large scales - II. The 21-cm emission features and statistical signals”. In: *Monthly Notices of the Royal Astronomical Society* 372.2, pp. 679–692. DOI: 10.1111/j.1365-2966.2006.10919.x. arXiv: astro-ph/0603518 [astro-ph].

Planck Collaboration, N. Aghanim, Y. Akrami, M. Ashdown, et al. (Sept. 2020). “Planck 2018 results. VI. Cosmological parameters”. In: *Astronomy & Astrophysics* 641, A6, A6. DOI: 10.1051/0004-6361/201833910. arXiv: 1807.06209 [astro-ph.CO].

Scoccimarro, Román, Emiliano Sefusatti, and Matias Zaldarriaga (May 2004). “Probing primordial non-Gaussianity with large-scale structure”. In: *Physical Review D* 69.10, p. 103513. DOI: 10.1103/PhysRevD.69.103513. arXiv: astro-ph/0312286 [astro-ph].

Liguori, Michele et al. (Jan. 2010). “Primordial Non-Gaussianity and Bispectrum Measurements in the Cosmic Microwave Background and Large-Scale Structure”. In: *Advances in Astronomy* 2010, p. 980523. DOI: 10.1155/2010/980523. arXiv: 1001.4707 [astro-ph.CO].

Bull, Philip et al. (Apr. 2015). “Late-time Cosmology with 21 cm Intensity Mapping Experiments”. In: *The Astrophysical Journal* 803.1, p. 21. DOI: 10.1088/0004-637X/803/1/21. arXiv: 1405.1452 [astro-ph.CO].

Obuljen, Andrej et al. (May 2018). “High-redshift post-reionization cosmology with 21cm intensity mapping”. In: *Journal of Cosmology and Astroparticle Physics* 2018.5, p. 004. DOI: 10.1088/1475-7516/2018/05/004. arXiv: 1709.07893 [astro-ph.CO].

Mellema, Garrelt, Léon V. E. Koopmans, et al. (Aug. 2013). “Reionization and the Cosmic Dawn with the Square Kilometre Array”. In: *Experimental Astronomy* 36.1-2, pp. 235–318. DOI: 10.1007/s10686-013-9334-5. arXiv: 1210.0197 [astro-ph.CO].

Mazumder, Aishrila et al. (Sept. 2022). “Observing the reionization: effect of calibration and position errors on realistic observation conditions”. In: *Monthly Notices of the Royal Astronomical Society* 515.3, pp. 4020–4037. DOI: 10.1093/mnras/stac1994. arXiv: 2207.06169 [astro-ph.CO].

Draine, Bruce T. (2011). *Physics of the Interstellar and Intergalactic Medium*. Princeton University Press.

Kovetz, Ely D. et al. (Sept. 2017). “Line-Intensity Mapping: 2017 Status Report”. In: *arXiv e-prints*, arXiv:1709.09066, arXiv:1709.09066. DOI: 10.48550/arXiv.1709.09066. arXiv: 1709.09066 [astro-ph.CO].

Kovetz, Ely et al. (May 2019). “Astrophysics and Cosmology with Line-Intensity Mapping”. In: *Bulletin of the American Astronomical Society* 51.3, p. 101. DOI: 10.48550/arXiv.1903.04496. arXiv: 1903.04496 [astro-ph.CO].

Carilli, C. L. (Apr. 2011). “Intensity Mapping of Molecular Gas During Cosmic Reionization”. In: *The Astrophysical Journal Letters* 730.2, p. L30. DOI: 10.1088/2041-8205/730/2/L30. arXiv: 1102.0745 [astro-ph.CO].

Keating, Garrett K., Daniel P. Marrone, Geoffrey C. Bower, and Ryan P. Keenan (Oct. 2020). “An Intensity Mapping Detection of Aggregate CO Line Emission at 3 mm”. In: *The Astrophysical Journal* 901.2, p. 141. DOI: 10.3847/1538-4357/abb08e. arXiv: 2008.08087 [astro-ph.GA].

Breysse, Patrick C., Shengqi Yang, et al. (Apr. 2022). “On Estimating the Cosmic Molecular Gas Density from CO Line Intensity Mapping Observations”. In: *The Astrophysical Journal* 929.1, p. 30. DOI: 10.3847/1538-4357/ac5a46. arXiv: 2106.14904 [astro-ph.CO].

Lamb, James W. et al. (July 2022). “COMAP Early Science. II. Pathfinder Instrument”. In: *The Astrophysical Journal* 933.2, p. 183. DOI: 10.3847/1538-4357/ac63c6. arXiv: 2111.05928 [astro-ph.IM].

Chung, Dongwoo T. (Dec. 2023). “Constraining the halo-ISM connection through multi-transition carbon monoxide line-intensity mapping”. In: *Journal of Cosmology and Astroparticle Physics* 2023.12, p. 024. DOI: 10.1088/1475-7516/2023/12/024. arXiv: 2309.03184 [astro-ph.CO].

Bowman, Judd D., Miguel F. Morales, and Jacqueline N. Hewitt (Feb. 2006). “The Sensitivity of First-Generation Epoch of Reionization Observatories and Their Potential for Differentiating Theoretical Power Spectra”. In: *The Astrophysical Journal* 638.1, pp. 20–26. DOI: 10.1086/498703. arXiv: astro-ph/0507357 [astro-ph].

Kuiack, Mark et al. (Jan. 2019). “AARTFAAC flux density calibration and Northern hemisphere catalogue at 60 MHz”. In: *Monthly Notices of the Royal Astronomical Society* 482.2, pp. 2502–2514. DOI: 10.1093/mnras/sty2810. arXiv: 1810.06430 [astro-ph.IM].

Ellingson, S. W. et al. (May 2013). “The LWA1 Radio Telescope”. In: *IEEE Transactions on Antennas and Propagation* 61.5, pp. 2540–2549. DOI: 10.1109/TAP.2013.2242826. arXiv: 1204.4816 [astro-ph.IM].

Tingay, S. J. et al. (2013). “The Murchison Widefield Array: The Square Kilometre Array Precursor at Low Radio Frequencies”. In: *Publications of the Astronomical Society of Australia* 30. DOI: 10.1017/pasa.2012.007. URL: https://doi.org/10.1017%2Fpasa.2012.007.

van der Tak, F. F. S. et al. (June 2007). “A computer program for fast non-LTE analysis of interstellar line spectra. With diagnostic plots to interpret observed line intensity ratios”. In: *Astronomy & Astrophysics* 468.2, pp. 627–635. DOI: 10.1051/0004-6361:20066820. arXiv: 0704.0155 [astro-ph].

Gao, Yu and Philip M. Solomon (May 2004). “The Star Formation Rate and Dense Molecular Gas in Galaxies”. In: *The Astrophysical Journal* 606.1, pp. 271–290. DOI: 10.1086/382999. arXiv: astro-ph/0310339 [astro-ph].

García-Burillo, S. et al. (Mar. 2012). “Star-formation laws in luminous infrared galaxies. New observational constraints on models”. In: *Astronomy & Astrophysics* 539, A8. DOI: 10.1051/0004-6361/201117838. arXiv: 1111.6773 [astro-ph.CO].

Hinshaw, G. et al. (Oct. 2013). “Nine-year Wilkinson Microwave Anisotropy Probe (WMAP) Observations: Cosmological Parameter Results”. In: *The Astrophysical Journal Supplement Series* 208.2, p. 19. DOI: 10.1088/0067-0049/208/2/19. arXiv: 1212.5226 [astro-ph.CO].

Watson, William A. et al. (Aug. 2013). “The halo mass function through the cosmic ages”. In: *Monthly Notices of the Royal Astronomical Society* 433.2, pp. 1230–1245. DOI: 10.1093/mnras/stt791. arXiv: 1212.0095 [astro-ph.CO].

Giri, Sambit K., Garrelt Mellema, Thomas Aldheimer, et al. (Oct. 2019). “Neutral island statistics during reionization from 21-cm tomography”. In: *Monthly Notices of the Royal Astronomical Society* 489.2, pp. 1590–1605. DOI: 10.1093/mnras/stz2224. arXiv: 1903.01294 [astro-ph.GA].

Mondal, Rajesh, Abinash Kumar Shaw, et al. (May 2020). “Predictions for measuring the 21-cm multifrequency angular power spectrum using SKA-Low”. In: *Monthly Notices of the Royal Astronomical Society* 494.3, pp. 4043–4056. DOI: 10.1093/mnras/staa1026. arXiv: 1910.05196 [astro-ph.CO].

Behroozi, Peter S., Risa H. Wechsler, and Charlie Conroy (Jan. 2013). “On the Lack of Evolution in Galaxy Star Formation Efficiency”. In: *The Astrophysical Journal Letters* 762.2, p. L31. DOI: 10.1088/2041-8205/762/2/L31. arXiv: 1209.3013 [astro-ph.CO].

Leroy, Adam K., Fabian Walter, Elias Brinks, et al. (Dec. 2008). “The Star Formation Efficiency in Nearby Galaxies: Measuring Where Gas Forms Stars Effectively”. In: *The Astronomical Journal* 136.6, pp. 2782–2845. DOI: 10.1088/0004-6256/136/6/2782. arXiv: 0810.2556 [astro-ph].

Leroy, Adam K., Fabian Walter, Frank Bigiel, et al. (June 2009). “Heracles: The HERA CO Line Extragalactic Survey”. In: *The Astronomical Journal* 137.6, pp. 4670–4696. DOI: 10.1088/0004-6256/137/6/4670. arXiv: 0905.4742 [astro-ph.CO].

Leroy, Adam K., Fabian Walter, Karin Sandstrom, et al. (Aug. 2013). “Molecular Gas and Star Formation in nearby Disk Galaxies”. In: *The Astronomical Journal* 146.2, p. 19. DOI: 10.1088/0004-6256/146/2/19. arXiv: 1301.2328 [astro-ph.CO].

Saintonge, Amélie et al. (July 2011). “COLD GASS, an IRAM legacy survey of molecular gas in massive galaxies - I. Relations between H_2, H I, stellar content and structural properties”. In: *Monthly Notices of the Royal Astronomical Society* 415.1, pp. 32–60. DOI: 10.1111/j.1365-2966.2011.18677.x. arXiv: 1103.1642 [astro-ph.CO].

Geach, James E. et al. (Apr. 2011). "On the Evolution of the Molecular Gas Fraction of Star-Forming Galaxies". In: *The Astrophysical Journal Letters* 730.2, p. L19. DOI: 10.1088/2041-8205/730/2/L19. arXiv: 1102.3694 [astro-ph.CO].

Daddi, E., D. Elbaz, et al. (May 2010). "Different Star Formation Laws for Disks Versus Starbursts at Low and High Redshifts". In: *The Astrophysical Journal Letters* 714.1, pp. L118–L122. DOI: 10.1088/2041-8205/714/1/L118. arXiv: 1003.3889 [astro-ph.CO].

Tacconi, L. J. et al. (May 2013). "Phibss: Molecular Gas Content and Scaling Relations in z ~1-3 Massive, Main-sequence Star-forming Galaxies". In: *The Astrophysical Journal* 768.1, p. 74. DOI: 10.1088/0004-637X/768/1/74. arXiv: 1211.5743 [astro-ph.CO].

Magdis, Georgios E. et al. (Oct. 2012). "The Molecular Gas Content of z = 3 Lyman Break Galaxies: Evidence of a Non-evolving Gas Fraction in Main-sequence Galaxies at z > 2". In: *The Astrophysical Journal Letters* 758.1, p. L9. DOI: 10.1088/2041-8205/758/1/L9. arXiv: 1209.1484 [astro-ph.CO].

Bauermeister, A. et al. (May 2013). "The EGNoG Survey: Molecular Gas in Intermediate-Redshift Star-Forming Galaxies". In: *The Astrophysical Journal* 768.2, p. 132. DOI: 10.1088/0004-637X/768/2/132. arXiv: 1304.0010 [astro-ph.CO].

van der Werf, P. P. et al. (July 2010). "Black hole accretion and star formation as drivers of gas excitation and chemistry in Markarian 231". In: *Astronomy & Astrophysics* 518, p. L42. DOI: 10.1051/0004-6361/201014682. arXiv: 1005.2877 [astro-ph.GA].

Papadopoulos, Padeli P. et al. (June 2010). "CO Spectral Line Energy Distributions of Infrared-Luminous Galaxies and Active Galactic Nuclei". In: *The Astrophysical Journal* 715.2, pp. 775–792. DOI: 10.1088/0004-637X/715/2/775. arXiv: 1003.5889 [astro-ph.CO].

Solomon, P. M. and P. A. Vanden Bout (Sept. 2005). "Molecular Gas at High Redshift". In: *Annual Review of Astronomy and Astrophysics* 43.1, pp. 677–725. DOI: 10.1146/annurev.astro.43.051804.102221. arXiv: astro-ph/0508481 [astro-ph].

Greve, T. R., F. Bertoldi, et al. (May 2005). "An interferometric CO survey of luminous submillimetre galaxies". In: *Monthly Notices of the Royal Astronomical Society* 359.3, pp. 1165–1183. DOI: 10.1111/j.1365-2966.2005.08979.x. arXiv: astro-ph/0503055 [astro-ph].

Bothwell, M. S. et al. (Dec. 2013). "SPT 0538-50: Physical Conditions in the Interstellar Medium of a Strongly Lensed Dusty Star-forming Galaxy at z = 2.8". In: *The Astrophysical Journal* 779.1, p. 67. DOI: 10.1088/0004-637X/779/1/67. arXiv: 1309.3275 [astro-ph.CO].

Lu, N. et al. (June 2014). "Warm Molecular Gas in Luminous Infrared Galaxies". In: *The Astrophysical Journal Letters* 787.2, p. L23. DOI: 10.1088/2041-8205/787/2/L23. arXiv: 1405.0313 [astro-ph.GA].

Liu, Daizhong et al. (Sept. 2015). "High-J CO versus Far-infrared Relations in Normal and Starburst Galaxies". In: *The Astrophysical Journal Letters* 810.2, p. L14. DOI: 10.1088/2041-8205/810/2/L14. arXiv: 1504.05897 [astro-ph.GA].

Mertens, Florent G., Jérôme Bobin, and Isabella P. Carucci (Jan. 2024). "Retrieving the 21-cm signal from the Epoch of Reionization with learnt Gaussian process kernels". In: *Monthly Notices of the Royal Astronomical Society* 527.2, pp. 3517–3531. DOI: 10.1093/mnras/stad3430. arXiv: 2307.13545 [astro-ph.CO].

Daddi, E., H. Dannerbauer, et al. (May 2015). "CO excitation of normal star-forming galaxies out to $z = 1.5$ as regulated by the properties of their interstellar medium". In: *Astronomy & Astrophysics* 577, A46. DOI: 10.1051/0004-6361/201425043. arXiv: 1409.8158 [astro-ph.GA].

Breysse, Patrick C., Ely D. Kovetz, and Marc Kamionkowski (Mar. 2016). "The high-redshift star formation history from carbon-monoxide intensity maps". In: *Monthly Notices of the Royal Astronomical Society* 457.1, pp. L127–L131. DOI: 10.1093/mnrasl/slw005. arXiv: 1507.06304 [astro-ph.CO].